Qubit arrays in germanium

Hendrickx, N.W.

DOI
10.4233/uuid:25bd462e-5d62-4b9d-9817-692d62a36eab

Publication date
2021

Document Version
Final published version

Citation (APA)
Hendrickx, N. W. (2021). *Qubit arrays in germanium*. [Dissertation (TU Delft), Delft University of Technology]. https://doi.org/10.4233/uuid:25bd462e-5d62-4b9d-9817-692d62a36eab

Qubit arrays in germanium

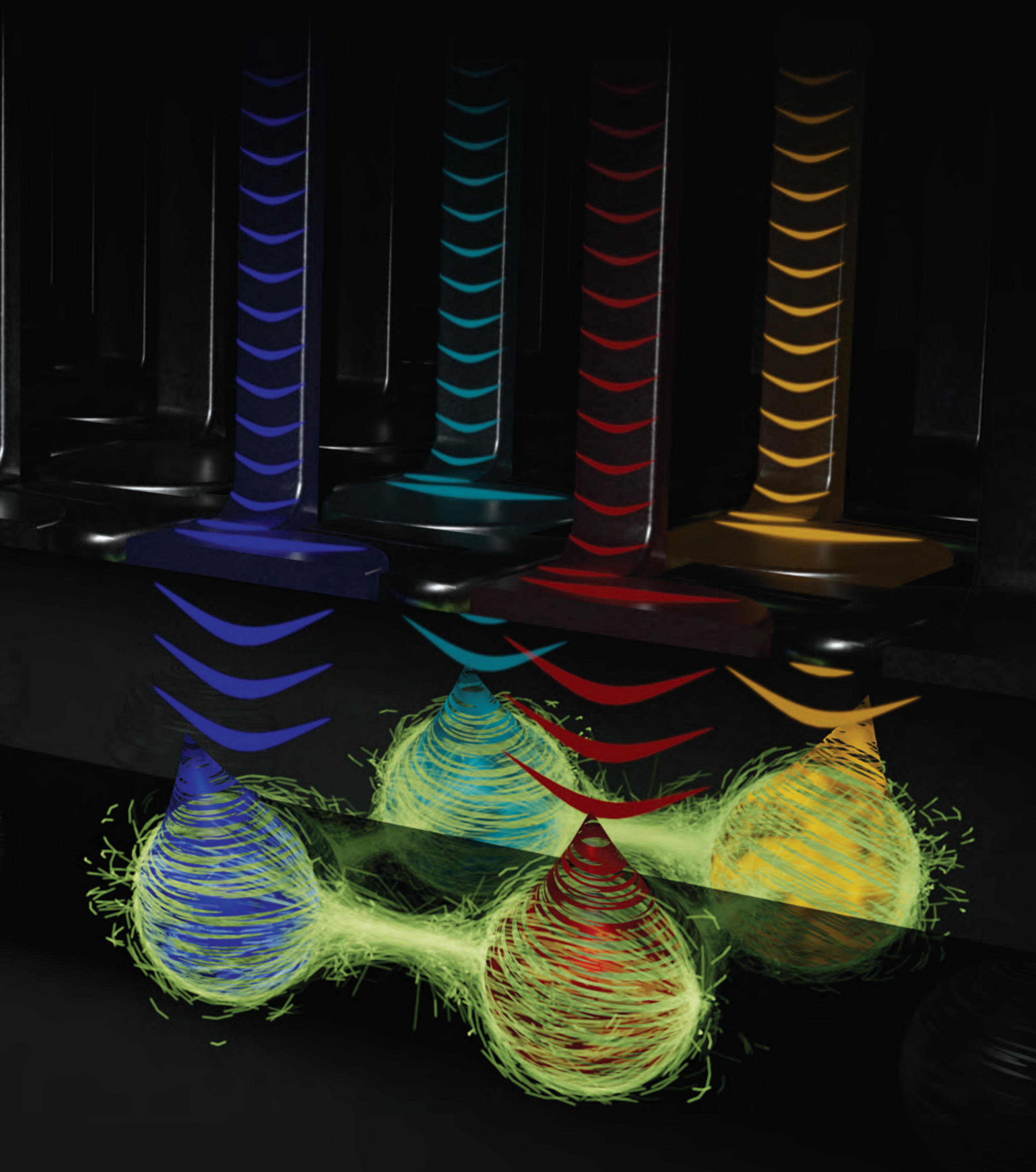

Nico W. Hendrickx

Propositions

accompanying the dissertation

QUBIT ARRAYS IN GERMANIUM

by

Nico Willem HENDRICKX

1. The germanium quantum well should be distanced sufficiently far from the wafer surface to fully benefit from the advantages that a heterostructure provides (chapter 6 of this thesis).
2. When the tunnel coupling between two quantum dots can be well controlled, the controlled-phase gate should always be preferred over the controlled-rotation gate (chapter 10 of this thesis).
3. The low degree of disorder combined with the high degree of electrical control positions germanium as the most appropriate platform for defining two-dimensional spin qubit arrays.
4. To carry out a successful experiment, it is vital for calibration routines to be significantly faster than the time scale over which the system remains stable.
5. Due to its fundamentally different motivations, an academic institution is not able to employ a mission-driven strategy with the same success as a private company.
6. A good understanding of the theory and the setup is essential to perform groundbreaking experiments.
7. Discussions about failure modes in academic device fabrication are mostly unproductive, due to the high level of process variability and the lack of proper metrics.
8. An opportunistic mindset will lead to increased scientific output.
9. Working from home hampers creativity.
10. The sustainability movement contributes to the positive connotation of an *all-electric* qubit.

These propositions are regarded as opposable and defendable, and have been approved as such by the (co)promotors prof. dr. ir. L.M.K. Vandersypen and dr. ir. M. Veldhorst.

Stellingen

behorende bij het proefschrift

Qubit arrays in germanium

door

Nico Willem Hendrickx

1. De germanium kwantumput dient op voldoende afstand van het grensvlak van de *wafer* te worden gegroeid om de voordelen van een heterostructuur optimaal te kunnen benutten (hoofdstuk 6 van dit proefschrift).
2. Wanneer men voldoende controle over de tunnelkoppeling tussen twee kwantumdots heeft, dient de gecontroleerde fasepoort altijd verkozen te worden boven de gecontroleerde rotatiepoort als tweekwantumbitpoort (hoofdstuk 10 van dit proefschrift).
3. De lage graad van wanorde, gecombineerd met de hoge graad van elektrische controle maakt germanium het meest geschikte platform voor het definiëren van tweedimensionale spinkwantumbitrasters.
4. Om een succesvol experiment uit te voeren, is het van belang dat de kalibratieroutines significant sneller zijn dan de tijdschaal waarover het systeem stabiel blijft.
5. Een academische instelling zal vanwege haar fundamenteel afwijkende motivaties niet met hetzelfde succes dezelfde doelgerichte werkwijze kunnen hanteren als een industrieel bedrijf.
6. Een goed begrip van onderliggende theorie en opstelling is essentieel voor het doen van grensverleggende experimenten.
7. Discussies over de manier van falen van academische nanofabricage zijn weinig productief, te wijten aan de hoge mate van variabiliteit in het proces en het gebrek aan goede statistieken.
8. Een opportunistische instelling leidt tot een hoger wetenschappelijk rendement.
9. Thuiswerken belemmert de creativiteit.
10. De huidige duurzaamheidsbeweging draagt bij aan de positieve connotatie van een *volledig elektrische* kwantumbit.

Deze stellingen worden opponeerbaar en verdedigbaar geacht en zijn als zodanig goedgekeurd door de (co)promotors prof. dr. ir. L.M.K. Vandersypen en dr. ir. M. Veldhorst.

QUBIT ARRAYS IN GERMANIUM

QUBIT ARRAYS IN GERMANIUM

Proefschrift

ter verkrijging van de graad van doctor
aan de Technische Universiteit Delft,
op gezag van de Rector Magnificus prof. dr. ir. T.H.J.J. van der Hagen,
voorzitter van het College voor Promoties,
in het openbaar te verdedigen op maandag 12 juli 2021 om 12:30 uur

door

Nico Willem HENDRICKX

Master of Science in Applied Physics,
Universiteit Twente, Nederland
geboren te Groningen, Nederland.

Dit proefschrift is goedgekeurd door de

promotor: prof. dr. ir. L.M.K. Vandersypen
copromotor: dr. ir. M. Veldhorst

Samenstelling promotiecommissie:

Rector Magnificus,	voorzitter
Prof. dr. ir. L.M.K. Vandersypen	Technische Universiteit Delft, promotor
Dr. ir. M. Veldhorst	Technische Universiteit Delft, copromotor
Onafhankelijke leden:	
Prof. dr. ir. L.P. Kouwenhoven	Technische Universiteit Delft
Prof. dr. ir. R. Hanson	Technische Universiteit Delft
Prof. dr. A.S. Dzurak	University of New South Wales
Prof. dr. D. Loss	Universität Basel
Overige leden:	
Dr. G. Scappucci	Technische Universiteit Delft

Trefwoorden: quantum computing, quantum dots, spin qubits, germanium, hole qubits, multi-qubit systems

Geprint door: Gildeprint

Omslag: Illustratie van elektrisch aangestuurde germanium spinkwantumbits in een tweedimensionaal raster. Ontwerp: Nico Hendrickx.

Casimir PhD Series, Delft-Leiden 2021-16

This work is supported by a FOM projectruimte, which is funded by the Dutch Research Council (NWO).

ISBN 978-90-8593-482-0

CONTENTS

1

INTRODUCTION

When John Bardeen, William Shockley, and Walter Brattain presented the first transistor in 1947, they marked the start of a new era. Using a slice of germanium crystal and a well-crafted set of gold contacts, they created an amplifier purely in the solid state [1]. Following this invention, in 1958, Jack Kilby defined an electronic circuit combining multiple transistors with capacitors and resistors within a single piece of semiconductor, creating the first integrated circuit [2]. For these initial developments, the use of germanium as a semiconductor was favoured over silicon, owing to its higher carrier mobility [3]. However, the superior properties of silicon dioxide and its interface to silicon compared to germanium oxides eased device fabrication and this led to the invention of the (silicon) MOSFET.

From here forward, development moved rapidly, with technological breakthroughs allowing for more and more transistors to be combined onto a single chip at an unprecedented rate, enabling home computers, self-driving cars and manned missions to the moon [4]. Currently, transistor counts are exceeding 50 billion in a single computing core [5], with footprints as low as 5 nm [6]. As the transistors are getting smaller, the properties of the individual particles rather than the larger, classical ensemble need to be considered and quantum effects emerge [7]. While this additional complexity can complicate the development of classical transistors, the richer physics also enable a realm of new possibilities [8, 9]. To put it in the words of the famous Dutch philosopher Johan Cruijff: *"Elk nadeel heb zijn voordeel"* [With every disadvantage there is an advantage]. The notion that these quantum effects can be used to enable more powerful simulations, calculations, and communications is central to the concept of quantum information technology.

The core building block of a quantum computer is the quantum bit (qubit). Like a classical bit, which can be either on (1) or off (0), a qubit is also defined by two eigenstates denoted by $|1\rangle$ and $|0\rangle$. Unlike its classical counterpart, however, the qubit does not solely reside in either of the eigenstates, but can also occupy a superposition state of both at the same time. This, combined with the ability to entangle multiple qubits, can greatly enhance the computational power of such a system, compared to a classical computer [10].

However, there is a caveat to this (it seems like Cruijff's quote is commutative). Quantum states are intrinsically fragile and can lose their 'quantum information' (or coherence) as a result of unwanted interactions with the environment. When the qubit is completely isolated from its environment, all operations are unitary and coherence is preserved. However, in practice, we want to interact with the qubits to initialise, control and measure them. This requires an interaction with the environment, which will inevitably also lead to decoherence. Establishing a good balance between having enough interaction to allow for fast qubit control, coupling, and measurements, while maintaining enough isolation to preserve the quantum state is one of the key challenges for quantum computation. Furthermore, qubits are sensitive to small errors in the operation signals. While a classic bit is purely digital and therefore insensitive to small variations in operation signals, qubits are sensitive to the smallest miscalibrations and these may rapidly lead to large errors when executing long algorithms.

The obvious route to try to overcome these issues is to improve the coherence of the qubits and the quality of the operations. Great improvements have been made to this end and error rates below 1 % were achieved in multiple qubit systems [11, 12]. These error rates and the system sizes have now reached the point at which calculations can be done that are deemed classically intractable, as was recently demonstrated by the authors of Ref. [12] on a superconducting quantum processor or the authors of Ref. [13] using a photonic system. This regime, in which we use noisy qubits to enable calculations surpassing the capability of classical computers, has been coined the noisy intermediate-scale quantum (NISQ) technology [14].

The ultimate method to overcome inevitable errors is to define an operation scheme in which the errors are acknowledged and subsequently fixed. Many *quantum error correction* schemes have been proposed [15–17], typically relying on thousands of physical qubits to encode a single logical (error-free) qubit [18]. The redundancy introduced by adding more physical qubits allows for the detection and correction of errors, making the quantum information processing *fault tolerant*. Consequently, large numbers of physical qubits are needed to create a practical quantum computer with low error rates. Currently, systems with several tens of (physical) qubits exist [12, 19] and developments are transitioning from a purely academic interest towards industrial efforts as well [20–24], scaling up the number of available qubits every year.

Many different types of physical qubits exist, with a handful being pursued by industry at the time of writing. Quantum dot spin qubits [25] are amongst these, partly due to their similarity to the classical transistor (which is well understood in the semiconductor industry, of course). Their small footprint and inherent compatibility with conventional semiconductor circuits are argued to benefit scalability [26]. Initial research focussed on the group III-V semiconductor GaAs, of which all isotopes possess a non-zero nuclear spin. When the nuclei in the host crystal carry a spin, they form a large (noisy) environmental bath for the spin qubit, resulting in a high degree of decoherence. Conversely, both of the group IV semiconductors silicon and germanium have a large abundance of net-zero nuclear spin isotopes and can be further isotopically purified to contain vanishing amounts of nuclear spins [27, 28]. Research focus thus shifted to using silicon as the host crystal, being the common material in the semiconductor industry. However, the limitations which stimulated the industry's shift towards silicon half a century ago, have been overcome by breakthroughs in materials science [29, 30]. The compatibility between germanium and high-κ gate dielectrics, eliminates the need for a stable native oxide [31]. Furthermore, the ability to heterogeneously integrate silicon and germanium obviates the necessity for expensive germanium substrates [30].

However, the unique properties that motivated the initial use of germanium remain. On top of this, the type-I band alignment in Ge/SiGe heterostructures does not only allow for the confinement of electrons but also enables the confinement of holes. The hole spin is typically subject to a much stronger spin-orbit coupling compared to the electron spin, facilitating an intrinsic ability to control the qubit all-electrically. Combined with the higher carrier mobility and lower effective mass, this could be beneficial for the fabrication of large arrays of spin qubits. The question thus arises whether, just like 60 years ago, it is time to switch between silicon and germanium.

THESIS OUTLINE

In this thesis, we address that question and study the ability to define, operate and couple spin qubits in planar germanium heterostructures. **Chapter 2** gives a short introduction and motivation to quantum computing, using the quantum Fourier transform as an example.

Chapter 3 provides the theoretical background relevant to the work in this thesis. We start by discussing the band structure of bulk germanium, adding step by step confinement, strain, electric, and magnetic fields, to clarify their influence on the material system properties. We then proceed to discuss quantum dot spin qubits, starting from basic quantum dot physics, spin readout and qubit operation.

Chapter 4 gives a short overview of the experimental techniques used throughout this thesis. Device fabrication is discussed briefly, as well as the (cryogenic) setup used for the electric measurements. Considerations for designing the setup are discussed, as well as their implications on the qubit measurements.

All experiments presented in this work are based on undoped strained germanium quantum wells. We therefore start by discussing the growth and properties of this material system in Chapters 5 and 6. In **Chapter 5**, we grow sharp, undoped, strained germanium quantum wells with high carrier mobility and confirm the light effective mass of the hole. In **Chapter 6**, we discuss the effect of the depth of the quantum well. Increasing the quantum well depth to 55 nm results in a very low percolation density and charge noise level, while maintaining sharp enough confinement potential to create well-defined quantum dots.

Gate defined quantum dots are discussed in more detail in **Chapter 7**. Using a single quantum dot in transport, we can probe various quantum dot properties, including cross capacitance, g-factor and orbital energy. To perform single-shot readout of a qubit, charge sensing is needed and we show this can be obtained using an additional quantum dot as a sensor. Finally, we compare the charging energy in four different quantum dots in a quadruple quantum dot array as a gauge for device uniformity.

Next, we operate a two-qubit device in transport in **Chapter 8**. The spin readout is realised by Pauli spin blockade and qubit rotations of the hole qubits are implemented through spin-orbit coupling mediated electric dipole spin resonance. Combined with conditional rotations as enabled by the controllable exchange coupling between the two quantum dots, this constitutes fast and universal quantum logic. Furthermore, we study qubit coherence and find an optimal point of noise insensitivity, making high-fidelity operation possible.

Transport measurements only allow for the average outcome of many shots to be sampled. However, single-shot readout of the individual qubit states is essential to many quantum algorithms [32]. We demonstrate single-shot measurements of the planar germanium hole qubits in **Chapter 9**, making use of an rf charge sensor for fast readout. This also allows us to isolate the qubits from their leads and significantly enhance the relaxation time scales.

With this, we have all the ingredients to define a two-by-two spin qubit array, demonstrating the ability to couple spin qubits in two dimensions in **Chapter 10**. Furthermore, we study different types of two-qubit gates and find that good control over the interdot coupling allows for fast controlled-phase gates. We use these gates to perform a rudimentary quantum algorithm on the four qubit system.

Finally, in **Chapter 11**, we explore the ability to couple the hole states to a superconductor, making use of the Fermi level pinning present in germanium structures. We demonstrate a Josephson supercurrent through the quantum well and study the properties of a superconducting quantum point contact junction, as a step towards superconductor semiconductor hybrid devices.

In **Chapter 12**, we conclude by discussing future research directions to extend spin qubit arrays in planar germanium beyond the demonstrations in this thesis.

2

QUANTUM PRELUDE

Nature isn't classical, dammit, and if you want to make a simulation of nature, you'd better make it quantum mechanical, and by golly it's a wonderful problem, because it doesn't look so easy.

Richard P. Feynman [8]

Nearly a century ago, the theory of quantum mechanics was developed, greatly benefiting our understanding of many physical observations such as the photo-electric effect, black-body radiation or the existence of chemical bonds. This development beyond the classical theory is sometimes dubbed the *first quantum revolution* and defined the tools to understand the rules of quantum mechanics. The first revolution enabled many new technologies such as the laser, the MRI machine and probably most importantly: the transistor. Physicists were also quick to learn that the same quantum mechanics that enable these technologies also pose limits on their development. However, in the 1980s, it was realised that the special quantum mechanical effects need not be a limitation, but can also be used to our advantage [8, 33].

Classical (non-quantum) computers perform particularly poor in simulating quantum mechanical systems, severely limiting our current understanding of quantum matter. Although the power of classical computers has increased at unprecedented rates, allowing for more complex calculations every year, a fundamentally different approach to computation is needed to create a more sustainable solution. Unlocking the full potential of quantum mechanics, rather than just acknowledging its implications, is what is often called the *second quantum revolution* [34]. Over the past decades, theoretical work has led to the development of quantum algorithms [35] to efficiently factorise prime numbers [36], search databases [37], and even understand complex chemical reactions [18]. What follows is a crude introduction to some basic principles behind these algorithms, to develop an understanding of the drive, concepts and promises of the field, as well as put the experiments in this thesis into context. For further details on these matters, we refer the reader to e.g. the textbook by Chuang and Nielsen [10].

2.1. QUANTUM BITS

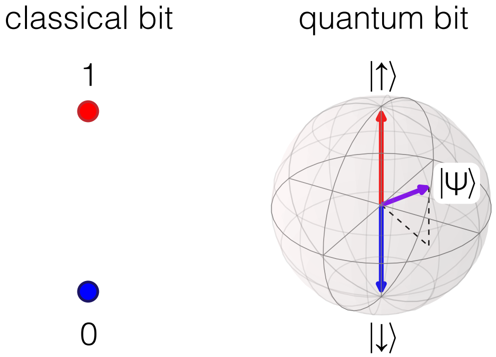

Figure 2.1: **Graphical representation of a classical and quantum bit. a**, A classical bit can either be a 0 or a 1. **b**, A quantum bit state $|\Psi\rangle$ can be represented by a unit vector on the Bloch sphere. The two poles correspond to the basis states, while the rest of the sphere describes the superposition states.

The core of any quantum computer is formed by *quantum bits* (qubits), just as a classical processor is defined by its classical bits. The qubit can be represented by a quantum mechanical two-level system, such as the spin of an elementary particle.

Analogous to a bit in computer science, which is defined by the on and off states, these quantum bits are defined by their two eigenstates, referred to as $|1\rangle$ and $|0\rangle$ (in the Dirac notation). For the spin system in the z basis, these two states are more commonly referred to as $|\uparrow\rangle$ and $|\downarrow\rangle$ for a spin up and spin down respectively. We will stick to the latter notation, as all experiments in this thesis are based on the spin system.

Unlike its classical counterpart, the quantum bit is not limited to either of the two basis states but can occupy any *superposition* of the two at the same time. Mathematically, we represent this by writing each state as the linear combination of its basis states $|\psi\rangle = \alpha_1 |\downarrow\rangle + \alpha_2 |\uparrow\rangle$, where α_1 and α_2 are complex coefficients. When we measure the qubit, it will collapse into one of the eigenstates of the measurement operator. Thus, if we measure the spin state with respect to the magnetic field along z, we will measure either $|\downarrow\rangle$ with a probability of $|\alpha_1|^2$ or $|\uparrow\rangle$ with probability $|\alpha_2|^2$. Graphically, we can represent the qubit as a vector on a spherical shell: the Bloch sphere (Fig. 2.1). The two poles of the sphere constitute the eigenstates of the qubit, with the rest of the shell describing the full two-dimensional Hilbert space.

When considering an ensemble of n isolated qubits, this would mean $\sum_n 2 = 2n$ coefficients would be needed to describe the system (n separated Bloch spheres). However, the ability to 'share' the quantum state between multiple qubits (*entanglement*) increases the number of coefficients needed to $\prod_n 2 = 2^n$. A system of n entangled qubits thus spans a Hilbert space of size 2^n and should be described by a (complex) 2^n-dimensional state vector. As an example, a system of 2 entangled qubits is described in terms of its four basis states $|\downarrow\downarrow\rangle$, $|\downarrow\uparrow\rangle$, $|\uparrow\downarrow\rangle$, and $|\uparrow\uparrow\rangle$:

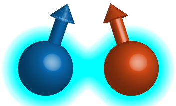

$$\Longrightarrow \begin{pmatrix}\alpha_1\\ \alpha_2\\ \alpha_3\\ \alpha_4\end{pmatrix} \begin{matrix}|\downarrow\downarrow\rangle\\ |\downarrow\uparrow\rangle\\ |\uparrow\downarrow\rangle\\ |\uparrow\uparrow\rangle\end{matrix} \tag{2.1}$$

with α_i the state amplitude of the corresponding basis state.

2.2. QUANTUM GATES

The qubit state can be manipulated using quantum gates, analogous to the classical logic gates. Such quantum gates can be represented by a transformation matrix acting upon an initial qubit state. We will illustrate these quantum gates using the (minimal) two-qubit system in this section, in the basis defined in Eq. 2.1. One-qubit gates act on a single qubit, independent of the state of the other qubit. An example of such a gate is the Hadamard gate, which maps the qubit basis states to a superposition state, corresponding to the equator of the Bloch sphere. The transformation matrix of a Hadamard gate acting upon the first qubit (in the two-qubit basis) is given by:

$$H = \frac{1}{\sqrt{2}} \begin{pmatrix} 1 & 0 & 1 & 0\\ 0 & 1 & 0 & 1\\ 1 & 0 & -1 & 0\\ 0 & 1 & 0 & -1 \end{pmatrix} \tag{2.2}$$

As an example, when the Hadamard is applied to the $|{\downarrow\downarrow}\rangle$ state ($\alpha_1 = 1$), we find:

$$H\,|{\downarrow\downarrow}\rangle = \frac{1}{\sqrt{2}}\left(|{\uparrow\downarrow}\rangle + |{\downarrow\downarrow}\rangle\right), \tag{2.3}$$

the symmetric superposition state, as expected for a Hadamard operation.

Two-qubit gates, however, change the state of a qubit, depending on the state of a second qubit. Again, many implementations exist, but one example is the controlled phase gate. It applies a phase factor θ to the $|{\uparrow}\rangle$ state, only when the other qubit is the $|{\uparrow}\rangle$ state as well. Its matrix representation is given by:

$$CZ(\theta) = \begin{pmatrix} 1 & 0 & 0 & 0 \\ 0 & 1 & 0 & 0 \\ 0 & 0 & 1 & 0 \\ 0 & 0 & 0 & e^{i\theta} \end{pmatrix} \tag{2.4}$$

For larger n-qubit systems, n-qubit gates can be established, where the qubit manipulation depends on the state of the n other qubit states. An example for $n = 3$ is the so-called *i*Toffoli gate, which is further discussed in Chapter 10. These manifold conditional qubit gates can also be compiled from a *universal set* of quantum gates, such as can be composed by one and two-qubit gates.

2.3. EXPONENTIAL SPEED UP

Quantum computers are often praised for the *exponential speed up* they promise to deliver. One of the canonical algorithms demonstrating this is Shor's algorithm for calculating the prime factors of a number. At the basis of Shor's algorithm lies the quantum Fourier transform (QFT), analogous to the classical discrete Fourier transform (DFT), which projects a classical vector onto its frequency components. The DFT is defined by the transformation matrix:

$$F_N = \frac{1}{\sqrt{N}} \begin{pmatrix} & \vdots & \\ \dots & \omega_N^{jk} & \dots \\ & \vdots & \end{pmatrix} \tag{2.5}$$

with $\omega_N = e^{2\pi i/N}$, j and k the row and column indices, and N the size of the input vector. Naively computing the Fourier transform by performing the matrix multiplication, would take $O(N)$ steps per input entry, which equates to a total of $O(N^2)$ steps for the full matrix. Assuming $N = 2^n$, the process can be slightly optimised to be $O(N \log_2(N) = n2^n)$ (the *fast* Fourier transform), which still scales exponentially with n [38].

Using the quantum gates discussed in the previous section, we can achieve the same mathematical multiplication, now making use of the entanglement of the quantum state. This time we do not write down the entire matrix and perform the calculation, but rather prepare a quantum state corresponding to the initial state vector. After applying a set of quantum gates to this system, the transformed vector is represented by the amplitudes of the final superposition state, rather than a list of the individual coefficients. As an example, the two-qubit QFT can be obtained by a sequence of a Hadamard, a controlled-phase, and another Hadamard gate, and a reshuffling of the qubits at the end to put them in the right order (SWAP gates). The combined transformation matrix given by the multiplication of the individual gate matrices is given by:

$$QTF(2) = \frac{1}{2}\begin{pmatrix} 1 & 1 & 1 & 1 \\ 1 & i & -1 & -i \\ 1 & -1 & 1 & -1 \\ 1 & -i & -1 & i \end{pmatrix} \tag{2.6}$$

which corresponds to the (inverse) DFT transformation matrix F_2^{-1}. In the case of the QFT, three quantum gates are needed to obtain this result. If we add a third qubit, three additional gates are needed (one H and two phase gates conditional on the previous two qubits). Analogously, we need another four gates for the fourth qubit, etcetera. For a system of n qubits, with at most n gates per qubit, the overall total amount of gates is therefore of order $O(n^2)$. The size of the input state vector N, however, does not scale with the number of qubits, but with the number of states 2^n. Comparing this to the $O(n2^n)$ scaling of the DFT, we can see the exponential speed up. While the Fourier transform can be calculated in polynomial time for the quantum computer, it takes exponential time on a classical computer. For a few qubits, this might seem like an irrelevant difference, but for $n = 100$, the amount of steps is equal to $2^{100} \approx 10^{30}$ for the classical system, compared to a mere $100^2 = 10^4$ for the quantum system.

2.4. PRACTICAL QUANTUM SYSTEMS

There are of course a few caveats to this. Initial state preparation can be difficult and hard to perform, often only a small subset of all quantum gates are available as native gates, and qubit state readout is probabilistic and thus only allows for a sampling of the final state, all potentially reducing the effective speed up. On top of this, in the real world, we have to deal with noise, and as a result, the information on the quantum state can be lost over time (*decoherence*). The field of *quantum error corrections* emerged to solve this problem, developing protocols that specify how to deal with these imperfections and protect the quantum state throughout the calculations. Despite all these considerations, recently first demonstrations were made in which a quantum processor is argued to perform a calculation that would be practically impossible on the most powerful supercomputers to date [12, 13]. This truly showcases (and strengthens) our motivation to build a practical quantum computer: enabling calculations never performed before to gain a deeper understanding of nature, *and by golly, it's a wonderful problem*.

3

SEMICONDUCTOR SPIN QUBIT SYSTEMS

> *Comparisons are easily done*
> *once you've had a taste of perfection.*
>
> Katy Perry [39]

This chapter aims to give an overview of the theoretical background needed to interpret the experiments in the rest of this thesis. The chapter consists of three parts, first (Section 3.1) briefly discussing different spin qubit implementations. Next, in Section 3.2, we consider the strained planar germanium hole system used for the experiments in this thesis. We derive the Hamiltonian of the valence band states and show the effects of 2D confinement and strain. Furthermore, we discuss spin-orbit and hyperfine interactions, essential for spin qubit operation. In the third part (Section 3.3) quantum dot spin qubits in general are discussed, covering qubit definition, initialisation, operation, and readout.

3.1. SPIN QUBIT IMPLEMENTATIONS

In search of qubits that can enable practical quantum information, dozens of different implementations of qubit systems are studied, with new ones still emerging. Many physical systems are used to define the qubit [32], including photons [40, 41], ions [42, 43], and charges [12, 44]. However, one of the most fundamental two-level systems is the spin of the electron, making it preordained to be used as a qubit. When an external magnetic field is applied, the Zeeman effect splits the spin up and down states in energy, aligned or opposed to the field direction. These states form the computational basis of the qubit known as the Loss-DiVincenzo (LD) qubit [25]. The electron spin state can be manipulated using spin resonance and when a weak coupling between two spins is present, two-qubit gates can be performed as well [25]. Early research focused on the spin state of nuclei within molecules [45]. While these systems were used to perform the first demonstrations of quantum algorithms, such as Shor's algorithm [46], they are generally hard to scale up. To this end, quantum dot (QD) spin qubits are promising, due to their inherent similarity to the classical transistor, the building block of all our electronic hardware today.

Early quantum dot research focused on gallium-arsenide (GaAs) heterostructures with very high charge carrier mobilities. The low level of disorder allowed for the study of spins in single [47, 48], double [49–51] and later larger arrays of quantum dots [52–54]. However, interactions between the spin qubit and the nuclear spins present in group III-V materials deteriorate the spin coherence. As a result, focus shifted towards the group IV material silicon, where net-zero nuclear spin isotopes are more abundant, in particular when the host crystal is isotopically enriched [27]. This enabled a sharp improvement of the qubit coherence times [55, 56]. The field progressed steadily and using tailored electronic pulses, one-qubit gate fidelities of over 99.9 % are obtained [57]. Different implementations of two-qubit gates have been studied as well [58–60], with fidelities up to 98 % [11]. This enabled the execution of rudimentary quantum algorithms, such as Grover's search algorithms in two-qubit systems [61], as well as tomography of multi-qubit entangled states [61, 62]. In parallel, research efforts focused on the integration of spin qubits with circuit quantum electrodynamics (cQED) elements, that form the basis of the superconducting qubit platform. Coupling the spin state to a microwave photon [63–65], could define a way to couple spin-qubits beyond the (local) exchange interaction. Furthermore, as a first step to the integration of spin qubits with classical electronics [26], the performance of spin-qubits at elevated temperatures has been studied, resulting in the demonstration of two-qubit logic at temperatures as high as $T = 1$ K [66, 67].

Recently, hole states in germanium also gained attention as a potential candidate for quantum information technology [30, 68, 69]. Germanium also has a low natural abundance of non-zero nuclear spin isotopes, which can be further reduced to vanishing concentrations through isotopic enrichment [27, 28]. The low degree of disorder [70, 71], combined with the relatively small effective mass [72, 73], enables the definition of fully gate-defined quantum dots, such that the quantum dot properties can be well-controlled [74]. Furthermore, in contrast to electron states in silicon, valence band states in germanium do not suffer from a valley degeneracy. Combined with the strain and confinement induced splitting of the different valence bands (as detailed in

Section 3.2), this results in a large splitting between the ground and excited state of the qubit [74, 75]. The strong spin-orbit coupling enables fast, all-electrical control of the spin state [69], eliminating the need for microscopic elements such as micromagnets [58, 61, 76, 77] or striplines [11, 49, 67, 78]. Finally, the Fermi level in germanium aligns with the valence band edge, enabling the integration of ohmic metal contacts and opening up the path to hybrid semiconductor-superconductor systems. Different germanium material systems have been studied, including Si/Ge core/shell nanowires [79–81], Ge hutwires [82–85] and planar germanium quantum wells [74, 86, 87], and qubit operations have been demonstrated in the latter two. An overview of the state-of-the-art in different semiconductor spin qubit platforms is presented in Fig. 3.1.

The experiments in this thesis are all based on valence band holes in strained planar germanium quantum wells. In the following section, the details of strained germanium quantum wells are treated, focusing on the properties of valence band holes. A more in-depth discussion of both Ge hut wire and Ge/Si core/shell nanowire systems can be found in Ref. [30]. Next, we will discuss quantum dot spin qubits in general, covering the different prerequisites for qubit operation. These sections are not complete but are intended to supply enough theoretical background to interpret the experiments in the following chapters, and references to more exhaustive literature are supplied where possible.

3.2. HOLE SPIN QUBITS IN PLANAR GERMANIUM

Quantum dot spin qubits are not solely limited to electron states in the conduction band. Around the time when the first demonstrations on electron spin qubits were performed [49–51], theoretical studies predicted that also unfilled valence band states (elegantly called *holes*) would be promising candidates for the definition of spin qubits [68, 69]. Valence band holes are characterised by their p-like orbital shape [110, 111], corresponding to $l = 1$, with l the azimuthal quantum number. From the Schrödinger equation, one would expect these orbital states to be three-fold degenerate, which combined with the two-fold spin degeneracy would lead to a total six-fold degeneracy. However, when relativistic effects are taken into account, a term $\delta_{\mathrm{SO}}\boldsymbol{L}\cdot\boldsymbol{S}$ can be derived from the Dirac equation [112], with $\hbar\boldsymbol{L}$ the orbital angular momentum (quantum numbers l and m_l) and $\hbar\boldsymbol{S}$ the spin of the electron (and corresponding quantum numbers s, m_s). This term is usually referred to as the *spin-orbit coupling* because it couples the spin and orbital degrees of freedom. As a result, both l and s are no longer 'good' quantum numbers, because they no longer describe independent physical quantities. Instead, one should consider their sum $\boldsymbol{J} = \boldsymbol{L} + \boldsymbol{S}$, corresponding to the total angular momentum, with the quantum numbers j and m_j.

To get a better understanding of the effect on the band structure of germanium, in bulk, in 2D, and with added strain, we will now discuss the relevant terms in the Hamiltonian, loosely following the derivation in Ref. [30]. A very thorough discussion of spin-orbit coupling in 2D semiconductor systems can be found in Ref. [111]. The spin and orbital momentum can either be parallel or antiparallel, corresponding to $j = 3/2$ or $j = 1/2$ respectively. Taking the dot product of $\boldsymbol{J}$ with itself, we find $\boldsymbol{J}^2 = \boldsymbol{L}^2 + \boldsymbol{S}^2 + 2\boldsymbol{L}\cdot\boldsymbol{S}$, from which we derive $\boldsymbol{L}\cdot\boldsymbol{S} = 1/2\left(\boldsymbol{J}^2 - \boldsymbol{L}^2 - \boldsymbol{S}^2\right)$, with $\boldsymbol{L}^2\left|\Psi\right\rangle = \hbar^2 l(l+1)\left|\Psi\right\rangle$,

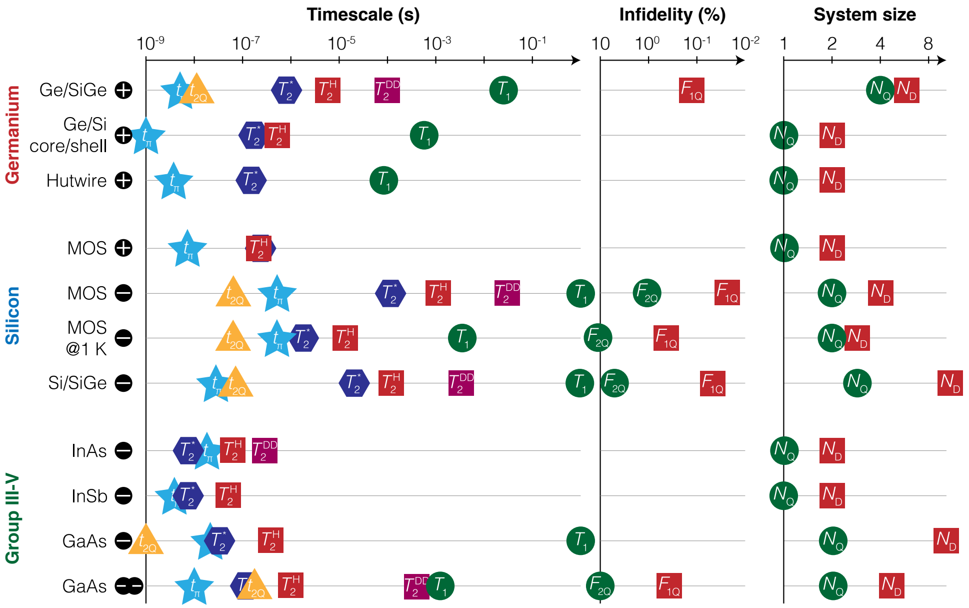

Figure 3.1: **Different semiconductor spin qubit platforms** We present an overview of the state-of-the-art (published at the time of writing) qubit coherence (T_2), relaxation (T_1), and manipulation ($t_{\pi,2Q}$) times, as well as one and two-qubit gate fidelities ($F_{1,2Q}$) and largest coupled qubit ($\mathrm{N_Q}$) and quantum dot ($\mathrm{N_D}$) system sizes (measured simultaneously, sensing dots included) for spin qubits in different semiconductor platforms. T_2^{H} corresponds to the coherence time of a Hahn echo experiment, while T_2^{DD} is the coherence time when more advanced decoupling sequences are used (typically CPMG). The charge carrier is indicated by the black circle with a + (hole) or − (electron) sign. A double circle corresponds to a singlet-triplet (ST) type of qubit. We note that different optima are typically obtained in different devices. Furthermore, different experimental methodology and parameters can lead to differences in observed timescales (such as for T_2^*), so while these numbers should not be compared one-to-one, they do give an overview of what is possible in the different systems. Ge/SiGe data from Ref. [86–88]; Ge/Si core/shell data from Ref. [80, 89–91]; hutwire data from Ref. [83–85]; pMOS data from Ref. [92, 93]; nMOS data from Ref. [11, 56, 57, 60, 67, 94–96]; nMOS at T=1 K data from Ref. [60, 66, 67]; Si/SiGe data from Ref. [55, 61, 62, 97–99]; InAs data from Ref. [100]; InSb data from Ref. [101]; GaAs (LD) data from Ref. [51, 53, 102–104]; and GaAs (ST) data from Ref. [51, 52, 105–109]. N_D was discounted by a factor of 2 for the ST qubit systems.

$S^2 |\Psi\rangle = \hbar^2 s(s+1) |\Psi\rangle$, and $\boldsymbol{J}^2 |\Psi\rangle = \hbar^2 j(j+1) |\Psi\rangle$. Thus, for a valence band electron with $l = 1$ and $s = 1/2$, it follows that the sixfold degenerate p-orbital splits into a fourfold degenerate $p_{3/2}$ orbital ($j = 3/2$) with eigenenergy $\delta_{\mathrm{SO}}/2$ and a twofold degenerate $p_{1/2}$ orbital ($j = 1/2$) with eigenenergy $-\delta_{\mathrm{SO}}$, the so-called split-off band. These two bands are thus separated by an energy gap of $\Delta_0 = 3\delta_{\mathrm{SO}}/2$ at the Γ point, which is often referred to as the spin-orbit gap. In bulk germanium this gap is quite large with $\Delta_0 \approx 0.3$ eV, resulting in well-separated energy bands, with the $j = 3/2$ band being closest to the valence band edge [111].

The states in the topmost valence band can be described using the Luttinger-Kohn

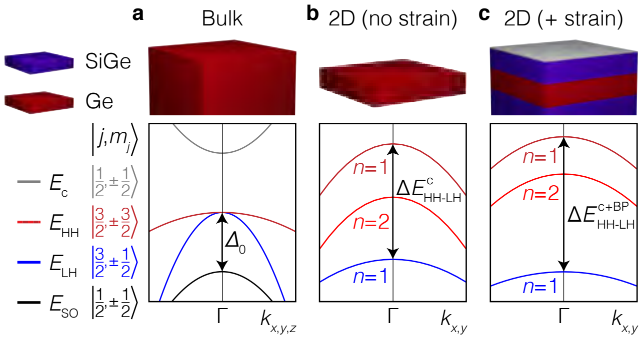

Figure 3.2: **Valence band states in germanium a**, The valence band of germanium has a three-fold degenerate *p*-like orbital state, with an additional two-fold spin degeneracy. For bulk germanium, the atomic spin-orbit coupling splits the $j = 3/2$ from the $j = 1/2$ states by an energy difference of Δ_0. **b**, Zooming in on the $j = 3/2$ states, these are split again into the so-called heavy hole (HH) and light hole (LH) states as a direct result of the 2D confinement. Furthermore, subbands with index n arise, with the first and second HH subband sketched in dark and light red respectively. **c**, The compressive strain imposed on the quantum well by the SiGe barrier layers splits the HH and LH bands even further.

(LK) Hamiltonian [113–115] in the spherical approximation [30, 116]:

$$H_{LK} = -\frac{\hbar}{2m_0}\left[\left(\gamma_1 + \frac{5}{2}\gamma_s\right)k^2 - 2\gamma_s\left(\boldsymbol{k}\cdot\boldsymbol{J}\right)^2\right] \tag{3.1}$$

with $k^2 = \boldsymbol{k}\cdot\boldsymbol{k} = k_x^2 + k_y^2 + k_z^2$ and $\boldsymbol{k}$ the wave vector, m_0 the free electron rest mass, $\hbar\boldsymbol{J}$ the spin-3/2 operator, and γ_1 and $\gamma_s = (2\gamma_2 + 3\gamma_3)/5$ the Luttinger parameters [114]. We choose the quantisation axis of $\boldsymbol{J}$ parallel to $\boldsymbol{k}$, such that the Hamiltonian eigenstates are defined by the eigenstates of J_z: $|m_j\rangle = \{|\pm 3/2\rangle, |\pm 1/2\rangle\}$, which can be grouped into two sets. The *heavy hole* (HH) band with $m_j = \pm 3/2$ and the *light hole* (LH) band with $m_j = \pm 1/2$. The naming of these bands becomes immediately apparent when we look at the eigenenergies of the bands. With $\boldsymbol{k}$ and $\boldsymbol{J}$ parallel, we can ignore k_x and k_y, such that $\boldsymbol{k}\cdot\boldsymbol{J} = kJ_z$. Using this, we derive $E_{HH} = -\hbar^2k^2/2m_{HH}$ and $E_{LH} = -\hbar^2k^2/2m_{LH}$, with $m_{HH} = m_0/(\gamma_1 - 2\gamma_s)$ and $m_{LH} = m_0/(\gamma_1 + 2\gamma_s)$ the effective mass in either band. In germanium, we have $\gamma_1 \approx 13$ and $\gamma_s \approx 5$ [117], leading to about an order of magnitude difference in the effective light hole mass $m_{LH} \approx 0.04m_0$ and heavy hole mass $m_{HH} \approx 0.33m_0$. These two bands are degenerate at the $k = 0$ point but split for non-zero k, with the HH band higher in energy due to its larger effective mass, as can be seen in Fig. 3.2a.

3.2.1. TWO-DIMENSIONAL SYSTEMS

The remaining fourfold degeneracy of the LH/HH bands is lifted when a confinement potential is applied [30, 75, 118]. In a Ge/SiGe heterostructure, the holes are confined to the (strained) germanium quantum well layer. Because of the strong confinement in the z-direction, the system can be considered to be a quasi two-dimensional (2D) system, with the quantisation axis fixed in the growth direction z. The wave vector k_z corresponding to the confinement direction is generally much larger than the in-plane momentum $k_{\parallel}$, such that the system eigenstates will be closely related to the bulk LH and HH eigenstates $\left|m_j\right\rangle$ and are usually referred to as LH-like or HH-like states. It is convenient to write the LK Hamiltonian in explicit matrix notation, again in the spherical approximation, using the J matrices as defined in e.g. Ref. [111]:

$$H_{\mathrm{LK}} = \begin{pmatrix} P+Q & L & M & 0 \\ L^* & P-Q & 0 & M \\ M^* & 0 & P-Q & -L \\ 0 & M^* & -L^* & P+Q \end{pmatrix}, \tag{3.2}$$

where

$$P = -\frac{\hbar^2}{2m_0}\gamma_1 k^2 \tag{3.3a}$$

$$Q = \frac{\hbar^2}{2m_0}\gamma_s(2k_z^2 - k_x^2 - k_y^2) \tag{3.3b}$$

$$L = \frac{\hbar^2}{2m_0}2\sqrt{3}\gamma_s k\_k_z \tag{3.3c}$$

$$M = \frac{\hbar^2}{2m_0}\sqrt{3}\gamma_s k_-^2, \tag{3.3d}$$

with $k_\pm \equiv k_x \pm ik_y$. Here, we express H_{LK} in a spinor basis formed by the eigenstates of J_z: $\{|3/2\rangle, |1/2\rangle, |-1/2\rangle, |-3/2\rangle\}$. The off-diagonal terms lead to mixing of the pure states for $k_{\parallel} \neq 0$. Assuming a hard wall confining potential leads to a quantisation $k_z^2 = \pi^2 n^2/L_z^2$, with n the subband index and L_z the quantum well width. The quantum wells in this thesis are all grown on the high symmetry [001] plane, allowing us to approximate the system using pure HH and LH states [30, 119] (i.e. neglecting the off-diagonal terms in 3.2). We then find the following dispersion relations:

$$E_{n_{\mathrm{HH}}} = -\frac{\hbar^2}{2m_0}\left(\frac{\pi^2 n_{\mathrm{HH}}^2\left(\gamma_1 - 2\gamma_s\right)}{L_z^2} + \left(\gamma_1 + \gamma_s\right)k_{\parallel}^2\right) \tag{3.4a}$$

$$E_{n_{\mathrm{LH}}} = -\frac{\hbar^2}{2m_0}\left(\frac{\pi^2 n_{\mathrm{LH}}^2\left(\gamma_1 + 2\gamma_s\right)}{L_z^2} + \left(\gamma_1 - \gamma_s\right)k_{\parallel}^2\right) \tag{3.4b}$$

From this it follows that even at the $k_{\parallel} = 0$ point, a splitting between the heavy hole and light hole like bands occurs as a result of the confinement:

$$\Delta E^{\mathrm{C}}_{\text{LH-HH}} = \frac{2\gamma_s\hbar^2\pi^2}{m_0 L_z^2}, \tag{3.5}$$

lifting the fourfold degeneracy as is also shown in Fig. 3.2b. Furthermore, we can see from Eq. 3.4a that the in-plane effective mass of the heavy hole like band is given by $m_{\parallel}^{\mathrm{HH}} = m_0/(\gamma_1 + \gamma_s) = 0.055m_0$. The effective mass of the light hole like band is given by the *heavier* $m_{\parallel}^{\mathrm{LH}} = m_0/(\gamma_1 - \gamma_s) = 0.125m_0$. This inversion of the effective mass compared to bulk is in agreement with calculations [75] and experiments [73] on these heterostructures, confirming the very low in-plane effective mass at the top of the valence band.

3.2.2. ADDING STRAIN

The lattice parameters of silicon and germanium are comparable, $a_{\mathrm{Si}} = 5.43$ Å and $a_{\mathrm{Ge}} = 5.66$ Å [120]. As a result, the two materials are miscible over the full range of compositions $\mathrm{Si}_{1-y}\mathrm{Ge}_y$, with $0 < y < 1$ [121]. However, the small lattice mismatch of 4.7 % between the thin, pure germanium quantum well and the SiGe buffer layers, will lead to a lateral compressive strain in the quantum well. This strain can be accounted for by adding a Bir-Pikus [75, 122, 123] term H_{BP} to the Hamiltonian matrix. The diagonal terms of H_{BP} are of the same form as H_{LK} and are given by $P_\epsilon + Q_\epsilon$ for the heavy hole manifold and $P_\epsilon - Q_\epsilon$ for the light hole manifold, with

$$P_\epsilon = a_v \left(\epsilon_{xx} + \epsilon_{yy} + \epsilon_{zz}\right) \tag{3.6a}$$

$$Q_\epsilon = b_v/2 \left(\epsilon_{xx} + \epsilon_{yy} - 2\epsilon_{zz}\right), \tag{3.6b}$$

with $a_v = 2.0$ eV and $b_v = -2.16$ eV the deformation potentials [75, 124] and ϵ_{ij} the components of the strain tensor. Subsequently, the strain will add an additional level splitting of $\Delta E^{\mathrm{BP}}_{\text{LH-HH}} = 2Q_\epsilon$ to the system. In the case of uniaxial strain $\epsilon_\parallel = \epsilon_{xx} = \epsilon_{yy}$, $\epsilon_{zz} = -2(C_{12}/C_{11})\epsilon_\parallel$, and $\epsilon_{xy} = \epsilon_{yz} = \epsilon_{zx} = 0$, with $C_{11} = 129.2$ GPa and $C_{12} = 47.9$ GPa the stiffness coefficients in Ge [125, 126]. We take $\epsilon_\parallel = -0.0063$ from Ref. [71], with $\epsilon_\parallel < 0$ corresponding to a compressive straining of the quantum well. We evaluate Eq. 3.6b using these material parameters and find a contribution to the level splitting of $\Delta E^{\mathrm{BP}}_{\text{LH-HH}} = 2Q_\epsilon \approx 49$ meV between the LH and HH bands as a result of the strain. A more accurate prediction for the level splitting can be acquired by numerically solving the Schrödinger-Poisson equation, taking into account the applied electric fields as is discussed in Chapter 5. Modulating the strain in the quantum well by adapting the stoichiometry of the SiGe buffer layers will change the LH-HH energy splitting, and will thus provide a method to tailor the spin-orbit interaction strength, as discussed in Section 3.2.3 below.

3.2.3. SPIN-ORBIT INTERACTION

So far, we have not lifted the spin degeneracy within the LH and HH manifold in Eq. 3.2. The presence of an inversion asymmetry will lift the spin degeneracy [111], as is commonly achieved by applying a magnetic field, thereby lifting time inversion symmetry. The presence of a spatial inversion asymmetry will also lift the degeneracy of the LH and HH bands and results in additional spin and momentum dependent terms in the Hamiltonian. Graphically, this can be thought of as a horizontal shift $\pm\delta\boldsymbol{k}$ of the dispersion of both spin states. Spatial inversion asymmetry in heterostructures usually stems either from the confinement potential leading to a structure inversion asymmetry (SIA) or from the crystal structure, causing a bulk inversion asymmetry (BIA). The first is commonly referred to as Rashba spin-orbit interaction (SOI), while the second is known as Dresselhaus SOI. Germanium has a diamond cubic structure, which has a centre of inversion, such that the Dresselhaus terms are zero and can be ignored [118, 127, 128].

The Rashba spin-orbit terms arise from the asymmetric electric field imposed by the quantum dot top gate. Since the spin-orbit coupling preserves time-reversal symmetry [111], only odd powers of the wave vector are allowed. For electrons in the conduction band, typically only a linear term in k is of relevance. However, due to the interaction between the different valence bands, for hole states, cubic terms in k should be considered as well. We start from the full LKBP Hamiltonian and add an asymmetric confinement potential in the growth direction, $eF_z z$. Next, following [75, 118, 123], by projecting the lowest-energy subbands in the Hamiltonian on the heavy hole subspace, we find the following Rashba spin-orbit terms in the Hamiltonian:

$$H_{\mathrm{SO,R}} = i\alpha_{R1}\left(k_+\sigma_+ - k_-\sigma_-\right) + i\alpha_{R2}\left(k_+^3\sigma_- - k_-^3\sigma_+\right) + i\alpha_{R3}\left(k_+k_-k_+\sigma_+ - k_-k_+k_-\sigma_-\right), \tag{3.7}$$

with $\sigma_\pm = \sigma_x \pm i\sigma_y$, $\sigma_{x,y,z}$ the Pauli spin matrices, and $\alpha_{R1,2,3}$ spin-orbit strength parameters. We can distinguish three terms, one linear in k and two cubic in k. For systems grown on a high-symmetry surface of the crystal (such as [001], as holds for the experiments in this thesis) the linear term is small and can be neglected [111, 115, 118]. The second term includes the isotropic component of the LK Hamiltonian, while the third term includes the cubic-symmetric corrections [75]. The latter thus vanishes in the spherical approximation and is usually not considered [115, 118], but turns out to be of relevance for qubit driving, as discussed in Section 3.2.5 below and in more detail in Ref. [75] and [127].

3.2.4. ZEEMAN SPLITTING

The Zeeman Hamiltonian for a 2D hole system is described by [129]:

$$H_Z = -2\kappa\mu_{\mathrm{B}}\boldsymbol{B}\cdot\boldsymbol{J} - 2q\mu_{\mathrm{B}}\boldsymbol{B}\cdot\boldsymbol{J}^3, \tag{3.8}$$

using the same spinor basis as before, with $\boldsymbol{J} = (J_x, J_y, J_z)$, and $J_{x,y,z}$ the angular momentum matrices for $j = 3/2$, as defined in Ref. [111]. Here, κ and q are Luttinger parameters [114, 129], and $\boldsymbol{B} = (B_x, B_y, B_z)$ is the applied magnetic field. Again, for now, we consider a pure heavy hole state, and neglect all terms outside the heavy hole manifold. As a result, the reduced effective Zeeman Hamiltonian simplifies to:

$$H_Z = -\left(3\kappa + \frac{27}{4}q\right)\mu_{\mathrm{B}}B_z\sigma_z - \frac{3}{2}q\mu_{\mathrm{B}}\left(B_x\sigma_x - B_y\sigma_y\right), \tag{3.9}$$

with $B_{i,i\in\{x,y,z\}}$ the $\boldsymbol{B}$ component in the i direction.

We can now define an effective g-factor for an in-plane and out-of-plane magnetic field, such that the linear Zeeman splitting is defined by $E_z = g_{\{\perp,\parallel\}}\mu_B B_{\{\perp,\parallel\}}$. From Eq. 3.9, we find these to be very anisotropic, with $g_\perp \approx 6\kappa + 13.5q \approx 21.4 \gg g_\parallel \approx 3q \approx 0.2$, using the band structure parameters for germanium [117]. This results from the fact that the (larger) in-plane $\kappa J_{x,y}$ terms only couple states that differ by ± 1 in m_j. As a result, the energy-separated HH states remain (almost) unaffected. The only contribution to the in-plane g-factor of the pure HH state thus comes from the (smaller) $qJ_{x,y}^3$ term.

However, when taking into account the spin-orbit coupling acting on the effective HH state, a correction to the Zeeman energy arises, which can lower the anisotropy [115, 127, 130]. Furthermore, because the spin-orbit parameters α_{R2} and α_{R3} depend on the applied electric field, this correction will also be electrically tunable. This means that the effective g-factor is strongly dependent on the applied electric field and can thus be modulated using the quantum dot gates [75, 88, 127, 131, 132], as is also demonstrated in chapters 8, 9 and 10.

When an in-plane magnetic field is applied, another spin-orbit term should also be considered, arising from the off-diagonal terms in the LKBP and the Zeeman Hamiltonians. This term is described by (in the spherical approximation) [69, 114, 133, 134]:

$$H_{\mathrm{SO,LKZ}} = \frac{3\gamma_s\kappa\mu_B}{m_0\Delta}\left(B_-k_-^2\sigma_+ + B_+k_+^2\sigma_-\right), \tag{3.10}$$

with $B\pm = B_x \pm iB_y$ the in-plane magnetic field, κ the Luttinger parameter [114], μ_B the Bohr magneton, and $\Delta = (E_\mathrm{H} - E_\mathrm{L})$ the splitting between the HH1 and LH1 band, with $E_{\mathrm{H,L}}$ the energy of the heavy and light hole band respectively. This spin-orbit component will lead to another correction to the in-plane g-factor of the qubit. As this term depends on $\Delta_{\mathrm{LH,HH}}$, which in turn depends on the applied electric field, this correction will be electrically tunable. While the electric modulation of the g-factor can provide a path for individual qubit addressability, it can also open up a path for decoherence, as will be further discussed in Section 3.3.6.

3.2.5. ELECTRIC DIPOLE SPIN RESONANCE

As detailed in Section 3.3, the qubits in this thesis are defined on the spin states of a hole in a quantum dot. As a result of the lateral confinement, quantum dot orbitals with quantised energy levels n arise [135]. Due to the effective $s = 3/2$ spin of the heavy hole like ground state, (single photon) magnetic dipole transitions with $\Delta s = \pm 1$ are not allowed [69]. In order to drive the hole spin, we make use of electric dipole spin resonance (EDSR), which allows for a transition using electric fields E_{ac}, mediated by the spin-orbit coupling [68, 69, 75, 127, 130]. Although the qubit is defined by two spin states within the same quantum dot orbital, the driving process involves a virtual transition to the first excited orbital state with $n = 1$. The ac electric excitation drives an orbital transition with $\Delta n = \pm 1$, while the SOC gives rise to the spin flip [75]. However, as can be seen in Eq. 3.7, the $k_\pm^3$ in the (dominant) α_{R2} term is only consistent with a $\Delta n = \pm 3$ transition, and does therefore not contribute to the EDSR driving. However, the $k_\pm k_\mp k_\pm$ dependence in the α_{R3}-Rashba term gives rise to the needed $\Delta n = \pm 1$ spin-flip transitions. Combined with the applied electric field excitation this allows for a second-order EDSR driving without a Dresselhaus or linear Rashba term present. As the driving originates from the SOC, the EDSR Rabi frequency is expected to depend both on B and $\Delta_{\mathrm{LH,HH}}$ [127]. As a result, the driving speed can also be modulated electrically, just like (but not independently of) the Zeeman energy [75, 127, 130].

3.2.6. HYPERFINE INTERACTION

When a spin qubit is defined in a host material containing isotopes with a nuclear spin, interactions between the qubit and the nuclear bath can lead to rapid decoherence [48]. The main nuclear spin interaction term in the Hamiltonian for electron spin qubits is the contact hyperfine interaction, originating from the overlap of the wave functions of the electron and the nuclei. The contact hyperfine interaction has an isotropic Heisenberg form [48]

$$H = \sum_{k}^{N} A_k^e \boldsymbol{S} \cdot \boldsymbol{I}_k, \tag{3.11}$$

with N the total number of nuclei, A_k^e the coupling strength of the electron to the kth nucleus, $\boldsymbol{S}$ and $\boldsymbol{I}_k$ the spin operators for the electron and the kth nucleus respectively.

However, because the valence band hole wave function is predominantly p-type, it vanishes at the atomic nucleus sites and the contact hyperfine interaction is suppressed. In return, due to its finite momentum ($l = 1$), a dipole-dipole interaction term and a term related to the coupling of the orbital momentum and the nucleus arise [136]. These terms can be quite significant and thus still lead to rapid qubit decoherence. For the pure heavy hole in 2D, these interactions take an Ising form [136, 137]:

$$H = \sum_{k}^{N} A_k^h S_z I_k^z, \tag{3.12}$$

with A_k^h the coupling strength of the HH to the kth nucleus, S_z the hole pseudospin-$\frac{1}{2}$ operator and I_k^z the z-component of the kth nuclear spin operator. As a result, the heavy hole spin will mostly couple to the z-component of the nuclear noise, as defined by the growth direction. Recent numerical simulations of the hyperfine tensors of heavy holes in germanium [138, 139] show that the hyperfine interaction in the HH subspace is indeed expected to be extremely Ising-like and that the non-Ising corrections should be small.

When the qubit is defined in a (sufficiently large) in-plane magnetic field, the nuclear fluctuations are purely transverse to the qubit quantisation axis, minimising qubit dephasing [136, 137, 140]. As a result, the heavy hole coherence time (as limited by hyperfine interactions) is expected to increase with increasing in-plane magnetic field, exceeding the expected out-of-plane coherence time by orders of magnitude [136]. However, the admixture of LH or conduction band states as a result of strain or anisotropic confinement could lead to larger non-Ising corrections and thereby increased sensitivity to nuclear spin fluctuations [141, 142].

All natural isotopes of germanium, except for ^{73}Ge, have a net-zero nuclear spin and will thus not contribute to nuclear spin noise. The abundance of ^{73}Ge (spin $\frac{9}{2}$) in natural germanium is relatively low at approximately 7.8 %. This compares favourably to most group III-V semiconductors with an almost 100 % abundance of non-zero nuclear spin isotopes. Germanium can furthermore be isotopically enriched to contain solely net-zero nuclear spin isotopes [27, 28], to eliminate decoherence due to hyperfine interactions entirely.

3.3. QUANTUM DOT SPIN QUBITS

In the late 1990s, David DiVincenzo defined five criteria for constructing a practical quantum computer [143], stating the need for:

- a scalable physical system with well-characterised qubits;
- the ability to initialise the state of the qubits to a simple fiducial state;
- long relevant decoherence times, much longer than the gate operation time;

- a ‘universal’ set of quantum gates;
- a qubit-specific measurement capability.

Building an actual quantum computer involves many more things than just ticking off these criteria [144], but they still inspire many experiments performed today. The experiments discussed in this thesis also tie back to these requirements, demonstrating their implementation in the planar germanium platform. Therefore, we will use them as a guideline in our theoretical discussion of spin qubits below. More elaborate reviews of spin qubits and quantum dot physics in general can be found in Refs. [26, 48, 135, 145, 146].

3.3.1. GATE-DEFINED QUANTUM DOTS

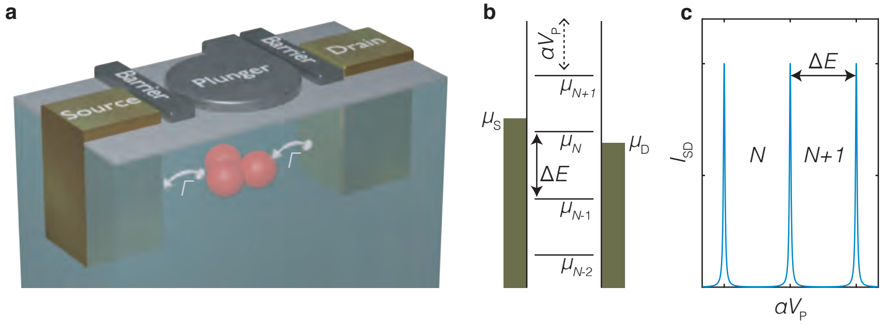

Figure 3.3: **Gate-defined quantum dot a**, Schematic representation of a single quantum dot coupled to two ohmic reservoirs with a tunnel rate Γ. Red spheres indicate the charges on the quantum dot. **b**, Energy diagram of the quantum dot system. μ_S and μ_D indicate electrochemical potentials of the source and drain respectively. The level spacing ΔE in the quantum dot is defined by the charging energy E_C and the orbital spacing E_O. **c**, When the source-drain current is measured as a function of the plunger gate potential energy αV_P, Coulomb peaks can be observed, corresponding to the individual quantum dot energy levels passing through the bias window $|\mu_S - \mu_D|$.

The idea of using the spin state of a single charge in a quantum dot as a **physical system** for the qubit (we will discuss the scalability in Chapter 12) was proposed about two decades ago by Daniel Loss and David DiVincenzo [25]. A quantum dot is a small system in which charges are confined in three dimensions and occupy quantised energy levels. In semiconductor systems, the confinement is usually achieved through material engineering, carefully designed electric field potentials, and often a combination of the two. Great results were achieved in platforms where two or even all three of the dimensions of confinement are defined by material engineering, such as nanowires [147–149] and self-assembled quantum dots [150–152]. However, we will focus on structures with the material only confining the charges in a single direction (*quantum wells*). The confinement in the vertical direction is achieved by the growth of a heterostructure. The stacking of materials with different band gaps, combined with the presence of an electric field, can give rise to the formation of a two-dimensional plane of charges: a two-dimensional electron or hole gas (2DEG and 2DHG respectively). Using lithographically defined metal gates, charges can be laterally confined as well, creating the quantum dot.

A schematic representation of an accumulation-mode single quantum dot device with two ohmic reservoirs is drawn in Fig. 3.3a. A plunger gate is used to define the potential well and also to modulate the quantum dot electrochemical potential μ_{QD}. Barrier gates BS and BD are used to control the coupling Γ between the quantum dot and the ohmic reservoirs. To understand the transport properties (between source S and drain D) of this system, we first need to look at the density of states in the quantum dot. Two separate effects should be considered. First, the classical Coulomb repulsion between charges on the island. As a result, adding another charge to the island will require a *charging energy* of $E_{\mathrm{c}} = e^2/C$, with e the elementary charge and C the total quantum dot capacitance. Since C is proportional to the quantum dot size, the charging energy will be larger for smaller quantum dots. Secondly, as a result of the spatial confinement of the wave function of the electron, its energy levels will quantise analogous to a particle in a box (Fig. 3.3b). As a result, energy levels resembling atomic orbitals arise, which is why quantum dots are sometimes referred to as *artificial atoms*.

To add an extra charge to the quantum dot, an energy difference of $\Delta E = E_{\mathrm{c}} + E_{\mathrm{orbital}}$ is needed, with the latter term being zero for degenerate orbital states. The discrete level spacing can only be observed if the level broadening of both the reservoirs and the dot is smaller than the addition energy ΔE. The first requirement can be achieved by cooling the system down such that $\Delta E \gg k_{\mathrm{B}} T_e$, with T_e the electron temperature and k_{B} the Boltzmann constant. Using the barrier gates, the quantum dot is decoupled from the leads such that $\Delta E \gg h\Gamma$, with h Planck's constant and Γ the tunnelling rate between the quantum dot and the leads. Transport through the quantum dot is now only possible when a QD energy level aligns between the electrochemical potentials $\mu_{\mathrm{S,D}}$ of the source and drain. Using the plunger gate, the electrochemical potential of the quantum dot can be modulated, thus shifting the energy levels with respect to $\mu_{\mathrm{S,D}}$. When the transport current I_{SD} through the quantum dot is measured as a function of the plunger gate voltage V_{P}, a narrow peak in current (*Coulomb peak*) can be observed for each quantum dot level (Fig. 3.3c) passing through the bias window $|\mu_{\mathrm{S}} - \mu_{\mathrm{D}}|$. The spacing between these peaks is equal to $\alpha \Delta V_{\mathrm{P}} = \Delta E$, with $\alpha = C_{\mathrm{gate}}/C$ the lever arm of the gate in meV/mV, which indicates how strongly a gate is coupled to the quantum dot.

3.3.2. OHMIC CONTACTS

The interface between a semiconductor and a metal will typically give rise to a Schottky barrier. Due to a mismatch in the work functions between the metal and the semiconductor, the semiconductor bands will bend upwards for an *n*-type contact, and downwards for a *p*-type contact, forming a potential barrier. This barrier has a rectifying effect and can thus significantly increase contact resistance, complicating quantum dot measurements. For electrons in silicon, this problem is typically resolved by defining local regions of high doping, lowering the Schottky barrier [94, 153]. Nanopatterned accumulation gates define ohmic 2DEGs used as quantum dot source and drain contacts [153]. In germanium, however, the high level of interface states [154] will cause the Fermi level to be *pinned* close to the valence band edge [155, 156], almost independent on the metal that is contacted. As a result, contacting *p*-type germanium with a metal will immediately result in the formation of a (low resistive) ohmic contact. This significantly simplifies quantum dot device fabrication, alleviating the need for ion implantation, thus also lowering the thermal stress on the heterostructure. Furthermore, it makes it possible to define local metal (or superconducting) contacts to the quantum dot for hybrid structures, as is further discussed in Chapter 11.

3.3.3. CHARGE SENSING

The magnetic moment corresponding to a single spin is extremely small and hard to measure directly. To allow for efficient **readout** of the spin qubit, we make use of spin-to-charge conversion. The different spin states will be projected onto different charge states. These charge states can in turn be measured using a nearby charge sensor. Typically, these charge sensors consist of another quantum dot, leveraging the large electric field sensitivity of the transport current dI/dV on the side of a Coulomb peak. When the charge sensor is capacitively coupled to the qubits, the small change in the electric field caused by the movement of a single electron charge will result in a measurable change in current through the charge sensor.

Due to the finite capacitance of a typical fridge wire connecting the device to the (room temperature) amplifier, the bandwidth of this measurement method is limited to several tens of kHz. This problem could be avoided by putting a first amplifying stage in the fridge, thus lowering its input capacitance and increasing the bandwidth. A more commonly employed method is the usage of radio frequency (rf) reflectometry. Using an inductor and the device capacitance, a tank circuit with a characteristic resonance frequency is formed, which is then loaded by the charge sensor. The reflection of the tank circuit can be measured using a resonant fixed frequency signal and is given by $\Gamma_{12} = (Z_{\mathrm{TC}} - 50))\,/\,(Z_{\mathrm{TC}} + 50))$, with Z_{TC} the tank circuit impedance and 50 Ω the source and line impedance. When Z_{TC} matches the source impedance, the reflected power is $\Gamma^2 = 0$, while it increases when there is a mismatch. When the system is driven at its resonance frequency $f_r = 1/\left(2\pi\sqrt{LC}\right)$, with L the total inductance and C the total capacitance, the matching condition is met for $R_{\mathrm{SD}} = L/\,(50C)$. Any change in R_{SD}, such as caused by a charge movement, is thus reflected in the reflected power signal, which can be measured at a bandwidth of several MHz, allowing for much faster measurements.

3.3.4. PAULI SPIN BLOCKADE

Historically, the spin-to-charge conversion was performed by so-called Elzerman readout [47]. When a magnetic field B is applied, the spin states of the electron or hole split by $E_Z = g\mu_{\mathrm{B}}B$, with g the g-factor and μ_{B} the Bohr magneton. When the spin states are aligned around the Fermi level of the quantum dot reservoir, spin-selective tunnelling is obtained. For a positive g-factor, the spin-up electron can tunnel into the lead, while the spin-down electron is energetically blocked from tunnelling, resulting in the spin-to-charge conversion. This requires that the level splitting is significantly larger than the thermal broadening of the reservoir Fermi level, i.e. $E_Z \gg k_{\mathrm{B}}T_e$. As a result, strong magnetic fields are typically required, potentially increasing spin relaxation [48, 157] and measurement equipment complexity. Furthermore, as discussed below, in hole systems the effective g-factor can be as low as $g = 0.2$, making Elzerman readout infeasible at typical operating temperatures and magnetic fields.

A different method to perform spin-to-charge conversion requires a double quantum dot (DQD). This mechanism is referred to as Pauli spin blockade (PSB) [158] readout as it relies on Pauli's exclusion principle. All quantum dot orbitals have a two-fold spin degeneracy, allowing for both a spin-up and spin-down electron. When one of the quantum dots has a partially filled orbital, the tunnelling into this dot is restricted by the spin orientation of the charge. Importantly, the relevant energy scale for this method is the excited state splitting, rather than the Zeeman splitting. As a result, PSB can be employed at elevated temperature [67] or very low magnetic fields [159], as long as the excited-state energy splitting is sufficiently large. Due to the low *g*-factor in germanium, as well as the lack of valley states, resulting in a large excited-state energy splitting, PSB is the preferred readout method.

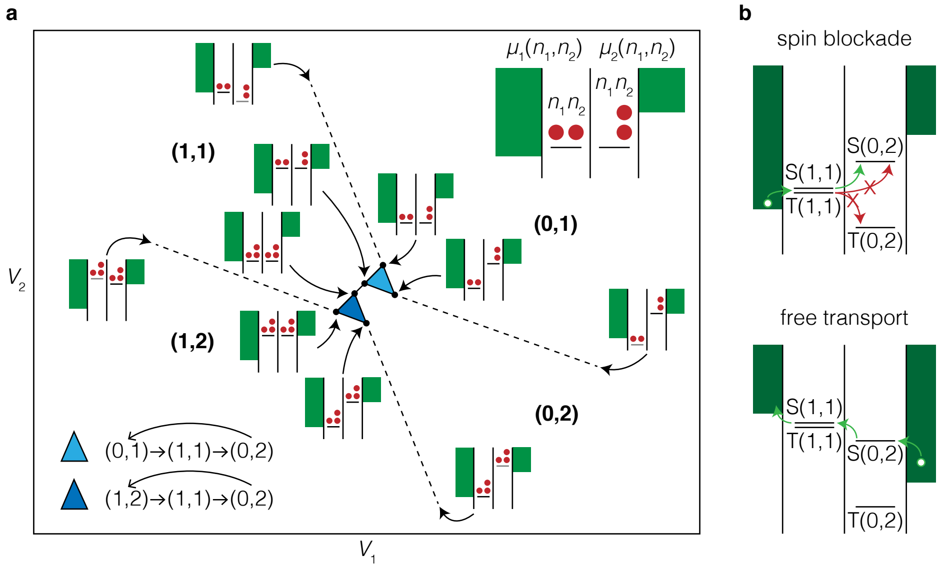

Figure 3.4: **Hole double quantum dot transport mechanisms**. **a**, The double quantum dot stability diagram around the (1,1)-(0,2) transition. Transport occurs within the bias triangles (blue) for positive bias voltage. The light blue triangle corresponds to a transport process cycling counter-clockwise through the (0,1)-(1,1)-(0,2) charge states. The dark blue triangle corresponds to a transport process cycling clockwise through the (1,2)-(1,1)-(0,2) charge states. Little energy diagrams illustrate the energy level alignment in different key voltage configurations, following the representation of Ref. [145], adapted for a hole quantum dot. $\mu_{1(2)}(n_1, n_2)$ corresponds to the energy needed to add the $n^{\text{th}}_{1(2)}$ hole to dot 1(2). **b**, Energy diagram illustrating Pauli spin blockade. For positive bias (top), loading a T(1,1) state will result in a blockade of the transport as indicated in red. For negative bias (bottom) transport is always possible.

PSB can be performed both in transport [158] (as done in Chapter 8) and using charge sensing [160] (as demonstrated in Chapters 9,11). In the following, we will discuss the process for the (1,1)-(0,2) charge transition, but this can be generalised for any filled orbital charge state. In transport, a finite bias is applied across the double dot system. As a result, *bias triangles* of finite current can be observed when the double dot energy levels align between the source and drain electrochemical potentials (Fig. 3.4a, with the bias triangles indicated in blue). Each triangle corresponds to a different charge transfer process, both resulting in a net charge transfer in the same direction. When the applied bias potential is large enough, these triangles will overlap and both processes will contribute to the transport current.

Spin blockade can occur when a tunnelling event from the (1,1) to the (0,2) state is part of the transport process. This is further illustrated in Fig. 3.4b. The energy splitting between the singlet and triplet (1,1) charge states is negligible, as the charges reside in different quantum dots. However, the S(0,2) and T(0,2) states are split by the (significantly larger) excited state splitting. For a positive bias (top panel), starting in the (0,1) charge state, first, the S(1,1) or T(1,1) state will be randomly loaded. In case of an S(1,1) state, transport will be possible through the S(0,2) and back to the (0,1) state (green arrows), repeating the cycle. However, as soon as an S(0,2) state is loaded (with a chance of 50 %), transport is blocked (red arrows), as the T(0,2) state is energetically unavailable. A similar process occurs for the dark blue bias triangle. When the bias direction is reversed (bottom panel), the S(0,2) is loaded first and tunnelling into the (1,1) state is always possible, not blocking transport. Alternatively, the blockade can be lifted by a spin-flip, such as induced by spin resonance [48, 145], resulting in an effective spin-to-charge conversion.

The presence of hole reservoirs connected to each qubit can negatively impact qubit performance [86] and complicate device design. In principle, PSB does not require a hole reservoir, as it solely relies on the double dot interaction for spin-to-charge conversion. The resulting charge state can subsequently be detected using a charge sensor, as discussed above. To get a better understanding of this process, we write down the energy diagram of the double dot system. Around the (1,1)-(0,2) transition the DQD can be described using the five lowest-lying energy states: $\{S(0,2) = \left|\frac{1}{\sqrt{2}}\left(\uparrow\downarrow - \downarrow\uparrow\right), 0\right\rangle, |\uparrow,\uparrow\rangle, |\downarrow,\uparrow\rangle, |\downarrow,\uparrow\rangle, |\downarrow,\downarrow\rangle\}$, with $|s_1, s_2\rangle$ the spin state in quantum dot 1 and 2 respectively. The Hamiltonian of the system can be approximated by [78, 161]:

$$H = \begin{pmatrix} U-\epsilon & 0 & t_0 & -t_0 & 0 \\ 0 & \overline{E_Z} & 0 & 0 & 0 \\ t_0 & 0 & \delta E_Z & 0 & 0 \\ -t_0 & 0 & 0 & -\delta E_Z & 0 \\ 0 & 0 & 0 & 0 & -\overline{E_Z} \end{pmatrix}, \tag{3.13}$$

with $\overline{E_Z}$ the average Zeeman energy on the two quantum dots, δE_Z the Zeeman energy difference, U the charging energy (assumed to be equal for both dots), and ϵ the detuning energy. The latter corresponds to the energy difference between the two quantum dots and is zero in the middle of the Coulomb diamond. t_0 is the interdot tunnel coupling, allowing only for spin-conserved tunnelling processes. Note that we will stick to the 'electron picture', with the lowest-energy state being the ground state. For holes, H can be multiplied by -1, such that the energy axis is inverted.

The corresponding energy eigenstates of the hole DQD are plotted as a function of ϵ in Fig. 3.5. Only the antiparallel spin states couple to the S(0,2) state, allowing for spin-selective tunnelling as long as $\epsilon < E_{\mathrm{orbital}}$, such that the T(0,2) states are unavailable. We note that the presence of spin-orbit coupling could add additional spin-flip tunnelling

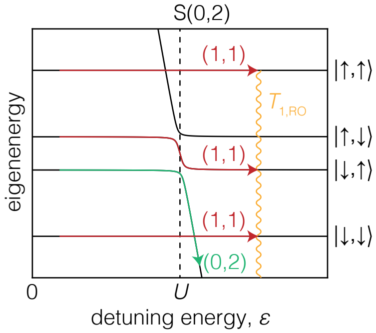

Figure 3.5: **Energy diagram of a DQD**. The five lowest-lying states near the (1,1)-(0,2) transition. When the system is adiabatically pulsed across the (1,1)-(0,2) interdot transition, spin-to-charge conversion occurs as a result of the singlet character of the lower (0,2) charge state. For the three spin initialisations in red, the system resides in the (1,1) charge state after the adiabatic passage, while the green initial spin state results in a (0,2) charge state. Spin relaxation (orange), will eventually decay the (1,1) states into the (0,2) ground state at the readout point.

terms to the Hamiltonian, resulting in a coupling between the S(0,2) and parallel spin states as well, possibly complicating the spin readout, as is further discussed in Chapter 10. If the double dot system is adiabatically pulsed from the (1,1) to the (0,2) charge occupation, only the lower-lying antiparallel spin state will tunnel into the (0,2) charge state. Tunnelling is blocked for the other three charge states, up to the spin relaxation time at the readout (RO) point $T_{1,\mathrm{RO}}$, after which the system (on average) relaxes into the (0,2) ground state. This process can also be used to realise reliable spin initialisation. When the system resides in the (0,2) charge state (prepared by fast charge relaxation), the $|\downarrow,\uparrow\rangle$ state can be **initialised** by adiabatically ramping into the (1,1) charge region. Due to the potentially long spin lifetimes of spin qubits [30, 95, 162], this can give a significant speed-up compared to initialisation methods based on spin relaxation.

3.3.5. QUANTUM LOGIC GATES

Most quantum algorithms are defined by combining a series of predefined quantum operations, also referred to as quantum logic *gates*, analogous to their classical counterparts. Quantum gates acting on *n* qubits are represented by a 2^nx2^n matrix, as previously discussed in Chapter 2. A minimal gate set is called **universal** when all other gates can be created using gates from this minimal set. For spin qubits, the universal gate set is usually formed by two-axis single spin rotations combined with a two-qubit gate. In Table 3.1, we list quantum gates relevant to the work in this thesis, combined with their circuit representation and effective matrix. All matrices are expressed in either the single-spin basis ($\{|\downarrow\rangle, |\uparrow\rangle\}$), two-qubit basis ($\{|\downarrow\downarrow\rangle, |\downarrow\uparrow\rangle, |\uparrow\downarrow\rangle, |\uparrow\uparrow\rangle\}$) or equivalent *n*-qubit basis.

ONE-QUBIT GATES

The single-qubit gates can be physically implemented using spin resonance. By applying a microwave tone resonant with the Zeeman splitting of the qubit $E_Z = g\mu_B B$, the qubit

Operator	Circuit representation	Matrix
X^2 (π rotation)	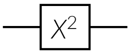	$\begin{pmatrix} 0 & 1 \\ 1 & 0 \end{pmatrix}$
X ($\pi/2$ rotation)	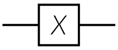	$\frac{1}{\sqrt{2}}\begin{pmatrix} 1 & -i \\ -i & 1 \end{pmatrix}$
Y^2 (π rotation)	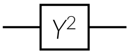	$\begin{pmatrix} 0 & -i \\ i & 0 \end{pmatrix}$
Y ($\pi/2$ rotation)	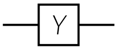	$\frac{1}{\sqrt{2}}\begin{pmatrix} 1 & -1 \\ 1 & 1 \end{pmatrix}$
Z^2 (π rotation)		$\begin{pmatrix} 1 & 0 \\ 0 & -1 \end{pmatrix}$
Z (S, $\pi/2$ rotation)	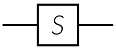	$\begin{pmatrix} 1 & 0 \\ 0 & i \end{pmatrix}$
Hadamard (H)	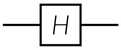	$\frac{1}{\sqrt{2}}\begin{pmatrix} 1 & 1 \\ 1 & -1 \end{pmatrix}$
X-CROT	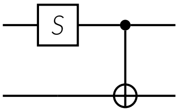	$\begin{pmatrix} 1 & 0 & 0 & 0 \\ 0 & 1 & 0 & 0 \\ 0 & 0 & 0 & i \\ 0 & 0 & i & 0 \end{pmatrix}$
CNOT	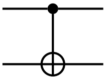	$\begin{pmatrix} 1 & 0 & 0 & 0 \\ 0 & 1 & 0 & 0 \\ 0 & 0 & 0 & 1 \\ 0 & 0 & 1 & 0 \end{pmatrix}$
CZ	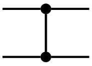	$\begin{pmatrix} 1 & 0 & 0 & 0 \\ 0 & 1 & 0 & 0 \\ 0 & 0 & 1 & 0 \\ 0 & 0 & 0 & -1 \end{pmatrix}$
Toffoli	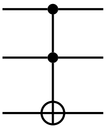	size=8x8 $\begin{pmatrix} 1 & 0 & \dots & 0 & 0 \\ 0 & 1 & \dots & 0 & 0 \\ \dots & \dots & \dots & \dots & \dots \\ 0 & 0 & \dots & 0 & 1 \\ 0 & 0 & \dots & 1 & 0 \end{pmatrix}$
*i*Toffoli [163]	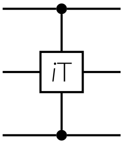	size=8x8 $\begin{pmatrix} 1 & 0 & \dots & 0 & 0 & 0 \\ 0 & 1 & \dots & 0 & 0 & 0 \\ \dots & \dots & \dots & \dots & \dots & \dots \\ 0 & 0 & \dots & 0 & 0 & i \\ 0 & 0 & \dots & 0 & 1 & 0 \\ 0 & 0 & \dots & i & 0 & 0 \end{pmatrix}$

Table 3.1: **Overview of the quantum gates relevant to this thesis.** One, two, and three-qubit gates are separated by a horizontal line, global phases are ignored.

will rotate between its eigenstates. The length and amplitude of the pulse determine the polar angle over which the qubit rotates. The phase offset between sequential microwave pulses will define the azimuthal angle between the axes of rotation. Together, control of the microwave pulse length and phase, as can be acquired using a vector source, will provide the two-axis control needed to access the full single qubit Hilbert space.

TWO-QUBIT GATES

Two-qubit control is typically implemented via the exchange interaction [25]. The presence of a finite tunnel coupling between two quantum dots gives rise to a virtual transition to doubly occupied charge states, effectively decreasing the energy of the singlet (for spin-conserving tunnelling) and triplet (for spin-flip tunnelling) states. When the Zeeman energy difference is large compared to the effective exchange interaction, this can be approximated by a shifting of the antiparallel spin states. This effect can then be used to, for example, perform controlled rotation (CROT), controlled phase (CZ) or SWAP operations. Again, we look at the six lowest-lying energy states of the double quantum dot system, now including both the $(2,0)$ and $(0,2)$ singlet states. In the orthonormal singlet-triplet basis $\{\left|T_{x,y}\right\rangle = i^{1/2\mp1/2}\left(\left|T_-\right\rangle \mp \left|T_+\right\rangle\right)/\sqrt{2}, \left|T_z\right\rangle = \left|T_0\right\rangle, \left|S\right\rangle, \left|S_{20}\right\rangle, \left|S_{02}\right\rangle\}$, the Hamiltonian can be described by:

$$H = i\vec{t}\cdot|\vec{T}\rangle\langle S_{02}| + t_0|S\rangle\langle S_{02}| + \text{H.c.}, \tag{3.14}$$

with $|\vec{T}\rangle = \left\{|T_x\rangle, \left|T_y\right\rangle, |T_z\rangle\right\}$ and $\vec{t} = \left\{t_{\mathrm{SO},x}, t_{\mathrm{SO},y}, t_{\mathrm{SO},z}\right\}$. Because the spin-orbit interaction couples the particle's spin to its motion, it enables a spin-flip upon tunnelling. The $\vec{t}$ term thus describes a spin-flip tunnelling, as a means to account for the spin-orbit interaction [161, 164]. A different method to model the exchange interaction between two hole qubits starting from a general anisotropic J-tensor is discussed in Ref. [165], but yields a similar result. By transforming Eq. 3.14 into the two spin basis $\{|2,0\rangle, |0,2\rangle, |\uparrow,\uparrow\rangle, |\uparrow,\downarrow\rangle, |\downarrow,\uparrow\rangle, |\downarrow,\downarrow\rangle\}$, we obtain the effective Hamiltonian:

$$H = \begin{pmatrix} U-\epsilon & 0 & -t_{\mathrm{SO},y}+it_{\mathrm{SO},x} & t_0-it_{\mathrm{SO},z} & -t_0-it_{\mathrm{SO},z} & -t_{\mathrm{SO},y}-it_{\mathrm{SO},x} \\ 0 & U+\epsilon & -t_{\mathrm{SO},y}+it_{\mathrm{SO},x} & t_0-it_{\mathrm{SO},z} & -t_0-it_{\mathrm{SO},z} & -t_{\mathrm{SO},y}-it_{\mathrm{SO},x} \\ -t_{\mathrm{SO},y}-it_{\mathrm{SO},x} & -t_{\mathrm{SO},y}-it_{\mathrm{SO},x} & E_Z & 0 & 0 & 0 \\ t_0+it_{\mathrm{SO},z} & t_0+it_{\mathrm{SO},z} & 0 & \frac{\delta E_Z}{2} & 0 & 0 \\ -t_0+it_{\mathrm{SO},z} & -t_0+it_{\mathrm{SO},z} & 0 & 0 & -\frac{\delta E_Z}{2} & 0 \\ -t_{\mathrm{SO},y}+it_{\mathrm{SO},x} & -t_{\mathrm{SO},y}+it_{\mathrm{SO},x} & 0 & 0 & 0 & -E_Z \end{pmatrix} \tag{3.15}$$

We perform degenerate perturbation theory [161, 166] on Eq. 3.15, projecting the system onto the 4x4 subspace spanned by the (1,1) states, assuming $\overline{E_Z}, \delta E_Z \ll \epsilon, U$:

$$H = \frac{1}{2}\begin{pmatrix} 2E_Z-J_{xx}-J_{yy} & iJ_{0x}+J_{0y}+J_{xz}-iJ_{yz} & -iJ_{0x}-J_{0y}+J_{xz}-iJ_{yz} & J_{xx}-2iJ_{xy}-J_{yy} \\ -iJ_{0x}+J_{0y}+J_{xz}+iJ_{yz} & \delta E_Z-J_{00}-J_{zz} & J_{00}+2iJ_{0z}-J_{zz} & iJ_{0x}+J_{0y}-J_{xz}+iJ_{yz} \\ iJ_{0x}-J_{0y}+J_{xz}+iJ_{yz} & J_{00}-2iJ_{0z}-J_{zz} & -\delta E_Z-J_{00}-J_{zz} & -iJ_{0x}-J_{0y}-J_{xz}+iJ_{yz} \\ J_{xx}+2iJ_{xy}-J_{yy} & -iJ_{0x}+J_{0y}-J_{xz}-iJ_{yz} & iJ_{0x}-J_{0y}-J_{xz}-iJ_{yz} & -2E_Z-J_{xx}-J_{yy} \end{pmatrix}, \tag{3.16}$$

with

$$J_{ij} = \frac{4Ut_it_j}{U^2-\epsilon^2} \tag{3.17}$$

When we now simplify this by assuming a homogeneous coupling to the different triplet states $t_{\mathrm{SO},x} = t_{\mathrm{SO},y} = t_{\mathrm{SO},z} = t_{\mathrm{SO}}$ and adding a global offset J_{SO}, we obtain:

$$H = \frac{1}{2}\begin{pmatrix} 2E_Z - J_{\mathrm{SO}} & (1-i)(J_{\mathrm{SO}} + iJ_{\mathrm{X}}) & (1-i)(J_{\mathrm{SO}} - iJ_{\mathrm{X}}) & -2iJ_{\mathrm{SO}} \\ (1+i)(J_{\mathrm{SO}} - iJ_{\mathrm{X}}) & \delta E_Z - J_0 & J_0 - J_{\mathrm{SO}} + 2iJ_{\mathrm{X}} & (1+i)(J_{\mathrm{X}} + iJ_{\mathrm{SO}}) \\ (1+i)(J_{\mathrm{SO}} + iJ_{\mathrm{X}}) & J_0 - J_{\mathrm{SO}} - 2iJ_{\mathrm{X}} & -\delta E_Z - J_0 & (-1+i)(J_{\mathrm{SO}} + iJ_{\mathrm{X}}) \\ 2iJ_{\mathrm{SO}} & (-1-i)(J_{\mathrm{SO}} + iJ_{\mathrm{X}}) & (-1-i)(J_{\mathrm{SO}} - iJ_{\mathrm{X}}) & -2E_Z - J_{\mathrm{SO}} \end{pmatrix}, \tag{3.18}$$

with

$$J_0 = \frac{4Ut_0^2}{U^2 - \epsilon^2} \tag{3.19}$$

$$J_{\mathrm{SO}} = \frac{4Ut_{\mathrm{SO}}^2}{U^2 - \epsilon^2} \tag{3.20}$$

$$J_{\mathrm{X}} = \frac{4Ut_0 t_{\mathrm{SO}}}{U^2 - \epsilon^2} \tag{3.21}$$

First, we consider the case where $t_{\mathrm{SO}} = 0$, so $J_{\mathrm{SO}} = J_{\mathrm{X}} = 0$. We can see that Eq. 3.18 reduces to the standard Heisenberg exchange Hamiltonian [161, 167]:

$$H = \begin{pmatrix} E_Z & 0 & 0 & 0 \\ 0 & \delta E_Z/2 - J_0/2 & J_0/2 & 0 \\ 0 & J_0/2 & -\delta E_Z/2 - J_0/2 & 0 \\ 0 & 0 & 0 & -E_Z \end{pmatrix} \tag{3.22}$$

The antiparallel spin states are shifted in energy by (in first order) $J_0/2$. As a result, the energy difference $\Delta E_{\downarrow\downarrow,\uparrow\downarrow}$ corresponding to the $|\downarrow\downarrow\rangle - |\uparrow\downarrow\rangle$-transition differs from that $\Delta E_{\downarrow\uparrow,\uparrow\uparrow}$ of the $|\downarrow\uparrow\rangle - |\uparrow\uparrow\rangle$-transition by J_0, as can be seen in Fig. 3.6. This enables a CROT gate by selectively driving either of the transitions, equivalent to a CNOT gate up to a single qubit phase, as shown in Table 3.1.

When J can be controlled, either through modulation of t_0 or ϵ, a CPHASE gate can be performed as well. When J is adiabatically pulsed, the qubits will pick up a conditional phase ϕ as a result of the (temporary) shift in their resonance frequency. If the total phase shift satisfies $\phi_{|\downarrow\uparrow\rangle} + \phi_{|\uparrow\downarrow\rangle} = (2n+1)\pi$, with $n \in \mathbb{Z}$, we acquire a CZ gate. In order to implement this gate fast yet with high fidelity, $\delta E_Z \gg J$ is required [25, 60]. Since the Zeeman energy is gate-tuneable for the heavy hole states [88], this requirement is typically easily satisfied. Alternatively, in the regime where $J \gg \delta E_Z$, (diabatically) pulsing J leads directly to SWAP rotations between the two anti-parallel spin states.

We now consider the effect of the spin-flip tunnelling term, resulting in a second shift of the parallel spin states by $J_{\mathrm{SO}}/2$. The relative shift of the parallel and anti-parallel spin states is therefore dependent on the ratio of t_0 and t_{SO}. When $J \ll E_Z, \delta E_Z$, we can approximate the effective exchange by $J_{\mathrm{eff}} \approx J_0 - J_{\mathrm{SO}}$. As long as the shifts induced by the regular and the spin-flip tunnelling are not identical, (adiabatic) CROT and CZ gates can thus still be obtained.

3.3.6. QUBIT RELAXATION AND DECOHERENCE

Any physical qubit will, to some degree, be coupled to its (noisy) environment, leading to a loss of the information on the quantum state. Two different relaxation processes

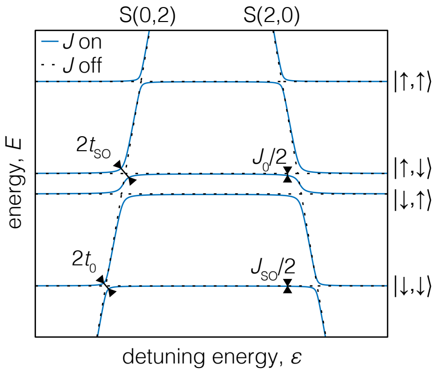

Figure 3.6: **Exchange interaction between two quantum dots**. The six lowest-lying states around the (1,1)-(0,2) and (1,1)-(2,0) transitions are shown. Dotted black lines indicate the situation when exchange is off, while the solid blue lines correspond to an exchange-on situation. The tunnelling term t_0 enables a coupling between the antiparallel spin states and the S(0,2t) state and shifts the states by $J/2$. The spin-flip tunnelling term t_{SO} enables a coupling between the parallel spin states and the S(0,2) and shifts them by $J_{SO}/2$.

should be distinguished. Firstly, (longitudinal) spin relaxation or T_1 relaxation, corresponding to an exchange of energy between the qubit and its environment, relaxing the qubit from its excited to its ground state. Secondly, transverse relaxation or *decoherence*, corresponding to a superposition state losing its phase information, again resulting from interactions with the bath.

The different processes are characterised by a typical decay timescale T. For longitudinal relaxation, this timescale is T_1, corresponding to a spin-flip process (Fig. 3.7a). The rate of transverse relaxation or decoherence is characterised by T_2 (Fig. 3.7b). When performing a single-shot experiment, many independent measurements (*shots*) are averaged, effectively sampling an ensemble of spins. As a result, the experiment is sensitive to fluctuations of the Larmor frequency of the qubit on the timescale of the experiment, and the corresponding ensemble coherence time is T_2^* (Fig. 3.7c).

RELAXATION

Contributions to spin relaxation are hyperfine interactions, interactions with ohmic leads and phonon-hole interactions mediated by the SOC. Typically, at finite magnetic field strength, the hyperfine mediated relaxation is not limiting the spin life time for holes [127, 168]. Virtual tunnelling processes with the ohmic leads can be relevant to spin relaxation, nonetheless, in particular when transport measurements are performed, as demonstrated in Chapter 8. However, by controlling the tunnel (and capacitive) coupling between the qubit and its reservoir, these can be eliminated as well [86, 169]. This leaves phonon-hole interaction as the dominant fundamental source of spin relaxation, caused by both the α_{R2} and α_{R3} Rashba terms [127]. The effect of this source of spin relaxation is estimated in Ref. [127] and is expected to strongly depend on the applied magnetic and electric field. Operating at low magnetic field and optimised electric field should therefore allow for relaxation times that are orders of magnitude longer than qubit operation times.

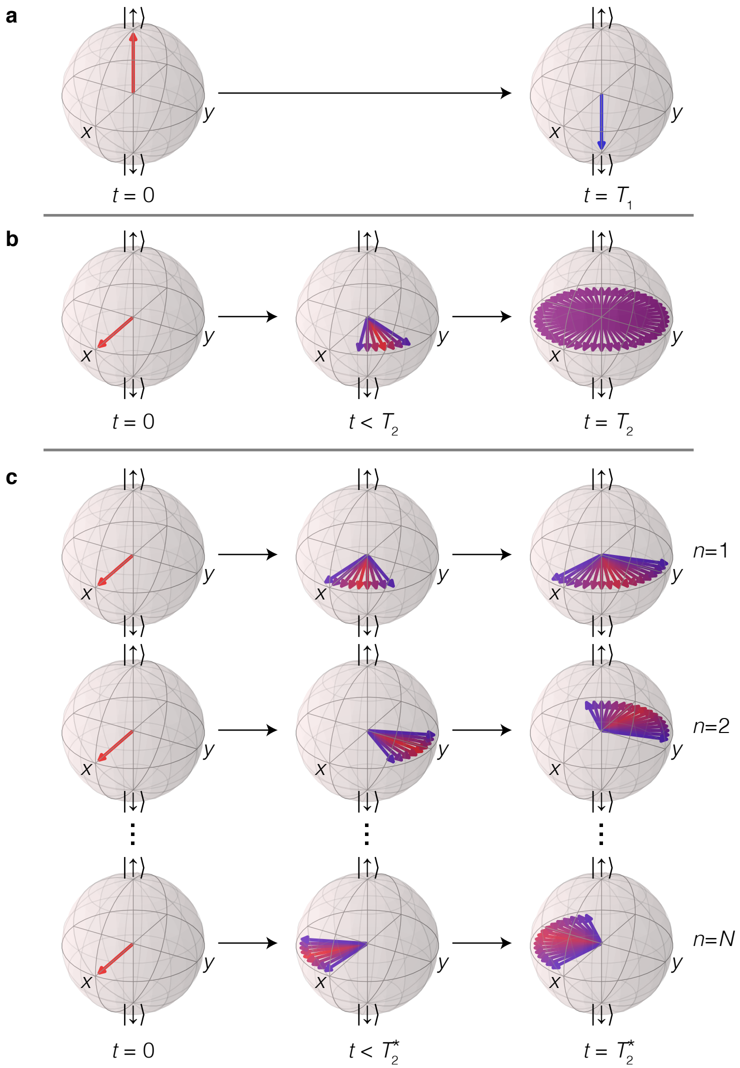

Figure 3.7: **Schematic illustration of relaxation and decoherence processes.** **a**, Longitudinal relaxation corresponding to the qubit excited state relaxing down to the ground state, with characteristic timescale T_1. **b**, Spin dephasing, with the initial spin along the x-axis. On average, after time $t = T_2$ the spin lost phase coherence entirely. **c**, The free induction decay time T_2^* corresponds to the time after which the spin ensemble (consisting of N different shots) lost its coherence, resulting from fluctuations in the field experienced by the ensemble.

DEPHASING

Spin dephasing for heavy hole states can also expected to be limited by electric field fluctuations, such as charge noise. Charge noise is omnipresent in semiconductor devices, typically caused by randomly fluctuating charge defects, often residing at the semiconductor-oxide interface. The resulting electric noise coming from a large ensemble of these two-level fluctuators has an effective $1/f$ noise frequency spectrum [127]. The electric field fluctuations cannot influence the spin state directly but affect it through either the exchange or spin-orbit interaction, which both couple the spin to electric field variations. This is also reflected by the fact that both the exchange interaction and the spin-orbit coupling allow for an electric modulation of the qubit Larmor frequency.

The exchange coupling can be turned off using the tunnel barrier gates to increase the single-qubit coherence, while charge symmetric sweet spots exist [170, 171] to minimise dephasing during two-qubit operations, as detailed in subsubsection 3.3.6 below. Sweet spots in the electric field are expected to exist for the spin-orbit coupling as well, where qubit coherence is protected to first order from electrical noise while optimising EDSR driving [127, 172].

Finally, it should be noted that while hyperfine interactions are expected to be suppressed for a heavy hole state in an in-plane field, the admixture of light hole or conduction band states can lead to increased sensitivity to nuclear spin noise [141, 142, 173]. Hyperfine interactions can thus not be excluded a priori as a source for decoherence in natural germanium quantum dots. Hyperfine interactions can be eliminated entirely by isotopic enrichment of the germanium [27, 174].

Charge insensitive operation

Initial experimental demonstrations of the CPHASE gate using spin qubits were performed by manipulating J by pulsing the detuning and moving toward the anticrossing [60, 61, 78]. While this strategy can lower the experimental constraints, pulsing the tunnel coupling instead can be beneficial [25, 58, 175]. When the system is pulsed towards the anticrossing, the slope of the resonance frequency with respect to the detuning ($\frac{df_q}{d\epsilon}$) increases. As a result, the qubit becomes more susceptible to charge noise [170, 171]. By operating the qubit at the charge insensitive point of symmetric detuning and pulsing the tunnel coupling t, the qubit sensitivity to charge noise remains, to first order, the same.

4

EXPERIMENTAL TECHNIQUES

All parts should go together without forcing. Therefore, if you can't get them back together again, there must be a reason. By all means, do not use a hammer.

IBM maintenance manual, 1975 [176]

In this chapter, we will briefly discuss the various experimental techniques used throughout this thesis. First, we go over device fabrication, focusing on the steps unique to germanium quantum devices, as well as the screening process used to select devices for a cool down in a dilution refrigerator. Next, the experimental setup is discussed, and we review the different setup components and considerations imperative to spin-qubit experiments. Finally, we introduce the differential transport measurement technique that is harnessed to improve the signal-to-noise ratio in Chapter 8.

4.1. DEVICE FABRICATION

The quantum dot devices measured in this thesis are fabricated using a multilayer fabrication scheme, as detailed in Ref. [94]. Details on the wafer growth can be found in Ref. [71] and Chapter 5 of this thesis. The heterostructure is grown on a 4-inch wafer, which is diced into 2x2 cm coupons for further processing. Each coupon consists of either 36 2x2 mm or 9 4x4 mm duplicate cells, depending on the device size. First, a ring of Si_3N_4 is deposited around the edge of each cell, to avoid wire bonds punching through the gate dielectric, potentially causing gate-to-substrate leakage. In a second step, we define aluminium (Al) ohmic contacts by means of electron beam lithography (EBL), electron beam evaporation (EBE), and lift off. The silicon oxide capping layer is removed before ohmic metal deposition using a buffered oxide etch (BOE). The Al ohmic is defined close to the quantum dots, resulting in a very low resistance channel ideally suited for radiofrequency (rf) circuits and enabling a tunnel contact that can even be made superconducting [177]. Next, an Al_2O_3 gate dielectric with a typical thickness of 7-10 nm is deposited using atomic layer deposition (ALD), to avoid gate leakage to the substrate. This process also doubles as a diffusion step for the ohmic leads, due to the thermal stabilisation step of 60 minutes at 300 °C in the ALD system vacuum chamber.

Further fabrication of the device utilises a titanium-palladium (Ti/Pd) gate stack with 3 nm of Ti deposited for each layer to assist with adhesion. Pd makes a good gate metal due to its low grain size [178]. Unlike the commonly used material Al, Pd does not self-oxidise and atomic layer deposition (ALD) is used to define sharp dielectric interfaces. We utilise a two-layer gate stack that we refer to as the barrier layer and plunger layer. In order to assist climbing of overlapping gate features, the initial layer is deposited at 20 nm total thickness, with the subsequent layers at 40 nm. The layers are isolated from one another via an ALD grown Al_2O_3 layer, typically at 7 nm thickness. We measure the dielectric strength of our Al_2O_3 to be greater than 6 MV/cm for gate-to-substrate paths (i.e. over a large area), comparable to values found in literature for thin-film alumina [179–181]. Therefore, potentials beyond 4 V can be applied between adjacent gate layers, sufficiently large for practical device application. Finally, the coupon is diced into the individual device cells, to allow for wire bonding and measurements.

4.2. DEVICE SCREENING

After the devices are fabricated, they undergo visual inspection as a first screening step, discarding dies that contain obvious defects from fabrication. Devices that pass this step are wire bonded onto a printed circuit board (PCB) and cooled down to $T = 4.2$ K in a liquid helium cryostat. Channel turn-on and gate leakage is tested for channels through every individual charge sensor, as well as between the different sensors (through the device area). In a fully automated transport measurement, all gates relevant to the respective channel are swept down to $V_{\mathrm{gate}} = -1.5$ V, after which they are individually swept back up and down to $V_{\mathrm{gate}} = 0$ V. These measurements are checked to confirm if (i) all channels turn on and (ii) all gates modulate the current as expected by the device design. Exemplary data of the screening of the device discussed in Chapter 10 is plotted in Fig. 4.1).

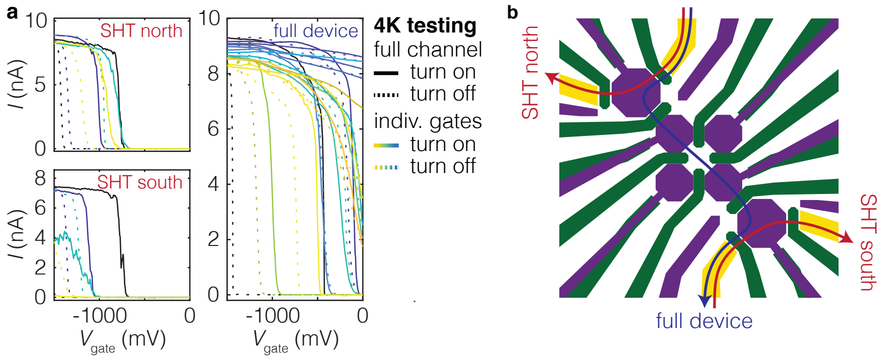

Figure 4.1: **Screening of qubit devices. a,b** 4.2-Kelvin transport data (**a**) of the device presented in Chapter 10. Three different channels (indicated by the arrows in **b**) are turned on by sweeping all gates down to $V = -1500$ mV (black), after which the effect of the individual gates is tested (coloured lines). All channels turn on and the gates affect the transport current as expected from the device layout (**b**). Not all gates are expected to fully turn off the *full device* channel, as some gates are physically in parallel. Furthermore, gates in different gate layers have different coupling strengths to the channel.

4.3. EXPERIMENTAL SETUP

A schematic overview of the measurement setup used for the qubit measurements in Chapter 10 is shown in Fig. 4.4 and is representative for all qubit measurements in this thesis. Qubit measurements are performed in a Bluefors LD-400 dry dilution refrigerator with a base temperature of $T_{\mathrm{base}} = 20$ mK. However, the effective electron temperature in the device is typically higher, due to the connections between the leads and the (warm) outside world and (even warmer) measurement electronics. The observed electron temperature in the devices ranges approximately between $T_{\mathrm{el}} = 70-150$ mK, as measured from the thermal broadening of the interdot transition [182]. The sample is mounted on a PCB supporting 100 direct-current (dc) connections through flat flexible cables (FFCs), as well as 32 rf lines through coaxial connectors and coplanar waveguides. The lines are filtered (dc) or attenuated (rf) at different stages of the fridge to reduce measurement noise and sample heating, as indicated in Fig. 4.4.

4.3.1. DIRECT-CURRENT COMPONENTS

We use homebuilt battery-powered voltage sources (serial peripheral interface (SPI) rack, module type D5a) to bias the electrostatic gates (orange in Fig. 4.4). The sources are physically separated and galvanically isolated from both the power net and other equipment, to eliminate any potential interference. Twisted pair wiring looms with 24 lines each are used to connect the 16-bit digital-to-analogue converters (DACs) to the sample. At the mixing chamber plate, the lines pass a two-stage, low pass RC filter with a cutoff frequency of $f_{\mathrm{co}} \approx 25$ Hz. Lines connected to device ohmics are filtered at a higher cutoff frequency $f_{\mathrm{co}} \approx 220$ kHz to allow for faster measurements. Furthermore, all lines pass a copper powder filter to filter out high-frequency components ($f > 1$ GHz) for which regular RC filters are ineffective. When the PCB layout allows for it, all device ohmics are (and should be) connected through the same wire loom, to avoid (noisy) pickup currents and thermal voltages being present across the device.

4.3.2. ALTERNATING-CURRENT COMPONENTS

On-PCB bias tees allow combining dc and rf signals such that the device gates can both be dc biased and ac pulsed for qubit operations. Electron dipole spin resonance (EDSR) qubit driving requires a signal resonant with the Zeeman frequency of the qubit, which can be up to several GHz for typical magnetic field strengths. We therefore use high-bandwidth superconducting coaxial lines connected to the plunger gates. The other gates (interdot and reservoir barriers) are contacted using lower bandwidth graphite coax cables, with significantly higher attenuation at frequencies above $f \approx 1$ GHz, higher than the arbitrary waveform generator (AWG) output bandwidth. All coaxial lines pass through a ferrite common mode choke at room temperature and are attenuated at different stages of the fridge, with the total attenuation amounting to $9-12$ dB.

Voltage pulses (red in Fig. 4.4) are created using Keysight M3202A arbitrary waveform generators (AWGs), with an output bandwidth of $\mathrm{BW}_{\mathrm{AWG}} = 400$ MHz. A microwave excitation for qubit driving is combined on the same physical line with the AWG signal through room temperature diplexers with passbands dc-400 MHz and 1.5-10 GHz. The use of diplexers was found to be essential, rather than using a resistive combiner. The output impedance of the vector sources is poorly defined (i.e. not 50 Ω) below its output frequency band, skewing the (low frequency) AWG signal. This can result in a slow drift of the AWG voltage levels, which can in turn lead to significantly decreased qubit performance.

The microwave excitation (purple in Fig. 4.4) is generated with a Rohde&Schwarz SGS-100A (Chapter 10) or a Keysight PSG E8267D vector source (Chapters 8-11). The output of the sources is modulated by quadrature modulation using signals generated on the AWGs (dark blue in Fig. 4.4). By applying sine waves with a phase difference of $\pi/2$ to the in-phase (I) and quadrature (Q) inputs of the vector source, a single sideband signal with controllable amplitude, frequency, phase and duration is acquired. As mixers are analogue devices, I and Q signal amplitude, phase, and offsets should always be calibrated to avoid image or carrier leakage [183]. The available output bandwidth is defined by a window $\Delta f = 2\mathrm{BW}_{\mathrm{AWG}}$ around the vector source carrier frequency. Additionally, we apply a pulse modulation (PM) envelope around the microwave pulse trains to enhance the microwave suppression to a total of -120 dB when no pulses are applied. The finite rearm time of the PM input of the vector source (on the order of 100 ns) prevents the suppression of microwave output for individual pulses, due to their close spacing.

REFLECTOMETRY SETUP

The charge sensors are connected to a resonant tank circuit consisting of an in-house fabricated niobium-titanium-nitride (NbTiN) kinetic inductor on a separated chip, combined with the parasitic device capacitance (as further discussed in Chapter 3). We apply rf tones to charge sensors at the resonance frequency of each tank circuit, using a homebuilt reflectometry setup. The rf generator outputs are triggered by the AWG to start approximately a hundred nanoseconds before the qubit readout, mitigating transient effects during readout. Using resistive rf combiners, the outputs of

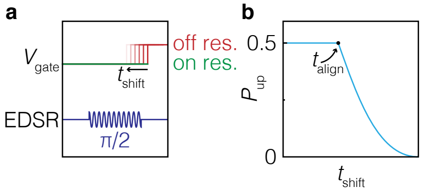

Figure 4.2: **Gate voltage and EDSR pulse alignment a**, An EDSR $\pi/2$-pulse is applied to the qubit, as well as a gate voltage step to push the qubit driving frequency off resonance (green, on resonance to red, off resonance). **b**, When measuring the spin-up probability P_{up} as a function of pulse time offset t_{shift}, the point of ideal pulse alignment t_{align} is characterised by the kink in the P_{up} signal.

multiple generators are combined onto a single line, to allow readout of multiple tank circuits. The rf signal is attenuated at different temperature stages of the fridge before reaching the PCB. Here, the signal propagates through two on-PCB bias-tees to the two NbTiN resonators, which are part of the tank circuits. It is then reflected by the charge sensor, split off using a directional coupler mounted to the mK-plate of the fridge, and amplified by 35 dB by a CITLF3 cryogenic amplifier at the 4K stage. Next, the signal is further amplified at room temperature and demodulated at every carrier frequency by an IQ mixer. The data are recorded using a Keysight M3102A digitiser card, triggered by the Keysight Hard Virtual Instrument (HVI) framework. The internal field programmable gate array (FPGA) of the digitiser card is used to temporally average a measurement segment, thus returning only a single data point per channel, per shot.

PULSE ALIGNMENT

As a result of propagation delays within the setup, different signals (e.g. EDSR driving and gate pulsing) can arrive at a time offset of tens of nanoseconds at the qubit gates. It is therefore important to measure and subsequently correct for these delays, to allow for minimised temporal separation of the pulses. Since it is impossible to connect an oscilloscope to the cryogenic side of the setup, the qubit itself should be used as a measurement apparatus. We do so by applying both an EDSR burst and a gate voltage pulse to the qubit. The latter will shift the qubit off-resonance, utilising the electric g-factor modulation. By shifting the EDSR pulse in time with respect to the gate voltage pulse, we can calibrate for any delay between the two (Fig. 4.2).

4.4. DIFFERENTIAL TRANSPORT MEASUREMENTS

When spin readout is performed by Pauli spin blockade in transport, the different qubit states are mapped onto different transport currents. In order to improve the quality of the transport measurements, we establish a lock-in measurement scheme where the measurement of interest is alternated with a reference measurement to account for slow variations in the transport current through the device, as well as temperature-dependent drifts in our transimpedance amplifier. A measurement cycle is continuously alternated with a reference measurement, to account for these drifts, as is illustrated in Fig. 4.3. The measurement cycle, consisting of the qubit readout as well as the manipulation phase, typically has a length of $\sim 1\ \mu$s. Using the AWG, we generate

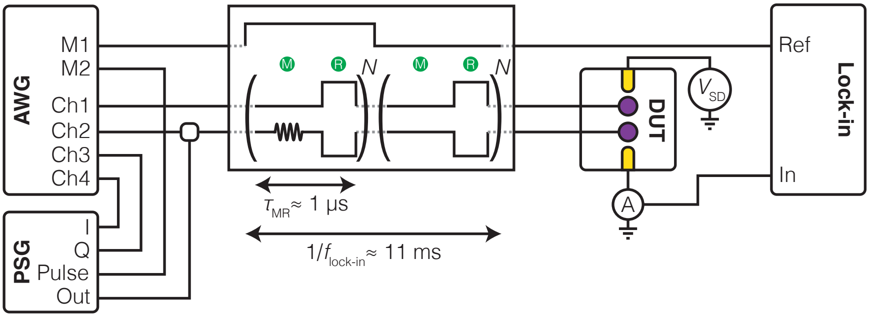

Figure 4.3: **Instrumentation setup for the lock-in transport measurements.** Illustration of the setup and relevant signals for the lock-in transport measurements. The AWG is used to generate alternating pulse cycles consisting of a repeated measurement and a repeated reference pulse. The signal is demodulated in a lock-in amplifier to give a direct measure of the difference between the two measurements and subtract slow variations in the transport signal.

a waveform that repeats the measurement cycle N times, followed by N repetitions of a similar reference measurement, with N chosen such that these cycles alternate at a lock-in frequency of $f_{\text{lock-in}} = 89.75$ Hz. The measured transport current is then demodulated by a lock-in amplifier, using a reference signal generated by the AWG. As a result, the lock-in output signal will be directly related to the difference in transport current between the measurement and the reference cycle. During the readout, no differential current is observed when the qubits are in their $|{\downarrow\downarrow}\rangle$ ground state (which is also the reference state), while a signal of typically $\Delta I_{\text{SD}} \approx 0.3$ pA is measured for all other configurations and a total cycle length of $t_{\text{cycle}} = 900$ ns. This is in good agreement with a bias current $\Delta I = 2e/t_{\text{cycle}} = 0.4$ pA, as expected for the random loading of a hole spin.

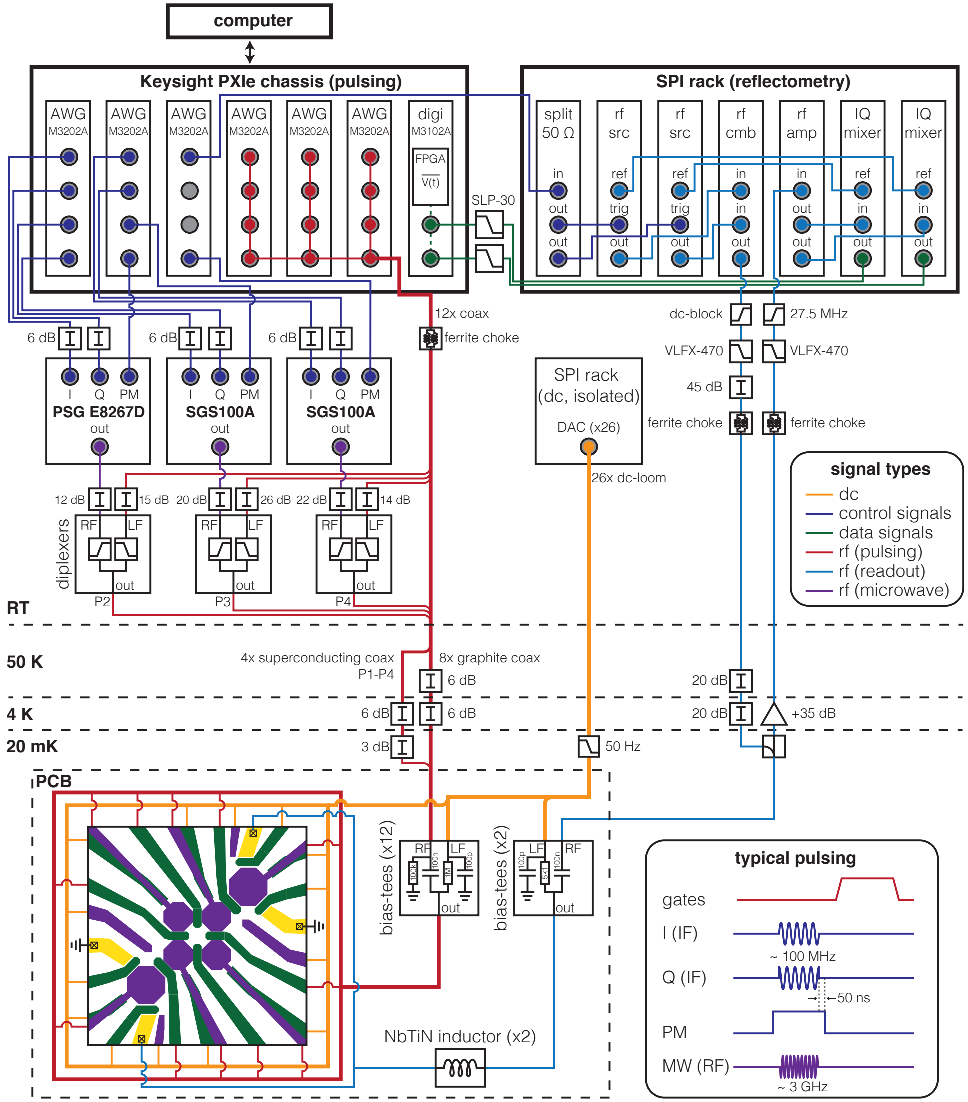

Figure 4.4: **Schematic of the measurement setup for a four-qubit experiment.** The different electronic signals are indicated using different colours. The diagram in the bottom right corner indicated the typical signals used for the spin qubit operation.

5

SHALLOW AND UNDOPED GERMANIUM QUANTUM WELLS

In this chapter, we will discuss the heterostructure growth and characterisation of strained, planar germanium quantum wells. A two-dimensional hole gas of high mobility ($\mu = 5 \times 10^5 cm^2 V^{-1} s^{-1}$) is accumulated in a shallow, strained germanium (Ge) channel, which is located only 22 nm below the surface. The top gate of an undoped field-effect transistor controls the channel carrier density confined in a Ge/SiGe heterostructure with reduced background contamination, sharp interfaces, and high uniformity. The high mobility leads to a mean free path of $L \approx 6$ µm, setting new benchmarks for holes in shallow field-effect transistors. The high mobility, along with a percolation density of $p_p = 1.2 \times 10^{11}$ cm^{-2}, light effective mass $m^* = 0.09 m_e$, and high effective g-factor (up to 9.2) highlight the potential of undoped Ge/SiGe as a low-disorder material platform for hybrid quantum technologies.

Parts of this chapter have been published in Advanced Functional Materials **29**, 14 (2019) [71].

5.1. INTRODUCTION

Germanium (Ge) has the highest hole mobility of all common semiconductors and can be integrated onto silicon (Si) substrates within a foundry-qualified process [29]. These properties make high-speed Ge transistors appealing for extending chip performance in classical computers beyond the limits imposed by miniaturisation. Ge is also emerging as a promising material for quantum technology as it contains crucial parameters for semiconducting, superconducting, and topological quantum electronic devices. The high mobility of holes and their low effective mass promote the confinement of spins in low-disorder Ge quantum dots by uniform potential landscapes [74]. Holes in Ge have a large and tuneable *g*-factor, and experience an inherent, strong spin-orbit interaction. These properties facilitate fast all-electrical qubit control [84] and qubit coupling at a distance via superconductors [184], and are key ingredients for the emergence of Majorana zero modes for topological quantum computing.

Like silicon, germanium can be isotopically purified into a nuclear spin-free material to achieve long spin lifetimes [28]. In contrast to silicon, the Fermi level in germanium is pinned close to the valence band edge [156], allowing the fabrication of low-resistive contacts to almost every metal, including superconductors with high critical fields. This facilitates the injection of holes and thus the formation of ohmic superconductor/semiconductor contacts, a key building block in hybrid quantum devices.

These enticing prospects have motivated the development of a theoretical framework for Ge-based spin-qubits [75] and Majorana fermions [185]. Experimental milestones in self-assembled Ge nanostructures include gate-tuneable superconductivity in Ge/Si nanowires [186], the demonstration of electrically driven spin qubits [84], and single-shot readout of single spins [83] in Ge hut wires.

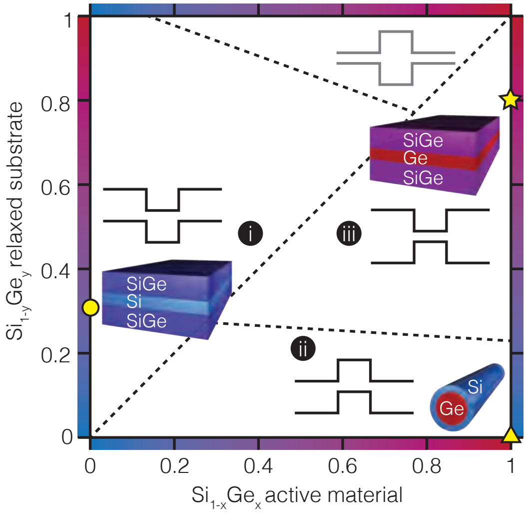

Figure 5.1: **Schematics of SiGe heterostructures band edge profile.** The band edge profile is sketched as a function of the Ge concentration *x* and *y* in the active material and in the relaxed substrate, respectively. Star, circle, and triangle refer to Ge/SiGe, Si/SiGe and Ge/Si heterostructures, respectively. Adapted from Ref. [187]

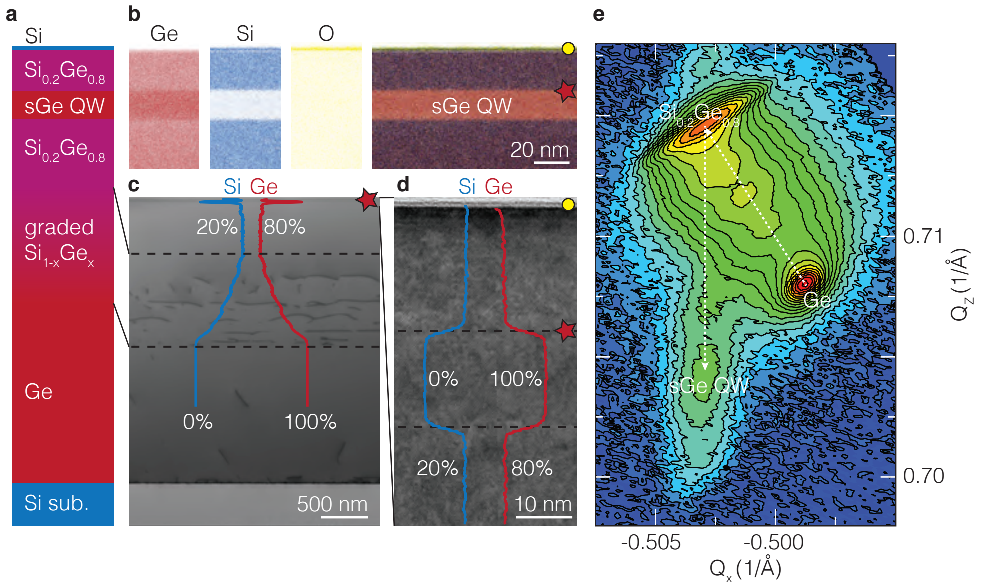

Figure 5.2: **Structural characterisation of a Ge/SiGe heterostructure.** **a**, Schematic illustration of the heterostructure layers. **b**, Germanium (Ge), silicon (Si), and oxygen (O) signals from scanning transmission electron microscopy with energy dispersive x-ray analysis (STEM/EDX) of the Ge quantum well and nearby $Si_{0.2}Ge_{0.8}$. **c**, STEM image of the heterostructure, with Si and Ge concentration profiles measured by secondary ion mass spectroscopy (SIMS). **d**, Transmission electron microscopy (TEM) image showing the quantum well/barrier interface (red star) and barrier/surface interface (yellow circle). Superimposed concentration profiles are measured by STEM/EDX. **e**, X-ray diffraction reciprocal space map of (-2-24) reflection.

Recently, Ge/SiGe heterostructures have emerged as a planar technology that can bring together low disorder, potential for fast qubit driving, and avenue for scaling due to the compatibility with large scale manufacturing. In Ge/SiGe, the band-edge profiles produce a type I band alignment [187] for quantum wells with a composition ranging from relaxed $Si_{1-y}Ge_y$ to a compressively strained pure Ge layer (Fig. 5.1; star, $y \approx 0.8$). This is different from Si/SiGe heterostructures (Fig. 5.1; circle, $y \approx 0.3$) and Ge/Si core-shell nanowires (Fig. 5.1; triangle), where a type II band alignment promotes confinement of either electrons or holes, respectively. Charge carriers can populate the quantum well either by doping of the heterostructure or by top gating. Holes confined in modulation-doped Ge/SiGe have shown an exceptionally high mobility of $1.5{\cdot}10^6$ cm^2/Vs, a strong spin-orbit coupling [70], large effective g-factors [188], and fractional quantum Hall physics [189]. A very light effective mass of $0.055m_e$ [190] was measured in Hall bar devices aligned with the <110> crystallographic direction, further reduced to $0.035m_e$ for the <100> direction.

However, ionised impurities in the doped supply layer are a major source of scattering, charge noise, leakage, and instability for the low-temperature operation of quantum devices [191]. In analogy to electron spin qubits in Si/SiGe [192], to fabricate gated Ge quantum devices it is preferable to completely eliminate dopant atoms from the Ge/SiGe heterostructure. Indeed, gate-controlled quantum dots [74], ballistic one-

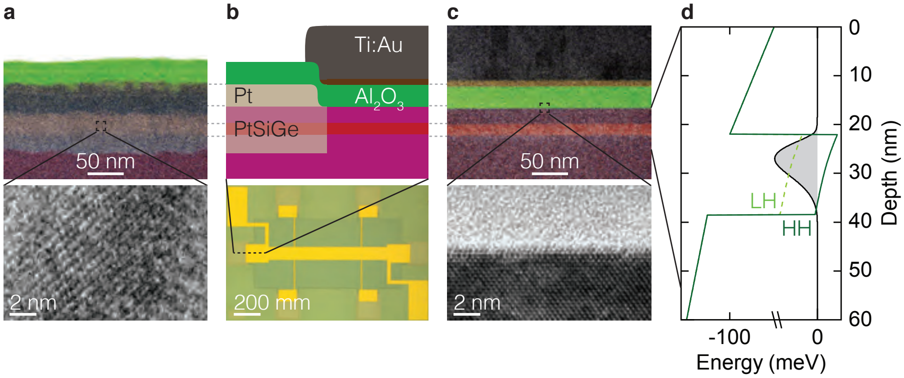

Figure 5.3: **Ge/SiGe heterostructure field-effect transistor.** **a**, STEM/EDX (top) and TEM (bottom) in the ohmic contact region. **b**, Device cross-section schematics and optical image (upper and lower panels, respectively). **c**, STEM/EDX (top) and TEM (bottom) in the channel region. **d**, Bandstructure simulation with heavy holes (HH), light holes (LH) and charge distribution in the first subband ($|\psi^*\psi|$).

dimensional channels [193], and ballistic phase-coherent superconductivity [177] were demonstrated recently by using undoped Ge/SiGe. So far the added complexity in developing reliable gate stacks has limited the investigation of quantum transport properties in undoped Ge/SiGe to devices with mobilities significantly inferior compared to modulation-doped structures [194–197].

In this chapter, we demonstrate state-of-the-art, very shallow, undoped Ge/SiGe heterostructures and devise a process for fabricating undoped heterostructure field-effect transistors (H-FETs) without compromising on material quality. The capacitively induced two-dimensional hole gas (2DHG) is positioned only 22 nm below the surface and therefore suitable for further nanofabrication of well-defined quantum devices [74]. A comprehensive investigation of key electrical properties such as carrier mobility, critical density for conduction, effective mass, and effective g-factor establishes undoped Ge/SiGe as a promising platform for future hybrid quantum technologies.

5.2. GE/SIGE HETEROSTRUCTURES.

Fig. 5.2 shows a schematic of the investigated Ge/SiGe heterostructure along with the results of structural characterisation to elucidate the crystallographic, morphological, and chemical properties of the stack. The Ge/SiGe heterostructure is grown on a 100 mm Si(001) substrate in a high-throughput reduced-pressure chemical vapour deposition reactor. The layer sequence comprises a $Si_{0.2}Ge_{0.8}$ virtual substrate obtained by reverse grading [198, 199], a 16-nm-thick Ge quantum well, a 22-nm-thick $Si_{0.2}Ge_{0.8}$ barrier, and a thin sacrificial Si cap (see Section 5.7.1). Compared to previous designs of Ge/SiGe stacks [196], the purpose of the additional Si cap is to provide a well-known starting surface for subsequent high-κ metal gate stack deposition [200] and to possibly achieve a superior dielectric interface than what SiGe could offer. Secondary ion mass spectroscopy (SIMS) shows constant oxygen (O) concentration of 2×10^{17} cm^{-3} within the SiGe regions surrounding the quantum well. However, by carefully engineering the growth temperature profile, both carbon and oxygen concentration within the quantum well are below the SIMS detection limit of 4×10^{16} cm^{-3} and 8×10^{16} cm^{-3}, respectively, pointing to a very low impurity background level.

Fig. 5.2c highlights the crystalline quality of the $Si_{0.2}Ge_{0.8}$ virtual substrate. The Si and Ge concentration profiles across the virtual substrate (Fig. 5.2c; blue and red curves respectively) confirm the achievement of linear reverse-graded SiGe with targeted alloy composition. Defects and dislocations are confined to the lower layers, at the Si/Ge interface and in the graded $Si_{1-y}Ge_y$. As the Si (Ge) concentration in the SiGe alloy is increased (decreased), relaxation of the upper layers is promoted. By performing preferential etching (see Section 5.7.2), we estimate an upper bound for the threading dislocation density of $(3.0 \pm 0.5) \times 10^7$ cm^{-2} for the $Si_{0.2}Ge_{0.8}$.

In-plane and out-of-plane lattice parameters are obtained from the x-ray diffraction reciprocal space map (XRD-RSM) in Fig. 5.2e. The Ge and $Si_{0.2}Ge_{0.8}$ buffer layers are over-relaxed compared to the Si substrate with a residual tensile strain of $\epsilon_{\parallel} = 0.2\%$ and 0.26%, respectively. This is typical in SiGe virtual substrates due to the difference in the thermal contraction of the materials after cooling from the high growth temperature [198, 201]. The peak corresponding to the Ge quantum well is vertically aligned to the peak of the $Si_{0.2}Ge_{0.8}$ buffer layer, indicating a pseudomorphic growth of the quantum well and resulting in an in-plane compressive strain of $\epsilon_{\parallel} = -0.63\%$.

Fig. 5.2b shows the individual and combined scanning transmission electron microscopy with energy dispersive x-ray (STEM/EDX) signals of Si, Ge, and oxygen from the strained Ge quantum well embedded between $Si_{0.2}Ge_{0.8}$. The Ge quantum well appears as a uniform layer of constant thickness and with sharp interfaces to the adjacent $Si_{0.2}Ge_{0.8}$. The increasing O and Si signals at the top of the heterostructure indicate that the Si cap has readily oxidised upon exposure to air. The absence of extended defects in the high-resolution transmission electron microscopy (TEM) images in Fig. 5.2d indicates high crystalline quality in the quantum well and adjacent $Si_{0.2}Ge_{0.8}$. The high degree of control achieved in the deposition process results in the Si and Ge composition profiles in Fig. 5.2d, with constant Ge composition within each layer of the $Si_{0.2}Ge_{0.8}$/Ge/$Si_{0.2}Ge_{0.8}$ structure. By fitting a high-resolution STEM/EDX Ge concentration profile at the quantum well interface with an error function [202, 203], we infer that the top interface of the quantum well is abrupt and characterised by a distance $\lambda \leq 0.8$ nm for transitioning between Ge and SiGe.

5.3. HETEROSTRUCTURE FIELD-EFFECT TRANSISTORS.

Hall-bar shaped heterostructure field-effect transistors (H-FETs) oriented along the <110> crystallographic directions were fabricated to investigate the magnetotransport properties of the undoped Ge/SiGe. An external electric field is applied to the insulated top gate thereby populating the Ge quantum well and creating a two-dimensional hole gas (2DHG). Compared to undoped Si/SiGe H-FETs [204], we adopted a low-thermal budget, implantation-free process to obtain direct contact between diffused platinum (Pt) metallic ohmic leads and the induced 2DHG (see Section 5.7.3). This approach is possible due to the very low Schottky barrier height for a *p*-type platinum germanosilicide contact [205, 206].

The optical image of the final device is displayed in Fig. 5.3b, together with the

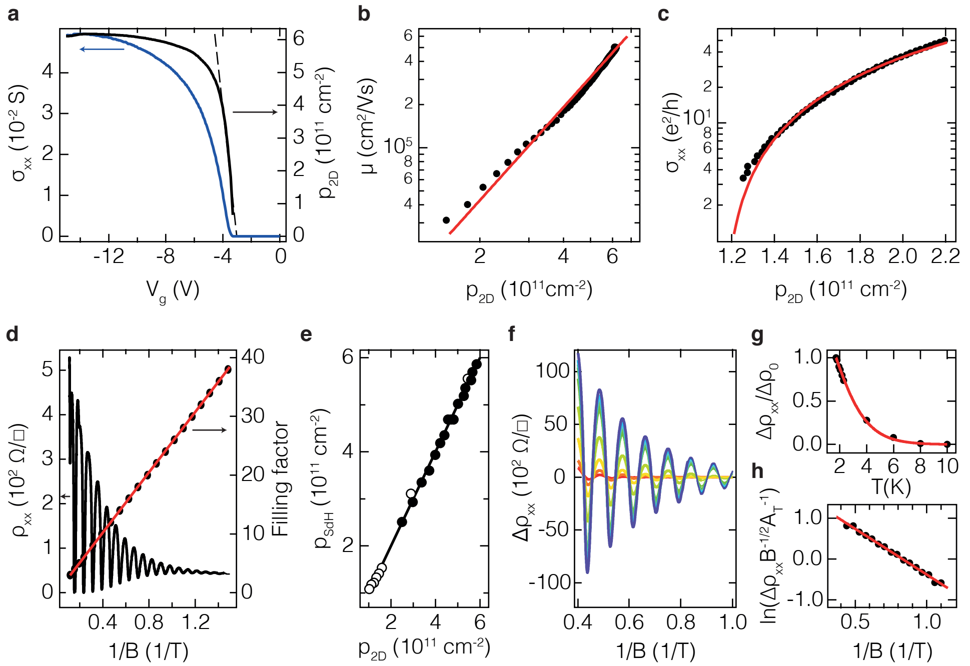

Figure 5.4: **Transport measurements at T = 1.7 K as a function of magnetic field and carrier density.** **a**, Conductivity σ_{xx} (blue line) and Hall density p_{2D} (black line) as a function of gate voltage V_g at 1.7 K. Dashed line is a linear fit of the gate-dependent density at low V_g. **b**, Density-dependent mobility μ (solid circles) and power law fit (red curve). **c**, Density-dependent σ_{xx} (solid circles) and fit to percolation theory (red line). **d**, Magnetoresistivity ρ_{xx} (black line) and filling factor (solid circles) at saturation density as a function of inverse magnetic field $1/B$. Red line is the fit to the filling factor progression. **e**, Density p_{SdH} obtained by the analysis of the Shubnikov-de Haas oscillations plotted as a function of the corresponding Hall density p_{2D}. Open and solid circles are measured at 1.7 K and 50 mK, respectively. **f**, Temperature dependence of the Shubnikov-de Haas oscillations $\Delta\rho$ in the range $T = 1.7$-10 K, after background subtractions. **g**, $\Delta\rho$ (solid circles) as a function of T, normalised at $\Delta\rho_0 = \Delta\rho(T_0 = 1.7\text{K})$. The red line is the fit used to extract m^*. **h**, Dingle plot at $T_0 = 1.7$ K. The red line is the linear fit used to extract τ_q.

schematics of the transistor cross section at the gate/ohmic contact overlap region. The upper panels in Fig. 5.3a and c show STEM/EDX analysis in the ohmic contact region and under the top-gate, respectively. In the ohmic region (Fig. 5.3a, top panel), Pt diffuses inside the SiGe barrier and surpasses the quantum well. A platinum germanosilicide alloy is formed, with a Ge concentration less than the value of 0.8 present in the as-grown material, due to the Pt dilution within. The formation of a platinum germanosilicide alloy is also supported by the presence of crystalline grains, as visible by transmission electron microscopy (Fig. 5.3a, bottom panel). Since Pt diffusion is achieved at a significantly lower temperature than the quantum well growth (300 °C vs. 500 °C, respectively) the crystalline quality of the heterostructure under the gate-stack is preserved. The critical Ge/SiGe interfaces after device fabrication (Fig. 5.3c, top panel) are as sharp as before processing (Fig. 5.2c). Furthermore, the high-resolution TEM image in the bottom panel of Fig. 5.3c highlights the atomically flat semiconductor/oxide interface.

Fig. 5.3d shows the band structure in the H-FET at a carrier density of 1×10^{11} cm^{-2}, obtained by solving the Schrödinger-Poisson equation as a function of the applied electric field at low temperatures. States in the quantum well with a heavy hole (HH) type symmetry are energetically favoured over light holes (LH) states, with the HH and LH band edges split in energy by 40 meV. The wave-function of the fundamental HH state is well confined within the Ge quantum well, with an energy splitting between the fundamental HH state and the fundamental LH state of 47 meV, and between the fundamental and the first excited HH state of 15 meV. These obtained energy splittings in Ge/SiGe are more than one order of magnitude larger than the valley splitting in the conduction band of Si/SiGe or Si/SiO$_2$ systems [146], supporting the possibility of obtaining well-defined qubits in this material platform.

5.4. MOBILITY, CRITICAL DENSITY, AND EFFECTIVE MASS.

Magnetotransport characterisation of the Ge/SiGe H-FET was performed at low temperatures to elucidate the quantum transport properties of the 2DHG. The device is operated in accumulation mode, in which carriers populate the undoped quantum well by applying a negative dc voltage bias (V_g) to the top-gate (relative to the drain contact). By applying a fixed ac voltage bias to the source and drain contacts (V_sd), standard four-probe lock-in techniques allow measuring the longitudinal and transverse components of the resistivity tensor (ρ_{xx} and ρ_{xy}, respectively), from which longitudinal (σ_{xx}) and transverse (σ_{xy}) conductivity are extracted. The active carrier density p_2D and the carrier mobility μ are measured by the Hall effect (see Section 5.7.4).

Fig. 5.4a shows the conductivity and the carrier density as a function of gate voltage (blue and black curves, respectively). At zero applied V_g, there are no carriers induced in the quantum well, so the undoped heterostructure is insulating and no conduction is measured. Above a threshold bias ($V_\mathrm{g} = -3.8$ V), current starts flowing in the channel and σ_{xx} increases monotonically as a function of V_g until saturation is reached. After turn on of the capacitively induced 2DHG, p_2D increases linearly as V_g becomes more negative. This is consistent with a simple parallel-plate capacitor model in which the Si$_{0.2}$Ge$_{0.8}$ and Al$_2$O$_3$ layers are the dielectric layers between the Ge quantum well and the metallic top-gate. However, the extracted effective gate capacitance obtained by fitting the linear portion of the $p_\mathrm{2D}(V_\mathrm{g})$ curve, is reduced to approximately 60 % of the expected value. At larger V_g, the $p_\mathrm{2D}(V_\mathrm{g})$ curve deviates from linearity and eventually p_2D saturates at a value of 6×10^{11} cm^{-2}.

Fig. 5.4b shows the density-dependent mobility. The mobility increases strongly with density over the entire range of accessible densities, without signs of saturation. By fitting the data to a power law dependence $\mu = p_\mathrm{2D}^{\alpha}$ we find a large exponent $\alpha = 2.1$. Including local field corrections [207, 208], exponents $\alpha \geq 1.5$ indicate that the mobility is still limited by scattering from remote impurities at the dielectric/semiconductor interface, as seen previously in Si/SiGe heterostructures [194, 209]. At saturation density $p_\mathrm{2D} = 6 \times 10^{11}$ cm^{-2}, we measure a maximum mobility of 5×10^5cm^2/Vs, corresponding to a mean free path of $L \approx 6$ µm, setting new benchmarks for holes in shallow H-FET devices.

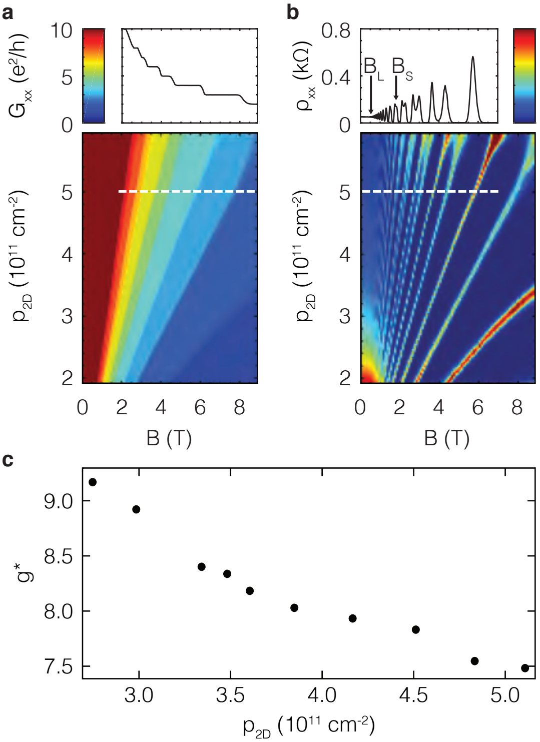

Figure 5.5: **Transport measurements at T = 50 mK as a function of magnetic field and carrier density.** **a**, The Hall conductance G_{xy} as a function of magnetic field B, showing clear quantised conductance. **b**, The longitudinal resistance ρ_{xx} shows the corresponding Shubnikov-de Haas oscillations. B_L and B_S mark the magnetic field at which Shubnikov-de Haas oscillations and Zeeman splitting are resolved, respectively. **c**, Effective g-factor as a function of carrier density $p_{2\mathrm{D}}$.

The critical density for establishing metallic conduction in the channel is extracted by fitting the density-dependent conductivity (Fig. 5.4c) in the low density regime to percolation theory [210, 211] $\sigma \propto A(p_{2\mathrm{D}} - p_p)^p$ cm^{-2}. By fixing the exponent to $p = 1.31$, as expected in a 2D system, we estimate a percolation threshold density $p_p = 1.15 \times 10^{11}$ cm^{-2} at 1.7 K, which sets an upper bound for p_p at the temperature at which qubits typically operate ($T \leq 100$ mK). Note that this value is in agreement with the qualitative estimate of critical density $p_c = 1.19 \times 10^{11}$ cm^{-2} obtained by extrapolating the linear regime of the $\mu(\log(p_{2\mathrm{D}}))$ curve to zero [212]. The obtained percolation threshold density is similar to the values reported in high quality Si metal oxide semiconductor field-effect transistors (MOSFETs) [210, 211], and approximately two times higher than the values reported in undoped Si/SiGe [204], possibly because the dielectric interface in our samples is much closer to channel (22 nm compared to 50 nm in Ref. [204]).

Fig. 5.4d shows the Shubnikov-de Haas (SdH) oscillations in the magnetoresistivity at saturation density. The oscillation minima reach zero at high magnetic field B and are periodic as a function of $1/B$. From the linear filling factor progression (Fig. 5.4d, red circles) we extract a density $p_{\mathrm{SdH}} = 6.1 \times 10^{11}$ cm^{-2}, in agreement with the Hall measurement data. The agreement $p_{\mathrm{SdH}} = p_{\mathrm{2D}}$ is verified throughout the range of investigated density and temperature (Fig. 5.4e). Fig. 5.4f shows the temperature-dependent magnetoresistance oscillation amplitude $\Delta\rho$ at a density $p_{\mathrm{2D}} = 5.4 \times 10^{11}$ cm^{-2}, as a function of $1/B$, after the subtraction of a polynomial background. The hole effective mass m^* is extracted by fitting the damping of the SdH-oscillation amplitude with increasing temperature at $B = 1.4$ T (Fig. 5.4g and Section 5.7.4). The obtained value $m^* = (0.090 \pm 0.002)m_e$, where m_e is the free electron mass, is comparable to previous reports in Ge/SiGe at similar densities [194, 197]. The quantum lifetime τ_q at 1.7 K is extracted by fitting the SdH-oscillation envelope [213]. From the Dingle plot in Fig. 5.4h, we estimate $\tau_q = 0.74$ ps, corresponding to a large Dingle ratio $\tau_t/\tau_q = 27$, where τ_t is the transport lifetime. The obtained large Dingle ratio confirms that the mobility is limited by scattering from charges trapped at the dielectric/heterostructure interface.

5.5. LANDAU FAN DIAGRAM AND EFFECTIVE g-FACTOR.

In Fig. 5.5a,b we show color plots of ρ_{xx} as well as the transverse (Hall) signal σ_{xy} at $T = 50$ mK, as a function of the out-of-plane magnetic field B and the carrier density p_{2D}, as obtained from the low-field Hall measurement data. In this Landau fan diagram, both the quantum Hall effect (Fig. 5.5a) and SdH-oscillations (Fig. 5.5b) fan out linearly towards higher field and density. Similar to the measurements at 1.7 K (Fig. 5.4f), we do not observe a beating in the SdH-oscillations. This prevents us from directly measuring the strength of the spin-orbit interaction. However, we estimate an upper bound of the spin splitting in the 2DHG of 1.5 meV from the peak width of 1.5 T^{-1} observed in the Fourier transform of ρ_{xx} against $1/B$. Observation of a Landau fan diagram of this quality confirms the low disorder in the 2D channel. Furthermore, these measurements allow for estimating the out-of-plane effective g-factor (g^*) [204] by comparing the field strength B_L at which SdH-oscillations appear to the field B_S at which the spin-splitting occurs, as a function of the density (see Section 5.7.4). We observe a decrease of g^* from $g^* \approx 9.2$ to $g^* \approx 7.5$ with increasing density, as shown in Fig. 5.5c. We attribute this decrease to a higher degree of admixture of the light hole states at higher densities, as a result of the non-parabolicity of the valence band [188].

5.6. DISCUSSION

The observed $p_{\mathrm{2D}}(V_{\mathrm{g}})$ and $\mu(p_{\mathrm{2D}})$ dependencies are in line with previous studies on shallow, undoped Si and Ge/SiGe heterostructures [196, 214]. At small electric fields, carrier tunnelling can occur from the shallow Ge quantum well to defect states in the band-gap of the dielectric/SiGe interface. While tunnelling reduces the gate capacitance, the passivation of the surface impurities by tunnelled carriers can also lead to enhanced carrier mobility [215]. We speculate that this mechanism is causing the observed upturn in the $\mu(p_{\mathrm{2D}})$ dependence above a density of $p_{\mathrm{2D}} = 3 \times 10^{11}$ cm^{-2}, as also described in Ref. [214]. At even higher electric fields, the Fermi level aligns with the valence band edge at the dielectric/SiGe interface. Population of the surface quantum well prevents, by screening, further carrier accumulation in the buried channel, which reaches saturation. Nevertheless, only the buried quantum well contributes to transport, since the surface quantum well carrier concentration is likely below the mobility edge threshold, which is typically high for a channel at the Al_2O_3/Si interface. This interpretation is supported by the matching densities p_{2D} and p_{SdH} (Fig. 5.4d), with no beating observed in the SdH-oscillations. This suggests only one high-mobility subband contributes to the measured transport.

In conclusion, we have shown that shallow and undoped Ge/SiGe heterostructures are a promising low-disorder platform for Ge quantum devices, by measuring key transport metrics at low temperatures. The reported half-million mobility sets new benchmarks for Si and Ge shallow-channel H-FETs [196, 214, 215], while even higher mobilities may be obtained by further improving the semiconductor/dielectric interface. Possible avenues in these directions include the removal of the native silicon oxide layer prior to high-κ dielectric deposition or the implementation of a post-metallisation thermal anneal. A better quality semiconductor/dielectric interface should furthermore improve the critical density, which is a crucial metric for quantum devices.

The measured hole effective mass of $0.09m_e$ is a factor two lighter than the corresponding value for electrons in silicon ($0.19m_e$), and is close to the effective mass of conduction band carriers in GaAs ($0.067m_e$). A lighter effective mass is beneficial for spin-qubit definition, since it will lead to a larger energy level spacing in quantum dots and also relaxes lithographic fabrication constraints, due to a larger extent of the wave function. Notice that an even lighter value of about $0.05m_e$ [75], should be within reach for undoped Ge/SiGe, upon improving the semiconductor/dielectric interface or alternatively increasing the distance separating the quantum well from the interface. Furthermore, because non-parabolic effects increase the effective mass [216], the effective mass is expected to be smaller in a low 2D hole density regime [194], due to the decrease of the Fermi vector at low density.

5.7. EXPERIMENTAL METHODS

5.7.1. HETEROSTRUCTURE GROWTH

The Ge/SiGe heterostructure is grown in a high-throughput reduced-pressure chemical vapour deposition (RP-CVD) reactor (ASMI Epsilon 2000) in one deposition cycle using germane (GeH_4) and dichlorosilane (SiH_2Cl_2) as precursor gases. Starting with a 100 mm Si(001) substrate, a 1.4-µm-thick layer of Ge is grown using a dual-step process. An initial low-temperature (400 °C) growth of a Ge seed layer is followed by a higher temperature (625 °C) overgrowth of a thick relaxed Ge buffer layer. Cycle anneals at 800 °C are performed to promote full relaxation of the Ge. The subsequent 900-nm-thick reverse-graded $Si_{1-y}Ge_y$ layer [198] is grown at 800 °C with y changing from 1 to 0.8. The SiGe virtual substrate is completed by a $Si_{0.2}Ge_{0.8}$ buffer layer of uniform composition, which is initially grown at 800 °C. For the final 160 nm, the growth temperature is lowered to match the growth temperature of the subsequent layers (500 °C). In this way, growth interruption for temperature equilibration is avoided at the critical quantum well/virtual substrate interface. The heterostructure is completed with the deposition of a 16-nm-thick Ge quantum well, a 22-nm-thick $Si_{0.2}Ge_{0.8}$ barrier, and a thin (<2 nm) sacrificial Si cap.

5.7.2. STRUCTURAL ANALYSIS

X-ray diffraction measurements were performed with a 9 kW Rigaku SmartLab diffractometer equipped with a Ge(400x2) crystal collimator and a Ge(220x2) crystal analyser using Cu-Kα1 radiation. The asymmetric (-2-24) reflection was used for reciprocal space mapping to determine in-plane and out-of-plane lattice parameters. Transmission electron microscope investigation was carried out using a FEI Tecnai Osiris. For EDX, the TEM was operated in scanning TEM (STEM) mode. The beam energy for all TEM measurements was 200 keV. Preferential etching techniques are used to estimate an upper bound for the threading dislocation density in the SiGe virtual substrate. We exposed the sample to a solution of 10 ml HF (50% vol) + 15 ml HNO_3 (69% vol) + 1 mg KI + 1 mg I_2 + 5 ml CH_3COOH (100%vol) + 60 ml H_2O for 6 seconds at a temperature of 273 K. Counting statistics are performed on the SiGe etched surfaces imaged by atomic force microscopy.

5.7.3. DEVICE FABRICATION

The fabrication process for undoped Ge/SiGe H-FETs consists of the deposition of metallic ohmics, a high-κ dielectric, and a metallic top-gate. Ohmic pads are deposited on top of a mesa structure by electron beam evaporation of 60 nm of Pt. A dip in hydrofluoric acid is performed prior to the Pt deposition to remove the native oxide at the surface and ensure that the Pt film is in direct contact with the underlying $Si_{0.2}Ge_{0.8}$. The subsequent atomic layer deposition of 30 nm of Al_2O_3 at 300 °C has a twofold purpose. The dielectric will electrically isolate the top-gate from the channel. Furthermore, the elevated temperature during the process also provides the thermal budget needed to drive the Pt ohmics into the $Si_{0.2}Ge_{0.8}$. Finally, the top-gate is fabricated by optical lithography and subsequent depositing of 10/150 nm of Ti/Au.

5.7.4. ELECTRICAL MEASUREMENTS

We obtained the magnetotransport data in the temperature range of 1.7 to 10 K in a ^{4}He refrigerator equipped with a variable temperature insert and a 9 T magnet. The magnetotransport data at 50 mK were obtained in a ^{3}He dilution refrigerator equipped with a 9 T magnet. An ac bias voltage of 0.1-1 mV with a frequency of 7.7 Hz is applied between the source and drain contacts. The source-drain current I_{sd}, the longitudinal voltage V_{xx}, and the transverse Hall voltage V_{xy} are measured using a lock-in amplifier. The longitudinal resistivity ρ_{xx} and transverse Hall resistivity ρ_{xy} are calculated as $\rho_{xx} = V_{xx}/I_{sd} \times W/L$ and $\rho_{xy} = V_{xy}/I_{sd}$, respectively (aspect ratio $L/W = 5$). The longitudinal (σ_{xx}) and transverse (σ_{xy}) conductivity are calculated from ρ_{xx} and ρ_{xy} by tensor inversion. The electrically active Hall carrier density p_{2D} is obtained from the linear dependence of the Hall resistivity in a perpendicular magnetic field ($\rho_{xy} = B/ep_{2D}$) at low magnetic field values ($B \leq 0.5$ T). The carrier mobility μ is obtained from the relationship $1/\rho_{xx} = p_{2D}e\mu$. The effective mass m*is fitted from the damping of the Shubnikov-de Haas oscillations by using the expression [217]:

$$\frac{\Delta\rho_{xx}}{\Delta\rho_0} = \frac{\Delta\rho/\rho_0\ (T)}{\Delta\rho/\rho_0\ (T_0)} = \frac{A_T}{A_{T_0}} = \frac{T\ \sinh(\alpha T_0)}{T_0\ \sinh(\alpha T)}\ , \tag{5.1}$$

with $\alpha = \dfrac{2\pi k_\mathrm{B} m^*}{\hbar e B}$, k_B the Boltzmann constant, $\hbar$ the Planck constant, ρ_0 the zero-field resistivity, and $T_0 = 1.7$ K the lowest temperature at which the SdH-oscillations are observed. We estimate the effective g-factor g^* (Fig. 5.5c) by comparing the onset of the SdH-oscillations to the onset of the Zeeman spin splitting. We define the magnetic field strength at which the Shubnikov-de Haas oscillations become apparent B_L. At this point, the Landau level spacing minus the Zeeman splitting equals the Landau level broadening:

$$\hbar e B_\mathrm{L}/m^* - g^* \mu_\mathrm{B} B_\mathrm{L} = \Gamma(B_\mathrm{L}), \tag{5.2}$$

with $\Gamma(B_\mathrm{L})$ the Landau level broadening and μ_B the Bohr magneton. Next, we define the magnetic field strength B_S at which the first Zeeman spin splitting is observed. At this point, the spin splitting is equal to the Landau level broadening:

$$g^* \mu_\mathrm{B} B_\mathrm{S} = \Gamma(B_\mathrm{S}), \tag{5.3}$$

Taking into account the field-dependent broadening of the Landau levels $\Gamma(B) = C\sqrt{B}$ [218], g^* can derived from Eqs. 5.2 and 5.3 and equals:

$$g^* = \frac{2m_e}{m^*} \frac{1}{1 + \sqrt{B_\mathrm{S}/B_\mathrm{L}}}. \tag{5.4}$$

6

LOW PERCOLATION DENSITY AND CHARGE NOISE WITH HOLES IN GERMANIUM

While the shallow quantum wells presented in the previous channel allow for sharp gate confinement potentials, the proximity of the channel to (disordered) gate dielectrics and interfacial trap states, could negatively impact device stability and qubit performance. In this chapter, we study planar Ge/SiGe heterostructures with varying quantum well depth and optimise the material for low disorder and quiet hole quantum dot operation by positioning the strained Ge channel 55 nm below the semiconductor/dielectric interface. In heterostructure field-effect transistors, we measure a percolation density for two-dimensional hole transport of 2.1×10^{10} *cm*$^{-2}$*, indicative of a very low disorder potential landscape experienced by holes in the buried Ge channel. These Ge heterostructures support quiet operation of hole quantum dots, and we measure an average charge noise level of* $\sqrt{S_E} = 0.6\ \mu\mathrm{eV}/\sqrt{\mathrm{Hz}}$ *at 1 Hz, with the lowest level below our detection limit* $\sqrt{S_E} = 0.2\ \mu\mathrm{eV}/\sqrt{\mathrm{Hz}}$*. These results establish planar Ge as a promising platform for scaled two-dimensional spin qubit arrays.*

Parts of this chapter have been published in Materials for Quantum Technology **1**, 011002 (2021) [219] and Nature Communications **9**, 2835 (2018) [74]

6.1. INTRODUCTION

The promise of quantum information with quantum dots [25] has led to extensive studies for suitable quantum materials. While initial research mainly focused on gallium arsenide heterostructures because of its extremely low level of disorder, hyperfine interaction with nuclear spins has limited the quantum coherence of spin qubits [49, 51]. Instead, silicon naturally contains only few non-zero nuclear spin isotopes and can furthermore be isotopically enriched, such that quantum coherence can be maintained for very long times [56, 220]. However, the relatively large effective mass and the presence of valley states complicates scalability [146] and warrants the search for alternative quantum materials.

Germanium has prospects to overcome these challenges and is rapidly emerging as a unique material for quantum information [30]. Holes in germanium exhibit strong and tuneable spin-orbit coupling allowing for fast and all-electrical control of spin qubits [68, 69, 84, 86]. The light effective mass along the Ge quantum well (QW) interface induces large orbital energy spacing for quantum dots and thereby relaxes the lithographic fabrication requirements [73]. In addition, ohmic contacts can be made to metals, which enabled the development of hybrid superconductor-semiconductor circuits [74, 177, 221], and promises novel approaches for long-range qubit links to engineer scalable qubit tiles [26].

Importantly, Ge QWs can be engineered in silicon-germanium (Ge/SiGe) heterostructures [71] that are fabricated using techniques compatible with existing semiconductor manufacturing [29], which facilitates large scale device integration. These advances enabled to define stable quantum dots [74], to operate quantum dot arrays [94], to realise single hole spin qubits [132] with long spin life-times [88], and to demonstrate full two-qubit logic [86]. In all these experiments, the Ge QW was located remarkably close to the semiconductor/dielectric interface at a depth of only 22 nm [71]. While this shallow heterostructure showed an ultra-high maximum mobility exceeding 5×10^5 cm^2/Vs, possibly due to passivation of surface impurities by tunnelled carriers from the QW, a rather high percolation density $p_p = 1.2 \times 10^{11}$ cm^{-2} was measured. This value is similar to the values reported for Si metal-oxide-semiconductor field-effect transistors [210, 211, 222] and about twice the value reported in Si/SiGe QWs [204, 223]. Since the percolation density characterises disorder at low densities, which is the typical regime for quantum dot operation, a significant development is still needed to make undoped Ge/SiGe heterostructures compatible with existing architectures for large-scale quantum information processing with quantum dots, all relying on highly uniform qubits that exhibit extremely low noise [26, 224].

6.2. LOW PERCOLATION DENSITY

Here, we demonstrate planar Ge/SiGe heterostructures with very low levels of disorder and charge noise, setting new benchmarks for semiconductor materials for spin qubits. We quantify disorder beyond the metric of maximum mobility and focus on the percolation density and the single-particle relaxation time (τ_q), which measures the time for which a momentum eigenstate can be defined even in the presence of scattering [225]. We report the associated quantum mobility $\mu_q = e\tau_q/m^*$ [226], with e the elementary charge and m^* the effective mass. By increasing the separation between the QW and the semiconductor/oxide interface to 55 nm, both p_p and μ_q improve, and we find percolation densities as low as $p_p = 2.1 \times 10^{10}$ cm^{-2} and quantum mobilities as high as $\mu_q = 2.5 \times 10^4$ cm^2/Vs. We introduce a method to measure charge noise in gate-defined quantum dots by scanning over Coulomb peaks to discriminate between measurement and device noise. We find that charge noise can be below our detection limit of $\sqrt{S_E} = 0.2$ µeV/$\sqrt{\text{Hz}}$ at 1 Hz, about an order of magnitude less than previously reported for germanium quantum dots [74].

We grow Ge/SiGe heterostructures by reduced-pressure chemical vapour deposition on a Si(001) wafer and fabricate Hall-bar shaped heterostructure field-effect transistors (H-FETs) for magnetotransport characterisation by four-probe low-frequency lock-in techniques as described in Ref. [71]. Figure 6.1a shows a cross-section schematic of the H-FET in the channel region. Figure 6.1b shows a high angle annular dark-field scanning transmission electron (HAADF-STEM) image of the active layers of the H-FET, with no visible defects or dislocations. The strained Ge QW is uniform, has a constant thickness of $d \approx 16$ nm, and is separated from the SiO$_x$/Al$_2$O$_3$ dielectric stack by a Si$_{0.2}$Ge$_{0.8}$ barrier. The QW thickness is in agreement with the values reported in Ref. [71], highlighting the reproducible growth process achieved by reduced-pressure chemical vapour deposition in an industrial reactor. We chose a Si$_{0.2}$Ge$_{0.8}$ barrier thickness $t = 55$ nm to suppress surface tunnelling from the strained Ge QW [196] and improve the electronic environment, whilst maintaining a sharp confinement potential for quantum dots with excellent tuneability. We achieve smooth interfaces between the Ge QW and nearby Si$_{0.2}$Ge$_{0.8}$ and between the Si$_{0.2}$Ge$_{0.8}$ barrier and the dielectric, highlighting the high-quality of epitaxy and device processing.

Applying a negative bias to the Ti/Au gate induces a two-dimensional hole gas and controls the carrier density in the QW. Figure 6.1c shows the transport mobility μ as a function of density p. The mobility increases steeply to 1×10^5 cm^2/Vs in the low-density range (2.4 to 3.9×10^{10} cm^{-2}) due to increased screening of scattering from remote charged impurities, likely at the semiconductor/dielectric interface. At higher density, the mobility also becomes limited by short-range scattering from impurities within or near the QW and saturates, reaching a maximum value of 2.5×10^5 cm^2/Vs at a density of 9.2×10^{10} cm^{-2}. The saturation of mobility upon increasing density indicates that surface tunnelling is suppressed in this H-FET. In shallow Ge/SiGe heterostructures, an upturn in $\mu(p)$ dependence was observed above $p = 3 \times 10^{11}$ cm^{-2} instead, with no sign of saturation [71]. Figure 6.1d shows the conductivity σ in the low density regime (up $p_p = 3.8 \times 10^{10}$ cm^{-2}) to percolation theory [71, 210, 211]. We extract a percolation density of $p_p = 2.14 \times 10^{10}$ cm^{-2} by fitting σ in the low density regime to percolation theory [71, 210, 211]. For measurements across two H-FETs fabricated on the same wafer we obtain a weighted average percolation density $\langle p_p \rangle = (2.17 \pm 0.02) \times 10^{10}$ cm^{-2}, pointing to uniform heterostructure deposition across the wafer and fabrication process. The obtained p_p is indicative of very low disorder at low density, which is the typical condition for quantum dot operation, representing an approximate 5 times improvement compared to previous heterostructures supporting Ge spin qubits [71], and setting a new benchmark for group-IV materials that have practical use for spin qubits.

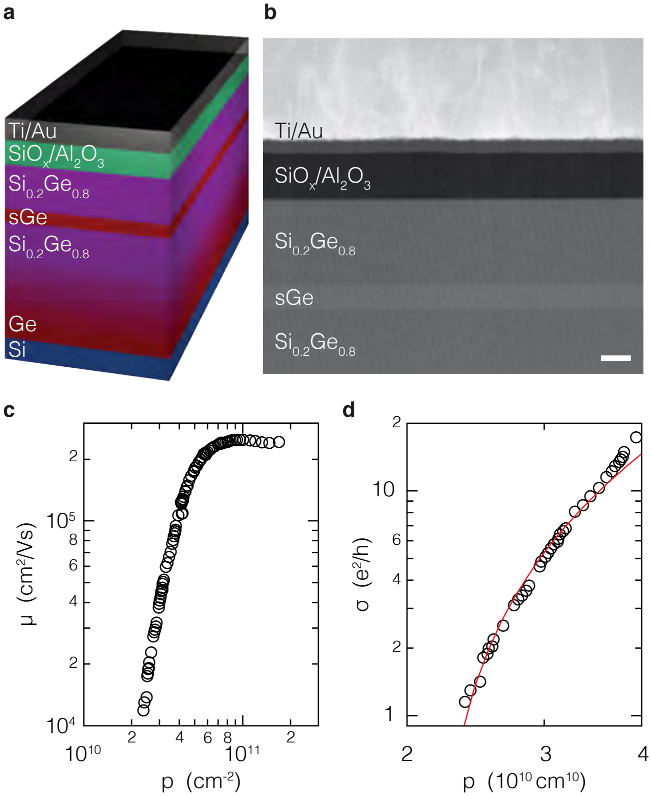

Figure 6.1: **A 60-nm-deep strained germanium quantum well.** **a**, Schematic of a Ge/SiGe heterostructure field-effect transistor. The strained Ge (sGe) quantum well is grown coherent to a strain-relaxed $Si_{0.2}Ge_{0.8}$ layer obtained by reverse grading. A $Si_{0.2}Ge_{0.8}$ barrier separates the QW from the dielectric stack—native silicon oxide followed by Al_2O_3— and from the Ti/Au metallic gate metal. **b**, High angle annular dark field scanning transmission electron image of the active layers of the Ge/SiGe heterostructure field-effect transistor. Scale bar is 20 nm. **c**, Mobility μ and d conductivity σ_{xx} as a function of density p at a temperature T = 1.7 K. The red line in d is a fit to percolation theory in the low density regime.

We further characterise disorder in the Ge H-FET by measuring the single-particle relaxation time τ_q and the associated quantum mobility μ_q. The single-particle relaxation time determines the quantum level broadening $\Gamma = \hbar/2\tau_q$ of the momentum eigenstates and is affected by all scattering events. This is distinct from the transport scattering time τ_t, which instead is unaffected by forward scattering [225] and determines the conductivity and the classical mobility $\mu = e\tau_t/m^*$. As such we argue that μ_q is a disorder qualifier less forgiving than μ and in principle is more informative of the qubit surrounding environment. This results from the fact that μ_q does not exclude a priori any source of scattering, which in turn might degrade qubit performance.

To measure τ_q and μ_q we probe the disorder-induced broadening of the 2DHG Landau levels in magnetotransport. Figure 6.2a shows the longitudinal resistivity ρ_{xx} and transverse Hall resistance R_{xy} as a function of B at a fixed density corresponding to the maximum transport mobility. We observe Shubnikov-de Haas oscillations above $B = 0.37$ T and Zeeman splitting above $B = 0.83$ T, from which we estimate an effective $g^* = 12.7$ following the methodology in Ref. [71]. The oscillation minima go to zero above $B = 4.3$ T, signalling high-quality magnetotransport from a single high-mobility subband corresponding to the heavy hole fundamental state in the Ge QW. R_{xy} develops flat plateaus corresponding to oscillation minima in ρ_{xx}, due to the integer quantum Hall effect. Signatures of the $\nu = 5/3$ fractional state are visible both in ρ_{xx} and R_{xy}, indicating a robust energy gap that survives thermal broadening at 1.7 K.

Figure 6.2b shows the low-field oscillation amplitude $\Delta\rho_{xx} = (\rho_{xx} - \rho_0)$ as a function of perpendicular magnetic field B, where ρ_0 is the ρ_{xx} value at $B = 0$. We estimate a single-particle relaxation time $\tau_q = 0.87$ ps from a fit of the Shubnikov-de Haas oscillation envelope to the function $\Delta\rho_{xx} \approx \rho_0 B^{1/2}\chi/\sinh(\chi)\exp\bigl(-\pi/\omega_c\tau_q\bigr)$, where $\chi = 2\pi^2 k_B T/\hbar\omega_c$, k_B is the Boltzmann constant, $\hbar$ is the Planck constant and ω_c is the cyclotron frequency[1] (Fig. 6.2b, red curve) [227]. Correspondingly, we estimate $\Gamma = 377$ μeV. This is approximately four times smaller than Γ at a comparable p in a shallow QW positioned 17 nm below the surface, signaling that disorder is greatly reduced in the heterostructure detailed in this work. We find a Dingle ratio $\tau_t/\tau_q = 10$, which is approximately three times smaller compared to shallower QWs [71], confirming that long-range scattering is reduced, as expected from the μ dependence on p in Fig. 6.1c.

In Figure 6.2c we show the quantum mobility μ_q as a function of the percolation density p_p measured for QWs positioned at different distance t from the semiconductor/dielectric interface. For each heterostructure, μ_q is evaluated at saturation density $p_{sat} \sim 1/t$ [73]. We observe a clear correlation: as the QW is separated from the impurities at the semiconductor/dielectric interface, both our disorder qualifiers p_p and μ_q improve and reach best values in the heterostructure with $t = 55$ nm. The observed correlation also implies that percolation density, which may be measured at higher temperatures and more easily than Shubnikov-de Haas oscillations, is sufficient to provide a fast feedback loop on heterostructure growth and device processing.

6.3. CHARGE NOISE

We now move on to the formation of quantum dots in this platform. We fabricate six quantum dots in three different devices, all consisting of a set of aluminium ohmic leads, as well as two metallic gate layers defining the quantum dots [94]. We operate the quantum dots in transport mode by applying a bias voltage across the quantum dot ohmic leads and measuring the resulting current for each dot. In Fig. 6.3a we measure the source-drain current I_{SD} in blue as a function of the applied plunger gate voltage V_{P} and a typical Coulomb peak in the device conductance can be observed.

To qualify the quantum dot environment, we measure the charge noise picked up by a single quantum dot. A 100-s long trace of I_{SD} is acquired and split into 10 segments of equal lengths. The power spectrum density of the noise S is obtained by averaging the

---

[1] For the analysis of τ_q and μ_q in Fig. 6.2b and c, we extrapolate the effective mass m^* from Ref. [73] at the relevant density. Specifically, for the 55-nm-deep quantum well discussed here, we assume $m^* = 0.062 \times m_0$ at the saturation density $p_{sat} = 2.1 \times 10^{11}$ cm^{-2}

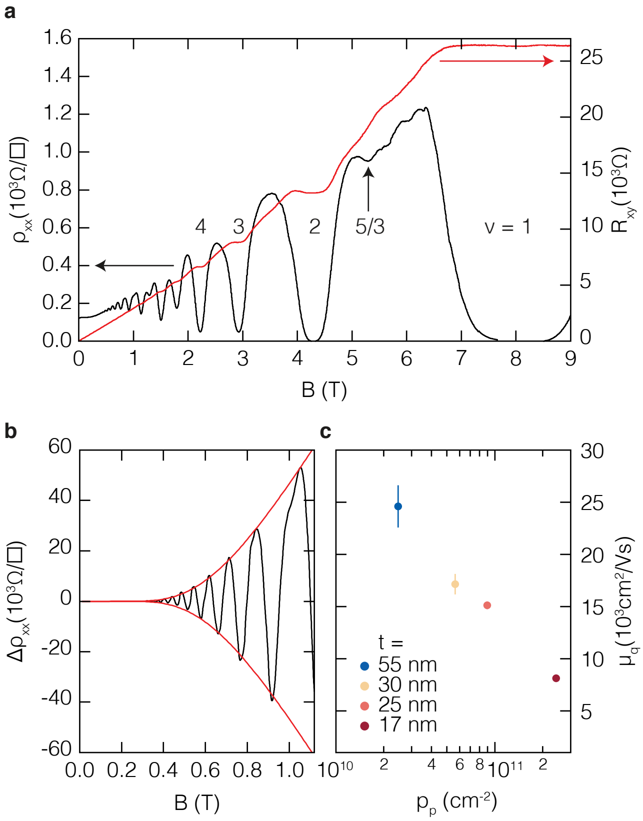

Figure 6.2: **Transport measurements on an H-FET device.** **a**, Longitudinal resistivity (ρ_{xx}, black curve) and transverse Hall resistance (R_{xy}, red curve) as a function of perpendicular magnetic field B measured at a density $p = 2.1 \times 10^{11}$ cm^{-2}. The first four Landau level integer filling factors (ν) are labeled, along with the 5/3 fractional state . **b**, Low-magnetic field oscillation amplitude ($\Delta\rho_{xx}$, black curve) as a function of B after polynomial background subtraction and theoretical fit of the envelope (red curve) to evaluate the single-particle relaxation time τ_q. **c**, Quantum mobility (μ_q) as a function of percolation density measured in heterostructures with barrier thickness t in the range of 17-55 nm.

discrete Fourier transform of the 10 segments. In order to distinguish noise caused by the measurement equipment from charge noise acting on the quantum dot, we repeat the same measurement for different quantum dot plunger gate voltages spanning a full Coulomb peak. Figure 6.3a shows I_{SD} (blue), as well as the numerical derivative $\delta I_{SD}/\delta V_P$ (red) indicating the sensitivity of the source-drain current to electric field variations, for all gate voltages where charge noise measurements are performed. In Figure 6.3b we show the noise spectrum density as a function of both V_P and frequency f. A clear increase of S can be observed on the flanks of the Coulomb peak, corresponding to the points of the highest sensitivity. At the top of the Coulomb peak, where the local derivative of the source-drain current is close to zero, the noise spectral density drops. This is a clear indication that the measured spectrum originates in the environment of the quantum dot and not the measurement equipment or other noise sources such as tunnelling noise [228, 229]. We argue that solely comparing the noise spectrum at the flank of a Coulomb peak to the noise spectrum in Coulomb blockade is not sufficient, as the noise floor of a transimpedance amplifier often strongly depends on the impedance of the load. By moving from Coulomb blockade to the flank of a Coulomb peak, the device impedance can typically change from $R_{\mathrm{block}} > 100$ GΩ to $R_{\mathrm{transport}} < 1$ MΩ, thereby rendering a comparison of the two noise spectra invalid. The difference in device impedance between the flank and top of a Coulomb peak is typically less than an order of magnitude and is therefore a good indicator of the source of the observed noise spectrum.

Fig. 6.3c shows the equivalent detuning noise spectral density S_{E} measured at $V_{\mathrm{P}} = -698.8$ mV, using a lever arm of $\alpha \approx 0.1$ as obtained from Coulomb diamond measurements for each dot. The spectrum follows an approximate $1/f$ trend at low frequencies [229], allowing us to extract an equivalent detuning noise at 1 Hz. We perform charge noise measurements on all six quantum dots and the results are presented in Fig. 6.3d. The average detuning noise at 1 Hz is $\overline{\sqrt{S_{\mathrm{E}}}} = 0.6\ \mu\mathrm{eV}/\sqrt{\mathrm{Hz}}$, with the lowest value being limited by our measurement setup at $0.2\ \mu\mathrm{eV}/\sqrt{\mathrm{Hz}}$. This is a factor of two smaller than the charge noise $\sqrt{S_{\mathrm{E}}} = 1.4\ \mu\mathrm{eV}/\sqrt{\mathrm{Hz}}$ reported in shallower 22-nm-deep Ge QWs [74], shown in Fig. 6.4. Moreover, the lowest charge noise values reported here compare favourably to other material systems, $0.5\ \mu\mathrm{eV}/\sqrt{\mathrm{Hz}}$ for Si/SiO$_2$ [230], $0.8\ \mu\mathrm{eV}/\sqrt{\mathrm{Hz}}$ for Si/SiGe [229], $\sim 1\ \mu\mathrm{eV}/\sqrt{\mathrm{Hz}}$ for InSb [231] or $7.5\ \mu\mathrm{eV}/\sqrt{\mathrm{Hz}}$ for GaAs [232].

6.4. DISCUSSION

In summary, we have engineered planar Ge/SiGe heterostructures for low disorder and quiet quantum dot operation. By positioning the Ge quantum well 55 nm below the semiconductor/oxide interface we achieve an excellent trade-off between an improved electronic environment and a sharp confinement potential for gate-defined quantum dots. We measure a percolation density for two-dimensional hole conduction $p_p = 2.14 \times 10^{10}\ \mathrm{cm}^{-2}$. At such low carrier density, measurements might be limited by the contact resistance leaving room for further improvement. In quantum dots, we observe an average charge noise of $\overline{\sqrt{S_{\mathrm{E}}}} = 0.6\ \mu\mathrm{eV}/\sqrt{\mathrm{Hz}}$ at 1 Hz, with the lowest value below the detection limit $\sqrt{S_{\mathrm{E}}} = 0.2\ \mu\mathrm{eV}/\sqrt{\mathrm{Hz}}$ of our setup. Since impurities at the semiconductor/oxide interface are the limiting factor of the electronic environment, even better percolation density and charge noise are expected in these Ge/SiGe heterostructures if a better quality semiconductor/dielectric interface is achieved. These results mark a significant step forward in the germanium quantum information route.

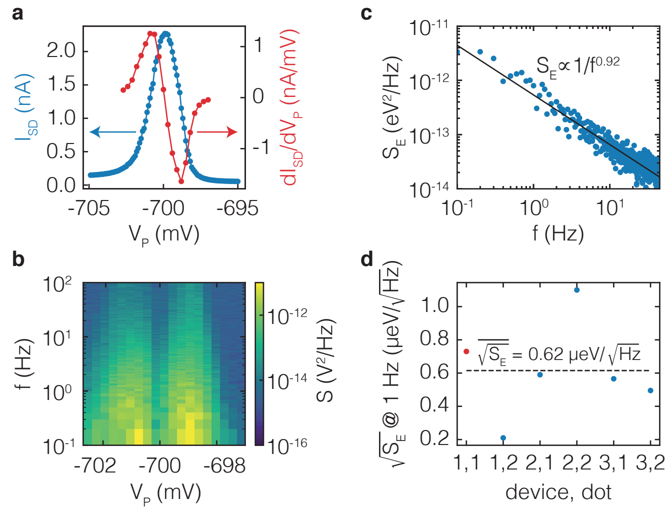

Figure 6.3: **Quantum dot charge noise spectrum for a 60-nm-deep quantum well.** **a**, Source-drain current I_{SD} (blue) through quantum dot 1 of device 1 as well as the numerical derivative (red) related to the sensitivity of the source-drain current to electric field variations. **b**, Frequency dependence of the power spectrum density of I_{SD}, for different plunger gate voltages V_P. Each trace consists of 10 averaged 10-second samples of the source-drain current. **c**, Power spectrum density of the noise picked up by quantum dot 1 of device 1, for $V_P = -698.8$ mV. The solid line corresponds to apparent linear fit to the data, yielding a slope of -0.92. **d**, The charge noise measured at $f = 1$ Hz for six different quantum dots in three different devices. The point in red corresponds to the data in panels (a-c). Dashed line indicates the mean value across all quantum dots.

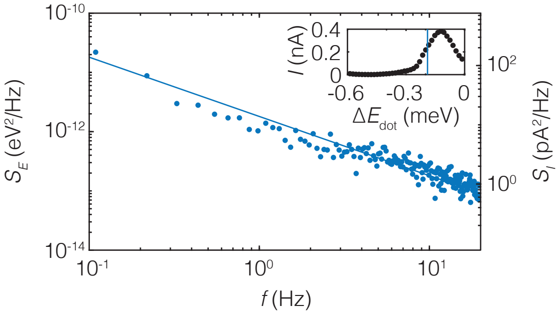

Figure 6.4: **Quantum dot charge noise spectrum for a 20-nm-deep quantum well.** Current noise power spectrum for the quantum dot in transport as indicated in the inset. Solid line corresponds to an apparent linear fit to the data, yielding a slope of -1.00(4).

7

GATE-CONTROLLED QUANTUM DOTS IN PLANAR GERMANIUM

Having established a clean and high-mobility material platform in the previous two chapters, we move to the fabrication of quantum dots. The quantum dot will be the host of the hole spin defining our qubit in the following chapters. Well-defined and gate-controllable quantum dots are therefore an essential prerequisite for the definition of high-quality qubits. In this chapter, we show the formation of a single quantum dot (Section 7.2) and find the charge noise in the device to be comparable to other quantum dot platforms. Next, we define a quadruple quantum dot array with reconfigurable charge sensors (Section 7.3) and observe a depletion of the quantum dots to the last hole, making use of high-bandwidth radio frequency charge sensing. Finally, we configure a sextuple quantum dot array in single-hole occupation (Section 7.4) and observe shell filling for three out of four quantum dots.

Parts of this chapter have been published in Nature Communications **9**, 2835 (2018) [74], Applied Physics Letters **116**, 080501 (2020) [94], and Applied Physics Letters **118**, 044002 (2021) [233].

7.1. INTRODUCTION

Solid-state quantum computing is actively pursued using superconducting and semiconducting materials [44, 51, 234]. The group-IV semiconductors silicon (Si) and germanium (Ge) come with central advantages for the realisation of spin quantum bits (qubits). Not only have their purity and technology been refined to a formidable level, but they also possess an abundant isotope with zero nuclear spin [27, 28], enabling spin qubits to reach extremely long coherence times [56, 174] and high fidelity [55]. These powerful properties have led to demonstrations of two-qubit logic gates [58, 78] and quantum algorithms [61]. The exchange interaction that is central in these demonstrations is local and cannot directly be used to couple qubits at a distance. Instead, the long-range coupling of spin qubits is being explored by incorporating superconductivity and in a first step, strong spin-photon coupling has been achieved [63, 64].

Hole quantum dots in Ge are particularly promising in this context. Ge has the highest hole mobility of all known semiconductors [29], reaching values up to $\mu = 1.5 \times 10^6$ cm^2(Vs)$^{-1}$ in doped heterostructures [70] and is expected to host strong spin-orbit coupling [75, 235], which facilitates electrical driving for fast qubit operations [84]. Furthermore, the valence band in Ge has no valley degeneracy, so, compared to electrons [236], hole qubits do not have the complication of these close quantum levels [75]. Experiments have shown readout of hole spins in Ge/Si nanowires [79, 237], self-assembled quantum dots [131], and hut wires [83], and promising spin lifetimes have been found [80, 83]. In addition, the strong Fermi level pinning at the valence band edge leads to ohmic behaviour for all metal-(*p*-type) Ge contacts [156]. The resulting strong coupling between the metal and semiconductor enables the fabrication of hybrid devices of quantum dot and superconducting structures [238, 239].

Now, the crucial next step is the development of a planar platform that can bring together low disorder, potential for fast driving, and avenue for scaling. Here, we address this challenge and present the formation of quantum dot structures in a planar Ge quantum well. Further, we implement direct aluminium-based ohmic contacts that eliminate the need for dopant implantation. In addition, the aluminium (Al) leads can proximity-induce superconductivity in the quantum well, and we can control the associated supercurrent by tuning electrical gates, as is discussed in Chapter 11.

7.2. A SINGLE QUANTUM DOT

7.2.1. DEVICE DESIGN

A scanning electron microscope (SEM) image of the single quantum dot nanostructure is shown in Fig. 7.1a. Here, the ohmic Al contacts are coloured in yellow and the isolated Ti/Pd gates are shown in green. In a first step, the Al contacts to the Ge quantum well are defined by electron beam lithography, local etching of the Si capping layer and thermal evaporation of Al. Subsequently, an Al_2O_3 gate dielectric is grown by atomic layer deposition at 300 °C, which also serves as an annealing step to enable the diffusion of Al into the SiGe spacer. In the Ti/Pd gate layer, we design a circular top gate between the two Al leads under which a single quantum dot will be formed. In addition, a central plunger gate P is included to control the dot occupation, as well as barrier gates (BS and BD) and additional finger gates (FS and FD) in the corners of the device. These allow

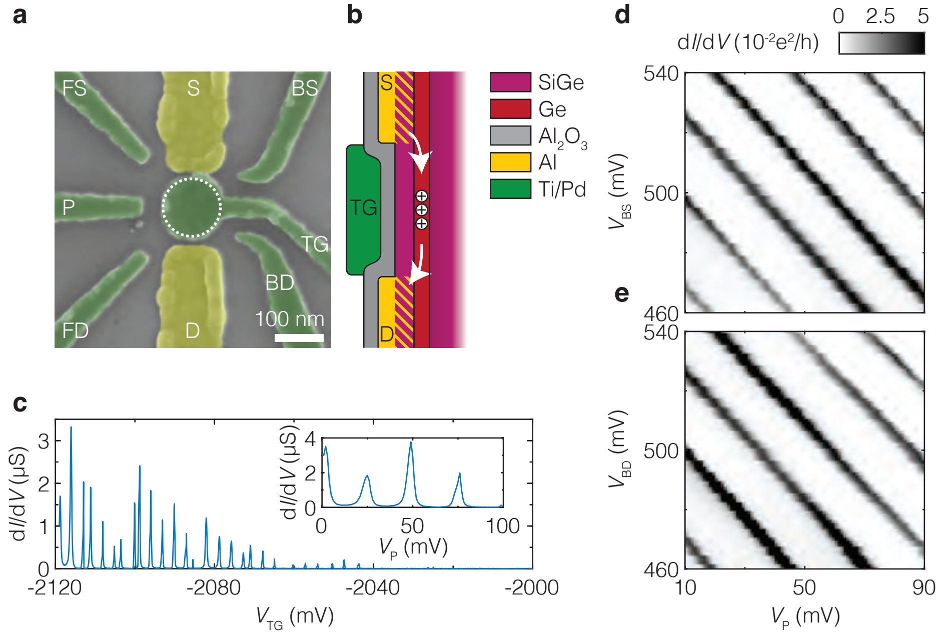

Figure 7.1: **Fabrication and operation of a gate-defined quantum dot.** **a**, False-coloured SEM image of the quantum dot device. The quantum dot is defined under the top gate TG (dotted circle) and its occupancy can be controlled by the central plunger gate P. BS and BD correspond to source and drain barriers, respectively, FS and FD are finger gates for additional control. Scale bar is 100 nm. **b**, Schematic of the device gate layers, showing the top gate and the ohmic contacts achieved by in-diffusion of Al. Scale bar is 50 nm. **c**, Transport measurements showing Coulomb oscillations as a function of the top gate, with $V_P = 0$ mV and as a function of the plunger gate, with $V_{TG} = -2120$ mV (inset). **d**, **e** Influence of the barrier gates BS with $V_{BD} = 500$ mV (**d**) and BD with $V_{BS} = 500$ mV (**e**) on the observed conductivity. The coupling of the two individual gates to the quantum dot is nearly identical, emphasising the excellent homogeneity reached in this system.

for additional control of the dot size and the tunnelling rates between the quantum dot and the source and drain leads.

A conceptual drawing of the device cross-section is shown in Fig. 7.1b, where the diffused Al leads that contact the Ge quantum well are indicated by the stripe-patterned regions. Because of the ohmic nature of the contact, the transport through the quantum dot can be measured without the need for additional reservoir gates and dopant implantation. As a result, no annealing step at temperatures higher than the quantum well deposition temperature (500° C) is needed during the fabrication, avoiding harmful Ge/Si intermixing at the interface [240].

7.2.2. COULOMB PEAKS AND DEVICE HOMOGENEITY

When measuring the source-drain conductance dI/dV as a function of the top gate voltage, conductance peaks are expected when the dot potential aligns between the source and drain potentials, which are the so-called Coulomb oscillations. This is shown in Fig. 7.1c, where dI/dV was measured as a function of the top gate voltage V_{TG}. The expected oscillations are observed, which is a clear sign of the formation of a quantum dot. The spacing between the peaks is quite regular, indicating the quantum dot is operated in the many-hole regime. From the period of the conductance peaks, we can extract a top gate capacitance of $\sim$ 56 aF, which is in very good agreement with the expected capacitance of 52 aF of a parallel plate capacitor using the lithographic dimensions of the top gate. When the top gate voltage is increased and the quantum dot is depleted, the amplitude of the observed peaks is reduced and eventually vanishes, as the tunnelling rates to source and drain reservoirs drop as an effect of the reduced size of the dot.

When TG is tuned to the quantum dot regime, similar oscillations are observed as a function of the plunger gate voltage V_P. Here, a larger spacing of the Coulomb peaks is observed, corresponding to a gate capacitance of $\sim$ 6.4 aF, in agreement with the expected weaker coupling of P to the quantum dot. Note that no additional tuning of the device is necessary, because of the structure of the source and drain leads. Equivalent to a classical transistor, the quantum dot can be defined using a single gate (TG), which bodes well for the scaling up of qubits in this system.

As shown in Fig. 7.1d,e, the dot occupancy can also be controlled using the barrier gates BS and BD. The observed conductance lines are diagonal and very equivalent for each of the two barriers and the plunger, indicating that the coupling to the quantum dot is nearly identical. This confirms that the quantum dot is formed in a central position under TG and that, as an effect of low disorder in the heterostructure, a very high level of control is achieved.

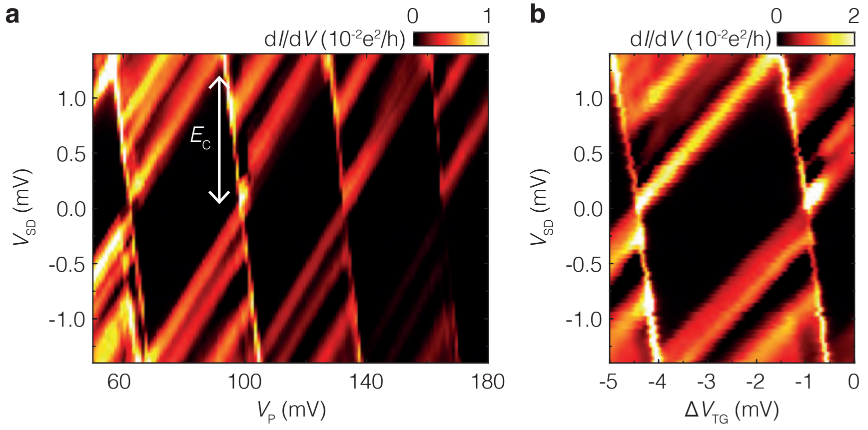

Figure 7.2: **Coulomb diamonds.** Colour plots of bias spectroscopy as a function of V_P (**a**) and $\Delta V_{TG} = V_{TG} + 2084$ mV (**b**), showing Coulomb diamonds with $E_C = 1.3(1)$ meV.

7.2.3. BIAS SPECTROSCOPY

To further characterise the quantum dot, we measure dI/dV as a function of V_P and the dc bias voltage V_{SD}. As shown in Fig. 7.2a, Coulomb diamonds are observed [48]. From the height and width of these diamonds, the charging energy E_C and the lever arm of the corresponding gate α can be extracted. In the regime shown here ($V_{\mathrm{BS}} = V_{\mathrm{BD}} = 550$ mV and $V_{\mathrm{FD}} = 600$ mV), we find $\alpha_{\mathrm{P}} = 0.037(3)$ and $E_{\mathrm{C}} = 1.3(1)$ meV.

Similar diamonds are observed as a function of V_{TG}. Here, the lever arm is found to be significantly larger ($\alpha_{\mathrm{TG}} = 0.41(3)$), as is expected because the dot is formed directly under TG. A substructure is clearly visible in the conducting areas. These additional lines could correspond to either charge transport via excited states of the dot or to a modulation of the density of states within the source and drain reservoirs [241].

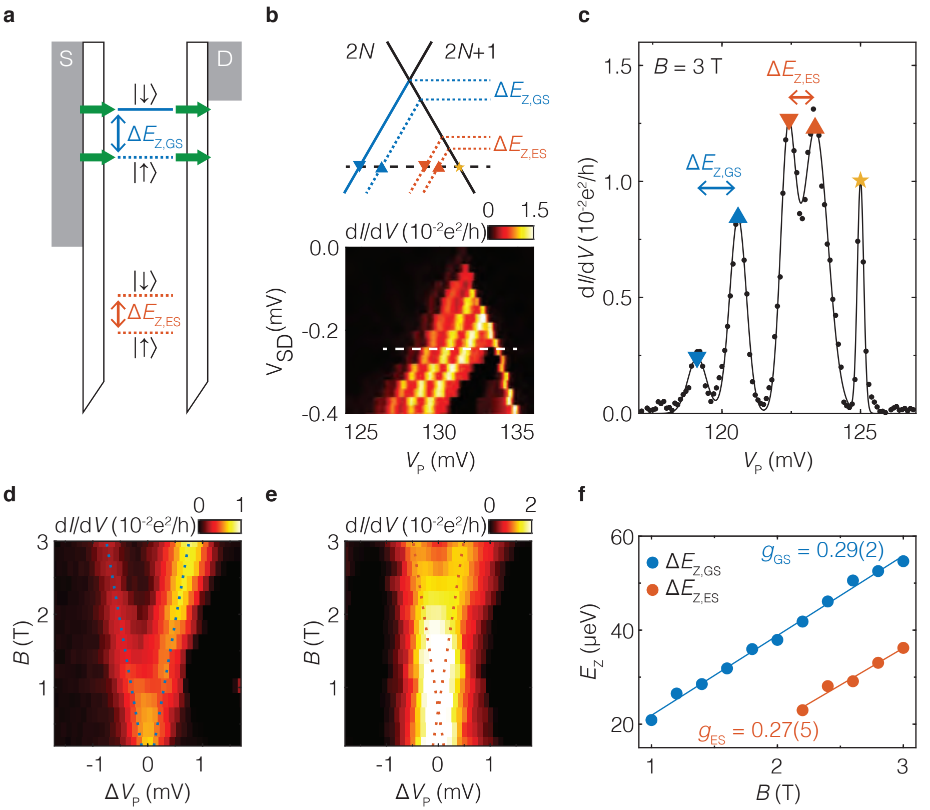

Figure 7.3: **Bias spectroscopy and g-factor measurements.** **a**, Schematic drawing of the Zeeman splitting $\Delta E_Z = g\mu_B B$ of the quantum dot levels, illustrating the hole transport via the Zeeman-split energy levels. **b**, Bias spectroscopy showing the line splitting in a 2.9 T in-plane field. Dashed line indicates the cut plotted in **c**. **c**, Differential conductance as a function of ΔV_{P} for $B = 3$ T, at $V_{SD} = -0.26$ mV. Solid line corresponds to a fit to the datgk=a using the sum of five Gaussian profiles. **d**, **e**, Differential conductance for both the ground (**d**) and the excited state (**e**) as a function of B and ΔV_{P}, with $\Delta V_{\mathrm{P}} = V_{\mathrm{P}} - \overline{V}_{\mathrm{peak}}$ and $\overline{V}_{\mathrm{peak}}$ being the average voltage of the two transition peaks corresponding to either the ground or the excited state. Dotted lines represent linear fits to the peak positions (same as in panel g). **f**, Energy splitting for the ground and excited state as a function of B. Solid lines are linear fits to the data yielding the corresponding g-factors.

When an external magnetic field B is applied, the energy levels of spin degenerate states are expected to split as a result of the Zeeman effect [48] (cf. Fig. 7.3a). This becomes apparent as a splitting of the conductance lines related to odd hole occupations $2N+1$ of the quantum dot, as shown in Fig. 7.2b for the first device in an in-plane magnetic field $B = 2.9$ T. Both the ground state and the excited state are subject to this splitting, which we extract by fitting the observed conductance for $V_{\mathrm{SD}} = -0.26$ mV using Gaussian profiles and multiplying the splitting in voltage with the measured lever arm α_{P} (Fig. 7.3c).

A linear trend is observed as a function of the applied magnetic field as shown in Fig. 7.2d,e. Note that a small splitting $\Delta E_Z < 20$ μeV could not be resolved because of the finite width of the conductance peaks. We find the effective g-factors $g_{\mathrm{GS}} = 0.29(2)$ and $g_{\mathrm{ES}} = 0.27(5)$ for the ground state and excited state, respectively, from the linear fits in Fig. 7.2f. For the excited state, our data point to either a non-linearity at lower fields or a significant zero-field spin splitting $\Delta E_{Z0} \approx -11$ μeV. The g-factor of the pure heavy hole state is expected to vanish completely for an in-plane field. However, the additional confinement of the holes in the x,y-plane leads to a significant admixture of light hole states and a non-zero in-plane Zeeman splitting [242].

The observed spin splitting of the first line parallel to the diamond edge ground state identifies it as belonging to the first excited state rather than being connected to the reservoir. The measured energy splitting with respect to the ground state $\Delta E \approx 100$ μeV remains unchanged as a function of magnetic field strength. It can be compared to the expected level splitting for a two-dimensional quantum dot with area A and effective hole mass m^*, which is given by $\Delta E = \pi\hbar^2/m^*A$ [135]. From the temperature dependence of the Shubnikov-de Haas oscillations measured for the Hall-bar structures, we find $m^* = 0.08m_e$, with the electron mass m_e, and with our device geometry ($A = 0.019$ μm^2) we obtain $\Delta E \approx 150$ μeV, in good agreement with the measured value.

7.3. DOUBLE QUANTUM DOTS AND CHARGE SENSING

Having established a proof-of-principle demonstration for the definition of quantum dots in strained planar germanium, we move to the fabrication of larger dot systems. As a result of the low in-plane g-factor in germanium, spin readout requires a two-dot system at a minimum, to enable Pauli spin blockade readout. The addition of further dots as charge sensors can significantly speed up measurements, as well as decouple the qubit from its leads, positively impacting spin relaxation [86]. We therefore now proceed to demonstrate charge sensing of a double quantum dot system in a two-by-two array of quantum dots.

7.3.1. DEVICE DESIGN

The two-by-two quadruple quantum dot array is shown in Fig. 7.4. Gates P_{1-4} are positioned clockwise around the array and define the lateral confinement of the dots. Each pair of adjacent dots share a barrier gate B_{12-41} capable of tuning the interdot tunnel coupling. The tunnel coupling of each dot to its reservoir can also be controlled via a barrier gate. This device can be operated as a quadruple quantum dot system in transport mode, but we intentionally tune half of the device to be operated as a charge sensor. This is accomplished by tuning the interdot barrier to form a single quantum dot along a dot channel that we subsequently use for charge sensing of the double

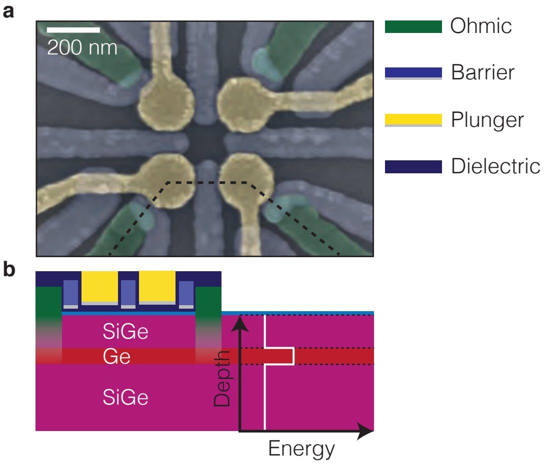

Figure 7.4: **Ge/SiGe quadruple quantum dot array.** **a**, SEM image of the two-by-two quadruple quantum dot array. The plunger gates (yellow), the barrier gates (blue) and the screening gates (red) define the quantum dots. Dotted line indicates the cross-section through the dot channel illustrated in panel b. **b**, Cross section and bandstructure of metal, dielectric (black) and semiconductor (pink/red).

quantum dot along the opposite channel.

7.3.2. CHARGE SENSING OF A DOUBLE QUANTUM DOT

In Fig 7.5 we demonstrate that double quantum dots can be formed on each side of the device. In each of the four cases, a sensing dot is formed in the channel parallel to the double dot to be sensed, by opening the interdot barrier such that a large single dot is formed. By configuring this sensor on the slope of a Coulomb peak, its impedance becomes sensitive to fluctuations in the local electric field, as can be caused by the loading or unloading of a hole on a nearby quantum dot. The sensor is read out by making use of radio frequency (rf) sensing, using an off-chip niobium-titanium-nitride superconducting resonator to form a tank circuit. The tank circuit impedance is modulated by the change in impedance of the sensor, which results in a change of the reflected rf signal.

In the opposite channel, the interdot barrier is closed, forming a double dot system in the low tunnel coupling regime. Each quantum dot is coupled to its corresponding reservoir, to ensure loading and unloading of the holes. Horizontal and vertical dark lines can be observed in the derivative charge sensor signal, corresponding to the loading of an additional hole in the respective quantum dot. As a result of using a charge sensor, the signal strength is decoupled from the tunnel rates of the quantum dot. Therefore, we can deplete the dot down to the last hole, unlike the situation with the transport measurements in Section 7.2. Depletion down to the last hole is demonstrated for each of the quantum dots as becomes apparent from the lack of extra addition lines in the top right corner of each diagram.

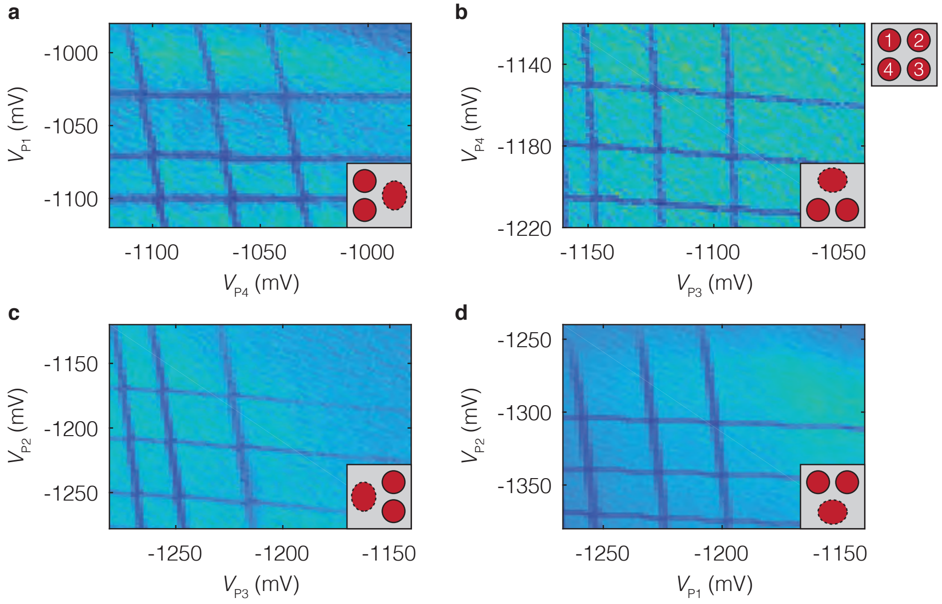

Figure 7.5: **Double quantum dot operation a-d** Double dots formed in each possible configuration within a two-by-two quantum dot array. In each case, a charge sensor is formed from the parallel channel by raising the interdot coupling to form a large, highly occupied single dot. Each charge stability diagrams shows RF-sensing of double quantum dots depleted to the last hole occupancy, in the low tunnel coupling regime.

7.4. A TWO-DIMENSIONAL ARRAY OF SINGLE-HOLE QUANTUM DOTS

Finally, we realise a two-dimensional six-quantum-dot array using materials compatible with existing CMOS technology. This allows us to operate the full quadruple quantum dot array with single-hole occupancy. We obtain excellent control over the charge occupancy and the interdot coupling. The device consists of the four-quantum-dot grid and an additional two quantum dots on the sides that are used for radio frequency charge sensing. We can tune each quantum dot to the single-hole occupancy, and we find shell filling to be consistent with a Fock-Darwin spectrum. This demonstrates a qubit state with large energy separation to the orbital excited states, as valley states are not present. We exploit the integrated barrier gates to gain independent control over the hole occupancy and the tunnel coupling between neighbouring quantum dots. We use this to demonstrate the single-hole occupancy in the full quadruple quantum dot array as a stepping stone toward two-dimensional arrays of quantum dot qubits.

7.4.1. A QUADRUPLE QUANTUM DOT

Fig. 7.6a shows a scanning electron microscopy (SEM) image of a quantum dot grid. Fabrication is based on a multilayer gate design [94]. The quantum dots are defined using plunger gates P and are coupled through barrier gates B. We have fabricated the barrier gates as the first layer and the plunger gates as the second layer, which results in a good addressability of both the tunnel couplings and quantum dot energy levels.

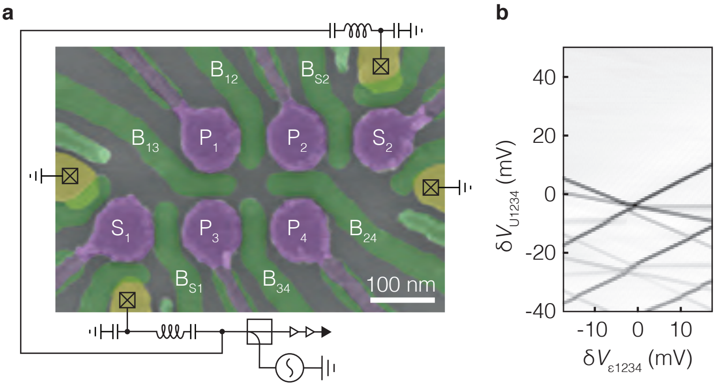

Figure 7.6: **Quadruple quantum dot a**, False coloured SEM image of a sample similar to the one on which the measurements are performed. The plunger gates of the quantum dots P are coloured in purple, the barrier gates B are coloured in green and the aluminium ohmics in yellow, which serve both as the source and drain contacts for rf sensing, as well as charge reservoirs for the quantum dots. **b**, Charge stability diagram of the four quantum dot system, obtained by simultaneous readout of S_1 and S_2. The colour map shows the derivative of the combined response signal, clearly revealing the charge addition lines for each of the quantum dots.

The aluminium ohmics serve as hole reservoirs for the charge sensors. Controllable loading of the quantum dots is obtained through an additional barrier gate between the sensor and the quantum dots (B_{S1} and B_{S2}). The charge occupation in the dots is measured with the nearby sensing dots. We use rf reflectometry to achieve a high measurement bandwidth of the sensor impedance, which allows for measuring charge stability diagrams in real time.

We show that we can form a quadruple quantum dot in the two-by-two array, reaching single-hole occupation for all four quantum dots simultaneously. With both sensors, we can detect charge transitions of each quantum dot within the array, although a significantly stronger sensitivity is obtained for the quantum dots neighbouring the sensor. In order to conveniently tune and demonstrate the single-hole occupation for all quantum dots, a virtual gate set is defined, such that the addition lines of all four dots have a distinctive slope. Taking the derivative of the charge sensors signal and summing them, allows us to clearly distinguish all four quantum dots (Fig. 7.6b). In this measurement, we preserve the sensitivity of the sensor, by offsetting the effect of a change in voltage on the plunger gate of the quantum dots with a small change in voltage on the plunger gate of the sensors.

7.4.2. SHELL FILLING

We now measure the charge addition energies for the first holes in all four quantum dots (Fig. 7.7). The addition energies are extracted from separate charge stability diagrams by analysing the spacing between the addition lines for all the dots. The change in gate voltage is converted into energy using a lever arm $\alpha = 0.19$ eV/V, as extracted from polarisation line measurements [233]. Steps in the addition energy are observed for

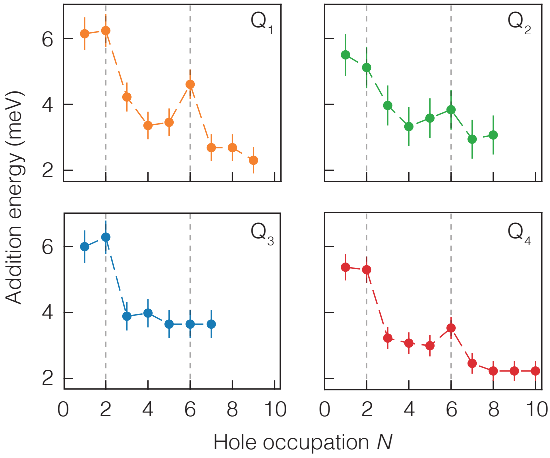

Figure 7.7: **Shell filling in a quadruple quantum dot** Addition energy for the four quantum dots, extracted from the corresponding stability diagrams and converted using a lever arm $\alpha = 0.19$ eV/V. The dashed grey lines correspond to the hole fillings for which increased addition energy is expected due to shell filling when considering a circular potential landscape and spin degeneracy.

hole occupations $N = 2$ and $N = 6$, consistent with shell filling for a circular quantum dot and considering the spin degree of freedom [243]. These experiments also highlight the absence of low-energy excited states such as valley states, which would give rise to a different shell filling pattern [244]. It is interesting to observe that quantum dot Q_1 and Q_4 show shell filling as expected of circular quantum dots, while for Q_2 and Q_3 the expected peaks in the addition energy are less pronounced. Moreover, Q_2 and Q_3 show an increased addition energy for $N = 4$. We ascribe this difference to Q_2 and Q_3 being positioned closer to the sensors quantum dots, which are operated using relatively large negative potentials. The electric field from the sensors might distort the circular potential to a more elliptical shape, which would in turn modify the electronic structure and cause an increased addition energy at half-filling [245].

7.5. DISCUSSION

In conclusion, we have shown the operation of a single, quadruple and sextuple hole quantum dot system in a planar, undoped and buried Ge quantum well with a record high hole mobility. The Al ohmic leads to the quantum dots significantly simplify the fabrication and tuning processes. Making use of a multilayer fabrication process, we define a quadruple quantum dot system, with dedicated tunnel coupling barriers and reconfigurable charge sensors, allowing detection of single-hole occupancy in all quantum dots. Finally, we define a two-dimensional quantum dot array with two dedicated charge sensors to study charging energy dynamics in the system, and we observe shell filling for three out of the four quantum dots. Hole quantum dots in planar Ge constitute thereby a versatile platform that can leverage semiconductor manufacturing to advance and broaden the field of quantum computing.

8

FAST AND UNIVERSAL QUANTUM LOGIC

Universal quantum information processing can be realised by executing single and two-qubit logic on a scalable platform. Across all qubit realisations [32], quantum dots have great promise to become the central building block for quantum computation [25]. Excellent control over the properties of the hosting quantum dot is achieved in GaAs [170, 171, 246], while long quantum coherence for spins and universal logic have been demonstrated in silicon quantum dots [11, 55, 58, 78], but a platform that can be operated with local control techniques is absent. In this chapter, we combine all of these aspects by demonstrating single and two-qubit operations based on holes in germanium that are directly contacted by aluminium. A high degree of control over the tunnel coupling and detuning is obtained by exploiting quantum wells with very low disorder, enabling operation at the charge symmetry point. Spin-orbit coupling obviates the need for microscopic elements and enables rapid qubit control with Rabi frequencies exceeding 100 MHz. We demonstrate a fast universal quantum gate set composed of single-qubit gates with a fidelity of 99.3 %, where $t_\pi = 20$ ns, and two-qubit gates executed within 75 ns. Planar germanium thus matured within one year from a material that can host quantum dots to a platform enabling two-qubit logic, positioning itself as a unique material for quantum information.

Parts of this chapter have been published in Nature **577**, 487-491 (2020) [86]

8.1. INTRODUCTION

Gate-defined quantum dots were recognised early on as a promising platform for quantum information [25] and a plethora of materials stacks has been investigated as host material. Initial research mainly focused on the low disorder semiconductor gallium arsenide [49, 51]. Steady progress in the control and understanding of this system culminated in the initial demonstration and optimisation of spin qubit operations [50] and the realisation of rudimentary analogue quantum simulations [246]. However, the omnipresent hyperfine interactions in group III-V materials seriously deteriorate the spin coherence. Drastic improvements to the coherence times could be achieved by switching to the group IV semiconductor silicon, in particular when defining spin qubits in an isotopically purified host crystal with vanishing concentrations of non-zero nuclear spins [56]. This enabled single-qubit rotations with fidelities beyond 99.9 % [55] and the execution of two-qubit logic gates with fidelities up to 98 % [11, 58, 78], underlining the potential of spin qubits for quantum computation. Nevertheless, quantum dots in silicon are often formed at unintended locations and control over the tunnel coupling determining the strength of two-qubit interactions is limited. Moreover, the absence of a sizable spin-orbit coupling for electrons requires the inclusion of microscopic components such as on-chip striplines or nanomagnets close to each qubit, which significantly complicates the design of large and dense 2D-structures. Scalability thereby remains an outstanding challenge for these systems and a platform that can overcome these limitations would be highly desirable.

Hole states in semiconductors [68] typically exhibit strong spin-orbit coupling which has enabled the demonstration of fast single-qubit rotations [69, 84, 93]. Furthermore, whereas valley degeneracy complicates qubit definition for electrons in silicon, this is absent for holes and excited states can be well separated in energy. In silicon, unfavourable band alignment prevents strain engineering of low disorder quantum wells for holes, restricting experiments to metal-oxide-semiconductor (MOS) structures [247]. Research on germanium mostly focused on self-assembled nanowires [80] and demonstrated single-shot spin readout [83] and coherent spin control [84]. However, strained germanium can reach hole mobilities [240] of $\mu > 1,000,000$ cm^2/Vs and undoped germanium quantum wells were recently shown to support the formation of gate-controlled hole quantum dots [74]. Now, the crucial challenge is the demonstration of coherent control in this platform and the implementation of qubit-qubit gates for scalable quantum information with holes.

Here, we make this step and demonstrate single and two-qubit logic with holes in planar germanium. We fabricate devices on silicon substrates, using standard manufacturing materials. We grow undoped strained germanium quantum wells, measured to have high hole mobilities $\mu >$ 500,000 cm^2/Vs and a low effective hole mass [71, 74] m_h = 0.09 m_e, extrapolated to reach m_h = 0.05 m_e at zero density [73], with m_e the electron rest mass. This allows us to define quantum dots of comparatively large size, and we find excellent control over the exchange interaction between the two dots. We operate in a multi-hole mode, significantly reducing challenges in tuning and characterisation, thereby being advantageous for scaling. We exploit the spin-orbit interaction for qubit driving and perform single-qubit rotations at frequencies exceeding 100 MHz. This advantage of fast driving becomes further apparent in coherently accessing the Hilbert

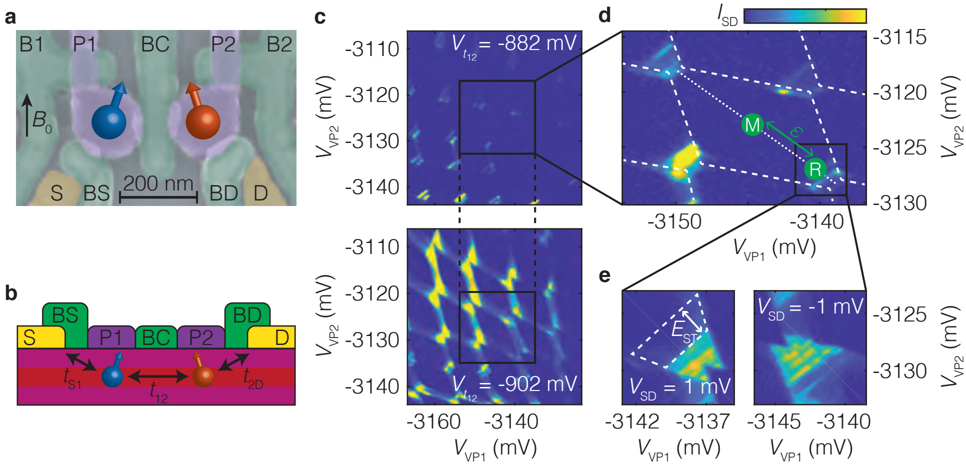

Figure 8.1: **Fabrication and operation of a planar germanium double quantum dot.** **a**, False-coloured SEM image of the two-qubit device. Two hole quantum dots are formed in a high-mobility Ge quantum well and controlled by the electric gates. The direction of the external field B_0 is indicated by the black arrow. **b**, Schematic cross section of the system, where quantum dots are formed below plunger gates P1 and P2, while the different tunnelling rates can be controlled by barrier gates BS, BD and BC. **c**, Transport current through the double dot as a function of plunger gates voltage for weak (top) and strong (bottom) interdot coupling, mediated by a virtual tunnel gate. **d**, Charge stability diagram of the qubit operation point. The detuning axis ε is indicated by the dotted line. To allow for coherent control of the isolated spin states, a two-level voltage pulse on gates P1 and P2 is used to detune the dot potentials and prevent tunnelling to and from the dots during the manipulation phase (label M in Fig. 8.1d). To allow for coherent control of the isolated spin states, a two-level voltage pulse on gates P1 and P2 is used to detune the dot potentials and prevent tunnelling to and from the dots during the manipulation phase (label M in Fig. 8.1d). To allow for coherent control of the isolated spin states, a two-level voltage pulse on gates P1 and P2 is used to detune the dot potentials and prevent tunnelling to and from the dots during the manipulation phase (label M). **e**, Transport current through the double dot as a function of plunger gate voltage for positive (left) and negative (right) bias. Pauli spin blockade becomes apparent from the suppression of the transport current for positive bias direction. **f**, Illustration of the energy landscape in our double quantum dot system. **g**, Resonance frequency of the two qubits as a function of the external magnetic field, showing the individual qubit resonances.

space of a two-qubit system. For example, in silicon, the execution of a controlled-NOT (CNOT) gate implemented with an on-chip stripline has been shown using microsecond long pulses [11, 78] and this timescale is typically reduced to 0.2-0.5 microseconds by incorporating nanomagnets [58]. Here, we demonstrate that the spin-orbit coupling of holes in germanium together with the sizable exchange interaction enables a CNOT within t_{CX} = 75 ns.

8.2. DOUBLE QUANTUM DOT DEVICE

A scanning electron microscope (SEM) image of the germanium two-qubit device is shown in Fig. 8.1a. In order to accumulate holes and define two quantum dots, the circular plunger gates are set to negative potential ($V_{P1}, V_{P2} \approx -2$ V). The tunnel coupling between the dots t_{12} and the tunnel couplings to the source and drain reservoirs (t_{1S}, t_{2D}) are controlled by the barrier gates BC, BS and BD, respectively. Working in a virtual gate voltage space (V_{VP1}, V_{VP2}, $V_{t_{1\mathrm{S}}}$, $V_{t_{2\mathrm{D}}}$, and $V_{t_{12}}$), we can independently tune these properties (see video mode operation online). We measure the transport current through the double dot system (Fig. 8.1c and 8.1d) and for certain hole occupations we observe a suppression of the transport current for a positive bias voltage $V_{\mathrm{SD}} = 1$ mV, caused by Pauli-spin blockade (PSB), see Fig. 8.1e. We make use of the blockade as an effective method for spin-to-charge conversion [25, 51], as well as to initialise our two-qubit system in the blocked $|\downarrow\downarrow\rangle$ ground state.

Taking advantage of the strong spin-orbit coupling [84], we are able to implement a fast manipulation of the qubit states by electric dipole spin resonance (EDSR). We tune the device to a readout point within the PSB-region (indicated by the label R in Fig. 8.1d) and apply an electric microwave excitation to gate P1. When the frequency of the microwave excitation matches the spin resonance frequency of either qubit, PSB is lifted and an increase in the transport current can be observed. We extract the resonance frequency of each qubit as a function of external magnetic field strength B_0 and observe two distinct qubit resonance lines with g-factors $g_1 = 0.35$ and $g_2 = 0.38$. The difference in g-factors between the two dots is likely caused by slightly different hole fillings and thus quantum dot orbitals. As an effect of the spin-orbit coupling (SOC), a strong orbital dependence of the effective g-factor is typically measured in hole quantum dots [242, 247]. Furthermore, the effective g-factor can be tuned electrically as a direct result of the SOC [248] (see e.g. Fig. 8.4c and 8.4d), thereby guaranteeing independent control of the different qubits. We observe that the resonance frequency of both qubits remains stable over several hours, with discrete jumps at longer time scales as presented in Fig. 8.9.

We developed a measurement technique in which we measure the averaged transport current over N repeated pulse cycles and subtract a reference measurement using a lock-in amplifier, to mitigate slow variations in the transport current (cf. Section 4.4), as is indicated in Fig. 8.2a. After readout, the system is left in the blocking $|\downarrow\downarrow\rangle$ state, serving as the initialisation of our qubits.

8.3. ONE-QUBIT GATES

We now operate the device in the single-qubit transport mode in an external field of $B_0 = 0.5$ T and use the second qubit as a readout ancilla. Coherent control over the qubit is demonstrated in a Rabi experiment, where the spin state of Q1 is measured as a function of microwave pulse length t_p and power P, as shown in Fig. 8.2b. By increasing the power of the microwave pulse, we can reach Rabi frequencies of over 100 MHz, at an elevated field $B_0 = 1.65$ T (Fig. 8.10).

To evaluate the performance of our device, we implement randomised benchmarking [249] of the single-qubit Clifford group (Fig. 8.2c). The measured decay curve of the qubit state as a function of sequence length m is shown in Fig. 8.2d, from which we extract a single-qubit control fidelity of $F_{\mathrm{C}} = 99.3\%$, using $t_\pi = 20$ ns and $t_{\pi/2} = 10$ ns. In Fig. 8.2e we show the gate fidelities for the different π and $\pi/2$ gates as obtained by interleaved randomised benchmarking, where each randomly drawn gate is followed by the interleaved gate (cf. Fig. 8.2c). All individual gate fidelities are $F_{\mathrm{C}} > 99\%$, with the infidelity for $\pi/2$ gates being approximately twice as low as for the π gates, on account of the difference in pulse length.

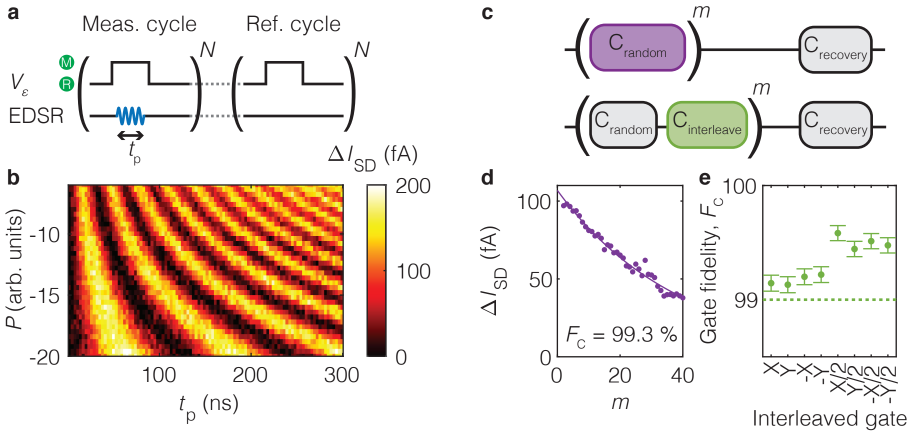

Figure 8.2: **Qubit control, gate fidelity and quantum coherence of planar germanium qubits.** **a**, Measurement sequence used for the Rabi driving measurements. Measurement cycles with EDSR pulses are alternated with reference cycles without a microwave tone, allowing for an efficient background current subtraction. Each cycle is repeated N times, such that measurement and reference cycles alternate at a typical lock-in frequency of $f_{meas} = 89.75$ Hz. **b**, Colour map of the differential bias current ΔI_{SD} as a function of microwave pulse time t and power P, where clear Rabi rotations on Q1 can be observed. **c**, Schematic illustration of the (interleaved) randomised benchmarking sequence applied to Q1. **d**, Differential bias current as a function of the number of applied Clifford gates in the randomised benchmarking sequence on Q1. The extracted control fidelity is $F_C = 99.3 \pm 0.05$ %. **e**, Gate fidelities for the different π and $\pi/2$ gates, error bars correspond to 1σ. **f**, Spin coherence and life times for Q1 and Q2, error bars correspond to 1σ.

We extensively characterize the coherence in our system at an exchange coupling of $J/h \approx 20$ MHz and find $T^*_{2,Q1} = 817$ ns and $T^*_{2,Q2} = 348$ ns, which can be extended by performing a Hahn echo to $T^H_{2,Q1} = 1.9$ µs and $T^H_{2,Q2} = 0.8$ µs (Fig. 8.3a,b). These coherence times compare favourably to $T^*_2 = 130$ ns for germanium hut wires [84] and $T^*_2 = 270$ ns for holes in silicon [92]. Electrons in GaAs have an even shorter dephasing time [51], with $T^*_2 = 10$ ns. The limited T^*_2 in GaAs is due to hyperfine interactions, which can be mitigated to a large extent by using nuclear notch filtering [107], leading to $T_2 = 800$ µs. This source of dephasing can be avoided altogether by using group IV materials with nuclear spin-free isotopes [28]. This has led to $T_2 = 28$ ms for electrons in isotopically purified silicon [56], and isotopic purification may also increase the quantum coherence in germanium. Furthermore, we observe spin lifetimes of $T_{1,Q1} = 9$ µs and $T_{1,Q2} = 3$ µs (Fig. 8.3c). We have found that these lifetimes increase exponentially when lowering the tunnel coupling between each qubit and its respective reservoir (Fig. 8.11) and relaxation times of $T_1 > 100$ µs have been reported for germanium nanowires [80, 83], both giving good prospect for significantly increasing the relaxation time by closing the reservoir barrier during operation.

8.4. TWO-QUBIT GATES

When the manipulation of both qubits is combined, the coupling of the two qubits (exchange interaction J) becomes apparent. As illustrated in Fig. 8.4a, the resonance

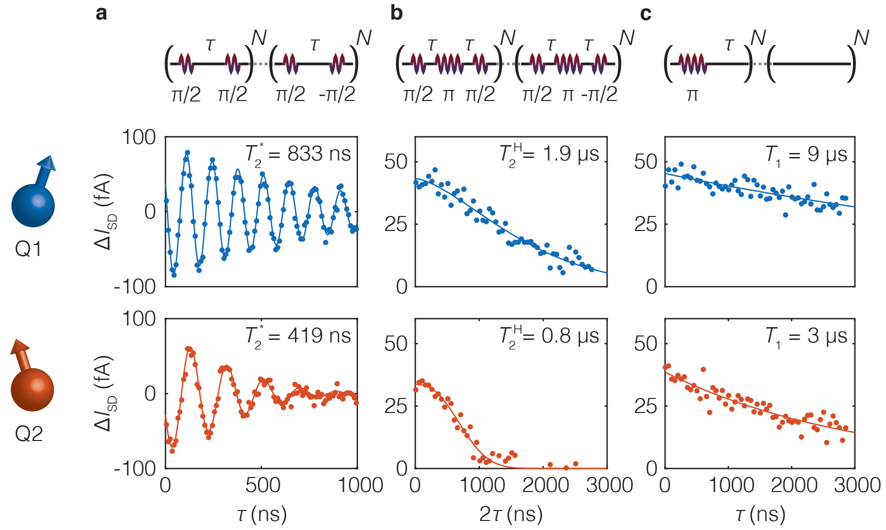

Figure 8.3: **Relaxation, dephasing and coherence times.** **a**, Ramsey experiment, in which two $\pi/2$ pulses are separated by time τ, during which the qubit will evolve as a result of the implemented detuning Δd. We fit the decay of the observed oscillations to $\Delta I_{SD} = a\cos(2\pi\Delta f\tau+\phi)\exp\left(-(\tau/T_2^*)^{\alpha^*}\right)$, with a a scaling factor and ϕ a phase offset and find a spin coherence time of $T^*_{2,\mathrm{Q1}} = 817$ ns and $T^*_{2,\mathrm{Q2}} = 348$ ns and decay coefficients of $\alpha^*_{\mathrm{Q1}} = 1.2 \pm 0.2$ and $\alpha^*_{\mathrm{Q2}} = 1.5 \pm 0.2$, for Q1 and Q2 respectively. **b**, The spin coherence can be extended by performing a Hahn echoing sequence, consisting of $\pi/2$, π and $\pi/2$ pulses separated by waiting times τ. Fitting the observed decay as a function of the total waiting time 2τ to a power law $\Delta I_{SD} = a\exp\left(-(2\tau/T_2^*)^{\alpha^H}\right)$, we find extended coherence times of $T^H_{2,\mathrm{Q1}} = 1.9$ μs and $T^H_{2,\mathrm{Q2}} = 0.8$ μs and decay coefficients of $\alpha^H_{\mathrm{Q1}} = 1.5 \pm 0.1$ and $\alpha^H_{\mathrm{Q2}} = 2.5 \pm 0.3$, for Q1 and Q2 respectively. **c**, The spin lifetime is measured by applying a single π pulse, after which we wait for a time τ. We fit the decay to $\Delta I_{\mathrm{SD}} = \exp(-(\tau/T_1))$ and find lifetimes of $T_{1,\mathrm{Q1}} = 9$ μs and $T_{1,\mathrm{Q2}} = 3$ μs.

frequency of each of the qubits is shifted when the respective other qubit is prepared in its $|\uparrow\rangle$ state. The strength of this interaction depends on the inter-dot tunnel coupling t_{12} as well as the detuning ϵ of the dot potentials. By changing the depth of voltage pulse to point M (dashed line in Fig. 8.1d), we can map J as a function of ϵ. This is shown in Fig. 8.4c and 8.4d, where the subtraction of two pulse sequences in the measurement (see Fig. 8.4b) results in a positive signal for the unprepared qubit resonances and a negative signal for the prepared states (cf. Fig. 8.7). As shown in Fig. 8.4e, the exchange coupling that is reflected in the frequency difference between the initial and prepared resonance positions, is very well described by a simple description [25, 167] using $J = 4Ut_{12}^2/(U^2-(\alpha\epsilon-U_0)^2)$. Here, U is the charging energy of the quantum dots, $\alpha = 0.23$ is the lever arm of P1 and P2, and the interdot tunnel coupling is $t_{12}/h = 1.8$ GHz. In addition, the strength of t_{12} can be tuned using the central barrier BC (Fig. 8.4f). Here, we use a virtual gate voltage [246] $V_{t_{12}}$, where V_{BC} is set while compensating its influence on the dot potentials by appropriate corrections to V_{P1} and V_{P2}. As a result of this full control over the coupling, we are able to operate the qubits at a mostly charge-insensitive point of symmetric detuning [170, 171] while choosing an exchange

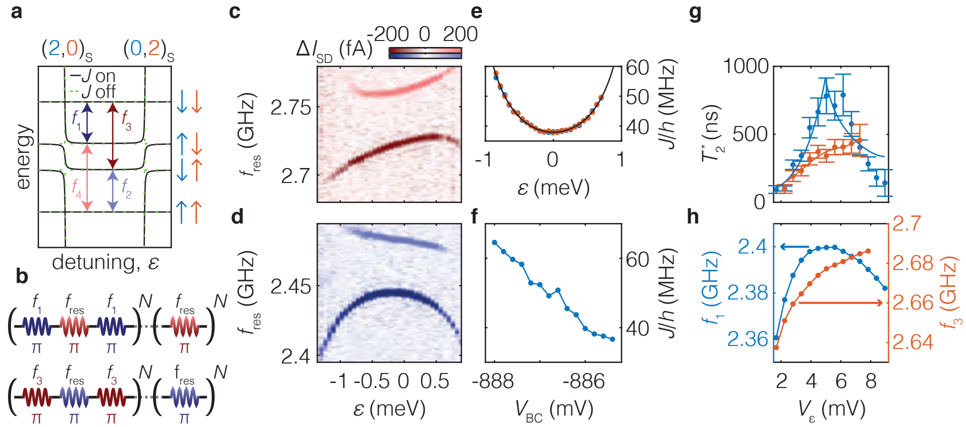

Figure 8.4: **Tunable exchange coupling and operation at the charge symmetry point.** **a**, Illustration of the relevant energy levels in our hole double quantum dot with zero (green) and finite (black) exchange coupling J between the dots. Six energy levels are considered, the four different (1,1)-charge states as well as the $(2,0)_S$ and $(0,2)_S$ singlet charge states where both holes occupy the same quantum dot. Four individual transitions can be driven, corresponding to the conditional rotations of the two-qubit system. The size of the exchange interaction is equal to $J/h = f_2 - f_1 = f_4 - f_3$. **b**, Measurement pulse cycles used to map out the exchange splitting of Q1 (top) and Q2 (bottom). As a result of the demodulation of the alternating cycles, transition $f_{1,(3)}$ gives a negative signal and transition $f_{2,(4)}$ results in a positive signal. **c**,**d**, EDSR spectra of Q1 (**c**) and Q2 (**d**) as a function of the detuning ε. The exchange splitting can be tuned to a minimum at $\varepsilon = 0$ and increases closer to the $(m,n)-(m+1,n-1)$ and $(m,n)-(m-1,n+1)$ charge transitions. **e**, Exchange interaction as a function of ε as extracted from **c**,**d**. Fitting the exchange coupling yields an interdot tunnel coupling $t_{12}/h = 1.8$ GHz and charging energy $U = 1.46$ meV. **f**, The interdot tunnel coupling can also be controlled by gate BC. Changing the potential on this gate, while keeping $\varepsilon = 0$, allows for good control over the exchange interaction between the two qubits. **g**, Coherence time T_2^* of both qubits as a function of detuning voltage V_ε. When the slope of the resonance line is equal to zero, the qubit is expected to be in first order insensitive to charge noise. Solid lines indicate fits of the data to $\left(a\frac{\delta f_{res}}{\delta V_\varepsilon} + T_0\right)^{-1}$, with $\frac{\delta f_{res}}{\delta V_\varepsilon}$ the numerical derivative of the resonance line frequency as a function of detuning, T_0 the residual decoherence and a a scaling factor. It can be observed that indeed T_2^* is the longest when the slope of the resonance line is closest to zero. Error bars correspond to 1σ. **h**, Resonance frequency of transition f_1 and f_3 as a function of detuning voltage.

coupling strength large enough for rapid two-qubit operations. The advantage of this reduced sensitivity to detuning noise is demonstrated in Fig. 8.4g, where the dephasing time T_2^* of both qubits is measured as a function of ϵ. Here, T_2^* strongly increases where the slope of $f_{1,(3)}$ with respect to the detuning for Q1 (Q2) is minimal, with the longest average phase coherence reached in the flat region at $V_\epsilon \approx 6$ mV.

The direct control over the tunnel coupling enables us to tune the exchange interaction to a sizable strength of $J/h = 39$ MHz at the symmetry point, as demonstrated in Fig. 8.5a. We exploit this to obtain fast selective driving and operate in an exchange always-on regime [11, 45]. Full control is obtained by applying microwave pulses at the four resonant frequencies, while further gate pulses controlling J are not needed. A pulse at a single resonance frequency will result in a conditional rotation of the target qubit, as we show in Fig. 8.5b. A CX-operation can be achieved by setting t_{CX} to give a maximum signal, corresponding to a conditional π-rotation on the target qubit.

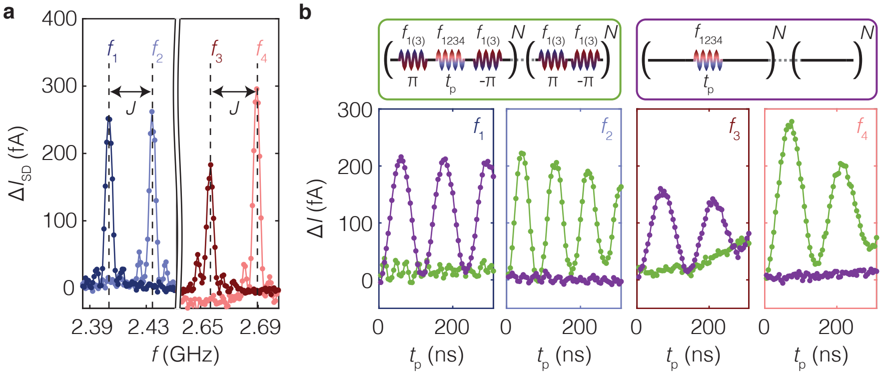

Figure 8.5: **Fast two-qubit logic with germanium qubits.** **a**, EDSR spectra of both qubits. Resonance peaks can be observed, corresponding to the four individual transitions indicated in Fig. 8.4a. The peaks are power broadened and the line width is thus determined by the Rabi frequency. **b**, Controlled qubit rotations can naturally be performed by selectively driving each of the four transitions. A CX gate is achieved at $t_{\mathrm{CX}} = t_\pi$ on f_1 (f_3). A small off-resonant driving effect can be observed, which we mitigate by tuning $t_{\mathrm{CX}} = t_{\pi,\mathrm{resonant}} = t_{4\pi,\mathrm{off\text{-}resonant}}$.

The slight off-resonant driving that can be observed on f_1 is mitigated by choosing the driving speed such that $t_{\mathrm{CX}} = t_{\pi,\mathrm{resonant}} = t_{4\pi,\mathrm{off\text{-}resonant}}$. A fast CX-operation is thus achieved within $t_{\mathrm{CX,Q1}} = 55$ ns and $t_{\mathrm{CX,Q2}} = 75$ ns, with Q1 and Q2 as the target qubits respectively.

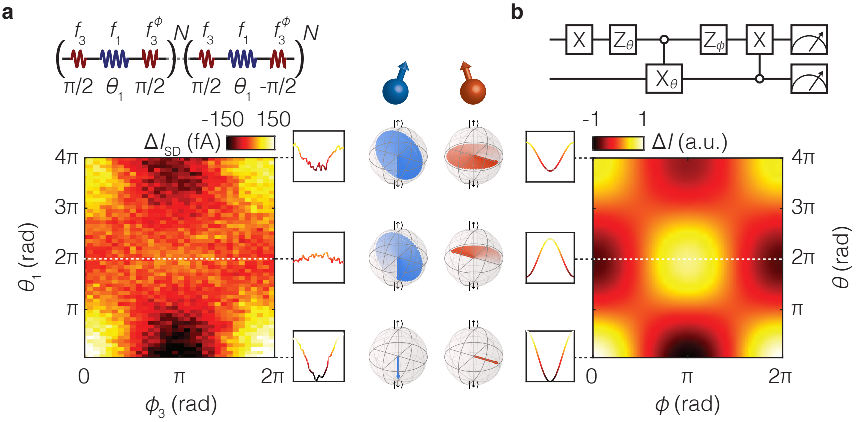

Figure 8.6: **Operation of a phase coherent two-qubit algorithm.** **a**, Colour plot of ΔI_{SD} as a function of Q1 CX-pulse length θ_1 and the phase of the second $\pi/2$-rotation on Q2 ϕ_3. Due to the $Z(\theta_1/2)$ rotation on the control qubit, a π phase shift can be observed on Q2 for a conditional 2π rotation on Q1 (f_1). **b**, Circuit diagram and simulation of the expected corresponding outcome, assuming the measured phase coherence time of Q2.

As a result of the pulsing, we observe a minor shift in the resonance frequency of both qubits, observed before in Si/SiGe quantum dots [250]. We compensate for the temporary change in resonance frequency by applying phase corrections to all following pulses (see Fig. 8.8). In Fig. 8.6 we show the effect of a controlled rotation on the control qubit with applied phase corrections. We observe a larger signal amplitude on Q1 after 0 and 4π rotations on Q2 as compared to a 2π rotation. This 4π periodicity is in agreement with fermionic statistics and suggests an echoing pulse correcting residual environmental coupling. The full π phase shift on Q2 for a conditional 2π rotation on Q1 as a result of the $\theta_1/2$ phase that is accumulated by the control qubit demonstrates the application of a coherent CX gate.

8.5. DISCUSSION

The demonstration of a universal gate set with all electrical control and without the need for any microscopic structures provide great prospects to scale up spin qubits using holes in strained germanium. The hole states do not suffer from nearby valley states and the quantum dots are contacted by superconductors [74] that may be shaped into microwave resonators for spin-photon coupling, providing opportunities for a platform that can combine semiconducting, superconducting, and topological systems for hybrid technology with fast and coherent control over individual hole spins. Moreover, the demonstrated quantum coherence and level of control make planar germanium a natural candidate to engineer artificial Hamiltonians for quantum simulation going beyond classically tractable experiments.

8.6. EXPERIMENTAL METHODS

8.6.1. DEVICE FABRICATION

Our Ge/SiGe heterostructures are grown on a 100 mm *n*-type Si(001) substrate, using an Epsilon 2000 (ASMI) RP-CVD reactor, as described in Ref. [71]. The device Ohmic contacts, as well as the electrostatic gates, are defined by electron beam lithography, electron beam evaporation and lift-off of Al and Ti/Pd. Ohmic contacts consist of a 20-nm-thick Al layer, followed by a 17-nm-thick ALD-grown Al_2O_3 gate dielectric grown at 300 °C. Next, the first layer of Ti/Pd (40 nm) gates is deposited, followed by 17 nm of Al_2O_3 and the second layer of overlapping Ti/Pd (40 nm) gates. Finally, vias contacting the lower gate layer are etched through the top Al_2O_3-layer, followed by the deposition of 1 μm thick $Al_{99}Si_1$ bond pads to protect the device during bonding.

8.6.2. EXPERIMENTAL SETUP

All measurements are performed in a Bluefors dry dilution refrigerator with a base temperature of $T_{\text{bath}} \approx 10$ mK. Using battery-powered voltage sources, dc-voltages are applied to the gates. The voltages on gates P1 and P2 are combined with an AC voltage by a bias-tee with a cut-off frequency of 3 Hz. The AC-voltage for gate P1 is generated by an arbitrary waveform generator (AWG) Tektronix AWG5014C, combined with a microwave signal generated by a Keysight PSG8267D vector source. The AC-voltage for gate P2 is solely the waveform generated by the AWG. EDSR pulses are generated by the PSG8267D using the internal IQ-mixer, driven by two output channels of the AWG. Both qubits can be addressed by setting the vector source to an intermediate frequency of typically $f_{\text{PSG}} = 2.56$ GHz, and IQ-mixing this with a (co)sine wave generated on channels 3 and 4 of the AWG. Because the on/off ratio of the IQ-modulation of our vector source is only 40 dB and small residual output power may lead to added infidelity, we use digital pulse modulation (PM) in series with the IQ modulation. The PM is driven by the AWG and is turned on 15 ns before the first pulse and turned off 7 ns after the last pulse in the sequence, resulting in a total suppression of 120 dB when the source is off.

We typically apply a source-drain bias voltage of $V_{\mathrm{SD}} = 0.3$ mV and measure the current through the device using an in-house built transimpedance amplifier, after which the signal is low-pass filtered at 10 kHz and measured using a Stanford Research SR830 lock-in amplifier, as described in Section 4.4.

8.6.3. VIRTUAL GATES

In order to allow independent control over the tunnel coupling and the charge occupation of the double dot system, we make use of virtual gates [246]. When changing the different barrier gate voltages, linear corrections are applied to the device's plunger gates to correct for the cross-capacitance between the different gates. These coefficients are obtained from the relative slopes of the charge-addition lines with respect to the different device gates and normalised to the respective plunger gate coefficient. We write

$$\begin{pmatrix} \mathrm{VP1} \\ \mathrm{VP2} \end{pmatrix} = \begin{pmatrix} \alpha_{\mathrm{P1,P1}} & \alpha_{\mathrm{P2,P1}} & \alpha_{\mathrm{BC,P1}} & \alpha_{\mathrm{BR1,P1}} & \alpha_{\mathrm{BR2,P1}} \\ \alpha_{\mathrm{P1,P2}} & \alpha_{\mathrm{P2,P2}} & \alpha_{\mathrm{BC,P2}} & \alpha_{\mathrm{BR1,P2}} & \alpha_{\mathrm{BR2,P2}} \end{pmatrix} \delta \begin{pmatrix} \mathrm{P1} \\ \mathrm{P2} \\ \mathrm{BC} \\ \mathrm{BR1} \\ \mathrm{BR2} \end{pmatrix}, \tag{8.1}$$

with VP1 and VP2 the virtual plunger gates, and P1, P2, BC, BR1, and BR2 the different physical device gates as indicated in Fig. 1a. The virtual gate matrix describes the different couplings and is given by

$$\begin{pmatrix} \alpha_{\mathrm{P1,P1}} & \alpha_{\mathrm{P2,P1}} & \alpha_{\mathrm{BC,P1}} & \alpha_{\mathrm{BR1,P1}} & \alpha_{\mathrm{BR2,P1}} \\ \alpha_{\mathrm{P1,P2}} & \alpha_{\mathrm{P2,P2}} & \alpha_{\mathrm{BC,P2}} & \alpha_{\mathrm{BR1,P2}} & \alpha_{\mathrm{BR2,P2}} \end{pmatrix} = \begin{pmatrix} 1 & 0 & 0.8 & 0.35 & 0 \\ 0 & 1 & 0.8 & 0 & 0.4 \end{pmatrix}. \tag{8.2}$$

We do not correct for the crosstalk between the two plunger gates, such that $\alpha_{\mathrm{P2,P1}} = \alpha_{\mathrm{P1,P2}} = 0$. The crosstalk between the quantum dot and the reservoir barrier of the other dot is negligible due to their physical separation. Furthermore, it can be observed that the coupling of the centre barrier to both dots is approximately twice as strong as the reservoir barriers as a direct effect of its increased size.

8.6.4. SEQUENCE DETAILS

For a Rabi experiment, the measurement cycle contains a single microwave pulse of duration t_{p}, while the reference cycle has no pulses. In the case of a Ramsey experiment, both the measurement and reference cycle contain a $\pi/2$ pulse, a wait time τ and a final $\pi/2$ pulse, but in the reference cycle, the final $\pi/2$ pulse is phase shifted by $\phi = \pi$. This will result in an opposite projection for the two measurements and thereby maximum differential signal. For the randomised benchmarking a similar scheme is used (see Fig. 8.7a), where the recovery pulse in the measurement cycle is chosen to project to the spin-up state, while the recovery pulse in the reference cycle projects to the

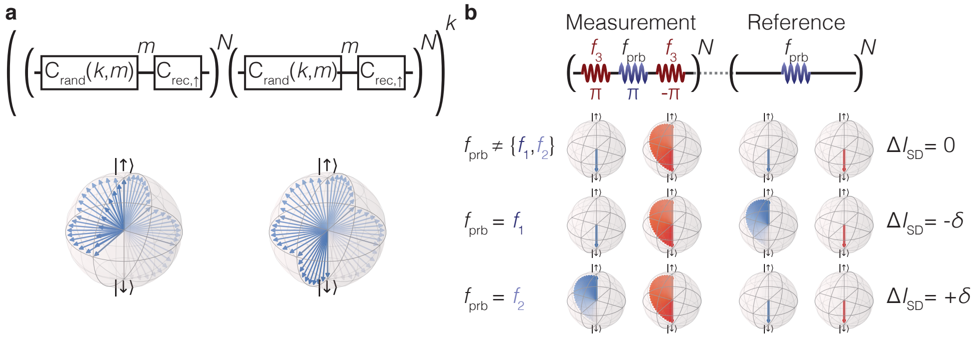

Figure 8.7: **Pulse cycles used for the transport measurements.** **a**, Pulse cycles used for the randomised benchmarking experiments. The measurement pulse cycle consists of m randomly drawn Clifford gates C_{rand} and a final Clifford projecting to spin-up. The reference pulse cycle consists of the same m Clifford gates and a different final Clifford projecting to spin-down. Each cycle is repeated N times, and a series of typically $k = 50$ independent randomly drawn measurement and reference pulse cycles are alternated. These $k = 50$ different draws are thus hardware averaged on the lock-in amplifier, and this entire experiment is repeated and averaged 30 times, yielding a total of approximately 100000 repetitions of 1500 different randomly drawn Clifford sequences of length m. An example of the qubit evolution for each pulse cycle is plotted on the Bloch sphere below. **b**, Pulse cycles used for the exchange mapping experiments. The measurement pulse cycle consists of a broad preparation and restoring pulse at frequency f_3 (f_1), around a probing pulse at frequency f_{prb}. The reference pulse cycle consists solely of the probing pulse at f_{prb}. The qubit evolution for the different resonance conditions is plotted on the Bloch sphere and illustrate the different signals measured in Fig. 8.4.

spin-down state, resulting in an exponential decay towards $\Delta I_{SD} = 0$. Each data point is averaged over approximately 100000 repetitions of 1500 randomly drawn gate sequences. Finally, for the exchange measurements, we alternate a measurement cycle where we apply a π and $-\pi$ pulse to Q1 (Q2) before and after the probing pulse respectively, with a reference cycle where Q1 (Q2) is not pulsed. When the probing pulse is off-resonant with both resonance frequencies, the measurement cycle gives effectively no rotation of Q1 (Q2) and the reference cycle does not result in any rotation. This will result in the demodulated signal being equal to zero. When the probing pulse frequency is on resonance with the unprepared resonance frequency f_3 (f_1), the measurement cycle will still be an effective zero rotation on Q1 (Q2) due to the selective driving of f_3 (f_1) and thus give no signal. The reference cycle will now result in a π rotation on Q2 (Q1) and will therefore give a signal, resulting in a negative demodulated signal. In the case where the probing pulse is resonant with the prepared resonance line f_4 (f_2), the measurement cycle will generate a signal while the reference cycle will give no signal, thus resulting in a positive demodulated signal. All different pulse cycle configurations and the respective qubit projections are illustrated in Fig. 8.7b.

8.6.5. PHASE CORRECTIONS FOR PULSING

We observe a shift of the resonance frequency of the qubits as a function of the microwave driving power. We attribute this to a rectification of the microwave signal, resulting in a dc voltage pulse that can modulate the resonance frequency through the SOC and exchange interaction. As a result of the shift during the pulsing, each qubit

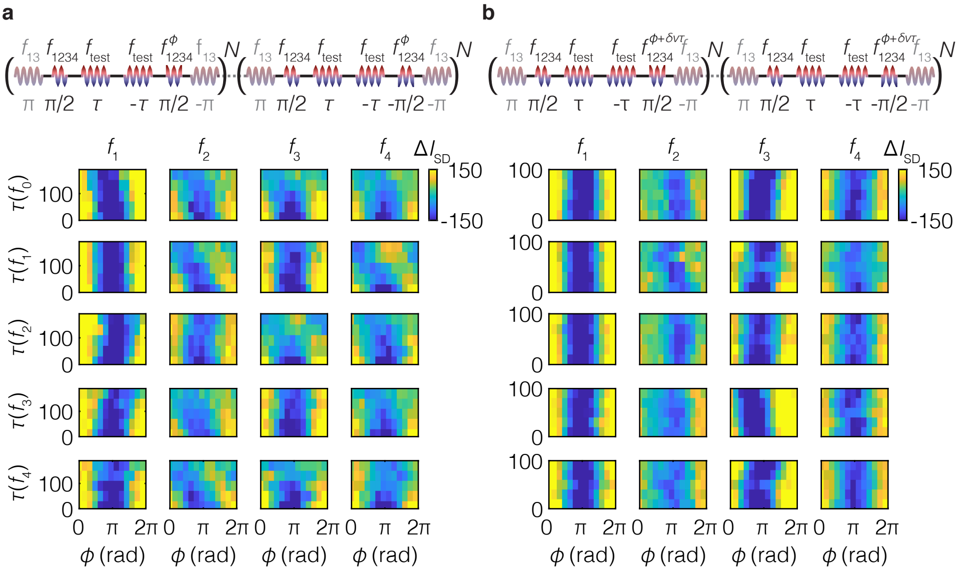

Figure 8.8: **Phase corrections on the qubits.** **a**, Extended Ramsey experiment on each of the four resonance line, using 5 different test gates in between the $\pi/2$-pulses to observe the effect on the resonance frequency. A linear phase shift as a function of test gate pulse length τ can be observed for some lines, indicating a frequency shift during the pulsing. **b**, We compensate for this effect by performing a software update of $\delta\phi = \delta\nu\tau$ to each additional pulse, with $\delta\nu$ the frequency shift of the qubit as a result of the power.

picks up a phase when it is idling, as well as an additional phase due to the pulses on the other qubit. We can calibrate these frequency shifts and correct all following pulses to counteract this phase shift.

In order to probe the effect of all possible pulses on all possible resonances, we perform an extended Ramsey experiment. We prepare a pulse sequence consisting of two $\pi/2$ pulses with a test gate (each of the four resonance lines, as well as idling) and π phase shifted test gate in between, as indicated in Fig. 8.8. For the experiment on f_2 and f_4, we add a preparation and projection pulse at the start and end respectively, as indicated in grey in Fig. 8.8. The back-and-forth rotation on the test gate cancels any driving effects, as well as the $\theta/2$ phase picked up due to the conditional rotation and leaves us with only the detuning phase. We now plot the transport current ΔI_{SD} as a function of the phase ϕ of the second $\pi/2$-pulse, as well as the length of the test gate. As a result of the frequency shift caused by the test gate, we observe a phase shift increasing linearly with the length of the test gate. We fit this phase shift for each gate, and we apply a correction to all following gates. Fig. 8.8 shows the phase evolution for all test gates on all four resonance lines, both without corrections (Fig. 8.8a) and with corrections applied (Fig. 8.8b).

8.6.6. SUPPLEMENTARY FIGURES

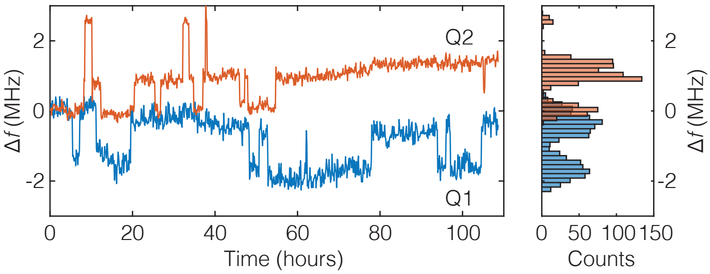

Figure 8.9: **Temporal dependence of the resonance frequency.** We track the resonance frequency of both Q1 and Q2 over the time of $\sim$ 110 hours. We observe that the qubit frequency remains remarkably stable over this period, but do observe discrete, uncorrelated steps in the resonance frequencies of both qubits. The resonance frequency of Q1 only shows steps of $\Delta f \approx 2$ MHz between two distinct levels, while for Q2 we observe both steps of $\Delta f \approx 1$ MHz and $\Delta f \approx 2$ MHz, between three different levels as also becomes apparent from the histogram. The origin of these steps could be e.g. the slow loading and unloading of charge traps, manipulating the qubit resonance frequency through the change in the electric field, or hyperfine coupling to a nearby nuclear spin [251].

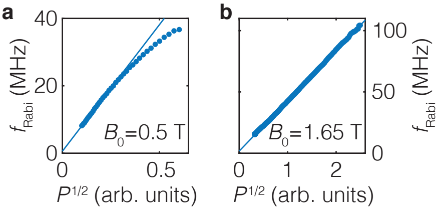

Figure 8.10: **Magnetic field dependence of the driving speed of Q1.** Rabi frequency dependence on the applied microwave power P in arbitrary units, for $B_0 = 0.5$ T (**a**) and $B_0 = 1.65$ T (**b**). Multiple mechanisms can be at play for the EDSR driving of the spins [252] and these are typically all linearly dependent on B_0. As a result of this, significantly higher driving frequencies can be reached at higher magnetic fields. We note that the exact microwave power cannot be compared between the two measurements due to the strong frequency dependence of the attenuation of our fridge lines.

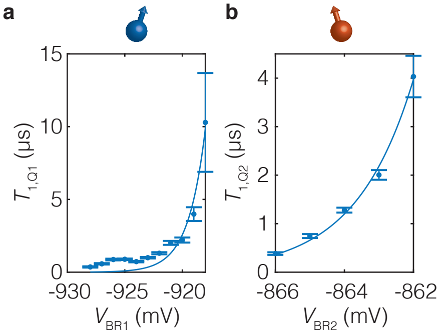

Figure 8.11: **Relaxation time T_1 as a function of dot-reservoir tunnel barrier gate voltage.** The relaxation time T_1 of both dots increases approximately exponentially as a function of the respective dot-reservoir gate voltage, both for Q1 (**a**) as well as for Q2 (**b**). The relaxation time of Q1 increases exponentially from $T_1 < 1\,\mu$s to $T_1 > 10\,\mu$s and a similar scaling is observed for Q2. For even smaller dot-reservoir couplings, the transport signal drops below our measurement limit, but switching to charge sensing could allow for an even further increase in T_1.

9

COHERENTLY CONTROLLING A SINGLE-HOLE SPIN

The demonstration of universal quantum logic in Chapter 8 was obtained in a many-hole quantum dot by performing transport measurements. However, single-shot qubit readout is essential to many quantum computing applications. In this chapter, we establish a single-hole spin qubit in germanium and demonstrate the integration of single-shot readout and quantum control. We deplete a planar germanium double quantum dot to the last hole, confirmed by radio-frequency reflectometry charge sensing, and achieve single-shot spin readout. To demonstrate the integration of the readout and qubit operation, we show Rabi driving on both qubits and find remarkable electric control over their resonance frequencies. Finally, we analyse the spin relaxation time, which we find to exceed one millisecond, setting the benchmark for hole-based spin qubits. The ability to coherently manipulate a single hole spin underpins the quality of strained germanium and defines an excellent starting point for the construction of novel quantum hardware.

Parts of this chapter have been published in Nature Communications **11**, 3478 (2020) [132]

9.1. INTRODUCTION

Group-IV semiconductor spin qubits [25] are promising candidates to form the main building block of a quantum computer due to their high potential for scalability towards large 2D-arrays [26, 59, 94, 224] and the abundance of net-zero nuclear spin isotopes for long quantum coherence [28, 56]. Over the past decade, all prerequisites for quantum computation were demonstrated on electron spin qubits in silicon, such as single-shot readout of a single electron [253], high-fidelity single-qubit gates [55, 57] and the operation of a two-qubit gate [11, 58, 61, 78]. However, hole spins may offer several advantages [68, 69], such as a strong spin-orbit coupling (SOC) and large excited-state energy. Early research demonstrated the feasibility of using the SOC for all-electric driving [254, 255], but these experiments were limited by nuclear spins and the coherent driving of a single hole spin remained an open challenge. More recently, hole spins in group-IV materials have gained attention as a platform for quantum information processing [84, 86, 93]. In particular hole states in germanium can provide a high degree of quantum dot tuneability [74, 197, 256], fast and all-electrical driving [84, 86] and Ohmic contacts to superconductors for hybrids [177, 221]. These experiments culminated in the recent demonstration of full two-qubit logic [86]. While hole spins have been read out in single-shot mode using the Elzerman technique [83], these experiments require magnetic fields impractical for hole qubit operation due to the strongly anisotropic g-factor of hole spins in germanium [193]. Pauli spin blockade readout allows for spin readout independent of the Zeeman splitting of the qubit, leveraging the large excited-state energy purely defined by the orbital energy for holes in germanium. Furthermore, achieving these assets on a single-hole spin demonstrates full control over the materials system and allows to tune the quantum dot occupancy at will, optimising the different qubit properties. Moreover, the ability to study a platform at the single-particle level would provide great insight into its physical nature, crucial for holes that originate from a more complicated band structure than electrons [247, 257].

In this work, we make this step and demonstrate single-shot readout and operation of a single hole spin qubit. We grow undoped strained germanium quantum wells [71] and fabricate devices using standard manufacturing techniques [94]. The high mobility and low effective mass [73] allow us to define quantum dots of relatively large size, alleviating the restraints on fabrication. We deplete the quantum dots to their last hole, confirmed by charge sensing using a nearby single-hole transistor (SHT). The use of radio-frequency (rf) reflectometry [258–260] enables a good discrimination of the charge state, while maintaining a high measurement bandwidth to allow for fast spin readout. We make use of Pauli spin blockade to perform the spin-to-charge conversion [158], maximally taking advantage of the large excited-state energy splitting of $E_{\mathrm{ST}} = 0.85$ meV and obtain single-shot spin readout. Finally, we demonstrate the integration of readout and qubit operation by performing all-electrically driven Rabi rotations on both qubits. Studying the control of a single hole qubit, we find a remarkably strong dependence of the resonance frequency on the electric field and show a tunability of almost 1 GHz using only small electric potential variations.

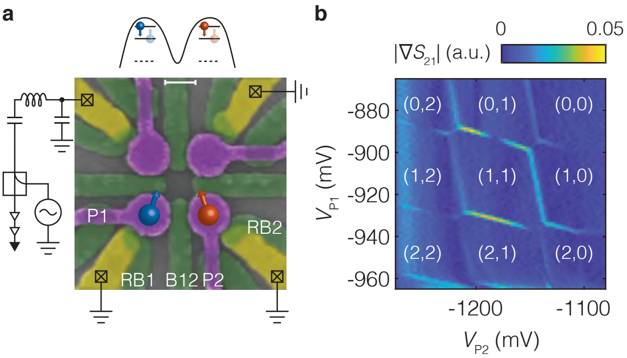

Figure 9.1: **Fabrication and operation of a planar germanium double quantum dot.** **a**, False-coloured scanning electron microscope image of the quadruple quantum dot device. Ohmic contacts are indicated in yellow, the first layer of electrostatic barrier gates is indicated in green and the second layer of plunger gates is coloured in purple (for details, see Section 9.5). The scale bar corresponds to 100 nm. We use the double quantum dot in the top channel as a single hole transistor (SHT) to sense changes in the charge occupation of the quantum dots formed under plunger gates P1 and P2. A schematic illustration of the electrostatic potential defining the two single-hole quantum dots is depicted above the figure. The charge sensor impedance is measured using reflectometry on a resonant circuit consisting of a superconducting resonator and the parasitic device capacitance. Barrier gates RB1 and RB2 can be used to control the tunnelling rate of each quantum dot to its respective reservoir and gate B12 controls the interdot tunnel coupling. **b**, Charge stability diagram of the double quantum dot system, where depletion of both quantum dots up to the last hole can be observed.

9.2. SINGLE HOLE QUANTUM DOT AND PAULI SPIN BLOCKADE

A false-coloured SEM picture of the quantum dot device is depicted in Fig. 9.1a. The device consists of a quadruple quantum dot system in a two-by-two array [94]. We tune the top two quantum dots into the many-hole regime, such that they can be operated as a single hole transistor. In order to perform high-bandwidth measurements of the sensor impedance, we make use of rf reflectometry, where the SHT is part of a resonant LCR-circuit further consisting of an off-chip superconducting resonator together with the parasitic device capacitance. We apply a microwave signal to the tank circuit and measure the amplitude of the signal reflected by the LCR-circuit (see Fig. 9.1a). The amplitude of the reflected signal $|S_{21}|$ depends on the matching of the tank circuit impedance with the measurement setup and is therefore modulated by a change in the charge sensor impedance caused by the movement of a nearby charge.

We make use of the rf sensor to map out the charge stability diagram of the double quantum dot system defined by plunger gates P1 and P2. The tunnel coupling of the quantum dots to their reservoirs, as well as the interdot tunnel coupling can be tuned by gates RB1, RB2 and B12 respectively. Next, we tune the device to the single hole regime for both quantum dots (Fig. 9.1b and Fig. 9.6), where (N_1,N_2) indicates the charge occupation, with N_1 (N_2) the hole number in the dot under P1 (P2). In our previous work [94], we further detail that we can deplete all four quantum dots in this device down to their last hole. In order to perform readout of the spin states, we make use of Pauli spin blockade (PSB), which is expected to be observed both at the (1,1)-(0,2) and

(1,1)-(2,0) charge transitions. We define the virtual gates [246] detuning V_ϵ and energy V_U (see Fig. 9.2a and details in Section 9.5) and sweep across the (1,1)-(2,0) and (1,1)-(0,2) transitions in this gate space. As a result of its triplet character, the $|\downarrow\downarrow\rangle$ state has a negligible coupling to the S(2,0) or S(0,2) singlet charge states (Fig. 9.2b). When pulsing across the (1,1)-S(2,0) or (1,1)-S(0,2) anti-crossings, PSB prevents charge movement when the system is in the $|\downarrow\downarrow\rangle$ ground state. However, when the system resides in the singlet-like lower antiparallel spin state (in this case $|\downarrow\uparrow\rangle$, with Q2 being the qubit with lower Zeeman energy), charge movement to a doubly occupied quantum dot state is possible, therefore leaving the system in a (0,2) or (2,0) charge state. This results in a spin-to-charge conversion, which in turn can be picked up in the reflectometry signal from the SHT.

Indeed, we find that by sweeping the detuning voltage across the interdot transition from the (1,1) into the (0,2) charge region (Fig. 9.2d), tunnelling is blocked up to the reservoir transitions (indicated in white) when the system is initialised in the $|\downarrow\downarrow\rangle$ state. In this case, we rely on the fast diabatic return sweep combined with fast spin relaxation compared to the sweep rate to prepare the system in the blocking $|\downarrow\downarrow\rangle$ state. When we invert the sweeping direction, the system remains in the (0,2) charge states at the same values of V_ϵ and V_U (Fig. 9.2c). After optimising the different tunnel rates in the device, we confirm the Pauli spin blockade at both the (1,1)-(2,0) and (1,1)-(0,2) anticrossings by loading a random spin before performing the readout, thereby not relying on a relaxation process for the initialisation (small panels of Fig. 9.2c,d). The diamond-shaped window of differential signal allows for a singlet/triplet readout of the system spin state, and we select readout point R. We note that the interdot transition line is shifted slightly towards positive detuning with respect to the reservoir transition lines. This is the direct result of a small voltage offset present across the device Ohmics, resulting in the unusual diamond-shaped spin readout window, but not limiting the readout. As holes in germanium do not have any valley states, the T(2,0) state is expected to be defined by the next quantum dot orbital. By increasing the bias voltage across the two quantum dots, we shift the interdot transition line further. At large enough bias, the Pauli spin blockade window is capped as a result of the T(2,0) state becoming available in energy and from this we extract an excited state energy of $E_{\mathrm{ST}} = 0.85$ meV, using a lever arm of $\alpha_\epsilon = 0.21$ as extracted from polarisation line measurements (Fig. 9.7).

9.3. QUBIT OPERATION

To coherently control the qubits, we implement a three-level voltage pulsing scheme (Fig. 9.3a) and operate at an external magnetic field of $B = 0.67$ T. We initialise the system by pulsing deep into the (2,0) region ($\alpha_\epsilon V_\epsilon > E_{\mathrm{ST}}$), where the spins quickly relax into the (2,0) singlet state. Next, we ramp adiabatically into the (1,1) region, preparing the system into the $|\downarrow\uparrow\rangle$ state. At this point (M) we perform the qubit operations by applying microwave pulses to gate P1, taking advantage of the SOC-mediated EDSR. Rotating Q1 (Q2) will bring the system into the $|\uparrow\uparrow\rangle$ ($|\downarrow\downarrow\rangle$) state. Finally, the spin-state is read out by pulsing adiabatically into the readout window. Only the $|\downarrow\uparrow\rangle$ will allow direct tunnelling into the (2,0) charge state, while tunnelling is blocked for all other states due to PSB.

Fig. 9.3b displays the charge sensor signal throughout the readout period, both for

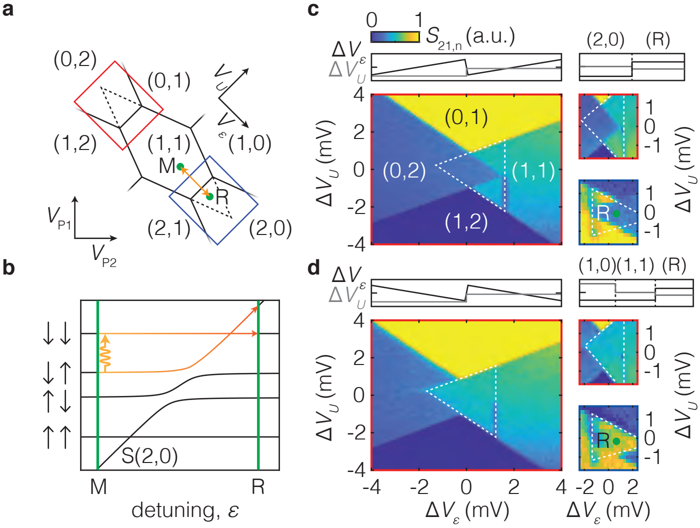

Figure 9.2: **Pauli spin blockade readout.** **a**, Schematic of a typical hole charge stability diagram with both possible regions of readout indicated in blue and red. The typical manipulation (M) and readout (R) points are indicated in green. **b**, Two-hole energy diagram, with the five lowest lying energy states around the (1,1)-S(2,0) anticrossing. **c**, Colour map of the normalised sensor response (normalisation in Section 9.5) as a function of the applied gate voltages V_U and V_ϵ. In the large panel, we linearly sweep V_ϵ and step V_U, as indicated in the inset above the figure. The smaller panels on the right show the same effect for the (1,1)-(0,2) anticrossing (top, red box in **a**), and the (1,1)-(2,0) anticrossing (bottom, blue box in **a**), now using a two-level voltage pulse (details in Section 9.5). **d**, Similar colour map as in **c**, but with a reversed sweeping direction from (1,1) into the (0,2) region. The triangular spin blockade window is indicated by the dashed white line. The smaller panels on the right again demonstrate the same effect for both the (1,1)-(0,2) (top) as well as the (1,1)-(2,0) (bottom) anti-crossings, by first loading a random spin in one of the dots (details in Section 9.5).

a $|{\downarrow\uparrow}\rangle$ state initialisation (blue) as well as a $|{\uparrow\uparrow}\rangle$ state initialisation (red) by applying a π-pulse to Q1. When no pulse is applied and the system is prepared in the $|{\downarrow\uparrow}\rangle$ state, a fast transition into the (1,1)-charge state, corresponding to a sensor signal of $S_{21} \approx -0.6$ can be observed. The remaining decay ($T_\text{decay} = 2\ \mu$s) in this case can be attributed to the response of the SHT-signal to the voltage pulses on the gates. However, when the system is prepared in the $|{\uparrow\uparrow}\rangle$ state, a significantly slower relaxation into the (1,1) state is observed, due to the spin blockade combined with the slow T_+(1,1)-S(2,0) relaxation. By fitting a double exponential decay, accounting for the SHT response, we extract a spin relaxation at the readout point of $T_{1,\text{RO}} = 26\ \mu$s. A sample of 100 single-shot traces is plotted in Fig. 9.3c, together with two individual traces using a post-processing integration time of 3 μs. A clear distinction of the (1,1) and (2,0) charge states can be observed from the sensor response. To determine the spin state of the qubits, we perform a threshold detection of the single-shot signal integrated from $\tau_0 = 1.0\ \mu$s up to $\tau_\text{meas} = 6.0\ \mu$s for maximised visibility, discarding the initial stabilisation of the SHT and optimising between the charge discrimination and spin relaxation. A histogram of 5000 single-shot events illustrates the clear distinction between the singlet ($S_{21} > -0.72$) and the triplet ($S_{21} < -0.72$) spin-state readout (Fig. 9.3d). We find a spin readout

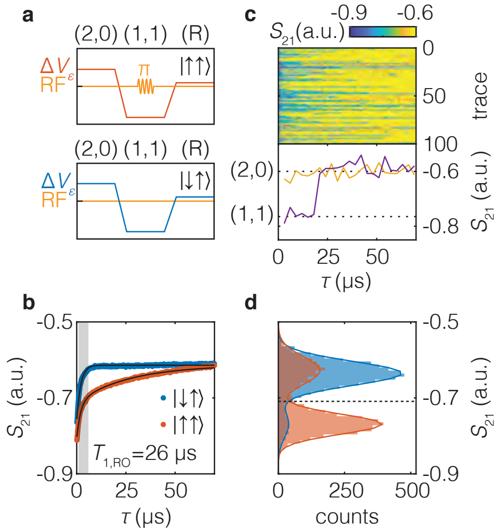

Figure 9.3: **Single-shot spin readout of a single hole.** **a**, Schematic illustration of the three-level pulses used in panels **b**-**d**, indicating the detuning voltage ΔV_ϵ in blue and red, and the rf pulses in orange. **b**, The averaged charge sensor response as a function of measurement time τ at R for $|\uparrow\uparrow\rangle$ initialisation (red) and $|\downarrow\uparrow\rangle$ initialisation (blue). The gray shaded area indicates the integration window for the threshold detection. **c**, A sample of 100 single-shot traces (top), averaged for 3 μs per data point, with $\tau = 0$ the start of the readout phase. The bottom panel shows two single traces, where the purple (yellow) trace corresponds to the readout of a blocked (not blocked) spin state. Dashed lines correspond to the sensor signal for the different charge states. **d**, Histogram of 5000 single-shot traces, integrating the signal for 5.5 μs as indicated in **c**. The blue (red) histogram corresponds to an initialisation in the $|\downarrow\uparrow\rangle$ ($|\uparrow\uparrow\rangle$) state. The dashed line corresponds to the optimised threshold for readout.

visibility of $v = 56\%$ as obtained from the difference in spin-up fraction between the two prepared states. A large part of this reduced visibility is caused by relaxation of the blocked triplet state during the measurement, expected to amount to a signal reduction of $P_{\text{relax}} = 1 - e^{-\tau_{\text{meas}}/T_{1,\text{RO}}} = 0.21$. This gives good prospects for increasing the readout fidelity by optimising the spin relaxation, for instance by optimising the reservoir tunnel rates and moving to latched PSB readout mechanisms [261, 262]. Alternatively, by using high-Q on-chip resonators [263] the signal-to-noise ratio could be significantly improved, thereby lowering the required integration time and reducing the effective relaxation. The remaining triplet fraction of 0.11 that can be observed for the readout of the $|\downarrow\uparrow\rangle$ state could be attributed to an anadiabaticity of the pulsing or a small coupling between the T(1,1) and S(2,0) states due to the SOC. This could be mitigated by further optimising the readout pulse sequence.

Now we probe the single spin relaxation time by initialising the system in the $|\downarrow\uparrow\rangle$ state and letting the system evolve at a detuning voltage $\Delta V_\epsilon = -7$ mV from the (1,1)-(2,0) anticrossing. Fig. 9.4a shows the spin-up fraction as a function of the waiting time t_{wait}, from which a single spin relaxation time of $T_{1,Q2} = 1.2$ ms can be extracted. This is substantially longer than reported before in planar germanium heterostructures [86], most likely as a result of the more isolated single hole spins as compared to the transport

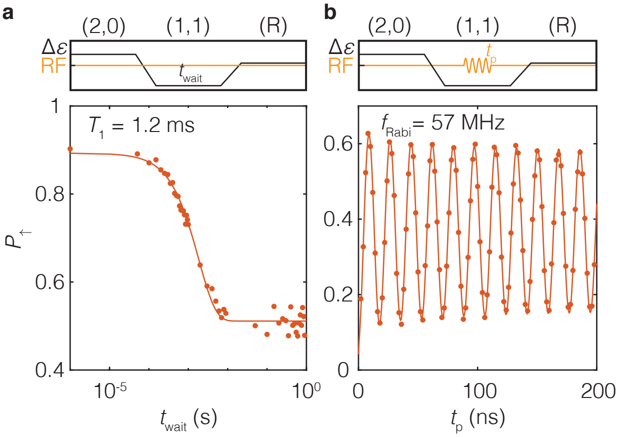

Figure 9.4: **Spin relaxation and coherent driving of a single hole.** **a**, The system is initialised in the $|\downarrow\uparrow\rangle$ state after which the qubits idle at the measurement point. The spin-up fraction $P_\uparrow$ of Q2 is measured as a function of waiting time t_{wait} and shows a typical T_1-decay with a relaxation time of $T_1 = 1.2$ ms. **b**, Driving of the single hole qubit Q2 shows coherent oscillations in $P_\uparrow$ as a function of the microwave pulse length t_p. The coherent operation of Q1 is shown in Fig. 9.8.

measurements with high reservoir couplings, and is also longer than all relevant time scales for qubit operation. Moreover, this relaxation time compares favourably to results obtained for holes in Ge nanowires [80], Ge hutwires [83] and other hole spins [264, 265].

To demonstrate coherent control of a single hole, we modulate the length of the driving microwave pulse and measure the spin-up fraction (Fig. 9.4b). A clear sinusoidal Rabi oscillation can be observed on Q2, with a Rabi frequency of $f_R = 57$ MHz. We probe the phase coherence of both qubits by performing a Ramsey sequence in which we apply two $\pi/2$-pulses, separated by a time τ in which we let the qubit freely evolve and precess at a frequency offset of $\Delta f = 7.4$ MHz and $\Delta f = 23.7$ MHz respectively. In Fig. 9.5b the Ramsey decay for Q1 and Q2 are plotted and we extract coherence times of $T^*_{2,Q1} = 380$ ns and $T^*_{2,Q2} = 140$ ns. These coherence times are of comparable order, but slightly lower than previously reported numbers in the same heterostructure for a many-hole quantum dot [86]. In order to explain the origin of this, we measure the resonance frequency of both qubits as a function of the detuning voltage ΔV_ϵ. We find a very strong dependence of the resonance frequency of both qubits on the detuning voltage over the entire range of voltages measured, with the g-factor varying between $g_{Q1} = 0.27$—0.3 and $g_{Q2} = 0.21$—0.29 (Fig. 9.5a). This strong electric field dependence of the resonance frequency will increase the coupling of charge noise to the qubit spin states, which in turn will reduce phase coherence [86]. The ratio in local slopes of the resonance frequency $\delta f_{Q2}/\delta f_{Q1} = 2$ is similar to the ratio in phase coherence of both qubits $T^*_{2,Q1}/T^*_{2,Q2} = 2.5$, consistent with charge-noise limited coherence. The strong modulation of the qubit resonance frequency by electric field could be explained from the strong SOC present [75, 127]. This is further supported by the Rabi frequency changing as a function of detuning voltage, as is predicted to be a result of the strong

SOC [75, 127]. We attribute the slightly different resonance frequency of Q1 and Q2 to an asymmetry in the potential landscape of the two dots. Although the strong g-factor modulation seems mainly a cause of decoherence, in this case, careful optimisation of the electric field landscape could render a situation in which the qubit Zeeman splitting is well controllable, while maintaining a zero local slope for high coherence [127].

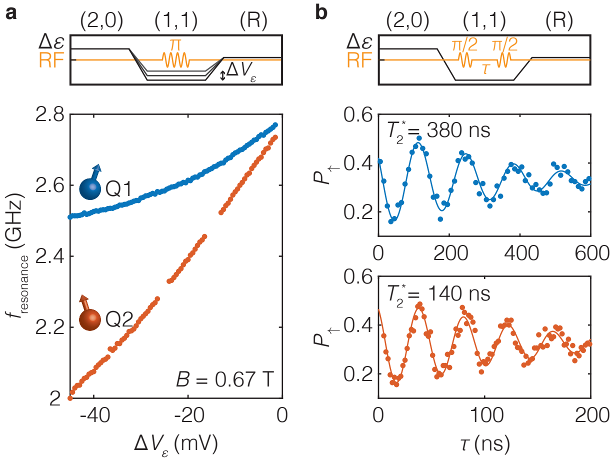

Figure 9.5: **Electric g-factor modulation and phase coherence of the qubit resonances.** **a**, The resonance frequency of both qubits shows a strong modulation as a function of the detuning voltage ΔV_ϵ. **b**, We perform a Ramsey experiment on both qubits to probe the phase coherence times, with $T^*_{2,Q1} = 380$ ns and $T^*_{2,Q2} = 140$ ns. The comparatively short phase coherence can be attributed to the strong dependence of $f_{\text{resonance}}$ to electric fields, coupling charge noise to the spin state, leading to increased decoherence.

9.4. DISCUSSION

The demonstration that single hole spins can be coherently controlled and read out in single-shot mode, together with the spin relaxation times $T_1 > 1$ ms, defines planar germanium as a mature quantum platform. These aspects are demonstrated on a two-dimensional quantum dot array, further highlighting the advancement of germanium quantum dots. Moreover, controlling a single hole spin represents an important step towards reproducible quantum hardware for scalable quantum information processing.

9.5. EXPERIMENTAL METHODS

9.5.1. DEVICE FABRICATION

We grow strained Ge/SiGe heterostructures in an Epsilon 2000 (ASMI) reduced-pressure chemical vapour deposition reactor on a 100 mm n-type Si(001) substrate. The growth sequence comprises a 1.6-μm-thick relaxed Ge layer; a 1-μm-thick step-graded $Si_{1-x}Ge_x$ layer with final Ge composition x=0.8; a 500-nm-thick strain-relaxed $Si_{0.2}Ge_{0.8}$ buffer layer; a 16-nm-thick strained Ge quantum well; a 22-nm-thick strain-relaxed $Si_{0.2}Ge_{0.8}$ barrier; a sacrificial Si cap layer <2 nm thick. Further details on the heterostructure are discussed in Ref. [71]. Ohmic contacts are defined by electron beam lithography, electron beam evaporation and lift-off of a 30-nm-thick Al layer. Electrostatic gates consist of a Ti/Pd layer with a thickness of 20 and 40 nm respectively for the barrier and plunger gate layer. Both layers are separated from the substrate and each other by 10 nm of ALD-grown Al_2O_3.

9.5.2. EXPERIMENTAL SETUP

We use a Bluefors dry dilution refrigerator with a base temperature of $T_{\text{bath}} \approx 20$ mK to perform the measurements. Battery-powered voltage sources are used to supply dc voltages on the gates. Additionally, ac voltages generated by a Tektronix AWG5014C arbitrary waveform generator can be supplied to the gates through a bias-tee with a cut-off frequency of ≈ 10 Hz. Similarly, we can also apply a microwave signal generated by a Keysight PSG8267D vector source to gate P1 for qubit driving. Driving both qubits at the same power on gate P2, we observe significantly slower Rabi oscillations in Q1. From this, we assume Q1 to be located under P1, and thus Q2 under P2, in correspondence with the trend in Rabi frequencies observed in a previous work [86].

We use an in-house built rf generator to supply the reflectometry signal. The signal is attenuated by 84 dB and applied to one of the sensor Ohmics via a Mini-Circuits ZEDC-15-2B directional coupler. The reflected signal is amplified by a Caltech CIRLF3 SiGe-amplifier at the 4K-stage of our fridge and an in-house built rf amplifier at room temperature, and finally IQ-demodulated to give a measure of S_{21}.

9.5.3. MEASUREMENT DETAILS

The large panels of Fig. 9.2c and Fig. 9.2d are measured by continuously sweeping ε and stepping U, while measuring the sensor response. The smaller panels in Fig. 9.2c show the sensor response after applying a two-level voltage pulse to load the (2,0) or (0,2) charge configuration and vary the readout point across the map. The signal is then integrated for 10 μs at each pixel. The smaller panels in Fig. 9.2d show the sensor response after applying a three-level voltage pulse to first randomly load a spin in the second dot by pulsing across the (1,0)-(1,1) reservoir transition. Next, we pulse across the (1,1)-(0,2) or (1,1)-(2,0) interdot transition to perform the spin readout. The colour scale of the signal in Fig. 9.2c left and Fig. 9.2d left panels is normalised by $S_{21,n} = 10S_{21} + 3.5$. The top right panel in Fig. 9.2c is normalised by $S_{21,n} = 12.5S_{21} + 5.375$. The bottom right panel in Fig. 9.2c is normalised by $S_{21,n} = 12.5S_{21} + 5$. The top right panel in Fig. 9.2d is normalised by $S_{21,n} = 20S_{21} + 16.8$. The bottom right panel in Fig. 9.2d is normalised by $S_{21,n} = 25S_{21} + 20.75$, with $S_{21,n}$ the normalised sensor signal as plotted in Fig. 9.2 and $S_{21,n}$ the demodulated sensor signal strength in mV.

For the measurements in Fig. 9.3b-d and Fig. 9.4 and 9.5, typical adiabatic ramp times of $T_{\text{ramp}} \approx 1\mu$s are used.

9.5.4. VIRTUAL GATES

In order to allow independent control over the detuning and energy of the quantum dots more easily, we define the virtual gate axes of $V_\varepsilon = V_{\text{P2}} - 0.5V_{\text{P1}}$ and $V_U = 0.5V_{\text{P2}} + V_{\text{P1}}$.

9.5.5. SUPPLEMENTARY FIGURES

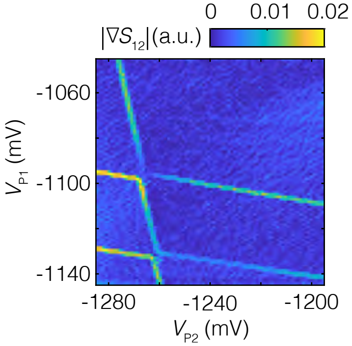

Figure 9.6: **Depletion of a hole double quantum dot in germanium.** Colour map of the sensor signal as a function of the voltages on plunger gates P1 and P2. No extra addition lines can be observed beyond $V_{P1} \approx -1100$ and $V_{P2} \approx -1260$, indicating the double quantum dot is fully depleted. This is the same anticrossing as observed in Fig. 9.1 and the slight decrease of plunger gate voltages can be attributed to a time-dependent hysteretic drift as a result of extensive gate voltage sweeping.

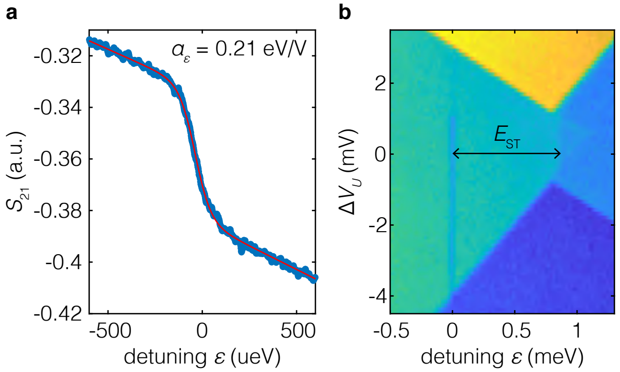

Figure 9.7: **Lever arm and excited state energy of the quantum dot. a**, Polarisation line measurement of the (1,1)-(0,2) anticrossing. We fit the thermally limited polarisation line to a model including cross-talk to the charge sensor and the effect of the charge state on the sensor sensitivity [182]. Assuming a hole temperature of 100 mK as measured previously [157], we find a lever arm of $\alpha_\epsilon = 0.21$ eV/V, in good agreement with results obtained on similar devices. **b**, We measure the excited state energy by applying a dc bias across the quantum dot ohmics, shifting the anticrossing toward the negative detuning voltage. For large enough bias, the readout window is capped off, as a result of the excited state becoming available in energy. From this we deduce an excited state splitting of $E_{ST} = 0.85$ meV.

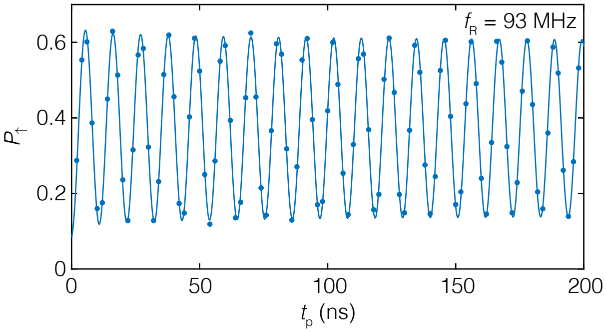

Figure 9.8: **Coherent operation of Q1.** We rotate Q1 by applying a resonant microwave pulse to gate P1 and observe fast Rabi oscillations, with a frequency of $f_R = 93$ MHz.

10

A FOUR-QUBIT GERMANIUM QUANTUM PROCESSOR

The prospect of building quantum circuits [18, 266] using advanced semiconductor manufacturing makes quantum dots an attractive platform for quantum information processing [25, 26]. Extensive studies on various materials have led to demonstrations of two-qubit logic in gallium arsenide [52], silicon [11, 58, 61, 67, 78, 267, 268], and germanium [86]. However, interconnecting larger numbers of qubits in semiconductor devices has remained an outstanding challenge. In this chapter, we demonstrate a four-qubit quantum processor based on hole spins in germanium quantum dots. Furthermore, we define the quantum dots in a two-by-two array and obtain controllable coupling in both directions. Qubit logic is implemented all-electrically and the exchange interaction can be pulsed to freely program one-qubit, two-qubit, three-qubit, and four-qubit operations, resulting in a compact and highly connected circuit. We execute a quantum logic circuit that generates a four-qubit Greenberger-Horne-Zeilinger state and we obtain coherent evolution by incorporating dynamical decoupling. These results are an important step towards quantum error correction and quantum simulation with quantum dots.

Parts of this chapter have been published in Nature **591**, 580-585 (2021) [87]

10.1. INTRODUCTION

Fault-tolerant quantum computers using quantum error correction [266] to solve relevant problems [18] will rely on the integration of millions of qubits. Solid-state implementations of physical qubits have intrinsic advantages to accomplish this formidable challenge and remarkable progress has been made using qubits based on superconducting circuits [12]. Although the development of quantum dot qubits has been at a more fundamental stage, their resemblance to the transistors that constitute the building block of virtually all our electronic hardware promises excellent scalability to realise large-scale quantum circuits [25, 26]. Fundamental concepts for quantum information, such as the coherent rotation of individual spins [49] and the coherent coupling of spins residing in neighbouring quantum dots [51], were first implemented in gallium arsenide heterostructures. The low disorder in the quantum well allowed the construction of larger arrays of quantum dots and the realisation of two-qubit logic using two singlet-triplet qubits [52]. However, spin qubits in group III-V semiconductors suffer from hyperfine interactions with nuclear spins that severely limit their quantum coherence. Group IV materials naturally contain higher concentrations of isotopes with a net-zero nuclear spin and can furthermore be isotopically enriched [28] to contain only these isotopes. In silicon electron spin qubits, quantum coherence can therefore be sustained for a long time [56, 220] and single-qubit logic can be implemented with fidelities exceeding 99.9 % [55, 57]. By exploiting the exchange interaction between two spin qubits in adjoining quantum dots or closely separated donor spins, two-qubit logic could be demonstrated [11, 58, 61, 67, 78, 267, 268]. Silicon, however, suffers from a large effective mass and valley degeneracy [146], which has hampered progress beyond two-qubit demonstrations.

Holes in germanium are emerging as a promising alternative [30] that combine favourable properties, such as a host material with a natural abundance of zero nuclear spin isotopes that can furthermore be enriched for long quantum coherence [27, 68], low effective mass and the absence of low-energy valley states [73] (allowing device design requirements to be relaxed), low charge noise [219] (providing a quiet qubit environment), and low disorder (enabling reproducible and well-controlled quantum dots) [74, 94]. In addition, strained germanium quantum wells defined on silicon substrates are compatible with semiconductor manufacturing [29]. Furthermore, hole states in general can exhibit strong spin-orbit coupling that allows for all-electric operation [69, 84, 86, 93] and that removes the need for microscopic components such as microwave striplines [11, 49, 67, 78] or nanomagnets [58, 61, 76, 77], which is particularly beneficial for the fabrication and operation of two-dimensional qubit arrays. The realisation of strained germanium quantum wells in undoped heterostructures [71] has led to remarkable progress. In two years, germanium has progressed from the formation of stable quantum dots and quantum dot arrays [74, 94, 233], to demonstrations of single-qubit logic [132], long spin lifetimes [88], and the realisation of fast two-qubit logic in germanium double quantum dots [86].

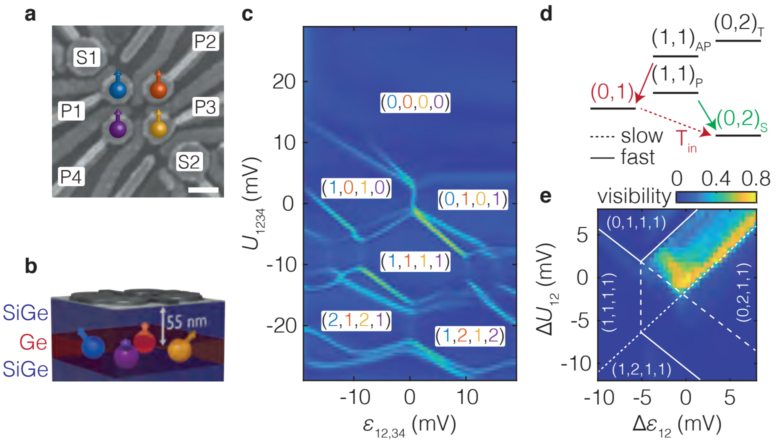

Figure 10.1: **A six-quantum-dot device in planar germanium a**, Scanning electron microscope image of the six-quantum-dot device. We define qubits underneath the four plunger gates indicated by P1-P4. The qubits can be measured using the two charge sensors S1 and S2. The scale bar corresponds to 100 nm. **b**, Schematic drawing of the Ge/SiGe heterostructure. Starting from a silicon wafer, a germanium quantum well is grown in between two $Si_{0.2}Ge_{0.8}$ layers at a depth of 55 nm from the semiconductor/dielectric interface. **c**, Four quantum dot charge stability diagram as a function of two virtual gates. At the vertical and diagonal bright lines, a hole can tunnel between two quantum dots or a quantum dot and its reservoir respectively. As a result of the virtual axes $\epsilon_{12,34}$ and U_{1234} (details in Section 10.7.3), the addition lines of the different quantum dots have different slopes, allowing for an easy distinction of the different charge occupations indicated in the white boxes as (N_{Q1},N_{Q2},N_{Q3},N_{Q4}), with N_m the number of holes in the mth quantum dot. **d**, Energy diagram illustrating the latched Pauli spin blockade readout. When pulsing from the (1,1) charge state to the (0,2) charge state, only the polarised triplet states allow the holes to move into the same quantum dot, leaving an (0,2) charge state (green). Interdot tunnelling is blocked for the two antiparallel spin states and as a result, the hole on the first quantum dot will subsequently tunnel to the reservoir leaving an (0,1) charge state (red), locking the different spin states into different charge states. **e**, Readout visibility as defined by the difference in readout between either applying no rotation and a π-rotation to Q2. The readout point is moved around the (1,1)-(0,2) anticrossing of the Q1Q2 system and a clear readout window can be observed bounded by the different (extended) reservoir transition lines indicated by the dotted lines.

10.2. A TWO-BY-TWO QUANTUM DOT ARRAY

Here, we advance beyond two-qubit logic in semiconductor quantum dots and execute a four-qubit quantum circuit using a two-dimensional array of quantum dots. We achieve this by defining the four-qubit system on the spin states of holes in gate-defined germanium quantum dots. Fig. 10.1a shows a scanning-electron-microscopy (SEM) image of the germanium quantum processor. The quantum dots are defined in a strained germanium quantum well on a silicon substrate [219] (Fig. 10.1b) using a double layer of electrostatic gates and contacted by aluminium ohmic contacts. A negative potential on plunger gates P1-P4 accumulates a hole quantum dot underneath that hosts qubits Q1-Q4, which can be coupled to neighbouring quantum dots through dedicated barrier gates. In addition, two quantum dots are placed to the side of the two-by-two array, and the total system comprises six quantum dots. Via an external tank circuit, we configure these additional two quantum dots as radio frequency (rf) charge sensors for rapid charge detection. Using the combined signal of both charge sensors [233], we measure the four quantum dot stability diagram as shown in Fig. 10.1c. Making use of two virtual gate axes $\epsilon_{12,34}$ and U_{1234}, we arrange the reservoir addition lines of the four quantum dots to have different relative slopes of approximately $-1, +1, -0.75, 0.75$ mV/mV for Q1, Q2, Q3, and Q4 respectively. Well-defined charge regions (indicated by (N_{Q1},N_{Q2},N_{Q3},N_{Q4}) in the white boxes, with N_m the number of holes in the mth quantum dot) are observed, with vertical anticrossings marking the different interdot transitions. The high level of symmetry in the plot is a sign of comparable gate lever arms and quantum dot charging energies, confirming the uniformity in this platform and simplifying the operation of quantum dot arrays.

For the qubit readout, we make use of Pauli-spin blockade to convert the spin states into a charge signal that can be detected by the sensors. In germanium, however, the spin-orbit coupling can substantially lower the spin lifetime during the readout process, in particular when the spin-orbit field is perpendicular to the external magnetic field, reducing the readout fidelity [132, 164]. Here, we overcome this effect by making use of a latched readout process [262, 269]. During the readout process, as illustrated in Fig. 10.1d, a hole can tunnel spin-selectively to the reservoir as a result of different tunnel rates of both quantum dots to the reservoir. After this process, the system is locked in this charge state for the slow reservoir tunnel time T_{in} (details in Sec. 10.7.4). The high level of control in germanium allows the tuning of T_{in} to arbitrarily long time scales by changing the potential applied to the corresponding reservoir barrier gates. We set $T_{\text{in}} = 200$ µs for Q2 and $T_{\text{in}} = 2.4$ ms for Q4 (Fig. 10.9), both much longer than the signal integration time $T_{\text{int}} = 10$ µs.

In our experiments, we configure the system such that the spin-orbit field is oriented along the direction of the external magnetic field $B_0 = 1.05$ T. This minimises relaxation, and we project all qubit measurements onto this readout direction, thus reading out qubit pairs Q1Q2 and Q3Q4. Each charge sensor can detect transitions in both qubit pairs but is most sensitive to their respective nearby quantum dots. We maximise the readout visibility as defined by the difference between the readout of a spin-up and spin-down state by scanning the readout level around the relevant anticrossing. This is illustrated for the Q1Q2 pair in Fig. 10.1e, where a clear readout window with maximum visibility can be observed bounded between the (extended) reservoir transitions of the two quantum dots.

10.3. FOUR SPIN QUBITS

Coherent rotations can be implemented by applying electric microwave signals to the plunger gates that define the qubits, exploiting the spin-orbit coupling for fast driving [69, 84]. We initialise the system in the $|{\downarrow\downarrow\downarrow\downarrow}\rangle$ state by sequentially pulsing both the Q1Q2 and Q3Q4 double quantum dot systems from their respective $(0,2)_{\text{S}}$ states adiabatically into their $(1,1)_{\text{T}_-}$ states. We then perform the qubit manipulations, after which we perform the spin readout as described above. Qubit resonances are observed at $f_{Q1} = 2.304$ GHz, $f_{Q2} = 3.529$ GHz, $f_{Q3} = 3.520$ GHz, and $f_{Q4} = 3.882$ GHz, corresponding to effective g-factors of $g_{Q1} = 0.16$, $g_{Q2} = 0.24$, $g_{Q3} = 0.24$, and $g_{Q4} = 0.26$. We note that these g-factors can be electrically modulated using nearby gates as a means to ensure individual qubit addressability [88], as can also be observed in Fig. 10.6. Fig. 10.2 shows the single-shot spin-up probability P_{up} for each of the four

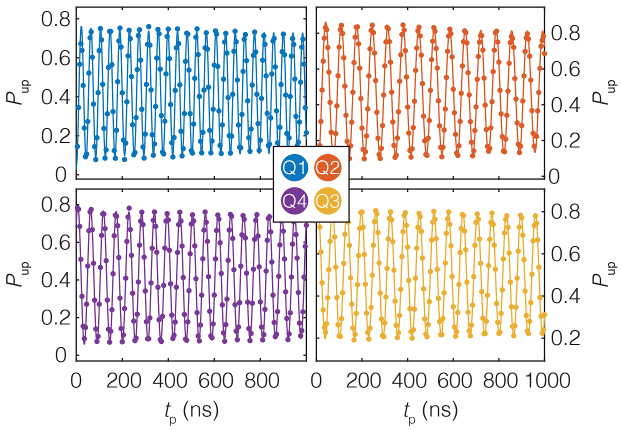

Figure 10.2: **Four germanium hole spin qubits.** Readout visibility as defined by the difference in readout between either applying no rotation and a π-rotation on Q2. The readout point is moved around the (1,1)-(0,2) anticrossing of the Q1Q2 system and a clear readout window can be observed bounded by the different (extended) reservoir transition lines indicated by the dotted lines. P_{up} indicates the single-shot spin-up probability.

qubits after applying an on-resonant microwave burst with increasing time duration t_{p}, resulting in coherent Rabi oscillations.

To quantify the quality of the single-qubit gates, we perform benchmarking of the Clifford group [249] (Fig. 10.3b) and find single-qubit gate fidelities exceeding 99 % for all qubits. The fidelity of Q3 reaches to 99.9 %, thereby comparing to benchmarks for quantum dot qubits in isotopically purified silicon [55, 57]. We find spin lifetimes between $T_1 = 1 - 16$ ms (Fig. 10.11), comparable to values reported before for holes in planar germanium [88]. Furthermore, we observe T_2^* to be between 150-400 ns for the different qubits (Fig. 10.3a), but are able to extend phase coherence up to $T_2^{\mathrm{CPMG}} = 100$ µs by performing Carr-Purcell-Meiboom-Gill (CPMG) refocusing pulses (Fig. 10.4a,b), more than two orders of magnitude larger than previously reported for hole quantum dot qubits [84, 86, 93]. This indicates the qubit phase coherence is mostly limited by low-frequency noise, which is confirmed by the predominantly $1/f^{\alpha}$ noise spectrum we observe by Ramsey and dynamical decoupling noise spectroscopy (Fig. 10.12). This noise could originate in the nuclear spin bath present in germanium, which could be mitigated by isotopic enrichment. Alternatively, it could be caused by charge noise acting on the spin state through the spin-orbit coupling, and it is predicted that the sensitivity to this type of noise could be mitigated by careful optimisation of the electric field environment [127] or moving to a multi-hole charge occupancy, screening the influence of charge impurities [270], potentially enabling even higher fidelity operations.

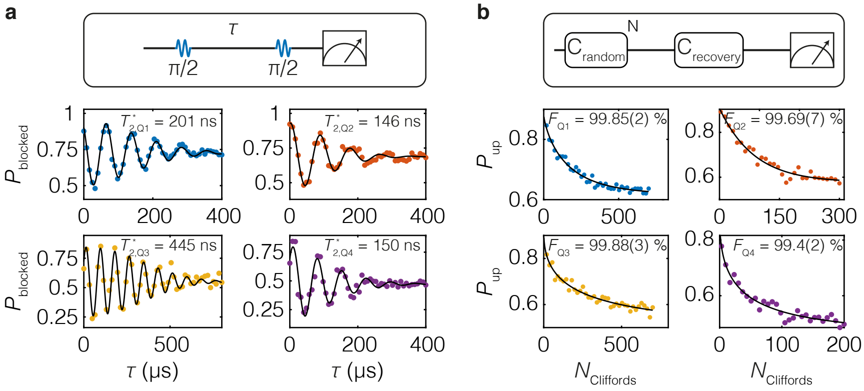

Figure 10.3: **Spin dephasing time and single-qubit randomised benchmarking.** **a**, The phase coherence time T_2^* is measured using a Ramsey sequence consisting of two X($\pi/2$)-pulses separated by a waiting time τ as illustrated in the schematic on top. By fitting the data to $P = \cos(2\pi\Delta f\tau + \phi_0)\exp(-(\tau/T_2^*)^\alpha)$, with Δf the frequency detuning, ϕ_0 a phase offset and α the power of the decay, we find spin dephasing times of $T^*_{2,\mathrm{Q1}} = 201$ ns, $T^*_{2,\mathrm{Q2}} = 146$ ns, $T^*_{2,\mathrm{Q3}} = 445$ ns, and $T^*_{2,\mathrm{Q4}} = 150$ ns for Q1-Q4 respectively. **b**, We quantify the quality of the single-qubit gates by performing randomised benchmarking of the single-qubit Clifford group [249]. The decay curve of the qubit state is measured as a function of the number of Clifford gates applied. Each data point consists of 1000 single shots for 30 different randomly selected Clifford sequences with length $N_{\mathrm{Cliffords}}$. The decay is fitted to $P_{\mathrm{up}} = a\exp(-(N_{\mathrm{Cliffords}}/m)^\alpha) + y_0$, with a the initial spin-up probability, m the decay parameter, α the decay power and y_0 an offset. $F_{\mathrm{ref}} = 1 - \frac{m}{2\cdot 1.875}$ is extracted based on the average single-qubit gate length of 1/1.875 Clifford gates.

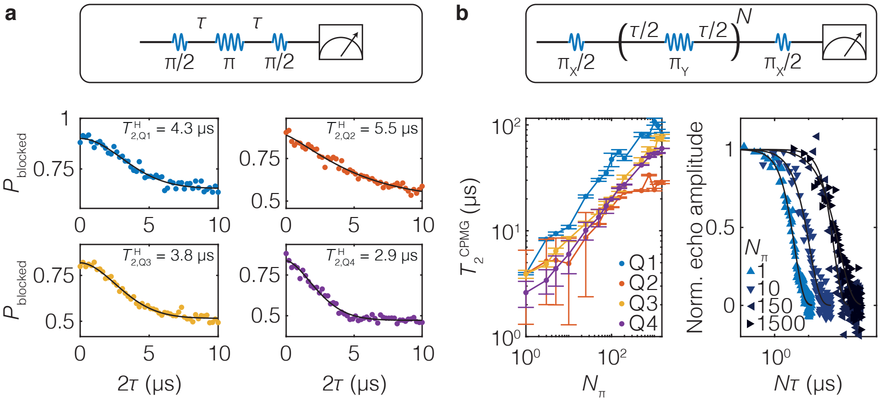

Figure 10.4: **Extended phase coherence using echo pulses a**, Using an additional X(π)-pulse, low-frequency fluctuations of the qubit resonance frequency can be echoed out, allowing to probe the Hahn-echo decay time T_2^{Hahn}. Fitting the data to $P = \exp\left(-(\tau/T_2^{\mathrm{Hahn}})^\alpha\right)$, we find Hahn echo times of $T^{\mathrm{Hahn}}_{2,\mathrm{Q1}} = 4.3\mu$s, $T^{\mathrm{Hahn}}_{2,\mathrm{Q2}} = 5.5\mu$s, $T^{\mathrm{Hahn}}_{2,\mathrm{Q3}} = 3.8\mu$s, and $T^{\mathrm{Hahn}}_{2,\mathrm{Q4}} = 2.9\mu$s. **b**, Using a CPMG sequence of repeated Y(π) pulses, we can increase the echo bandwidth and extend the phase coherence to over $T^{\mathrm{CPMG}}_{2,\mathrm{Q1}} > 100$ μs. The phase coherence can be observed to increase with the amount of refocusing pulses (left), with exemplary decay traces for Q1 plotted in the right panel.

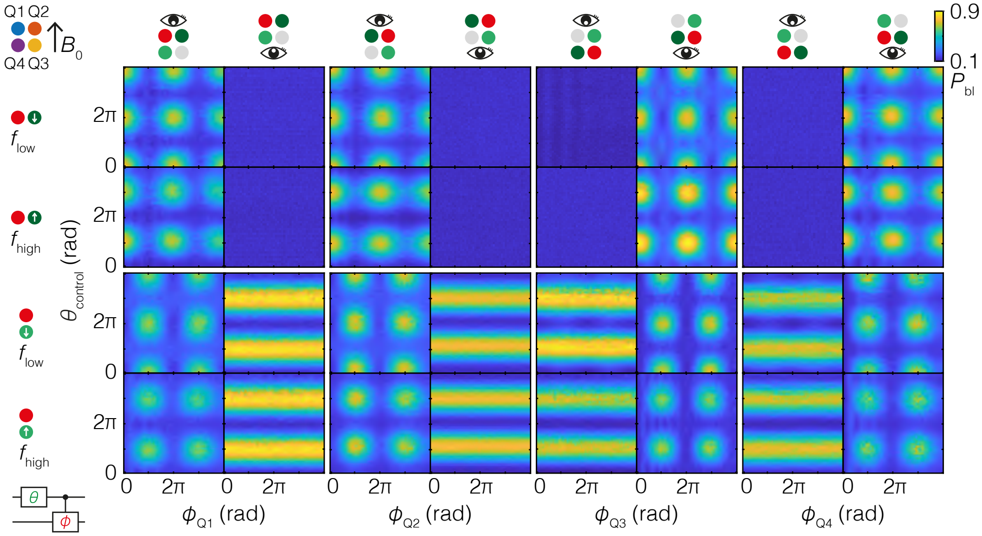

Figure 10.5: **Controlled rotations between all nearest-neighbour qubit pairs.** By selectively enabling the exchange interaction between each pair of qubits, we can implement two-qubit controlled rotations (CROTs). The pulse sequence consists of a single-qubit preparation gate with length θ on the control qubit (labelled green), followed by a controlled rotation on one of the two resonance lines of the target qubit (labelled in red). Both qubit pairs Q1Q2 and Q3Q4 are read out in single-shot mode with P_{bl} the blocked state probability, and the position of the eye on top of each column indicates the respective readout pair. Each of the four main columns corresponds to conditional rotations on a different qubit as indicated by the red dot. Rows one and two show the results for the horizontal interaction (dark green), while rows three and four show the two-qubit interaction for the vertical direction (light green) with respect to the external magnetic field, as indicated in the top left. Rows one and three correspond to driving the lower frequency f_{low} conditional resonance line, while rows two and four show driving of the other resonance line f_{high}.

10.4. ONE, TWO AND THREEFOLD CONDITIONAL ROTATIONS

Universal quantum logic can be accomplished by combining the single-qubit rotations with a two-qubit entangling gate. We implement this using a conditional rotation (CROT) gate [11, 58, 61, 67], where the resonance frequency of the target qubit depends on the state of the control qubit, mediated by the exchange interaction J between the two quantum dots. The exchange interaction between the quantum dots is controlled using a virtual barrier gate (details in Sec. 10.7.3), coupling the two quantum dots while keeping the detuning and on-site energy of the quantum dots constant and close to the charge-symmetry point. We demonstrate CROT gates between all four pairs of quantum dots in Fig. 10.5, proving that spin qubits can be coupled in two dimensions. A sequence of qubit pulses is applied, as indicated in the diagram, consisting of a single-qubit control pulse (green) and a target qubit two-qubit pulse (red). We vary the length of both the control pulse $\theta_{control}$ and the length of the target qubit pulse $\phi_{Q1\text{-}Q4}$, with $t_p(\phi = \pi) = 50-110$ ns (details in Table 10.1). The conditional rotations are performed on all four target qubits (main four columns) for both the horizontally interacting qubits (rows 1 and 2), as well as the vertically interacting qubits (rows 3 and 4), by driving the $|{\downarrow\downarrow}\rangle$-$|{\uparrow\downarrow}\rangle$ transitions with f_{low} (rows 1 and 3), as well as the inverse $|{\downarrow\uparrow}\rangle$-$|{\uparrow\uparrow}\rangle$ transitions with f_{high} (rows 2 and 4), with $\left|\mathrm{Q}_{\mathrm{target}}\mathrm{Q}_{\mathrm{control}}\right\rangle$. We then perform a measurement on both readout pairs by sequentially pulsing the Q1Q2 (left sub-columns), and the Q3Q4 qubit pairs (right sub-columns) to their respective readout points. Because the target qubit resonance frequency depends on the control qubit state, the conditional rotation is characterised by the fading in and out of the target qubit rotations as a function of the control qubit pulse length. The observed pattern is therefore shifted by a π rotation on the control qubit, for driving the two separate transitions. When the control qubit is in a different readout pair as the target qubit (rows 3 and 4), we can independently observe the single-qubit control and two-qubit target qubit rotations in the two readout systems. By setting the pulse length equal to $\phi_{\mathrm{Q}} = \pi$, a fast controlled-X (CX) gate can be obtained within approximately $t_p = 100$ ns between all the four qubit pairs.

The low effective mass and high uniformity in the material allow full control over the interdot coupling by dedicated tunnel barrier gates. To demonstrate this, we measure the qubit resonance frequency as a function of the eight possible permutations of the different basis states of the other three qubits, as illustrated in Fig. 10.6a,b. Without any exchange present, the resonance frequency of the target qubit should be independent of the preparation of the other three qubits, as schematically depicted in Fig. 10.6c. When the exchange interaction with one of the neighbouring quantum dots is enabled by pulsing the virtual barrier gate, the resonance line splits in two (Fig. 10.6d,e), allowing for the operation of the CROT gate. When both barriers to the nearest-neighbours are pulsed open at the same time, we observe the expected fourfold splitting of the resonance line (Fig. 10.6f-i). This allows the performance of a resonant *i*-Toffoli three-qubit gate (Fig. 10.6k and Fig. 10.13), which has theoretically been proposed as an efficient manner to create the Toffoli, Deutsch, and Fredkin gates [163]. We observe a difference in the efficiency at which the different conditional rotations can be driven, as can also be seen from the width of the resonance peaks in Fig. 10.6f-i. This is expected to happen when the exchange energy is comparable to the difference in Zeeman splitting and is caused by the mixing of the basis states due to the exchange interaction between the holes [165] (details in Sec. 10.7.5). Finally, we open three of the four virtual barriers and observe the resonance line splitting in eight, being different for all eight permutations of the control-qubit preparation states (Fig. 10.6j). This enables us to execute a resonant four-qubit gate and in Fig. 10.6l we show the coherent operation of a three-fold conditional rotation (see Fig. 10.13 for the coherent operation of the other resonance lines). The good control over the interdot coupling thus enables a demonstration of the localised nature of the exchange interaction [25], coupling the different spins with electric gate pulses.

10.5. CONDITIONAL PHASE GATES

While the demonstration of these conditional rotations can be beneficial for the simulation of larger coupled spin systems, the ability to dynamically control the exchange interaction allows for faster two-qubit operations. We efficiently implement controlled-phase (CPHASE) gates [61, 67, 78] between the different qubit pairs by adiabatically pulsing the exchange interaction using the respective virtual barrier gate. Increasing the exchange interaction, the antiparallel spin states will shift in energy with respect

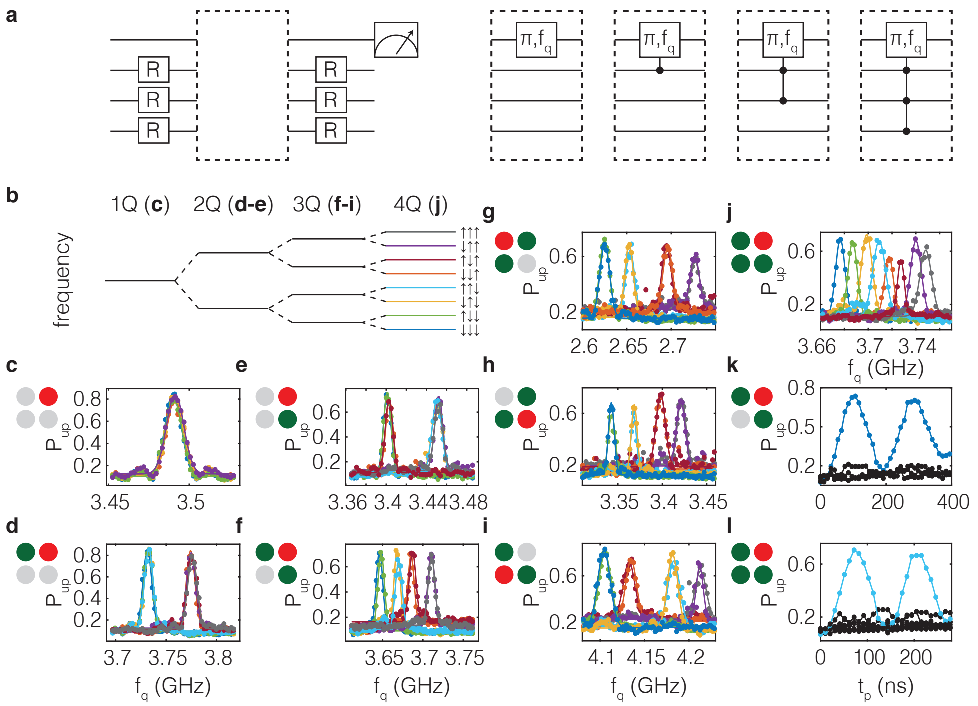

Figure 10.6: **Resonant one, two, three, and four-qubit gates.** **a**, Circuit diagram of the experiment performed in panels **c-l**. All eight permutations of the three control qubit eigenstates are prepared, with R being either no pulse or a π-pulse on the respective qubit. Next, the resonance frequency of the target qubit is probed using a π-rotation with varying frequency f_q. Finally, the prepared qubits are projected back and the target qubit state is measured. By changing the different interdot couplings J, we can switch between resonant single, two, three, and four-qubit gates as indicated in the dashed boxes. **b**, Turning on the exchange interaction between the different qubit pairs splits the resonance frequency in two, four, and eight for 1, 2 and 3 enabled pairs respectively. The colours of the line segments correspond to the colours in panels **c-l**. **c**, By turning all exchange interactions off, the qubit resonance frequency of Q2 is independent of the prepared state of the other three qubits, resulting in an effective single-qubit rotation. **d-e**, By turning on a single exchange interaction J_{12} (**d**) or J_{23} (**e**), the resonance line splits in two. **f-i**, Turning on both exchange interactions to the neighbouring quantum dots results in the resonance line splitting in four, for Q2 (**f**), Q1 (**g**), Q3 (**h**), Q4 (**i**) respectively. **j**, Turning on the exchange interactions between three pairs of quantum dots J_{12}, J_{23}, J_{41} splits the resonance line in eight. **k-l**, Resonant driving of the three-qubit gate (**k**) and the four-qubit gate (**l**) with Q2 being the target qubit, shows Rabi driving as a function of pulse length t_p, demonstrating the coherent evolution of the operation.

to the parallel spin states, giving rise to a conditional phase accumulation. We control the length and size of the voltage pulse (Fig. 10.14) to acquire a controlled-Z (CZ) gate, in which the antiparallel spin states accumulate a phase of exactly $\theta = \pi$ with respect to the parallel spin states. We demonstrate this in Fig. 10.7a,b, where we employ a Ramsey sequence to measure the conditional phase. After the exchange pulse U_{CZ} we apply a software Z gate to both the target and control qubits to compensate for individual single-qubit phases. The virtual barrier pulses enable fast CZ gates between all neighbouring qubit pairs, all executed well within 10 ns (details in Table 10.2).

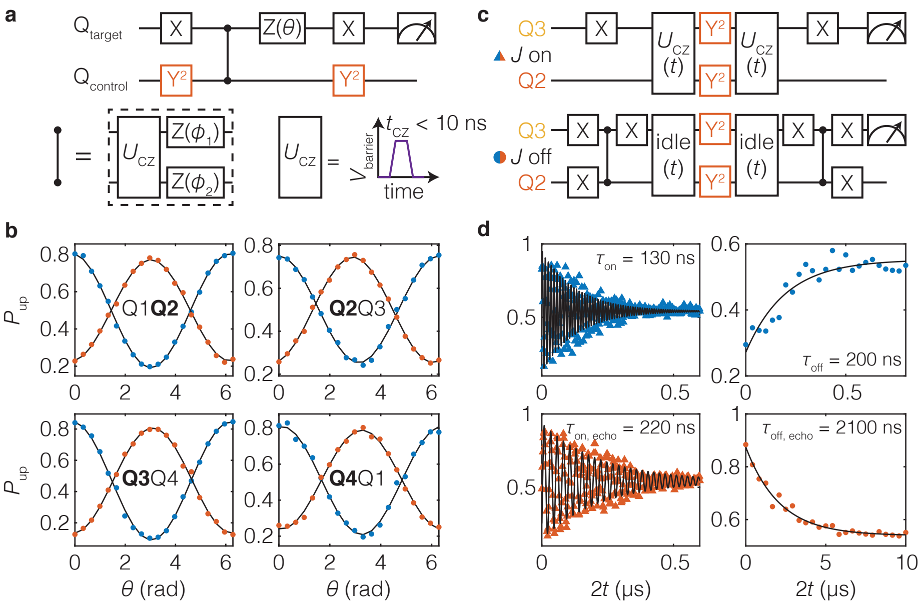

Figure 10.7: **Controlled phase gate and dynamical decoupling.** **a**, Circuit diagram of the experiment performed in panel **b**. The controlled phase gate is probed by performing a Ramsey sequence on the target qubit for both basis states of the control qubit. The phase of the second X($\pi/2$) gate (indicated by X) is swept by performing an update of the microwave phase through quadrature modulation. Additionally, a phase update is performed on both the target and control qubit to compensate for any single-qubit phases picked up as a result of the gate pulsing to achieve a controlled-Z (CZ) gate. **b**, The spin-up probability P_{up} of the target qubit (in bold) as a function of the phase θ of the second X gate, for the control qubit initialised in the $|{\downarrow}\rangle$ (blue) and $|{\uparrow}\rangle$ (red) state. By applying an exchange pulse and single-qubit phase updates, we achieve a CZ gate at $\theta = 0$ rad. **c**, Circuit diagrams of the experiment performed in panel **d**. The phase coherence throughout the two-qubit experiment is probed using a Ramsey sequence, both for the case with J on (top) and off (bottom) and both with (orange) and without (blue) applying an echo pulse. **d**, Spin-up probability as a function of the experiment length, for the situation with the exchange interaction on (left, triangles) and off (right, circles). From the decay data we extract characteristic decay times τ of $\tau_{\mathrm{on}} = 130$ ns, $\tau_{\mathrm{on,\,echo}} = 220$ ns, $\tau_{\mathrm{off}} = 200$ ns, and $\tau_{\mathrm{off,\,echo}} = 2100$ ns (details in Sec. 10.7.6).

To prepare our system for quantum algorithms, we implement decoupling pulses into the multi-qubit sequences to extend phase coherence, as demonstrated in Fig. 10.7c,d. To probe the effect of a decoupling pulse when the exchange interaction is on (Fig. 10.7d, left, triangles), we perform a CPHASE gate between qubits Q2 and Q3 and compare the decay of the resulting exchange oscillations as a function of the operation time for the situations with (orange) and without (blue) a Y^2 echo pulse. We observe an extended duration for the conditional phase rotations of $\tau = 220$ ns when applying a decoupling pulse, compared to $\tau = 130$ ns for a standard CPHASE gate. A more relevant situation, however, is the coherence of the two-qubit entangled state. We probe this by entangling Q2 and Q3 by forming the $|\Psi^{+}\rangle$ Bell state and letting the system evolve for time $2t$ (Fig. 10.7d, right, circles). Next, we disentangle the system again and measure the spin-up probability of Q3 as a function of the evolution time. Without the decoupling pulse, we observe the loss of the two-qubit coherence after a characteristic time $\tau = 200$ ns. However, by applying the additional Y(π) pulse on both Q2 and Q3, we can significantly extend this timescale beyond 2 µs, enough to perform a series of single and multi-qubit gates, owing to our short operation times.

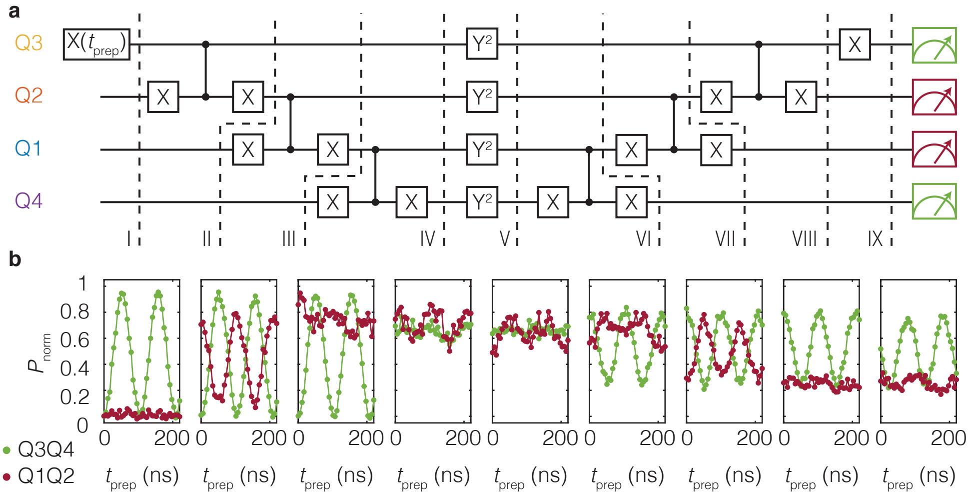

Figure 10.8: **Coherent generation of a four-qubit Greenberger-Horne-Zeilinger (GHZ) state. a-b**, A four-qubit GHZ state is created by applying three sequential two-qubit gates, each consisting of an X-CZ-X gate circuit. Next, a Y^2 decoupling pulse is applied, after which we disentangle the GHZ state again (circuit diagram in **a**). Pulses pictured in the same column are applied simultaneously. The initial state of Q3 is varied by applying a preparation rotation of length t_{prep}. For different stages throughout the algorithm (dashed lines), we measure the non-blocked state probability as a function of t_{prep} for both the Q1Q2 and Q3Q4 readout system, normalised to their respective readout visibility. At the end of the algorithm, the qubit states reflect the initial single-qubit rotation, and the clear oscillations confirm the coherent evolution of the algorithm from isolated qubit states to a four-qubit GHZ state. (**b**).

10.6. FOUR-QUBIT GREENBERGER-HORNE-ZEILINGER STATE

We show this by coherently generating and disentangling a four-qubit Greenberger-Horne-Zeilinger (GHZ) state (Fig. 10.8). Making use of the fast two-qubit CZ gates, as well as a decoupling pulse on all qubits, we can maintain phase coherence throughout the experiment. We perform parity readout on both the Q1Q2 (red) and Q3Q4 (green) qubit system at different stages of the algorithm (I-IX). Both qubit systems are sequentially readout after each experiment and the observed blocked state fraction is normalised to the readout visibility. We prepare a varying initial state by applying a microwave pulse of length t to Q3, as visible at point I. After applying CZ gates between all four qubits, the system resides in an entangled GHZ type state at point IV/V, for a $\pi/2$ preparation pulse on Q3. The effective spin state oscillates between the antiparallel $|1010\rangle$ and $|0101\rangle$ states as a function of t_{prep}, resulting in a high readout signal for all t. The small oscillation that can still be observed for the Q1Q2 system, is caused by a small difference in readout visibility for the two distinct antiparallel spin states. Next, we deploy a Y^2 decoupling pulse to echo out all single-qubit phase fluctuations during the experiment (Fig. 10.15). After disentangling the system again, we project the Q3 qubit state by applying a final $X(\pi/2)$ gate and indeed recover the initial Rabi rotation as a demonstration of the coherent evolution of a multi-spin entangled state.

The demonstration of a two-by-two array of four qubits shows that quantum dot qubits can be coupled in two-dimensions and multi-qubit logic can be executed. The hole states used are subject to strong spin-orbit coupling, enabling all-electrical driving of the spin state, beneficial for scaling up to even larger systems. In future experiments, the performance of the qubit gates can be further optimised, by making use of tailored pulses and quantifying their performance using benchmarking sequences. The ability to freely couple one, two, three and four spins using electric gate pulses has great prospects both for performing high-fidelity quantum gates and studying exotic spin systems using analogue quantum simulations. Furthermore, we envision that the low-disorder in planar germanium and the potential to leverage advanced semiconductor manufacturing will be beneficial for the realisation of scalable qubit tiles [59, 224, 271] for fault-tolerant quantum processors.

10.7. EXPERIMENTAL METHODS

10.7.1. DEVICE FABRICATION

The device was fabricated on a Ge/SiGe heterostructure with a 55-nm-deep buried quantum well, grown in an industrial reactor by reduced vapour deposition, as detailed in Ref. [71, 219]. Ge quantum wells are fully compatible with a 300 mm semiconductor foundry line [29, 30]. Starting from a Si wafer, the heterostructure comprises a 1.6 μm relaxed Ge layer; a 1 μm step graded $Si_{1-x}Ge_x$ layer with a final Ge composition of $x = 0.8$; a 500 nm relaxed $Si_{0.2}Ge_{0.8}$ buffer layer; the 16-nm-thick compressively strained Ge quantum well; a 55 nm $Si_{0.2}Ge_{0.8}$ spacer layer and finally a sacrificial Si cap layer (< 2 nm). We define ohmic contacts by electron beam lithography and subsequent etching of the oxidised Si cap layer and deposition of a 30 nm Al contact layer [74]. Electrostatic gates are defined in two layers (20 nm and 40 nm Ti/Pd respectively), separated from both the substrate and each other by 7 nm of Al_2O_3, grown by atomic layer deposition.

10.7.2. EXPERIMENTAL SETUP

Details on the experimental setup are described in Chapter 4. Qubits Q2 and Q4 are driven using the vector source connected to P3, Q1 is driven from gate P4, and Q3 is driven from gate P2. In Fig. 10.5, when driving the $|\downarrow\downarrow\rangle$-$|\uparrow\downarrow\rangle$ transition of the qubit pairs used for readout (row 1), we apply an additional single-qubit π-pulse to the preparation qubit to preserve symmetry with the other measurements, as the control qubit also serves as the readout ancillary qubit. The data in Fig. 10.8 are normalised with respect to the readout visibility as obtained from a Rabi measurement. We find $P_{\text{Q1Q2, not blocked}} = 0.15$, $P_{\text{Q1Q2, blocked}} = 0.78$, $P_{\text{Q3Q4, not blocked}} = 0.10$, and $P_{\text{Q3Q4, blocked}} = 0.93$.

10.7.3. VIRTUAL GATE MATRICES

In order to map out the transition lines of all four quantum dots in a single measurement, we define the following virtual gates [246] as linear combination of the physical gates P_1-P_4, as well as the sensor plunger gates P_{S1} and P_{S2}. We write:

$$\begin{pmatrix} P_1 \\ P_2 \\ P_3 \\ P_4 \\ P_{S1} \\ P_{S2} \end{pmatrix} = \begin{pmatrix} 1 & 1 \\ -1 & 1 \\ 0.75 & 1 \\ -0.75 & 1 \\ -0.1 & -0.4 \\ -0.05 & -0.51 \end{pmatrix} \begin{pmatrix} \Delta\epsilon_{12,34} \\ \Delta U_{12,34} \end{pmatrix} \tag{10.1}$$

with $\Delta\epsilon_{12,34}$ and $\Delta U_{12,34}$ the virtual gates used in Fig. 10.1c.

In addition, we define a virtual gate system to allow independent control of the different interdot couplings and quantum dot detuning and on-site energy and write:

$$\begin{pmatrix} P_1 \\ P_2 \\ P_3 \\ P_4 \\ B_{12} \\ B_{34} \\ B_{23} \\ B_{41} \\ P_{S1} \\ P_{S2} \end{pmatrix} = \begin{pmatrix} 1.26 & 0.74 & 0.31 & -0.17 & -0.55 & 0 & 0 & -0.49 \\ -1.39 & 0.61 & -0.36 & -0.36 & -1.03 & 0 & -0.6 & 0 \\ 0.28 & -0.28 & 1.39 & 0.61 & 0 & -0.47 & -0.6 & 0 \\ -0.3 & -0.3 & -1.39 & 0.61 & 0 & -0.91 & 0 & -0.92 \\ 0 & 0 & 0 & 0 & 1 & 0 & 0 & 0 \\ 0 & 0 & 0 & 0 & 0 & 1 & 0 & 0 \\ 0 & 0 & 0 & 0 & 0 & 0 & 1 & 0 \\ 0 & 0 & 0 & 0 & 0 & 0 & 0 & 1.0 \\ -0.09 & -0.15 & 0.01 & -0.03 & 0 & 0 & 0 & 0 \\ 0 & 0 & -0.09 & -0.15 & 0 & 0 & 0 & 0 \end{pmatrix} \begin{pmatrix} \epsilon_{12} \\ U_{12} \\ \epsilon_{34} \\ U_{34} \\ vB_{12} \\ vB_{34} \\ vB_{23} \\ vB_{41} \end{pmatrix} \tag{10.2}$$

with ϵ_{mn} the detuning voltage and U_{mn} the voltage controlling the on-site energy of quantum dots *m* and *n*, vB_{mn} the virtual barrier gate controlling the coupling between quantum dots *m* and *n*, and P_n, B_{mn} and P_{S1-2} the various physical gates.

10.7.4. LATCHED READOUT MECHANISM

To reduce readout infidelity as a result of spin relaxation, we make use of charge latching through the reservoir [262, 269]. We achieve this effect by pulsing into the area in the (0,2) charge region bounded by the extended (1,1)-(0,1) (fast) and the extended (1,1)-(1,2) (slow) transitions (dotted lines in Fig. 10.1e). When the interdot tunnelling into the (0,2) charge state is blocked, the hole in the first quantum dot will quickly tunnel into the reservoir. This locks the spin state in the metastable (0,1) charge state, with the decay to the (0,2) ground state governed by the slow tunnel rate T_{in} between the second quantum dot and the reservoir.

We operate in a parity readout mode where we observe both antiparallel spin states to be blocked (Fig. 10.10a,b), opposite to conventional parity Pauli spin blockade readout [272]. This may be explained by the strong spin-orbit coupling mixing the parallel (1,1) states with the (0,2) state and causing strong relaxation of the upper parallel spin state. We note that both singlet-triplet readout for single state discrimination and parity readout are compatible with the execution of quantum algorithms [272]. However, by both increasing the interdot coupling and elongating the ramp between the manipulation and readout point, we can transition into a state selective readout where only the $|\downarrow\uparrow\rangle$ state results in spin blockade (Fig. 10.10c,d), with a slightly reduced readout visibility. Optimal parity readout is obtained for a ramp time of $t_{\text{ramp}} \approx 20$ ns, while single state readout is optimal at $t_{\text{ramp}} \approx 800$ ns.

10.7.5. SHIFT IN RABI FREQUENCY DUE TO EXCHANGE

When exchange interaction is present in the quantum dot system, the energy levels of the qubit are modified and the qubit basis states hybridise. Conditional driving of the spin states is a direct consequence of the shift of the energy levels, which allows for controlled multi-qubit gates as previously employed to drive two-qubit gates [58, 61, 78, 167]. The hybridisation of the qubit states on the other hand gives rise to conditional Rabi frequencies that also depend on the strength of the exchange interaction [167]. Furthermore, the exchange interaction can become anisotropic in the presence of spin-orbit coupling [165]. When only considering the exchange interaction between neighbouring quantum dots, a general Hamiltonian can be written for the four quantum dots in the (1,1,1,1) charge regime as:

$$H = \sum_{\langle i,j \rangle} S_i \cdot \overline{\mathcal{J}}_{ij} S_i + \sum_{i=1}^{4} \left(\boldsymbol{\mathcal{B}} + \boldsymbol{\mathcal{B}}_{\mathrm{ac}} \cos(2\pi f t + \phi) \right) \cdot S_i, \tag{10.3}$$

where the first sum runs along every neighbouring quantum dot pair $\langle i, j \rangle$ with the corresponding tensorial exchange interaction $\overline{\mathcal{J}}_{ij}$. We note that the term $\boldsymbol{\mathcal{B}}$ consists of both the Zeeman effect due to the external magnetic field, and the contribution due to the spin-orbit interaction. We also explicitly separate the static Zeeman interaction from the field induced by the electric driving.

We take $\mathcal{D}$ to be the unitary matrix which diagonalises Hamiltonian (10.3) for $\boldsymbol{\mathcal{B}}_{ac} = 0$. Now, the effective Rabi amplitude between the eigenstates of the undriven Hamiltonian $|\xi\rangle$ and $|\zeta\rangle$ in the adiabatic limit of exchange is given by:

$$\Omega_{|\xi\rangle \to |\zeta\rangle} = \frac{1}{4} \langle \xi | \, \mathcal{D}^{\dagger} \boldsymbol{\mathcal{B}}_{\mathrm{ac}} \mathcal{D} \, | \zeta \rangle \,, \tag{10.4}$$

where the prefactor 1/4 is coming from the spin and the rotating wave approximation. Therefore, the Rabi amplitude depends on the exact form of the exchange interaction, as well as which transition is driven.

10.7.6. FITTING OF THE TWO-QUBIT DECAY DATA

In order to extract the decay timescale in Fig. 10.7d, we fit the exchange interaction data to the model function $P = A\cos(2\pi(f_0 + t\delta)t + \phi_0)\exp(-t/\tau) + y_0$, with amplitude A, frequency f_0, phase offset ϕ_0, and offset y_0. We note that we allow for a small linear shift of the precession frequency δ, typically of size $\delta = 10$ MHz/μs, as a result of pulse imperfections in these relatively large and extended exchange pulses. We observe a small creep towards the final pulse amplitude to be present, most likely caused by the skin effect in the coaxial lines, explaining the small observed frequency shift throughout the experiment. The data for the situation with no exchange present is fitted to the exponential decay $P = \exp(-t/\tau) + y_0$, from which we deduce the decay timescale τ.

10.7.7. SPECIFICATION OF THE CROT AND CZ GATE TIMES

The different two-qubit gate times are listed below both for the CROT (Table 10.1) and the CZ (Table 10.2) gates.

target	transition	control	$t_{\pi,\mathrm{control}}$ (ns)	$t_{\pi,\mathrm{target}}$ (ns)
1	$\lvert\downarrow\downarrow\rangle$-$\lvert\downarrow\uparrow\rangle$	2	67	85
1	$\lvert\downarrow\uparrow\rangle$-$\lvert\uparrow\uparrow\rangle$	2	67	95
1	$\lvert\downarrow\downarrow\rangle$-$\lvert\downarrow\uparrow\rangle$	4	61	104
1	$\lvert\downarrow\uparrow\rangle$-$\lvert\uparrow\uparrow\rangle$	4	61	108
2	$\lvert\downarrow\downarrow\rangle$-$\lvert\downarrow\uparrow\rangle$	1	45	105
2	$\lvert\downarrow\uparrow\rangle$-$\lvert\uparrow\uparrow\rangle$	1	41	105
2	$\lvert\downarrow\downarrow\rangle$-$\lvert\downarrow\uparrow\rangle$	3	38	113
2	$\lvert\downarrow\uparrow\rangle$-$\lvert\uparrow\uparrow\rangle$	3	38	100
3	$\lvert\downarrow\downarrow\rangle$-$\lvert\downarrow\uparrow\rangle$	2	65	53
3	$\lvert\downarrow\uparrow\rangle$-$\lvert\uparrow\uparrow\rangle$	2	65	83
3	$\lvert\downarrow\downarrow\rangle$-$\lvert\downarrow\uparrow\rangle$	4	49	83
3	$\lvert\downarrow\uparrow\rangle$-$\lvert\uparrow\uparrow\rangle$	4	45	68
4	$\lvert\downarrow\downarrow\rangle$-$\lvert\downarrow\uparrow\rangle$	1	45	105
4	$\lvert\downarrow\uparrow\rangle$-$\lvert\uparrow\uparrow\rangle$	1	45	120
4	$\lvert\downarrow\downarrow\rangle$-$\lvert\downarrow\uparrow\rangle$	2	38	68
4	$\lvert\downarrow\uparrow\rangle$-$\lvert\uparrow\uparrow\rangle$	2	38	74

Table 10.1: CROT gate properties used in the experiment shown in Fig. 10.5.

two-qubit system	t_{ramp} (ns)	t_{gate} (ns)
Q1Q2	3	6
Q2Q3	10	4
Q3Q4	10	5
Q4Q1	3	6

Table 10.2: CZ gate properties, as used in this work.

10.7.8. SUPPLEMENTARY FIGURES

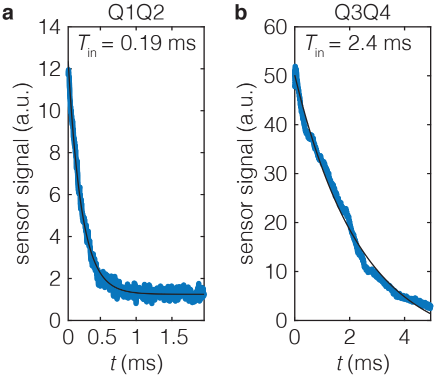

Figure 10.9: **Decay of the readout signal at the readout point a,b**, We measure the difference in charge sensor signal between the blocked and non-blocked states as a function of the measurement time at the readout point. An exponential decay can be observed related to the tunnel time T_{in} of Q2 (Q4) to the reservoir for the Q1Q2 (**a**) and Q3Q4 (**b**) readout system respectively.

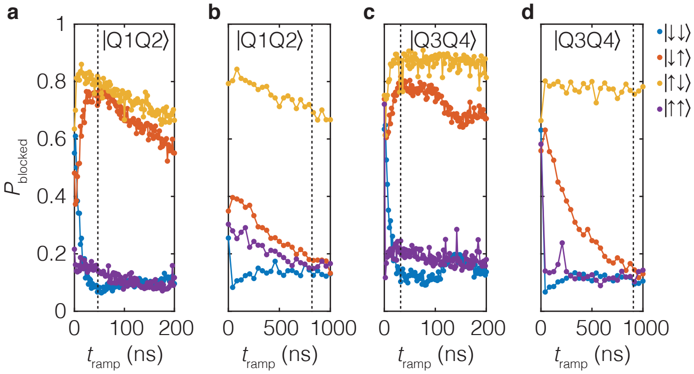

Figure 10.10: **Readout visibility of the different two-qubit states. a-d**, We vary the ramp time between the manipulation phase and the readout phase and measure the blocked state probability of the four different two qubit basis states by applying preparation π pulses to the relevant qubits, both for the Q1Q2 readout system (**a**,**b**) and the Q3Q4 readout system (**c**,**d**). By increasing the interdot coupling during the readout and elongating the ramp between the manipulation and readout point, we can switch between a parity readout (**a**,**c**) and a single state readout (**b**,**d**). The dashed line corresponds to the optimised readout ramp time used for the measurements in this manuscript.

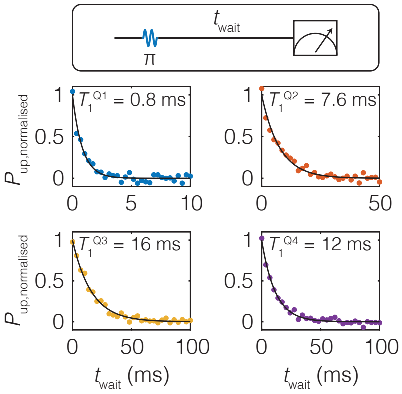

Figure 10.11: **Spin lifetimes of the four qubits.** The spin relaxation time T_1 is measured at the manipulation point by applying a π_X-pulse separated by a waiting time t_{wait} from the readout phase, as illustrated in the schematic on top. By fitting the normalised spin-up fraction to $P = \exp(-t_{\text{wait}}/T_1)$, we find spin relaxation times of $T_{1,Q1} = 0.8$ ms, $T_{1,Q2} = 7.6$ ms, $T_{1,Q3} = 16$ ms, and $T_{1,Q4} = 12$ ms for Q1-Q4 respectively.

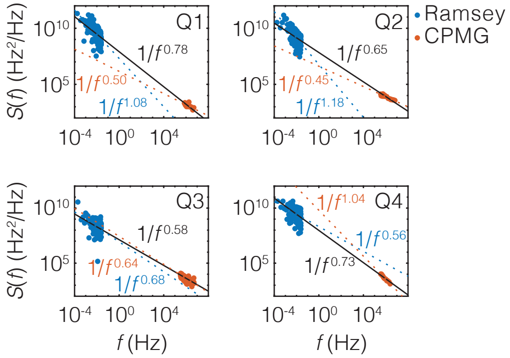

Figure 10.12: **Noise spectroscopy using Ramsey and CPMG measurements.** We measure the effective noise spectrum acting on the qubit, both tracing the resonance frequency using repeated Ramsey measurements [55] (in blue), as well as by using the filter function of a dynamical decoupling measurement [220, 273] (in red). Dashed blue and red lines are fits to the Ramsey and CPMG data respectively. The black line is a fit to the combined data set, where the weight of both sets is normalised to the number of data points. The effective noise can be observed to increase towards low frequencies, consistent with the upwards trend of T_2^{CPMG} observed in Fig. S1c. The effective charge noise measured in this heterostructure is $S_{\text{cn}}(f) = 6\ \mu\text{V}/\sqrt{\text{Hz}}$ at 1 Hz [219]. Combining this with a typical resonance frequency slope of $df/dV = 5$ MHz/mV [88], results in an effective resonance frequency noise power of $S(f) = 9 \cdot 10^8\ \text{Hz}^2/\text{Hz}$, comparable to what is observed experimentally, suggesting coherence is limited by charge noise in our system.

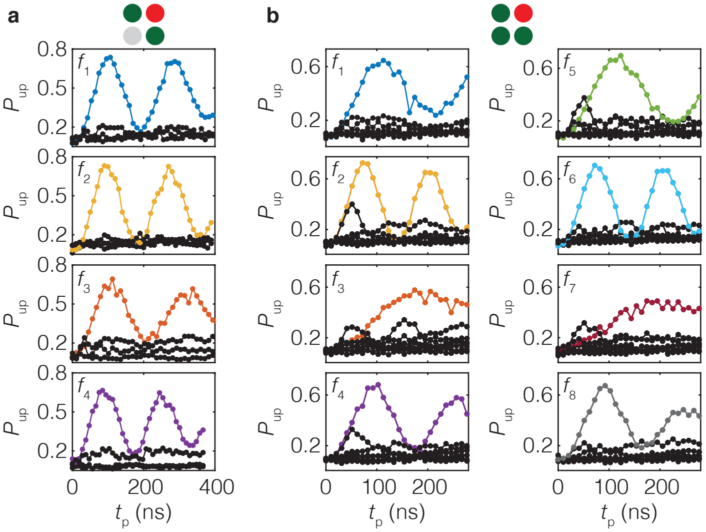

Figure 10.13: **Driving of all resonance lines of the coupled three and four qubit system. a**, Both the coupling between Q2 and Q1 as well as Q2 and Q3 are enabled, using the respective virtual barrier gates. This splits the resonance line in four, as shown in Fig. 10.6. Driving each of the separate lines results in the conditional rotation of Q2 depending on the states of Q1 and Q3. We measure the spin up probability after driving each of the four resonance lines for time t_p, for all four permutations of the Q1 and Q3 basis states as an initial state, following the colour scheme of Fig. 10.7. The driving power is adjusted for each of the transitions to synchronise the π-rotation times, with $a_{f1} = 330$ mV, $a_{f2} = 500$ mV, $a_{f3} = 280$ mV, and $a_{f4} = 400$ mV, for $f1 - 4$ from top to bottom. **b**, Similarly, by additionally opening up the coupling between Q3 and Q4 as well, the resonance line splits in four and we can drive all separate lines individually. The eight lines are driven using the same microwave power in this figure and a strong difference in rotation frequencies can be observed for the different transitions. This also results in a small off-resonant driving effect for some of the lines.

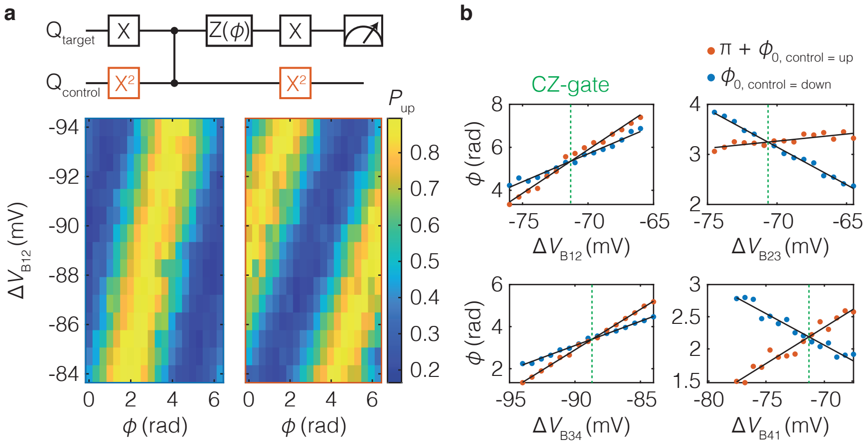

Figure 10.14: **Tuning of the CZ-gates.** **a,b**, The CZ-gates between all four qubit pairs are tuned using a Ramsey sequence (analogous to Fig. 10.7), where the spin-up probability is measured as a function of the phase ϕ of the final $\pi/2$ pulse as well as the depth of the exchange pulse V_{Bmn}, with m and n the relevant qubits (**a**). We choose to tune the height of the voltage pulse rather than its length, due to the limited temporal resolution of the exchange pulses (1 ns). The acquired phase ϕ_0 is obtained by fitting each line to $P = A\cos(\phi + \phi_0) + y_0$, with A the visibility and y_0 an offset. A CZ-gate is achieved when the difference in the acquired phase is exactly $\Delta\phi = \pi$, for the situation where the control qubit is $|\downarrow\rangle$ (blue) compared to $|\uparrow\rangle$ (orange). The barrier gate voltage at which this occurs is obtained from the intersection of two locally linear fits to the extracted acquired phase (**b**).

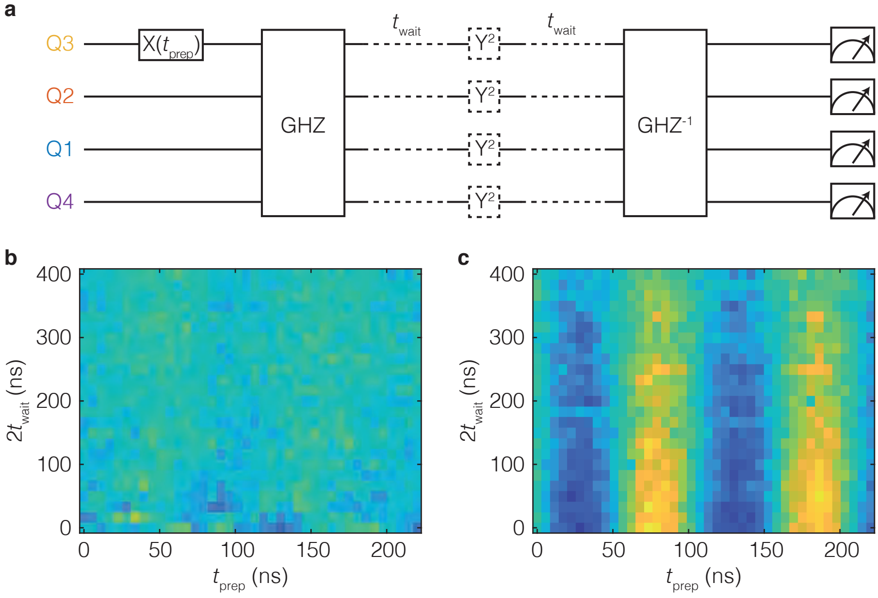

Figure 10.15: **Time evolution of the four-qubit GHZ state.** **a**, Circuit diagram of the experiments performed in panels **b,c**. We first apply a preparation pulse to Q3 and then generate a four qubit GHZ-state analogous to Fig. 10.8. Next, we let the entangled system evolve for time t_{wait}, then apply an optional Y^2 decoupling pulse and finally disentangle the GHZ-state again. **b,c**, We vary both the waiting time and preparation time t_{prep} and plot the spin-up fraction of Q3 in the case without (**b**) and with (**c**) decoupling pulse. Without any echo pulse, the system has fully decohered at the end of the algorithm. However, by applying the decoupling pulse, the coherence of the entangled system can be maintained for a prolonged time scale, with a characteristic decay time of $\tau = 390$ ns.

11

SUPERCONDUCTOR-SEMICONDUCTOR HYBRIDS

As discussed in Chapter 7, the ohmic leads contacting the quantum dots can be formed by a superconducting metal, enabling the integration of hybrid semiconductor-superconductor technology. In this chapter, we fabricate Josephson field-effect-transistors in germanium quantum wells contacted by superconducting aluminium and demonstrate supercurrents carried by holes that extend over junction lengths of several micrometres. In superconducting quantum point contacts, we observe discretisation of supercurrent, as well as Fabry-Perot resonances, demonstrating ballistic transport. The magnetic field dependence of the supercurrent follows a clear Fraunhofer-like pattern and Shapiro steps appear upon microwave irradiation. Multiple Andreev reflections give rise to conductance enhancement and evidence a transparent interface, confirmed by analysing the excess current. These demonstrations of ballistic superconducting transport are promising for hybrid quantum technology in germanium.

Parts of this chapter have been published in Physical Review B **99**, 075435 (2019) [177]

11.1. INTRODUCTION

Quantum information processing in the solid-state is being pursued using superconducting and semiconducting platforms [44, 51]. In both platforms, rudimentary quantum algorithms have already been demonstrated [61, 274]. While decoherence is a central topic, advanced superconducting systems are now capable of entangling 10 qubits [275]. Spin qubits based on silicon (Si) and germanium (Ge), on the other hand, can be isotopically enriched to remove magnetic decoherence [27, 28], resulting in extremely long coherence times [56, 174]. Crucially, these qubits can be defined using conventional semiconductor technology. A hybrid approach may build upon the strengths of each platform motivating extensive research. Superconducting qubits with semiconductor elements have led to electric gate-tuneable superconducting qubits [239, 276], or gatemons, while spin qubits interfaced with superconducting resonators have reached the regime of strong spin-photon coupling [63–65], an important step toward long-range entanglement.

Furthermore, hybrid superconductor-semiconductor systems can host exotic excitations. In particular, a topological phase transition may occur in superconductor-semiconductor systems in the presence of spin-orbit coupling and magnetism [277, 278]. At the topological transition, excitations emerge that represent Majorana fermion states that can exhibit non-Abelian exchange statistics. Next to their fundamental interest, these states are argued to be excellent building blocks for quantum computation as they bear topological protection against decoherence. Quantum information transfer between spin and topological qubits could make topological systems universal [279] and offer spin qubits topologically protected long-range links [280, 281].

Holes in germanium are an excellent material platform for the construction of these hybrid systems. Germanium can be isotopically purified, thereby removing decoherence by nuclear spins [27], and it can host strong-spin orbit coupling [282]. In addition, mobilities reaching 1,500,000 cm^2/Vs have been reported [70] and high-quality gate-defined quantum dots have been realised [74] in strained SiGe/Ge/SiGe heterostructures. Electrically driven spin qubits have been constructed [84], single spins can be readout in single-shot mode [83], and strained germanium quantum wells [71] have several additional favourable properties for spin qubit operation [75], including a small effective mass and large energy splitting to excited states. Gate-tuneable superconductivity has been studied for 0D and 1D hole systems in self-assembled Ge quantum dots [238] and in Ge/Si nanowires [186], respectively. More recently induced superconductivity was also first observed in a 2D Ge hole system [74], which greatly enhances the flexibility of the fabrication of nanostructures and allows quantum dots to be defined solely by lithography. Now it has to be determined whether ballistic phase-coherent superconductivity can be induced in the germanium platform over the length scales required for long-scale coupling in hybrid systems.

Here, we demonstrate gate-tuneable Josephson supercurrents in a 2D germanium quantum well system with junction lengths L up to 6 µm and find a characteristic decay length $\xi^* = 1.0$ µm. In quantum point contacts, we observe discretisation of the supercurrent and conductance, demonstrating ballistic transport. From the excess current and multiple Andreev reflections, we deduce an interface transparency T between the leads and germanium of 0.6-0.7. Furthermore, we demonstrate the direct-current (dc) and alternating-current (ac) Josephson effect in planar germanium via Fraunhofer-like patterns that arise in magnetic fields and Shapiro steps resulting from microwave irradiation.

11.2. A PLANAR GERMANIUM JOFET

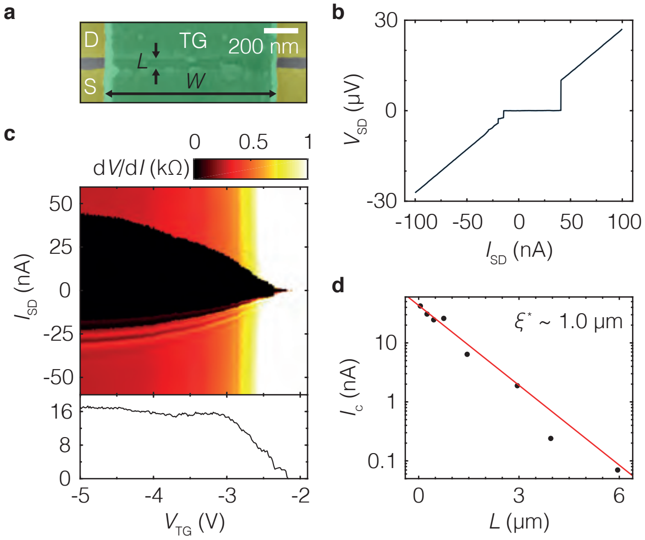

Figure 11.1: **a**, False-coloured SEM image of a planar Josephson junction device with width $W = 1$ μm and length $L = 50$ nm. The top gate TG (indicated in green) is used to induce a 2DHG in the strained germanium quantum well contacted by a superconducting Al source S and drain D (depicted in yellow). **b**, IV-curve of a junction with $L = 50$ nm at $V_{TG} = -4$ V, showing a clear supercurrent with $I_S = 43$ nA. **c**, Colour plot of the differential resistance of the junction dV/dI as a function of the bias current I_{SD} and top-gate voltage V_{TG} (top panel) and derived $I_S R_N$ product as a function of V_{TG} (bottom panel). **d**, Length dependence of the supercurrent. A purely exponential decay is observed over the entire junction length range, with a decay length of 1.0 μm.

Fig. 11.1a shows a scanning electron microscope (SEM) image of a germanium Josephson field-effect transistor (JoFET). The heterostructure is grown by reduced pressure chemical vapour deposition and consists of a $Si_{0.2}Ge_{0.8}$ virtual substrate, a 16-nm-thick strained Ge quantum well, a 22-nm-thick $Si_{0.2}Ge_{0.8}$ barrier, and finally a 1-nm-thick Si cap [71]. Superconducting leads are defined by thermal evaporation of aluminium (Al) after electron beam lithography and local etching of the Si capping layer. The accumulation top gate TG defining the junction is fabricated by depositing a titanium/palladium layer on top of an aluminium oxide dielectric layer grown by atomic layer deposition (ALD) at 300 °C. The JoFETs are fabricated with junction lengths L between 50 nm and 6 μm. The Al contacts are 1 μm wider than the width of TG to ensure that superconductivity is present along the entire width of the junction.

A two-dimensional hole gas (2DHG) is formed by applying a negative gate voltage to the top gate and a clear supercurrent becomes apparent in the IV-curve. Fig. 11.1b shows a typical trace at a fridge base temperature of $T_{\mathrm{bath}} = 10$ mK, where we find a switching current $I_{\mathrm{S}} = 43$ nA. The steps visible for negative bias are likely caused by self-induced Shapiro steps, as we discuss below. The switching current can be tuned by changing the hole density using the top gate, as shown in the top panel of Fig. 11.1c, plotting the maximum out of 10 switching events, in order to reduce the statistical spread in I_{S} and approximate I_{C}. By measuring the normal state resistance R_{N} at high bias, we determine the characteristic voltage $I_{\mathrm{S}}R_{\mathrm{N}}$ as a function of V_{TG}, as shown in the bottom panel of Fig. 11.1c. The observed value increases with more negative V_{TG} and saturates around $I_{\mathrm{S}}R_{\mathrm{N}} \approx 17$ µV, comparable to values recently reported for Ge 2DHG devices [221]. Fig. 11.1d shows the length dependence of I_{S} for $V_{\mathrm{TG}} = -4$ V, showing supercurrents with a purely exponential decay length $\xi^* = 1.0$ µm, extending over remarkably long length scales of several micrometers. For the junction with length $L = 6.0$ µm, we measure $I_{\mathrm{S}} = 70$ pA, indicating the high quality of the quantum well. In comparison, supercurrents in semiconductors were reported over lengths up to 1.5 µm in graphene [283], 1.6 µm in GaAs [284], 2 µm in InAs/GaSb [285], and 3.5 µm in Bi_2Te_3 [286]. From hall bar magnetotransport data, we derive a carrier mobility $\mu = 500,000$ cm^2/Vs and mean free path of $L_m = 6$ µm at a saturation hole density of $p = 6 \times 10^{11}$ cm^{-2} [71], suggesting that our junctions are in the ballistic limit. The superconducting coherence length in the ballistic limit is given by $\xi_{\mathrm{N}} = (\hbar v_F)/\Delta_0$, with v_F the Fermi velocity in the semiconductor and $\Delta_0 = 0.2$ meV the gap size in the superconducting lead. Using the effective mass $m^* = 0.09 m_e$ [71], we estimate the Fermi velocity to be $v_F \approx 2.3 \times 10^7$ cm/s, giving $\xi_{\mathrm{N}} \approx 770$ nm. We note that the switching current of a ballistic SNS junction is expected to saturate for junction lengths shorter than the superconducting coherence length ξ_{N} at low temperature [287]. The fact that we do not observe this, suggests either an unusual small ξ_{N} or a larger effective junction length, as will be discussed below.

11.3. THE DC AND AC JOSEPHSON EFFECT

To verify the Josephson nature of the supercurrent, we perform phase-sensitive experiments. Fig. 11.2a shows a colour plot of the source-drain resistance (dV/dI) as a function of the external out-of-plane magnetic field B for a junction with $L = 450$ nm and $W = 1.5$ µm. The clear modulation of the switching current, corresponding to the edge of the black area in the colour plot, follows a clear Fraunhofer-like pattern, demonstrating the dc Josephson effect. It should be noted that the supercurrent does not drop to 0 at integer flux quanta, which we attribute to an asymmetric current distribution in the device [288]. In addition, we observe multiple steps above I_{S} that are linearly spaced in voltage. The first step can be seen as the resistance peak at higher bias in Fig. 11.2a. We speculate these steps to originate from finite coupling of the junction to some cavity mode, with a frequency of $f \approx 100$ MHz, in or outside the device.

Based on the junction area and taking into account the increased thin-film penetration depth $\lambda_{\mathrm{film}} \approx 105$ nm, as discussed in Section 11.7, one would expect a single flux quantum Φ_0 through the junction at $B = 2$ mT, a magnetic field $\sim$3 times larger than measured in Fig. 11.2. This deviation suggests significant flux focusing due to the superconducting aluminium leads next to the junction. We further observe that

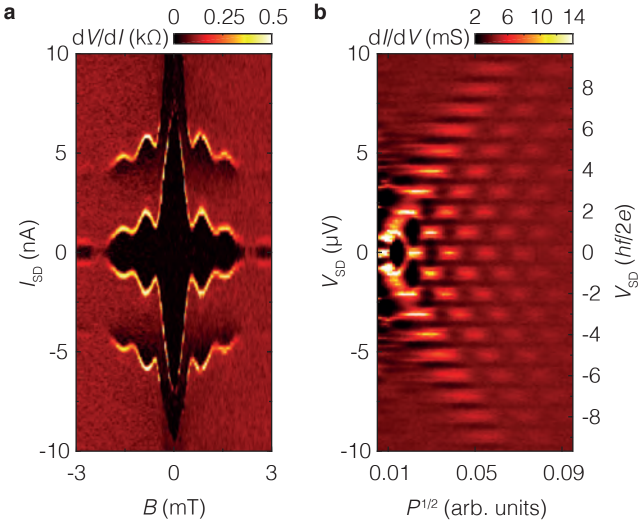

Figure 11.2: **a**, Colour map of the differential resistance dV/dI of the junction as a function of magnetic field B and bias voltage V_{SD} at $V_{TG} = -5$ V. A Fraunhofer-like modulation of the switching current as a function of B is observed, confirming the Josephson nature of the devices. **b**, Differential conductance dI/dV of the junction as a function of bias current I_{SD} and microwave excitation amplitude $P^{1/2}$, showing clear Shapiro steps at $V_{SD} = nhf/2e \approx n \times 1.03$ μV, with excitation frequency $f = 500$ MHz.

the Fraunhofer period increases with an increasing magnetic field and this could be explained by reduced flux focusing as the Al layer is leaving the Meissner state.

In the presence of microwave irradiation, the ac Josephson effect gives rise to Shapiro steps in the source-drain voltage as a function of bias current. When applying a dc excitation with frequency $f = 500$ MHz using an antenna near the junction with $L = 50$ nm and $W = 1$ μm, we observe clear peaks in the conductance (see Fig. 11.2b) at $V_n = nhf/2e = n \times 1.03$ μV, corresponding to plateaus in the source-drain voltage. We also observe small conductance peaks positioned at $\delta = 0.22$ μV on either side of a Shapiro conductance peak. The steps are independent of applied microwave frequency and observed in multiple junctions. These steps are not yet understood but may be of the same origin as the steps observed without microwave radiation.

11.4. MULTIPLE ANDREEV REFLECTIONS

In an SNS-system, multiple Andreev reflections (MAR) are expected to lead to resonances in the conductance at finite, subgap bias voltages $V_m = 2\Delta/me$, with m the number of Andreev reflections and Δ the superconducting gap of the superconductor. We observe kinks in the differential resistance, that pronounce as resistance peaks at elevated temperatures, see Fig. 11.3a, which we attribute to MAR and investigate by plotting the numerical derivative of the device resistance to extract the peak positions as a function of temperature, see Figs. 11.3b and c. For a tunnel contact, one would expect MAR to cause a dip in the resistance, while for transparent contacts higher-order

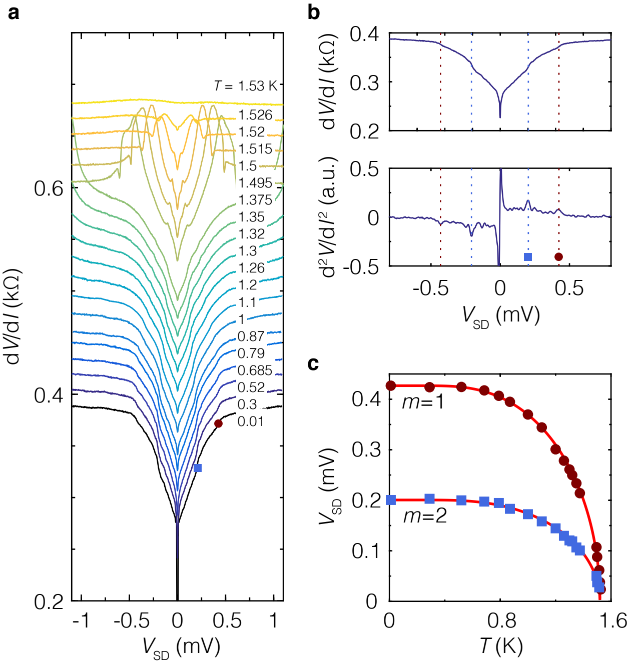

Figure 11.3: **a**, Temperature dependence of the junction resistance at $V_{TG} = -5.0$ V. The traces are offset for clarity. **b**, Resistance curve taken at 0.3 K (top panel) and its numerical derivative (bottom panel). The dotted lines show the position of the first and second MAR. Below 1.5 K their position is determined by the peaks in the numerical derivative, while above 1.5 K clear resistance peaks are visible. **c**, Temperature dependence of the first and second MAR features. Red lines are BCS fits scaled to match the MAR position at $T \approx 10$ mK.

Andreev reflections still contribute significantly and MAR can cause a peak in resistance [289], as recently measured for an epitaxial aluminium/indium arsenide junction [290]. By analysing the excess current, as seen from the conductance enhancement in Fig. 11.3a and details in Fig. 11.5, we find a junction transparency T between 0.6 and 0.7, consistent with the small peak observed in the resistance due to MAR [290]. The MAR feature disappears when the temperature is raised above the aluminium film critical temperature $T_C = 1.52$ K. We fit the data in Fig. 11.3c with a BCS-like gap as obtained from a self-consistent solution of the gap equation, scaled to the MAR positions at 10 mK [290] and using the Al film critical temperature. We find $\Delta = 0.2$ meV, as extracted from the low-temperature value of the $m = 1$ MAR feature. The data suggests that $V_{m=2} \neq 2V_{m=1}$, which may be a result of the resistance not peaking at exactly $V = 2\Delta/me$ [290] or our analysis of the derivative of the resistance. This is also supported by the slight mismatch between the derived gap from the $m = 1$ MAR feature and the observed critical temperature $\Delta_{BCS} = 1.76k_BT_C = 0.23$ meV, with k_B Boltzmann's constant.

At very high bias voltages, we observe another resistance peak, as can be seen in the traces for $T > 1.49$ K in Fig. 11.3a. At base temperature, the peak is observed at $V_{SD} = 2$ mV, which is a bias voltage ~ 10 times above the observed superconducting gap (see Fig. 11.6n). The peak shifts to lower bias voltages with increasing temperature and disappears at T_C, indicating it has a superconducting origin. A similar peak has been observed before [290–292] and was attributed to non-equilibrium effects appearing in planar junctions where the high-mobility 2DHG extends underneath the superconducting contacts. Such an extended interface may increase the probability for Andreev reflection and could thereby be a contribution to the observed transparent superconductor-semiconductor interfaces in planar structures.

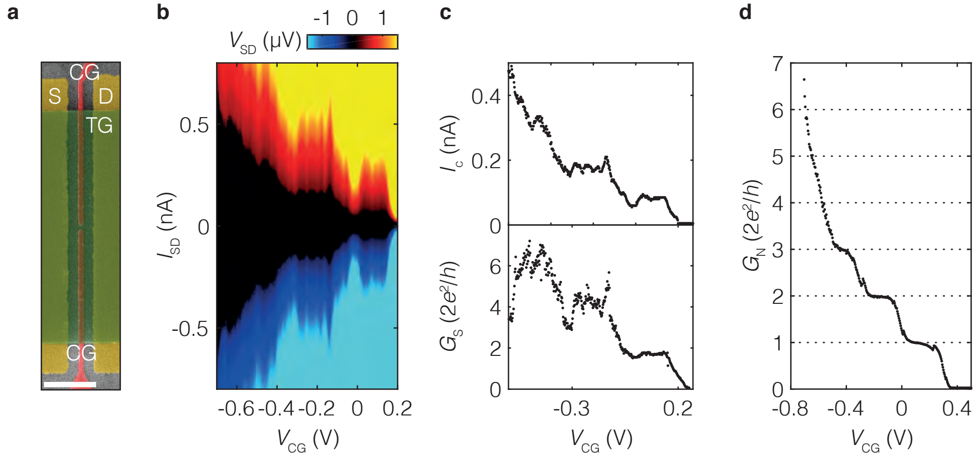

Figure 11.4: **a**, False-coloured SEM image of the superconducting QPC. A set of constriction gates CG (illustrated in red) are added to confine the number of transport channels through the junction. The scale bar is 1 μm. **b**, Colour plot showing the effect of CG on the IV-curve of the device, measured at $V_{TG} = -2.8$ V. Clear plateaus in the switching current are observed, demonstrating the supercurrent discretisation due to the discrete number of modes in the SQPC. The additional oscillations are reproducible and likely an effect of Fabry-Perot interference. **c**, Discretisation of switching current I_S (top panel) and sub-gap conductance G_S (bottom panel), demonstrating the ballistic nature of the superconducting device. Andreev reflection causes an enhanced conductance resulting in steps exceeding $2e^2/h$. **d**, Normal state QPC conductance G_N as a function of constriction gate voltage V_{CG}, in an out-of-plane magnetic field sufficiently large to drive the aluminium ohmic leads normal. For $V_C > -0.6$ V, the device conductance quantises in steps of $G_0 = 2e^2/h$. For $V_C < -0.6$ V, a current can flow underneath the constriction gates, resulting in a large conductance.

11.5. SUPERCONDUCTING QUANTUM POINT CONTACTS

An important aspect for hybrid devices is whether transport can be restricted to individual channels. Quantum point contacts (QPCs) form an excellent playground to study the quantised nature of conductance. In germanium, this was recently used to measure the strong *g*-factor anisotropy of heavy holes in strained SiGe/Ge/SiGe heterostructures [193]. Here we focus on superconducting QPCs (SQPCs), which are predicted to give rise to a discretisation of the switching current in a superconducting junction [293, 294]. Signatures of discrete supercurrents have been observed in InAs heterostructures [295–297] and Si/Ge nanowires [186].

To study this effect in planar germanium, we have fabricated devices similar to the junctions discussed above, but with a set of additional constriction gates CG allowing us to deplete the 2DHG locally. The accumulation top gate TG overlaps CG but is electrically isolated by a 17 nm ALD grown Al_2O_3 layer. Figures 11.4b and 11.4c show the transport characteristics of such a device. We tune the constriction gates to be more positive than the top gate TG. Upon increasing the voltage V_{CG} we see that the conductance is reduced as first the transport underneath the constriction gates is turned off (see Fig 11.4d, for $V_{CG} < -0.7$ V) and for large enough positive voltages ($V_{CG} > 0.3$ V) also the current through the constriction vanishes.

In the intermediate regime, superconducting transport is carried by discrete modes, yielding clear discretisation of the supercurrent and conductance. In Fig. 11.4c, the extracted switching current is shown together with the subgap conductance G_s, measured at a bias current of $I_{SD} = 0.9$ nA $> I_S$, such that a finite voltage $0 < V_{SD} < \Delta$ drops over the junction for all values of V_{CG}. The supercurrent increases in steps $\delta I_S = 85$ pA. On top of the supercurrent discretisation, we also observe oscillations in the switching current and subgap conductance. We ascribe these to Fabry-Perot like interference effects in the QPC [298]. Finite scattering at the constriction interfaces most likely causes the oscillations and may also be related to the reduced QPC $I_S R_N = 1.1$ µV that we observe for these devices, as compared to the JoFET $I_S R_N = 17$ µV (cf. Fig. 11.1c). In the short and low-temperature limit, each mode in the QPC is expected to contribute $\delta I_S = e\Delta/\hbar = 49$ nA, about three orders of magnitude larger than measured in our SQPC. This is consistent with the observed SQPC $I_S R_N$ also being approximately three orders of magnitude smaller than the expected $I_S R_N = \pi\Delta/e = 0.63$ meV for a short and ballistic junction in the low-temperature limit [299], using the aluminium film superconducting gap Δ as obtained from the measured MAR.

Owing to the conductance doubling caused by the Andreev reflection, the subgap conductance can raise in steps with an amplitude larger than $2e^2/h$ [300] and we measure an average step height of $G_S = 3.4e^2/h$. This can be compared to the normal state conductance of the device G_N around zero bias current, measured at an out-of-plane field of several mT, as shown in Fig. 11.4d, where quantisation in steps of $G_N = 2e^2/h$ can be observed. Furthermore, we observe a dip structure in the conductance at the transition between the plateaus, which is not present in the normal state conductance. This was also observed in InAs nanowires [301] and quantum wells [302] and is attributed to a strong subband mixing near the opening of a new channel due to the van Hove singularity, cancelling the Andreev enhancement of the conductance.

11.6. DISCUSSION

The observation of a relatively low $I_S R_N$ product provides room for further investigation and possible optimisation. A possible reason could be the presence of a strong suppression of the induced superconducting gap as a result of the diffusion process of the Al contacts. Research could thus focus on epitaxial interfaces in order to reduce contact transparency, although we already find rather high transparency from excess current measurements. Alternatively, it may also be that transport is in the long-junction limit, even for the shortest junctions, with a corresponding reduced $I_S R_N$ [299]. This would also explain the pure exponential length dependence of the switching current we measure for junction lengths down to 50 nm, typically observed in long junctions. A possible origin could be an extended interface that propagates underneath the Al contacts. This increased effective junction length could also explain the observed resistance peak at high bias. Alternatively, the coherence length could be unexpectedly short, for example, due to transport carried by heavy holes with spin $J = 3/2$, strong spin-orbit coupling, and very anisotropic g-factors.

While these speculations provide avenues for future research, the experimentally measured $I_\mathrm{S}R_\mathrm{N} = 17$ µV already exceeds significantly the thermal energy at base temperature and demonstrates proximity superconductivity in planar germanium. The gate-tuneable Josephson supercurrent ranging over micrometre length-scales provides great opportunities for hybrid superconductor-semiconductor devices. Single-channel transport as demonstrated in the superconducting quantum point contact provides further scope for experiments requiring individual modes, such as Andreev spectroscopy of the superconducting gap. Planar gate-tuneable superconducting qubits are within reach and could be coupled to nuclear spin-free spin qubits fabricated on the same platform. Topological qubits may require further development such as the demonstration of a hard gap but could profit from the large g-factor of heavy holes and the low disorder environment found in our systems. These demonstrations are an essential building block for the development of hybrid technologies and show that germanium is a strong candidate for novel quantum electronic devices.

11.7. EXPERIMENTAL METHODS

11.7.1. THIN FILM CHARACTERISTIC LENGTHS

The characteristic lengths of a thin film superconductor can differ significantly from the bulk values. From the observed critical temperature $T_\mathrm{c,film} = 1.52$ K, the bulk aluminium critical temperature $T_\mathrm{c,bulk} = 1.2$ K [299], and coherence length $\xi_\mathrm{bulk} = 1.6$ µm we can calculate the reduced thin film coherence length, using the same methods as [303, 304], yielding $\xi_\mathrm{film} = \xi_\mathrm{bulk}\frac{T_\mathrm{c,bulk}}{T_\mathrm{c,film}} = 1.26$ µm. Following [305, 306], we can now estimate the thin film penetration depth, using the film thickness $d = 30$ nm and bulk aluminium penetration depth $\lambda_\mathrm{bulk} = 16$ nm. $\lambda_\mathrm{film} = \lambda_\mathrm{bulk}\sqrt{1 + \xi/d} = 105$ nm.

11.7.2. EXCESS CURRENT ANALYSIS

By analysing the excess current in the junction, we can estimate the junction contact transparency. The excess current I_e is defined as the intercept at $V = 0$ of a linear fit to $V(I)$ for $V > \Delta/e$, with Δ being the aluminium gap and e the elementary charge as shown in Fig. 11.5a. Note that the fit is taken for $V < 2$ mV, i.e. below the non-equilibrium feature discussed in Section 11.4, as this effect reduces the excess current [291]. The slope of the fit yields the normal state resistance R_N. For a fully transparent, ballistic junction I_e can be related to the gap via $eI_eR_N = 8/3\Delta$ and for decreasing transparency, the I_eR_N decreases. Using $\Delta = 0.21$ meV, as obtained from the MAR data, we analyse the excess current for 8 junctions of different length up to $L = 6$ µm in the framework of the OBTK-theory [307, 308]. These data are shown in Fig. 11.5b and it can be seen that for all junctions the transparency lies in the range $T \approx 0.55 - 0.7$. This is in good agreement with $T \approx 0.5 - 0.7$, from analysing the Sharvin resistance for a ballistic junction of width $W = 1.5$ µm, at a carrier density of $p = 5 \cdot 10^{11}$ cm^{-2}, as obtained from previous Hall bar measurements (see Ref. [74]).

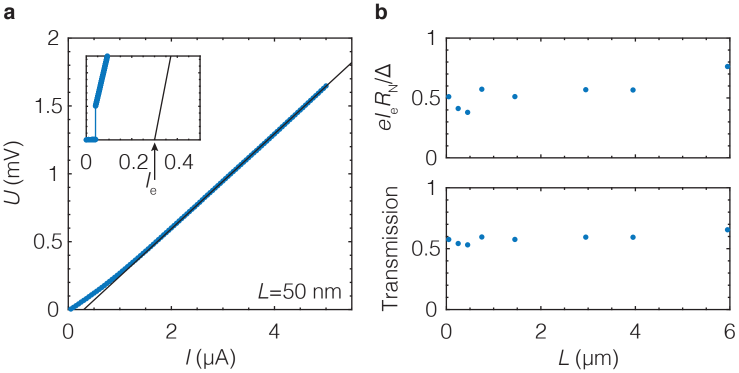

Figure 11.5: **a**, IV-curve (IVC) of the SNS-junction with length $L = 50$ nm, with the black line indicating the fit to $V(I)$ for $V > \Delta/e$. Inset shows a zoom-in of the supercurrent and the $V = 0$ intercept of the IVC, defining the excess current I_e. **b**, Top panel: eI_eR_N/Δ as a function of the junction length L. Bottom panel: Transparency as obtained from eI_eR_N/Δ in the OBTK-framework.

11.7.3. HIGH BIAS SPECTROSCOPY

At elevated temperatures, we observe an additional feature in the bias spectroscopy of the device, as seen in Fig. 11.3a. At base temperature, this feature is still present at a bias voltage $V_{SD} \approx \pm 2$ mV, as can be seen in Fig. 11.6. The origin of this peak is discussed in Section 11.4, and we attribute this to non-equilibrium effects appearing in planar junctions.

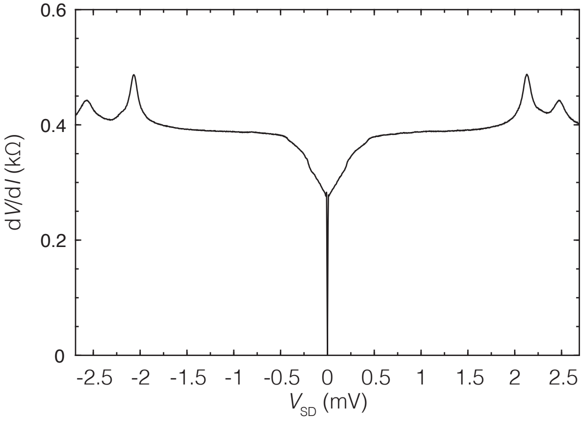

Figure 11.6: Bias spectroscopy of the junction with $L = 50$ nm at $V_{TG} = -5$ V. A peak in resistance is observed at a bias voltage of $V_{SD} \approx \pm 2$ mV.

12

OUTLOOK

> *Always watch where you are going. Otherwise, you may step on a piece of the Forest that was left out by mistake.*
>
> A.A. Milne [309]

In this thesis, we discussed the evolution of the planar germanium material system, starting from high-quality heterostructure growth and ending with multi-qubit systems. Furthermore, we explored the integration of superconductivity with one and two-dimensional transport, as a first step towards superconductor-semiconductor hybrid technology. In this chapter, we briefly review these results and explorer potential future devices and experiments on the road towards a scalable spin qubit quantum processor.

12.1. THE ROAD AHEAD

The progress on spin qubits in the planar germanium system has been rapid. Over the past four years the system progressed from optimizing materials growth (Chapters 5 and 6), to the definition of quantum dots (Chapter 7), few-qubit systems (Chapters 8 and 9) to the definition of one of the largest interconnected spin qubit systems to date (Chapter 10). The swift progress can be attributed to the beneficial material properties like low effective mass of the holes and high quality of the heterostructure, easing fabrication and enabling a high degree of control using electrostatic gates.

However, performing practical quantum algorithms requires many more qubits and/or much lower error rates (and preferably both). When considering the often-cited implementation to solve the nitrogen fixation problem [18], 10^5 qubits running 10 ns gates with error rates as low as 10^{-6} are necessary to perform the calculations within a reasonable time frame. Even considering the best qubit systems in general at this moment, we are far from these numbers. For superconducting qubits, the first system to break the 'quantum supremacy' barrier [12], error rates are 10^{-3} at best, with system sizes on the order of 10^2 qubits [310]. For spin qubits, these numbers are even lower, with one-qubit error rates around 10^{-3} [55, 57], two-qubit error rates approaching 10^0 [11], and system sizes of 4 [86].

Although it looks like the road towards the implementation of practical quantum algorithms is still long, there might be some useful stops en route. Systems of just 50-100 qubits are already too complicated to simulate classically and can thus outperform a classical computer on certain very specific tasks [12]. Therefore, it might be possible to perform specific, yet 'useful' calculations on such a pre-fault tolerant *Near Intermediate Scale Quantum (NISQ)* system [14], often relating to Feynman's original vision on quantum computation [8]: to simulate nature using quantum mechanics. An example of such an implementation is discussed in Ref. [311], and it is argued to only require a system of 50 qubits, with error rates below 10^{-4}. The focus of near-future research for spin qubits in general, but also for germanium quantum computing thus lies in (i) scaling up the number of operational qubits and (ii) improving the quality of the qubit gates. A different way of looking at this is by defining the *quantum volume* of a system $V_Q = \min(n, d)^2$ [312, 313], depending both on the number of qubits n and circuit depth d (the amount of error-free operations possible). Both aforementioned focus points are thus essential to increasing the available quantum volume and developments should go hand-in-hand. Importantly, I would like to stress that these are by no means *all* challenges that need to be solved towards the realisation of a practical quantum computer. These only comprise (some) issues within the quantum layer, while a full-stack quantum computer consists of many more layers [314, 315], each with its challenges.

12.2. INCREASING THE SYSTEM SIZE

Increasing the number of qubits will present us with several challenges, such as managing the interconnects, dealing with imperfect device yield, qubit calibration, and qubit readout.

12.2.1. INTERCONNECT MANAGEMENT

The four qubit quantum processor presented in this thesis is the largest interconnected spin qubit processor to date. If we consider the design of this processor and imagine scaling it up through copy-pasting, we need three gate lines per qubit (one plunger and two barrier gates). Without further optimization, the number of required input-output (IO) lines is thus equal to the number of qubits multiplied by the number of connections per qubit, quickly requiring an unmanageable number of connections. Just considering a 1000-qubit system, we already need 3000 connections from the (cryogenic) qubits to the (room temperature) outside world, far beyond what is currently feasible. A similar problem was encountered in the 60s of the last century when engineers were trying to cram an increasing amount of transistors into an integrated circuit. E.F. Rent, working for IBM, empirically observed a power-law between the number of terminals T, the number of components g and the number of connections per component t: $T = tg^p$. Here, p is the Rent's exponent corresponding to the level of optimisation, correlated to the circuit topology. The authors of Ref. [313] propose a similar rule for quantum systems, with different exponents corresponding to different layers of the system, p_g, p_{IO}, and p_{RT} for gates, chip IOs, and room temperature wires respectively. For the current implementations, we thus have $p_{\mathrm{RT}} = p_{\mathrm{IO}} = p_g \approx 1$.

Different proposals for scaling spin qubits exists, targeting the exponents in different layers. One example is the design of a crossbar array [224], in which electrostatic gates are shared between different qubits. This can significantly reduce p_g, at the cost of increasing the demands on reproducibility in fabrication. The current variability in gate voltages, e.g. as used in Chapter 10, is still larger than the typical charging energy of a quantum dot. While optimizing homogeneity through material growth and fabrication is desirable, other strategies to account for these dot-to-dot variations should be considered as well.

In experiments, we often observe a stable hysteresis effect in the electric field experienced by the quantum dot as a function of gate voltage, likely caused by the occupation of defect states at the wafer interface [219] or in the gate dielectric. One could consider deliberately manipulating these offset voltages through local gate pulses to equalise the electric field between the quantum dots. A calibration routine has to be defined in which the gate voltages are manipulated such that the local electric field at the different quantum dot sites is equalised. Going one step further, this modus operandi could also be considered in the materials design, such that the heterostructure is tailored to allow sufficient local charge manipulation.

Alternatively, if individual control over the qubit barriers is obtained, isolating all qubits from their environment makes them insensitive to dot-to-dot electric field variations. As the low effective mass in germanium eases the requirements on feature size, a possible path towards individual barrier control with a limited amount of gates would be the implementation of shared, double barriers (Fig. 12.1a). By indexing these barriers using word and bit lines, similar to dynamic random access memory, individual selection could be acquired. When neighbouring dots are addressed by separate plunger gates, the electric field variations can be compensated when performing a two-qubit gate and the isolation is necessarily broken. Another approach to achieving individual control is by the use of charge-storage electrodes, addressed (again) by a word and bit line architecture, as proposed in Ref. [59]. Although these architectures allow reducing p_g, even for finite qubit variability, calibrations are still complicated by increased qubit variability. Calibrations should therefore be automated (preferably running 'in the background') and take significantly less time than the qubit stability, while supporting the required error rates ϵ_r, i.e. $t_{\text{calibration}} \ll t_{\text{stability}}(\epsilon_r)$.

An even further reduction of the number of interconnects can be achieved by also targeting the other two exponents. Decreasing p_{IO} could be achieved by integrating qubit control and multiplexing electronics at the qubit stage [26, 313, 316–318]. To this end, it could be beneficial to raise the qubit operation temperature, as the amount of available cooling power typically increases rapidly with temperature. The large excited-state splitting possible in quantum dots allows for qubit operation at elevated temperatures without risking the thermal population of this state [157]. Recently, two-qubit logic in silicon quantum dots has been demonstrated at a temperature of $T = 1$ K [66, 67]. Finally, not only incorporating control and multiplexing electronics at the qubit stage but also integrating feedback logic circuits, could even further reduce the number of room temperature connections needed, by also lowering p_{RT} [313].

12.2.2. QUBIT READOUT

The most common method to readout the qubit spin state is by spin-to-charge conversion, measuring the charge signal with a single-electron (or hole) transistor (SET or SHT). Using cryogenic amplification [319] or reflectometry techniques [258], high readout fidelities of > 99.9 % have been obtained [320]. Typically, charge sensors are positioned at the edges of a quantum dot array, as they require ohmic channels to allow for a transport measurement. Charge sensors in silicon require (microscopic) areas of ion implantation to create a low-resistive contact to the channel. As a result, the charge sensor leads are defined by a 2DEG-channel cutting the qubit plane, which only allows for the positioning of the sensor at the periphery of an array. As the array size increases, the direct coupling between the qubits in the centre and the sensor on the edge decreases quickly. To resolve this issue, readout protocols relying on spin shuttling should be harnessed, or sensors should be included within the array, either vertically or in the plane. For group IV materials, germanium presents a unique possibility for the latter approach, as ohmic contacts can be defined solely using nano-patterned metallic electrodes, removing the need for (microscopic patches of) ion implantation. This makes it possible to vertically route the ohmic leads into the array and position sensors within the quantum dot grid (example of such a design in Fig. 12.1b).

A second approach is to make use of gate-based dispersive readout [321–323], based on a resonant circuit connected to the qubit gate. While high fidelity readout was obtained using this technique [263], it necessitates the presence of high-quality resonators. The footprint of these resonators is typically 100x100 μm [315], significantly increasing the device size.

12.3. INCREASING THE CIRCUIT SIZE

The second number defining the quantum volume is the circuit depth. As the available circuit depth is defined both by the qubit coherence and the gate time, these are the two

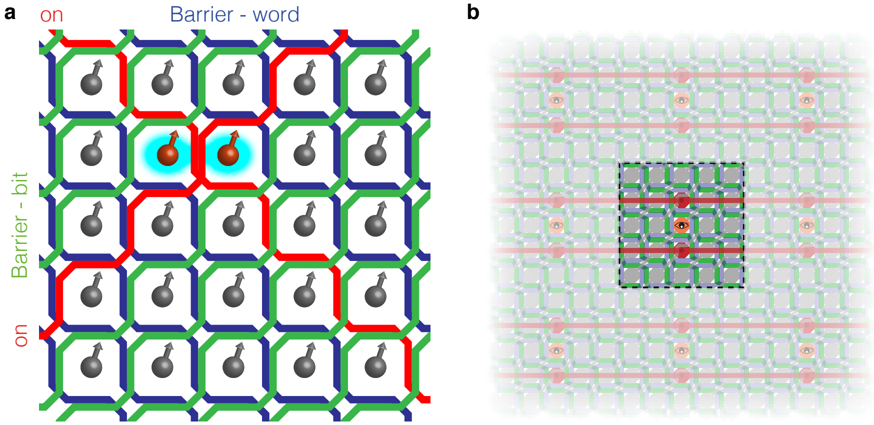

Figure 12.1: **Extensible 5-by-5 grid of germanium spin qubits with integrated charge sensors.** **a** Schematic drawing illustrating the word and bit line indexed qubit barriers. By turning on (in red) both a word (blue) and bit (green) line barrier, a single tunnel barrier is opened, coupling only two qubits (in red). **b** Computer-aided design (CAD) of a repeated minimal 5-by-5 unit cell (highlighted), including a single integrated charge sensor in the middle. Blue and green layers correspond to the barrier gates as in panel a, the grey layer defines the quantum dot plungers, and the red layer defines the ohmic reservoirs to the charge sensor highlighted in orange. The black circles correspond to vias connecting the ohmic layer to the fanout layer.

parameters to optimize. The gate times, both for one and two-qubit gates, are already comparatively short for germanium hole spin qubits (tens of nanoseconds), owing to the large degree of electrical control. Qubit coherence, however, is still short compared to other (spin) qubit systems, with dephasing times of about one microsecond, that can be extended up to 100 µs by incorporating dynamical decoupling pulses.

Two main potential contributors to qubit dephasing should be discussed for this system. First, the nuclear spins present in the natural germanium. While natural germanium consists mostly of net-zero nuclear spin isotopes, the ^{73}Ge isotope with a nuclear spin of 9/2 has a 7.8 % abundance. While it should be possible to suppress the hyperfine interaction for an ideal heavy hole system [136], the qubit can remain sensitive to nuclear spin noise as discussed in detail in Chapter 3. To avoid dephasing due to the nuclear spins entirely, the germanium can be purified to contain almost solely spin-free isotopes [27, 28], which has increased coherence times by orders of magnitude for electron spins in silicon [56, 57].

Secondly, qubit coherence can be deteriorated by local fluctuations of the electric field, as caused by defect states in the heterostructure or gate stack. While the qubit is defined by the (magnetic) spin state of the hole, electric fields couple to the qubit states through the spin-orbit interaction or the exchange interaction. In Chapter 8 we demonstrated how the sensitivity to charge noise coupling via the exchange interaction can be optimized by making use of a sweet spot in the electric field. Similarly, such sweet spots are predicted to exist for the spin-orbit interaction as well [127, 324], potentially supporting significant improvements to qubit coherence times. Future experiments could thus focus on studying the respective contributions of mechanisms to qubit coherence, as well as ways to minimize their effect by tuning the quantum dot and device parameters. Furthermore, errors also occur as a result of (lack of) calibration and adiabatic effects, such as unaccounted interactions or qubit crosstalk. In particular, the latter can be of relevance for the hole qubit system, due to the increased sensitivity to electric fields. While these errors can typically be corrected, it requires careful characterisation of the underlying principles to model and rectify them. Finally, making use of benchmarking sequences, the quality of different types of qubit gates can be assessed and potentially tailored [57, 60], to optimize the operations given the specific infidelity sources present in the system.

SUMMARY

Spin quantum bits (qubits) defined in semiconductor quantum dots have emerged as a promising platform for quantum information processing. Various semiconductor materials have been studied as a host for the spin qubit. Over the last decade, research focussed on the roup-IV semiconductor silicon, owing to its compatibility with semiconductor manufacturing technology and the ability to eliminate magnetic noise through isotope purification. However, to this end, hole states in germanium can be considered as well. Furthermore, their low effective mass and high carrier mobility allow for well-controlled devices, the lack of valley states ensures a well-defined qubit manifold and the intrinsic spin-orbit coupling enables all-electric control. In this thesis, we study strained planer germanium quantum wells, with a focus on applications for quantum information processing.

In Chapter 5, we discuss the material platform growth and properties. We show that starting from a silicon wafer, using a reverse grading process, defect-free, undoped, strained, and shallow germanium quantum wells can be grown, as confirmed by transmission electron microscopy, secondary ion mass spectrometry, and x-ray measurements. Using heterostructure field-effect transistors, we characterise the transport properties of the material and find a carrier mobility of $\mu > 500,000$ cm^2/Vs. Furthermore, we study the effect of the quantum well depth on the quantum mobility and charge noise sensitivity (Chapter 6) and observe an improvement in both parameters when the quantum well depth is increased from 20 nm to 60 nm.

The spin qubit is defined by a hole spin confined in a gate-defined quantum dot. In Chapter 7 we study the properties of a quantum dot in planar germanium. We describe the nanofabrication process we use to define gate-controllable quantum dots, contacted by metallic ohmic leads. A nearby quantum dot is used as a charge sensor, which can be read out using high-bandwidth reflectometry measurements. This allows us to deplete a two-by-two quantum dot array to the single-hole charge occupation, as a host for the spin qubits.

Having established a fabrication integration scheme to define quantum dots and ohmic regions, we move to qubit operation in Chapter 8. We measure a double quantum dot in transport and observe a blockade of the transport current for certain hole occupation numbers. This is found to be caused by Pauli spin blockade and can be used to perform the spin-to-charge conversion. When a microwave tone resonant with the magnetic field induced Zeeman splitting is applied, the blockaded transport current recovers. This is the result of an induced spin flip, mediated by electric dipole spin resonance (EDSR). Using a tailored measurement technique to increase the signal-to-noise ratio of the transport measurements, we demonstrate coherent rotations of the spins in both quantum dots at a Rabi frequency of up to 100 MHz. By operating at the point of the lowest charge noise sensitivity, we find qubit dephasing times beyond 800 ns and a single qubit control fidelity above 99 %. To form a universal quantum gate set, an

entangling operation is needed as well. We implement a two-qubit conditional rotation gate, mediated by the exchange interaction between the qubits. Using the dedicated tunnel barrier gate, we can set the exchange interaction as high as 60 MHz, enabling fast and coherent two-qubit rotations.

Transport measurements only allow for sampling of the average measurement outcome over an ensemble of individual shots. In Chapter 9 we establish single-shot measurements of a single-hole spin qubit by making use of a separate radio-frequency charge sensor. This allows us to isolate the qubits from their hole reservoirs, and we find increased spin relaxation times of over 1 ms. Furthermore, we observe a strong electric modulation of the hole g-factor that can be attributed to the spin-orbit coupling and ensures individual qubit addressability.

Practical quantum computing applications require large numbers of qubits and many proposals rely on two-dimensional (2D) layouts to achieve this. As a first step towards 2D grids of spin qubits, we operate a two-by-two qubit array in Chapter 10. A latched readout process is implemented to increase the readout visibility and overcome spin relaxation during spin-to-charge conversion. Fast single-qubit gates are achieved using EDSR, with control fidelities of over 99 % for all four qubits. By implementing dynamical decoupling sequences, low-frequency noise can be mitigated and the phase coherence of the qubit can be increased by several orders of magnitude, up to 100 µs.

Harnessing the electric control over the quantum dot coupling, we show the gate-controlled isolation and coupling of all four qubits, enabling one-, two-, and threefold conditional qubit rotations. The large range of control over the exchange interaction also allows performing a controlled phase (CZ) two-qubit gate in only 10 ns. Implementing a quantum circuit based on CZ gates between all qubits, we coherently entangle and disentangle the four qubits in a Greenberger-Horne-Zeilinger (GHZ) state.

Finally, in Chapter 11 we study the integration of superconductors into the platform and define gate-controlled Josephson junctions. We observe a supercurrent through the quantum well over a length up to 6 µm. The critical current of the junction can be modulated using the top gate, up to a maximum $I_c R_N$ of 17 µV. We demonstrate the Josephson nature of the supercurrent by showing the presence of both the dc and ac Josephson effect. From multiple Andreev reflection and excess current measurements, we extract a characteristic superconducting gap size of 0.2 meV and a junction transparency of 0.6. Finally, we define a superconducting quantum point contact and observe discretisation of the supercurrent, showing superconducting transport restricted to individual channels.

We concluded the introduction by questioning if it is time to switch host semiconductor for quantum dot spin qubits. While a conclusive answer to this question cannot be given yet (and maybe only time will tell), the qualities of germanium that enabled the discovery of the transistor in 1948, are beneficial to quantum information processing as well. Combined with the unique properties of hole spins, strained planar germanium is certainly a strong candidate as host material on the route toward fault-tolerant quantum computing.

Nico Hendrickx

SAMENVATTING

Spinkwantumbits gebaseerd op kwantumdots in een halfgeleider zijn opgekomen als een veelbelovend platform voor kwantuminformatietechnologie. Verscheidene halfgeleidende materialen zijn bestudeerd om de kwantumbits in te definiëren. Aangezien de siliciumtechnologie ten tijde van de halfgeleiderrevolutie sterk ontwikkeld is, is het onderzoek het laatste decennium toegespitst op het gebruik van silicium. Daarnaast is het voor groep-IV halfgeleiders (zoals silicium) mogelijk om middels isotooppurificatie ruisveroorzakende isotopen te verwijderen, hetgeen niet mogelijk is voor groep-III-V halfgeleiders. Echter, op basis van deze criteria moeten we ook gatstaten in de valentieband van germanium beschouwen. Deze kennen daarnaast nog enkele extra voordelen, zoals: een lage effectieve massa en hoge mobiliteit voor een gemakkelijk in te stellen potentiaallandschap, een afwezigheid van een vallei-ontaarding voor geïsoleerde energieniveaus van de kwantumbit, en een intrinsieke spinbaankoppeling die een volledig elektrische aansturing mogelijk maakt. In dit proefschrift bestuderen we gespannen tweedimensionale kwantumputten in germanium, met een focus op toepassingen voor de kwantuminformatiekunde.

In Hoofdstuk 5 wordt de groei van de heterostructuur en haar eigenschappen besproken. Door gebruik te maken van een gegradeerde gelaagdheid, kunnen defectvrije, ongedoteerde, gespannen en ondiepe germanium kwantumputten worden gegroeid op een siliciumwafer. De hoge kwaliteit van de heterostructuur wordt bevestigd middels transmissie-elektronmicroscopie, secondaire-ionmassaspectroscopie, en röntgenkristallografie. Met behulp van heterostructuur-veldeffecttransistors karakteriseren we de transporteigenschappen van het materiaal en we vinden een dragermobiliteit van $\mu > 500,000$ cm^2/Vs. Verder wordt het effect van de gekozen kwantumputdiepte op de kwantummobiliteit en de hoeveelheid ladingsruis experimenteel bepaald (Hoofdstuk 6) en een verbetering van beide parameters wordt behaald door de kwantumputdiepte te vergroten van 20 nm naar 60 nm.

De spinkwantumbit wordt gevormd door een gatspin die we opsluiten in een door elektrodes gedefinieerde kwantumdot. In Hoofdstuk 7 worden de eigenschappen van kwantumdots in germanium bestudeerd. Het nanofabricageproces van deze structuren wordt uiteengezet, waarbij palladium elektrodes worden gebruikt om het potentiaalveld vorm te geven en aluminium aansluitingen de transportcontacten vormen. We gebruiken een nabije kwantumdot als ladingssensor, die met behulp van reflectometrie met een hoge bandbreedte uitgelezen kan worden. Dit stelt ons in staat om de kwantumdots in een twee bij twee raster ieder met een enkel gat te vullen, als basis voor de kwantumbits.

In Hoofdstuk 8 worden deze kwantumbits experimenteel bestudeerd. De transportstroom door een dubbele kwantumdot wordt gemeten en we observeren een afname van de stroom voor bepaalde gatbezettingen. Dit fenomeen wordt veroorzaakt door Pauli spinblokkade en kan gebruikt worden om spin-ladingsconversie uit te voeren.

Deze blokkade kan worden opgeheven door de spin van een van de gaten te roteren middels elektrische dipoolspinresonantie (EDSR). We zien dat de transportstroom inderdaad hersteld kan worden door op een van de elektrodes een microgolftoon aan te bieden die in resonantie is met de Zeemanenergie, opgelegd door het externe magnetische veld. We ontwikkelen een meettechniek om de signaal-ruisverhouding van transportmetingen te verbeteren en demonstreren hiermee coherente spinrotaties in beide kwantumdots, met Rabisnelheden hoger dan 100 MHz. Door te opereren op het elektrostatische punt met de laagste ladingsruisgevoeligheid, vinden we een kwantumbitcoherentietijd langer dan 800 ns en een aansturingsbetrouwbaarheid van de eenkwantumbitoperaties groter dan 99 %. Om een universele kwantumpoortset te vormen, is daarnaast ook nog een verstrengelende poort nodig. We implementeren een conditionele tweekwantumbitrotatiepoort, gemedieerd door de uitwisselingsinteractie tussen de kwantumbits. Met behulp van een specifieke tunnelbarrière-elektrode kan de uitwisselingsinteractie tot 60 MHz ingesteld worden, om snelle en coherente tweekwantumbitrotaties mogelijk te maken.

Wanneer transportmetingen uitgevoerd worden, kan alleen de gemiddelde uitkomst van een reeks kwantumexperimenten bemonsterd worden. In Hoofdstuk 9 lezen we de individuele uitkomsten van de reeks metingen uit, door gebruik te maken van een extra ladingssensor. Dit maakt het mogelijk om de kwantumbits te isoleren van hun respectievelijke gatreservoirs en de spinvervaltijd neemt hierdoor toe tot meer dan 1 ms. Verder observeren we dat de g-factor van de gaten een sterke elektrisch veldafhankelijkheid kent, hetgeen toegeschreven kan worden aan de spinbaankoppeling en het individuele aansturen van de kwantumbits mogelijk maakt.

Praktische toepassingen van kwantumcomputers vereisen grote hoeveelheden kwantumbits en veel voorstellen om deze te integreren zijn gebaseerd op tweedimensionale (2D) ontwerpen. Als een eerste stap naar een dergelijk 2D-raster van spinkwantumbits, definiëren en opereren we een twee bij twee matrix van kwantumbits in Hoofdstuk 10. We maken gebruikt van een uitlezingsmethode waarbij de uitkomst wordt vergrendeld in een stabiele ladingstoestand, om zo een hogere uitleeszichtbaarheid te verkrijgen. Snelle eenkwantumbitoperaties kunnen middels EDSR uitgevoerd worden, met een betrouwbaarheid van boven de 99 % voor alle vier de kwantumbits. Door de kwantumbits te ontkoppelen van laagfrequente ruis, kan de coherentie van de kwantumbits worden verlengd tot meer dan 100 µs.

Door gebruik te maken van de elektrische stuurbaarheid van de interactie tussen de kwantumdots, kunnen we de vier kwantumbits gecontroleerd isoleren en koppelen, om zo een-, twee- en drievoudig conditionele spinrotaties mogelijk te maken. Daarnaast kan deze stuurbaarheid gebruikt worden om een conditionele fasepoort (CZ) uit te voeren in slechts 10 ns. We implementeren een kwantumpoortenschema op basis van een CZ-poort tussen alle kwantumbitparen, om de vier kwantumbits coherent te verstrengelen in een zogenaamde Greenberger-Horne-Zeilinger-staat.

Tot slot bestuderen we in Hoofdstuk 11 de mogelijkheid om supergeleiders te integreren in het platform. We definiëren elektrisch stuurbare Josephson-juncties en observeren een superstroom door de germanium kwantumput over een lengte van 6 µm. De kritische stroom van de junctie kan worden gemoduleerd met de bovenliggende elektrode, tot een maximaal $I_\mathrm{c}R_\mathrm{N}$-product van 17 µV. We laten de karakteristieke eigenschappen van een Josephson-superstroom zien, middels een demonstratie van zowel het *dc* als *ac* Josephson-effect. Uit metingen van meervoudige Andreev-reflecties en de overmaatstroom, wordt een karakteristieke supergeleidende energiekloof van 0.2 meV en junctietransmissiecoëfficiënt van 0.6 afgeleid. Tot slot realiseren we een supergeleidende kwantumpuntcontactjunctie en observeren dat de kritische stroom stapsgewijs toeneemt, als een teken dat het transport gelimiteerd is tot enkele kanalen.

We eindigden de introductie met de vraag of het tijd is om te wisselen van halfgeleider als drager voor spinkwantumbits. Hoewel het nog te vroeg is om een sluitend antwoord op deze vraag te geven, kunnen we wel stellen dat de kwaliteiten van germanium die de ontdekking van de transistor in 1948 mogelijk maakten ook voordelen bieden voor de kwantuminformatietechnologie. Gecombineerd met de unieke eigenschappen van gaten in de valentieband, maakt dit de gespannen germanium heterostructuur een sterke kandidaat als kwantumbitplatform op de weg naar fouttolerante kwantumcomputers.

Nico Hendrickx

ACKNOWLEDGEMENTS

Je kunt beter serieus over niks lullen;
dan niks lullen over iets serieus.

Nando Tolboom

As they say, time flies when you are having fun, and this was certainly true for the past four years. I am thankful for all the fruitful interactions I have had with the people around me. None of these results in this dissertation could have been realised without the help of many others. Below, I hope I can thank all of you for your contributions to this effort and the fun I had working on it.

First of all, let me start by thanking you, **Menno**. We met during my internship in Sydney, and I remember you mentioning that you wanted to *"wegkapen voor een PhD in Delft"* me before we even met. I am very glad that you managed to do that very thing. Your inexhaustible enthusiasm and creativity is something I appreciate a lot and I remember being full of new ideas and inspiration after every meeting we had. At the same time, you have always allowed me to pursue my own ideas and included me in all aspects of doing science. I have learnt an incredible amount of things from you and could not have wished for a better supervisor.

Lieven, thank you for being my promotor. I admire the way you manage the spin qubit efforts, always looking forward, yet ensuring we learn from the past. You always ask the right questions and make sure we focus on the right details. I am sure Qutech will flourish under your scientific guidance.

Giordano, although my research project was supposed to be based on silicon, you convinced me to give your germanium quantum wells a try, four years ago. This turned out to be a gold mine, and I am proud of all results that we achieved. None of these would have been possible without your continuous efforts on materials growth and characterisation, aiming for ever better heterostructures. I am convinced this material system is nowhere near exhausted and many more interesting results are yet to come!

Gertjan, my fellow Twente → Sydney → Delft traveller. We started our PhDs around the same time and in these early days we spent a lot of time in the cleanroom together. As anyone with experience in nanofabrication will know, this can be a struggle sometimes, but I have good memories of figuring out these problems together with you. Your jokes during our coffee walks in hunt of storks always were a nice distraction from work. I wish you all the best at Single Quantum!

Luca, although we never really worked on the same project, you have taught me a lot. We spent many days (or weekends) alongside each other in the lab. You are a talented scientist, always trying to get a better understanding of experimental data. Thank you for keeping us sharp at all times. I really enjoyed working with you and also have good memories of the different conferences we visited and trips we made (except for maybe that hut in Big Sur...). Oh, and if you ever need anyone to spray some apple juice on your hero sample, you know how to find me!

Will, the final one to join the first four. Your presence really is the social glue that keeps the group together. Thank you for everything, both outside and inside of the lab. You were always there to talk to, be it about paper citations, lekkere biertjes, or just to vent about a broken experimental setup. Of course, you have also proven to be a true wizard of the cleanroom: being never late, nor early in delivering a perfect batch of samples. Best of luck on finishing your PhD!

When starting somewhere new, the amount of new things to learn is often overwhelming, but I was lucky to have excellent teachers. **Roy** and **Marco**, you taught me many of the skills that were essential during the rest of my PhD. Covering everything from bonding eight-probe devices to operating fridges to understanding (disordered) quantum dot physics. Roy, you always told me the hole qubit is the best spin qubit and I was usually sceptical. Maybe you were right all along. **David**, you were the first one to join me on the germanium project and I could not have wished for a better partner. From the second you joined the project you started contributing (if only we would have ever received those *good beers*...). In fact, you have enabled many of the results in this thesis and I am extremely thankful for this. Your creativity and scientific skills are inspiring and I am proud of the papers we share. **Max**, you are one of these exceptional physicists that can perfectly bridge the gap between theory and experiment. You already contributed to (and enabled) many of our experimental works and I am convinced many more are to follow.

I see a bright new generation of researchers to continue our group's efforts in the future. **Floor**, you are extremely well-organised and always set on understanding every part of the experiment and data. I am sure the germanium qubit project is in excellent hands with you! **Marcel**, with your attention to detail, I am sure the Si/SiGe project will thrive. **Chien** and **Hanifa**, I wish you luck exploring some of the exotic physics germanium has to offer. **Francesco**, I enjoyed doing my last measurements in the group together with you. You really hit the ground running and I am confident you will bring this project to a good end!

I believe the close ties between the different spin-qubit teams at Qutech is what enables many of our great results. **Stephan** your contribution to (almost all) software used is equally impressive as the efficiency with which you push out data now working devices are flowing your way. **Mario**, I always love chatting with you, about physics, good whisky (no e), or Mazepin's latest crash. The same goes for you, **Brian**, I always enjoy our hallway/coffee conversations. All other members of our groups, past and current: **Anne-Marije**, **Xiao**, **Udit**, **Alberto**, **Kostas**, **Toivo**, **JP**, **Tom**, **Christian**, **Guoji**, **Alice**, **Sjaak**, **Patrick**, **Tobias**, **Tzu-Kan**, **Matheusz**, **Andrea**, **Pablo**, **Florian**, **Jurgen**, **Luka**, **LaReine**, and **Andrea**, it was a pleasure working with you! **Max**, **Mark**, **Patrick**, my small pack of cleanroom warriors, thank you for always pushing on.

I would like to thank my committee members for accepting the invitation and taking the time to read my dissertation: **Leo Kouwenhoven**, **Ronald Hanson**, **Daniel Loss**, and **Andrew Dzurak**. I have also been lucky to be involved in discussions and collaborations with many experienced scientists, such as **Slava Dobrovitski**, **Alexander**

Brinkman, **Alexander Hamilton**, **Bill Coish**, **Alessandro Rossi**, **Amir Yacoby**, and **Dimitrie Culcer**. I have learnt a lot from all of you.

No measurements would be possible without the endless efforts of people pushing the limits of fabrication. **Amir**, thank you for growing all ~ 30 wafers needed for this work, as well as your efforts in setting up the (essential) database system. **Sergey**, your drive to help anyone is admirable and your efforts lie at the basis of most fabrication efforts in our groups. **Elfi**, thank you for showing me the ropes of the VLL cleanroom. The same can be said for **Jelmer**, **Gabriel**, **Kanwal**, **Nima**, **Nodar**, **Delphine**, **Diego**, **Stefan**, and **Saurabh**. I also owe my gratitude to the technicians that ensure the cleanroom keeps running smoothly: **Marc**, **Eugene**, **Marco**, **Charles**, **Ewan**, **Hozanna**, **Arnold**, **Anja**, **Pauline**, **Lodi**, **Bas**.

Outside of the cleanroom, there are also many people providing the support needed to perform our experiments. **Marja**, **Joanna**, **Leonie**, **Rianne**, and many others, your support has been very helpful. **Raymond**, you enable the high-quality research that is performed at Qutech. The ease with which you can point out something stupid we did in connecting our setups is incredible. You, **Raymond**, **Marijn**, and **Roy** always find a way to explain our issues and come up with a solution for them as well. **Jack**, **Hans**, **Kees**, **Erik**, **Sowmini**, and the rest of the DEMO team, thank you for your help in making and fixing our electronics at all time. **Jason**, **Olaf**, **Matt**, **Jelle**, **Remco**, **Siebe**, **Mark**, **Nico**, thank you for keeping our fridges and labs running smoothly. If there is one thing I realised over the past years, it is that as the experiments become more complicated, the software becomes just as important as the hardware it controls. Thank you, **Pieter** and **Luc** for your support. **Sander**, your help has been invaluable and it is the main reason that the same software is now being used across the entire lab. Not only do you fix bugs and introduce requested new software functionalities at lightning speed, but you also often come up with unique experimental ideas or implementations, making our measurements even more efficient. **Kees**, **Charlotte**, **Leo**, **Leo**, **Ronald**, and all other PIs, thank you for forming the great and inspiring working environment that Qutech is today.

Naast iedereen die ondersteuning op het werk bood, moet ik ook hen bedanken die voor de nodige afleiding hebben gezorgd. Allereerst **Kit** en **Nando**, onze dagelijkse diepgaande analyses van het nieuws, de geopolitieke situatie en de ontwikkelingen van Raymond van Barneveld, bieden een welkome afwisseling op het werk. Ik hoop dat we de komende jaren nog vele recordjes kunnen zetten. Helaas kon ons jaarlijkse *fluitkaas*reisje met **Matthijs**, **Alexander**, en **Roelof-Jan** afgelopen jaar niet doorgaan, maar hopelijk kunnen we dat de komende jaren goedmaken! **Jorik**, een jaar na jou vertrok ik ook vanuit het oosten naar Delft en daarmee konden we onze racefietsavonturen weer voortzetten. Een echt rondje is natuurlijk nooit compleet zonder even volle bak over een gravelstrook te knallen. Ook dank aan de rest van **ULMEK**; het enige positieve aan de coronapandemie was dat ik de borrels ineens weer kon bijwonen. **Pim**, ik hoop dat er nog maar flink gestruind mag worden. **Floor**, onze lama- en koekjesuitwisselingen waren altijd een lichtpuntje in het afgelopen jaar. **Virginia**, keep that gossip flowing my way!

Ik wil ook mijn familie bedanken voor alle steun en aanmoediging de afgelopen 27 jaar. **Papa**, **mama**, jullie zijn altijd een voorbeeld voor mij geweest en ik ben trots nu ook de doctorstitel te mogen voeren. **Agnes**, wat ben jij sterk, jouw kracht is een inspiratie voor iedereen. **Opa** en **oma**, al sinds dat ik een klein kind was, hebben jullie mij gemotiveerd met natuur en techniek bezig te zijn. Vele tripjes naar (wetenschaps)musea en allerlei technische bouwwerken hebben mij geleerd om altijd nieuwsgierig te blijven. Bedankt voor jullie onuitputtelijke interesse, steun en trots door de jaren heen. **Cees**, **Nelline**, en **Anja**, ik ben blij dat ik deel van jullie familie heb mogen worden. Jullie staan altijd klaar om te helpen, zoals wel blijkt uit jullie enorme bijdrage aan de verbouwing van ons huis!

En bovenal, **Linda**. Zonder jouw onvoorwaardelijke steun was mij dit nooit gelukt. Jij vrolijkt me op wanneer dingen tegenzitten en jij bent er voor mij wanneer dat nodig is. Bedankt voor alles, ik kijk met veel plezier uit naar de avonturen die de toekomst ons samen gaat brengen.

REFERENCES

[1] M. Riordan, L. Hoddeson, and C. Herring, *The invention of the transistor*, Rev. Mod. Phys. **71**, S336 (1999).

[2] J. Kilby, *Turning potential into realities: the invention of the integrated circuit*. Noble lecture (2000).

[3] P. Siffert and E. Krimmel, *Silicon: Evolution and Future of a Technology* (Springer Science & Business Media, 2013).

[4] G. Moore, *Cramming More Components Onto Integrated Circuits*, Electronics **38**, 114 (1965).

[5] `https://www.nvidia.com/content/dam/en-zz/Solutions/Data-Center/nvidia-ampere-architecture-whitepaper.pdf`, [Accessed: 2020-11-06].

[6] `https://www.tsmc.com/english/dedicatedFoundry/technology/logic/l_5nm`, [Accessed: 2020-11-09].

[7] R. P. Feynman, *Quantum mechanical computers*, Found Phys **16**, 507 (1986).

[8] R. P. Feynman, *Simulating physics with computers*, Int. J. Theor. Phys. **21**, 467 (1982).

[9] J. Preskill, *Quantum computing and the entanglement frontier*, arXiv:1203.5813 (2012).

[10] M. A. Nielsen and I. L. Chuang, *Quantum Computation and Quantum Information* (Cambridge University Press, New York, 2000).

[11] W. Huang, et al., *Fidelity benchmarks for two-qubit gates in silicon*, Nature **569**, 532 (2019).

[12] F. Arute, et al., *Quantum supremacy using a programmable superconducting processor*, Nature **574**, 505 (2019).

[13] H.-S. Zhong, et al., *Quantum computational advantage using photons*, Science **370**, 1460 (2020).

[14] J. Preskill, *Quantum Computing in the NISQ era and beyond*, arXiv:1801.00862 (2018).

[15] P. W. Shor, *Scheme for reducing decoherence in quantum computer memory*, Phys. Rev. A **52**, R2493 (1995).

[16] A. G. Fowler, M. Mariantoni, J. M. Martinis, and A. N. Cleland, *Surface codes: Towards practical large-scale quantum computation*, Phys. Rev. A **86**, 032324 (2012).

[17] I. Georgescu, *25 years of quantum error correction*, Nature Reviews Physics **2**, 519 (2020).

[18] M. Reiher, et al., *Elucidating reaction mechanisms on quantum computers*, PNAS **114**, 7555 (2017).

[19] C. D. Bruzewicz, J. Chiaverini, R. McConnell, and J. M. Sage, *Trapped-ion quantum computing: Progress and challenges*, Applied Physics Reviews **6**, 021314 (2019).

[20] `https://ionq.com/`, [Accessed: 2020-11-09].

[21] `https://www.intel.com/content/www/us/en/research/quantum-computing.html`, [Accessed: 2020-11-09].

[22] `https://www.ibm.com/quantum-computing/`, [Accessed: 2020-11-09].

[23] `https://www.microsoft.com/en-us/quantum/`, [Accessed: 2020-11-09].

[24] `https://www.rigetti.com/`, [Accessed: 2020-11-09].

[25] D. Loss and D. P. DiVincenzo, *Quantum computation with quantum dots*, Phys. Rev. A **57**, 120 (1998).

[26] L. M. K. Vandersypen, et al., *Interfacing spin qubits in quantum dots and donors—hot, dense, and coherent*, npj Quantum Information **3**, 34 (2017).

[27] K. Itoh, et al., *High purity isotopically enriched 70-Ge and 74-Ge single crystals: Isotope separation, growth, and properties*, J. Mater. Res. **8**, 1341 (1993).

[28] K. M. Itoh and H. Watanabe, *Isotope engineering of silicon and diamond for quantum computing and sensing applications*, MRS Commun. **4**, 143 (2014).

[29] R. Pillarisetty, *Academic and industry research progress in germanium nanodevices*, Nature **479**, 324 (2011).

[30] G. Scappucci, et al., *The germanium quantum information route*, Nature Reviews Materials , 1 (2020).

[31] Y. Kamata, *High-k/Ge MOSFETs for future nanoelectronics*, Materials Today **11**, 30 (2008).

[32] T. D. Ladd, et al., *Quantum computers*, Nature **464**, 45 (2010).

[33] I. I. Manin, *Vychislimoe i nevychislimoe [Computable and incomputable]*, Kibernetika ("Sov. radio,", Moskva, 1980).

[34] A. G. J. MacFarlane, J. P. Dowling, and G. J. Milburn, *Quantum technology: the second quantum revolution*, Philosophical Transactions of the Royal Society of London. Series A: Mathematical, Physical and Engineering Sciences **361**, 1655 (2003).

[35] `https://quantumalgorithmzoo.org`, [Accessed: 2020-10-26].

[36] P. W. Shor, *Polynomial-Time Algorithms for Prime Factorization and Discrete Logarithms on a Quantum Computer*, SIAM Rev. **41**, 303 (1999).

[37] L. K. Grover, *A fast quantum mechanical algorithm for database search*, in *Proceedings of the twenty-eighth annual ACM symposium on Theory of Computing*, STOC '96 (Association for Computing Machinery, Philadelphia, Pennsylvania, USA, 1996) pp. 212–219.

[38] L. Tan, *Digital signal processing: fundamentals and applications* (Academic Press, Amsterdam ; Boston, 2008).

[39] K. Perry, *Thinking of you*, in *One of the Boys* (Capitol, 2008).

[40] E. Knill, R. Laflamme, and G. J. Milburn, *A scheme for efficient quantum computation with linear optics*, Nature **409**, 46 (2001).

[41] A. Politi, J. C. F. Matthews, and J. L. O'Brien, *Shor's Quantum Factoring Algorithm on a Photonic Chip*, Science **325**, 1221 (2009).

[42] J. I. Cirac and P. Zoller, *Quantum Computations with Cold Trapped Ions*, Phys. Rev. Lett. **74**, 4091 (1995).

[43] R. Blatt and D. Wineland, *Entangled states of trapped atomic ions*, Nature **453**, 1008 (2008).

[44] Y. Nakamura, Y. A. Pashkin, and J. S. Tsai, *Coherent control of macroscopic quantum states in a single-Cooper-pair box*, Nature **398**, 786 (1999).

[45] L. M. K. Vandersypen and I. L. Chuang, *NMR techniques for quantum control and computation*, Rev. Mod. Phys. **76**, 1037 (2005).

[46] L. M. K. Vandersypen, et al., *Experimental realization of Shor's quantum factoring algorithm using nuclear magnetic resonance*, Nature **414**, 883 (2001).

[47] J. M. Elzerman, et al., *Single-shot read-out of an individual electron spin in a quantum dot*, Nature **430**, 431 (2004).

[48] R. Hanson, et al., *Spins in few-electron quantum dots*, Rev. Mod. Phys. **79**, 1217 (2007).

[49] F. H. L. Koppens, et al., *Driven coherent oscillations of a single electron spin in a quantum dot*, Nature **442**, 766 (2006).

[50] S. Foletti, et al., *Universal quantum control of two-electron spin quantum bits using dynamic nuclear polarization*, Nature Physics **5**, 903 (2009).

[51] J. R. Petta, et al., *Coherent Manipulation of Coupled Electron Spins in Semiconductor Quantum Dots*, Science **309**, 2180 (2005).

[52] M. D. Shulman, et al., *Demonstration of Entanglement of Electrostatically Coupled Singlet-Triplet Qubits*, Science **336**, 202 (2012).

[53] C. Volk, et al., *Loading a quantum-dot based "Qubyte" register*, npj Quantum Information **5**, 1 (2019).

[54] H. Qiao, et al., *Coherent Multispin Exchange Coupling in a Quantum-Dot Spin Chain*, Phys. Rev. X **10**, 031006 (2020).

[55] J. Yoneda, et al., *A quantum-dot spin qubit with coherence limited by charge noise and fidelity higher than 99.9%*, Nature Nanotechnology **13**, 102 (2018).

[56] M. Veldhorst, et al., *An addressable quantum dot qubit with fault-tolerant control-fidelity*, Nat. Nanotech. **9**, 981 (2014).

[57] C. H. Yang, et al., *Silicon qubit fidelities approaching incoherent noise limits via pulse engineering*, Nat Electron **2**, 151 (2019).

[58] D. M. Zajac, et al., *Resonantly driven CNOT gate for electron spins*, Science **359**, 439 (2018).

[59] M. Veldhorst, H. G. J. Eenink, C. H. Yang, and A. S. Dzurak, *Silicon CMOS architecture for a spin-based quantum computer*, Nat. Commun. **8**, 1766 (2017).

[60] L. Petit, et al., *High-fidelity two-qubit gates in silicon above one Kelvin*, arXiv:2007.09034 (2020).

[61] T. F. Watson, et al., *A programmable two-qubit quantum processor in silicon*, Nature **555**, 633 (2018).

[62] K. Takeda, et al., *Quantum tomography of an entangled three-qubit state in silicon*, Nat. Nanotechnol. , 1 (2021).

[63] N. Samkharadze, et al., *Strong spin-photon coupling in silicon*, Science **359**, 1123 (2018).

[64] X. Mi, et al., *A coherent spin–photon interface in silicon*, Nature **555**, 599 (2018).

[65] A. J. Landig, et al., *Coherent spin–photon coupling using a resonant exchange qubit*, Nature **560**, 179 (2018).

[66] C. H. Yang, et al., *Operation of a silicon quantum processor unit cell above one kelvin*, Nature **580**, 350 (2020).

[67] L. Petit, et al., *Universal quantum logic in hot silicon qubits*, Nature **580**, 355 (2020).

[68] D. V. Bulaev and D. Loss, *Spin Relaxation and Decoherence of Holes in Quantum Dots*, Phys. Rev. Lett. **95**, 076805 (2005).

[69] D. V. Bulaev and D. Loss, *Electric Dipole Spin Resonance for Heavy Holes in Quantum Dots*, Phys. Rev. Lett. **98**, 097202 (2007).

[70] M. Failla, et al., *Terahertz quantum Hall effect for spin-split heavy-hole gases in strained Ge quantum wells*, New J. Phys. **18**, 113036 (2016).

[71] A. Sammak, et al., *Shallow and Undoped Germanium Quantum Wells: A Playground for Spin and Hybrid Quantum Technology*, Advanced Functional Materials **29**, 1807613 (2019).

[72] R. Winkler, M. Merkler, T. Darnhofer, and U. Rössler, *Theory for the cyclotron resonance of holes in strained asymmetric Ge-SiGe quantum wells*, Phys. Rev. B **53**, 10858 (1996).

[73] M. Lodari, et al., *Light effective hole mass in undoped Ge/SiGe quantum wells*, Phys. Rev. B **100**, 041304 (2019).

[74] N. W. Hendrickx, et al., *Gate-controlled quantum dots and superconductivity in planar germanium*, Nature Communications **9**, 2835 (2018).

[75] L. A. Terrazos, et al., *Theory of hole-spin qubits in strained germanium quantum dots*, Phys. Rev. B **103**, 125201 (2021).

[76] M. Pioro-Ladrière, et al., *Electrically driven single-electron spin resonance in a slanting Zeeman field*, Nature Physics **4**, 776 (2008).

[77] Y. Tokura, W. G. van der Wiel, T. Obata, and S. Tarucha, *Coherent Single Electron Spin Control in a Slanting Zeeman Field*, Phys. Rev. Lett. **96**, 047202 (2006).

[78] M. Veldhorst, et al., *A two-qubit logic gate in silicon*, Nature **526**, 410 (2015).

[79] Y. Hu, et al., *A Ge/Si heterostructure nanowire-based double quantum dot with integrated charge sensor*, Nat. Nanotech. **2**, 622 (2007).

[80] Y. Hu, F. Kuemmeth, C. M. Lieber, and C. M. Marcus, *Hole spin relaxation in Ge–Si core–shell nanowire qubits*, Nature Nanotechnology **7**, 47 (2012).

[81] M. Brauns, et al., *Highly tuneable hole quantum dots in Ge-Si core-shell nanowires*, Appl. Phys. Lett. **109**, 143113 (2016).

[82] H. Watzinger, et al., *Heavy-Hole States in Germanium Hut Wires*, Nano Lett **16**, 6879 (2016).

[83] L. Vukušić, et al., *Single-Shot Readout of Hole Spins in Ge*, Nano Lett. **18**, 7141 (2018).

[84] H. Watzinger, et al., *A germanium hole spin qubit*, Nature Communications **9**, 3902 (2018).

[85] D. Jirovec, et al., *A singlet-triplet hole spin qubit in planar Ge*, Nat. Mater. , 1 (2021).

[86] N. W. Hendrickx, et al., *Fast two-qubit logic with holes in germanium*, Nature **577**, 487 (2020).

[87] N. W. Hendrickx, et al., *A four-qubit germanium quantum processor*, Nature **591**, 580 (2021).

[88] W. I. L. Lawrie, et al., *Spin Relaxation Benchmarks and Individual Qubit Addressability for Holes in Quantum Dots*, Nano Lett. **20**, 7237 (2020).

[89] A. P. Higginbotham, et al., *Hole Spin Coherence in a Ge/Si Heterostructure Nanowire*, Nano Lett. **14**, 3582 (2014).

[90] F. N. M. Froning, et al., *Ultrafast hole spin qubit with gate-tunable spin–orbit switch functionality*, Nature Nanotechnology , 1 (2021).

[91] K. Wang, et al., *Ultrafast Operations of a Hole Spin Qubit in Ge Quantum Dot*, arXiv:2006.12340 (2020).

[92] L. Hutin, et al., *Si MOS technology for spin-based quantum computing*, in *2018 48th European Solid-State Device Research Conference (ESSDERC)* (2018) pp. 12–17.

[93] R. Maurand, et al., *A CMOS silicon spin qubit*, Nature Communications **7**, 13575 (2016).

[94] W. I. L. Lawrie, et al., *Quantum dot arrays in silicon and germanium*, Appl. Phys. Lett. **116**, 080501 (2020).

[95] C. H. Yang, et al., *Spin-valley lifetimes in a silicon quantum dot with tunable valley splitting*, Nat. Commun. **4**, 2069 (2013).

[96] E. Chanrion, et al., *Charge Detection in an Array of CMOS Quantum Dots*, Phys. Rev. Applied **14**, 024066 (2020).

[97] C. B. Simmons, et al., *Tunable Spin Loading and* T_1 *of a Silicon Spin Qubit Measured by Single-Shot Readout*, Phys. Rev. Lett. **106**, 156804 (2011).

[98] X. Xue, et al., *Benchmarking Gate Fidelities in a Si/SiGe Two-Qubit Device*, Phys. Rev. X **9**, 021011 (2019).

[99] A. R. Mills, et al., *Shuttling a single charge across a one-dimensional array of silicon quantum dots*, Nature Communications **10**, 1063 (2019).

[100] S. Nadj-Perge, S. M. Frolov, E. P. A. M. Bakkers, and L. P. Kouwenhoven, *Spin–orbit qubit in a semiconductor nanowire*, Nature **468**, 1084 (2010).

[101] J. W. G. van den Berg, et al., *Fast Spin-Orbit Qubit in an Indium Antimonide Nanowire*, Phys. Rev. Lett. **110**, 066806 (2013).

[102] J. Yoneda, et al., *Fast Electrical Control of Single Electron Spins in Quantum Dots with Vanishing Influence from Nuclear Spins*, Phys. Rev. Lett. **113**, 267601 (2014).

[103] F. H. L. Koppens, K. C. Nowack, and L. M. K. Vandersypen, *Spin Echo of a Single Electron Spin in a Quantum Dot*, Phys. Rev. Lett. **100**, 236802 (2008).

[104] S. Amasha, et al., *Electrical Control of Spin Relaxation in a Quantum Dot*, Phys. Rev. Lett. **100**, 046803 (2008).

[105] O. E. Dial, et al., *Charge Noise Spectroscopy Using Coherent Exchange Oscillations in a Singlet-Triplet Qubit*, Phys. Rev. Lett. **110**, 146804 (2013).

[106] H. Bluhm, et al., *Enhancing the Coherence of a Spin Qubit by Operating it as a Feedback Loop That Controls its Nuclear Spin Bath*, Phys. Rev. Lett. **105** (2010).

[107] F. K. Malinowski, et al., *Notch filtering the nuclear environment of a spin qubit*, Nature Nanotechnology **12**, 16 (2017).

[108] P. Cerfontaine, et al., *Closed-loop control of a GaAs-based singlet-triplet spin qubit with 99.5% gate fidelity and low leakage*, Nature Communications **11**, 4144 (2020).

[109] J. M. Nichol, et al., *High-fidelity entangling gate for double-quantum-dot spin qubits*, npj Quantum Information **3**, 1 (2017).

[110] M. Cardona and F. H. Pollak, *Energy-Band Structure of Germanium and Silicon: The k·p Method*, Phys. Rev. **142**, 530 (1966).

[111] R. Winkler, *Spin-orbit coupling effects in two-dimensional electron and hole systems* (Springer, Berlin, Heidelberg, 2003).

[112] W. Nolting and A. Ramakanth, *Quantum Theory of Magnetism* (Springer-Verlag, Berlin Heidelberg, 2009).

[113] J. M. Luttinger and W. Kohn, *Motion of Electrons and Holes in Perturbed Periodic Fields*, Phys. Rev. **97**, 869 (1955).

[114] J. M. Luttinger, *Quantum Theory of Cyclotron Resonance in Semiconductors: General Theory*, Phys. Rev. **102**, 1030 (1956).

[115] R. Winkler, et al., *Spin orientation of holes in quantum wells*, Semicond. Sci. Technol. **23**, 114017 (2008).

[116] A. Baldereschi and N. O. Lipari, *Direct Exciton Spectrum in Diamond and Zinc-Blende Semiconductors*, Phys. Rev. Lett. **25**, 373 (1970).

[117] P. Lawaetz, *Valence-Band Parameters in Cubic Semiconductors*, Phys. Rev. B **4**, 3460 (1971).

[118] E. Marcellina, A. R. Hamilton, R. Winkler, and D. Culcer, *Spin-orbit interactions in inversion-asymmetric two-dimensional hole systems: A variational analysis*, Phys. Rev. B **95**, 075305 (2017).

[119] R. Winkler, *Spin density matrix of spin-3/2 hole systems*, Phys. Rev. B **70**, 125301 (2004).

[120] N. W. Ashcroft and N. D. Mermin, *Solid State Physics* (Holt, Rinehart and Winston, 1976).

[121] Y. M. Haddara, P. Ashburn, and D. M. Bagnall, *Silicon-Germanium: Properties, Growth and Applications*, in Springer Handbook of Electronic and Photonic Materials, Springer Handbooks (Springer International Publishing, Cham, 2017) pp. 481–498.

[122] G. L. Bir and G. E. Pikus, *Symmetry and Strain-induced Effects in Semiconductors* (Wiley, New York, 1974).

[123] D. Culcer, A. C. Keser, Y. Li, and G. Tkachov, *Transport in two-dimensional topological materials: recent developments in experiment and theory*, 2D Mater. **7**, 022007 (2020).

[124] M. V. Fischetti and S. E. Laux, *Band structure, deformation potentials, and carrier mobility in strained Si, Ge, and SiGe alloys*, Journal of Applied Physics **80**, 2234 (1996).

[125] J. J. Wortman and R. A. Evans, *Young's Modulus, Shear Modulus, and Poisson's Ratio in Silicon and Germanium*, Journal of Applied Physics **36**, 153 (1965).

[126] W. Mason, *Physical Acoustics* (Elsevier, 1958).

[127] Z. Wang, et al., *Optimal operation points for ultrafast, highly coherent Ge hole spin-orbit qubits*, npj Quantum Information **7**, 1 (2021).

[128] M. V. Durnev, M. M. Glazov, and E. L. Ivchenko, *Spin-orbit splitting of valence subbands in semiconductor nanostructures*, Phys. Rev. B **89**, 075430 (2014).

[129] H. W. van Kesteren, E. C. Cosman, W. A. J. A. van der Poel, and C. T. Foxon, *Fine structure of excitons in type-II GaAs/AlAs quantum wells*, Phys. Rev. B **41**, 5283 (1990).

[130] B. Venitucci and Y.-M. Niquet, *Simple model for electrical hole spin manipulation in semiconductor quantum dots: Impact of dot material and orientation*, Phys. Rev. B **99**, 115317 (2019).

[131] N. Ares, et al., *Nature of Tunable Hole g Factors in Quantum Dots*, Phys. Rev. Lett. **110**, 046602 (2013).

[132] N. W. Hendrickx, et al., *A single-hole spin qubit*, Nature Communications **11**, 3478 (2020).

[133] F. Nichele, et al., *Characterization of spin-orbit interactions of GaAs heavy holes using a quantum point contact*, Phys. Rev. Lett. **113**, 046801 (2014).

[134] P. M. Mutter and G. Burkard, *Cavity control over heavy-hole spin qubits in inversion-symmetric crystals*, Phys. Rev. B **102**, 205412 (2020).

[135] L. P. Kouwenhoven, et al., *Electron Transport in Quantum Dots*, in *Mesoscopic Electron Transport*, NATO ASI Series (Springer, Dordrecht, 1997) pp. 105–214.

[136] J. Fischer, W. A. Coish, D. V. Bulaev, and D. Loss, *Spin decoherence of a heavy hole coupled to nuclear spins in a quantum dot*, Phys. Rev. B **78**, 155329 (2008).

[137] C. Testelin, F. Bernardot, B. Eble, and M. Chamarro, *Hole-spin dephasing time associated with hyperfine interaction in quantum dots*, Phys. Rev. B **79**, 195440 (2009).

[138] P. Philippopoulos, S. Chesi, and W. A. Coish, *First-principles hyperfine tensors for electrons and holes in GaAs and silicon*, Phys. Rev. B **101**, 115302 (2020).

[139] Private discussions with W.A. Coish.

[140] R. J. Warburton, *Single spins in self-assembled quantum dots*, Nature Materials **12**, 483 (2013).

[141] F. Maier and D. Loss, *Effect of strain on hyperfine-induced hole-spin decoherence in quantum dots*, Phys. Rev. B **85**, 195323 (2012).

[142] J. Fischer and D. Loss, *Hybridization and Spin Decoherence in Heavy-Hole Quantum Dots*, Phys. Rev. Lett. **105**, 266603 (2010).

[143] D. P. DiVincenzo, *The Physical Implementation of Quantum Computation*, Fortschritte der Physik **48**, 771 (2000).

[144] M. H. Devoret and R. J. Schoelkopf, *Superconducting Circuits for Quantum Information: An Outlook*, Science **339**, 1169 (2013).

[145] W. G. van der Wiel, et al., *Electron transport through double quantum dots*, Rev. Mod. Phys. **75**, 1 (2002).

[146] F. A. Zwanenburg, et al., *Silicon quantum electronics*, Rev. Mod. Phys. **85**, 961 (2013).

[147] S.-W. Chung, J.-Y. Yu, and J. R. Heath, *Silicon nanowire devices*, Appl. Phys. Lett. **76**, 2068 (2000).

[148] L. J. Lauhon, M. S. Gudiksen, D. Wang, and C. M. Lieber, *Epitaxial core–shell and core–multishell nanowire heterostructures*, Nature **420**, 57 (2002).

[149] M. T. Björk, et al., *Few-Electron Quantum Dots in Nanowires*, Nano Lett. **4**, 1621 (2004).

[150] D. L. Klein, et al., *An approach to electrical studies of single nanocrystals*, Appl. Phys. Lett. **68**, 2574 (1996).

[151] Z. R. Wasilewski, S. Fafard, and J. P. McCaffrey, *Size and shape engineering of vertically stacked self-assembled quantum dots*, Journal of Crystal Growth **201-202**, 1131 (1999).

[152] M. A. Cusack, P. R. Briddon, and M. Jaros, *Electronic structure of InAs/GaAs self-assembled quantum dots*, Phys. Rev. B **54**, R2300 (1996).

[153] S. J. Angus, A. J. Ferguson, A. S. Dzurak, and R. G. Clark, *Gate-Defined Quantum Dots in Intrinsic Silicon*, Nano Lett. **7**, 2051 (2007).

[154] X. Luo, T. Nishimura, T. Yajima, and A. Toriumi, *Understanding of Fermi level pinning at metal/germanium interface based on semiconductor structure*, Appl. Phys. Express **13**, 031003 (2020).

[155] T. Nishimura, K. Kita, and A. Toriumi, *Evidence for strong Fermi-level pinning due to metal-induced gap states at metal/germanium interface*, Appl. Phys. Lett. **91**, 123123 (2007).

[156] A. Dimoulas, P. Tsipas, A. Sotiropoulos, and E. K. Evangelou, *Fermi-level pinning and charge neutrality level in germanium*, Appl. Phys. Lett. **89**, 252110 (2006).

[157] L. Petit, et al., *Spin Lifetime and Charge Noise in Hot Silicon Quantum Dot Qubits*, Phys. Rev. Lett. **121**, 076801 (2018).

[158] K. Ono, D. G. Austing, Y. Tokura, and S. Tarucha, *Current Rectification by Pauli Exclusion in a Weakly Coupled Double Quantum Dot System*, Science **297**, 1313 (2002).

[159] G. Yamahata, et al., *Magnetic field dependence of Pauli spin blockade: A window into the sources of spin relaxation in silicon quantum dots*, Phys. Rev. B **86**, 115322 (2012).

[160] A. C. Johnson, et al., *Singlet-triplet spin blockade and charge sensing in a few-electron double quantum dot*, Phys. Rev. B **72**, 165308 (2005).

[161] T. Meunier, V. E. Calado, and L. M. K. Vandersypen, *Efficient controlled-phase gate for single-spin qubits in quantum dots*, Phys. Rev. B **83**, 121403 (2011).

[162] J. J. Pla, et al., *A single-atom electron spin qubit in silicon*, Nature **489**, 541 (2012).

[163] M. J. Gullans and J. R. Petta, *Protocol for a resonantly driven three-qubit Toffoli gate with silicon spin qubits*, Phys. Rev. B **100**, 085419 (2019).

[164] J. Danon and Y. V. Nazarov, *Pauli spin blockade in the presence of strong spin-orbit coupling*, Phys. Rev. B **80**, 041301 (2009).

[165] B. Hetényi, C. Kloeffel, and D. Loss, *Exchange interaction of hole-spin qubits in double quantum dots in highly anisotropic semiconductors*, Phys. Rev. Research **2**, 033036 (2020).

[166] J. R. Schrieffer and P. A. Wolff, *Relation between the Anderson and Kondo Hamiltonians*, Phys. Rev. **149**, 491 (1966).

[167] M. Russ, et al., *High-fidelity quantum gates in Si/SiGe double quantum dots*, Phys. Rev. B **97**, 085421 (2018).

[168] S. I. Erlingsson, Y. V. Nazarov, and V. I. Fal'ko, *Nucleus-mediated spin-flip transitions in GaAs quantum dots*, Phys. Rev. B **64**, 195306 (2001).

[169] T. Fujisawa, et al., *Allowed and forbidden transitions in artificial hydrogen and helium atoms*, Nature **419**, 278 (2002).

[170] M. Reed, et al., *Reduced Sensitivity to Charge Noise in Semiconductor Spin Qubits via Symmetric Operation*, Phys. Rev. Lett. **116**, 110402 (2016).

[171] F. Martins, et al., *Noise Suppression Using Symmetric Exchange Gates in Spin Qubits*, Phys. Rev. Lett. **116**, 116801 (2016).

[172] J. Salfi, J. A. Mol, D. Culcer, and S. Rogge, *Charge-Insensitive Single-Atom Spin-Orbit Qubit in Silicon*, Phys. Rev. Lett. **116**, 246801 (2016).

[173] J. H. Prechtel, et al., *Decoupling a hole spin qubit from the nuclear spins*, Nature Materials **15**, 981 (2016).

[174] A. Sigillito, et al., *Electron Spin Coherence of Shallow Donors in Natural and Isotopically Enriched Germanium*, Phys. Rev. Lett. **115**, 247601 (2015).

[175] R. C. C. Leon, et al., *Bell-state tomography in a silicon many-electron artificial molecule*, Nat Commun **12**, 3228 (2021).

[176] `https://www.ibm.com/downloads/cas/1V29LE4Z`, [Accessed: 2020-10-26].

[177] N. W. Hendrickx, et al., *Ballistic supercurrent discretization and micrometer-long Josephson coupling in germanium*, Phys. Rev. B **99**, 075435 (2019).

[178] M. Brauns, S. V. Amitonov, P.-C. Spruijtenburg, and F. A. Zwanenburg, *Palladium gates for reproducible quantum dots in silicon*, Scientific Reports **8**, 5690 (2018).

[179] H. C. Lin, P. D. Ye, and G. D. Wilk, *Leakage current and breakdown electric-field studies on ultrathin atomic-layer-deposited* Al_2O_3 *on GaAs*, Appl. Phys. Lett. **87**, 182904 (2005).

[180] Y. Q. Wu, H. C. Lin, P. D. Ye, and G. D. Wilk, *Current transport and maximum dielectric strength of atomic-layer-deposited ultrathin* Al_2O_3 *on GaAs*, Appl. Phys. Lett. **90**, 072105 (2007).

[181] J. Yota, H. Shen, and R. Ramanathan, *Characterization of atomic layer deposition* HfO_2, Al_2O_3, *and plasma-enhanced chemical vapor deposition* Si_3N_4 *as metal–insulator–metal capacitor dielectric for GaAs HBT technology*, Journal of Vacuum Science & Technology A: Vacuum, Surfaces, and Films **31**, 01A134 (2013).

[182] L. DiCarlo, et al., *Differential Charge Sensing and Charge Delocalization in a Tunable Double Quantum Dot*, Phys. Rev. Lett. **92**, 226801 (2004).

[183] S. W. Jolin, et al., *Calibration of mixer amplitude and phase imbalance in superconducting circuits*, Review of Scientific Instruments **91**, 124707 (2020).

[184] C. Kloeffel, M. Trif, P. Stano, and D. Loss, *Circuit QED with hole-spin qubits in Ge/Si nanowire quantum dots*, Phys. Rev. B **88**, 241405 (2013).

[185] F. Maier, J. Klinovaja, and D. Loss, *Majorana fermions in Ge/Si hole nanowires*, Phys. Rev. B **90**, 195421 (2014).

[186] J. Xiang, et al., *Ge/Si nanowire mesoscopic Josephson junctions*, Nat. Nanotech. **1**, 208 (2006).

[187] M. Virgilio and G. Grosso, *Type-I alignment and direct fundamental gap in SiGe based heterostructures*, J. Phys.: Condens. Matter **18**, 1021 (2006).

[188] I. L. Drichko, et al., *Effective g factor of 2D holes in strained Ge quantum wells*, Journal of Applied Physics **123**, 165703 (2018).

[189] Q. Shi, M. A. Zudov, C. Morrison, and M. Myronov, *Spinless composite fermions in an ultrahigh-quality strained Ge quantum well*, Phys. Rev. B **91**, 241303 (2015).

[190] C. Morrison and M. Myronov, *Electronic transport anisotropy of 2D carriers in biaxial compressive strained germanium*, Appl. Phys. Lett. **111**, 192103 (2017).

[191] M. G. Borselli, et al., *Pauli spin blockade in undoped Si/SiGe two-electron double quantum dots*, Appl. Phys. Lett. **99**, 063109 (2011).

[192] B. M. Maune, et al., *Coherent singlet-triplet oscillations in a silicon-based double quantum dot*, Nature **481**, 344 (2012).

[193] R. Mizokuchi, et al., *Ballistic One-Dimensional Holes with Strong g-Factor Anisotropy in Germanium*, Nano Lett. **18**, 4861 (2018).

[194] D. Laroche, et al., *Magneto-transport analysis of an ultra-low-density two-dimensional hole gas in an undoped strained Ge/SiGe heterostructure*, Appl. Phys. Lett. **108**, 233504 (2016).

[195] T. M. Lu, et al., *Effective g factor of low-density two-dimensional holes in a Ge quantum well*, Appl. Phys. Lett. **111**, 102108 (2017).

[196] Y.-H. Su, et al., *Effects of surface tunneling of two-dimensional hole gases in undoped Ge/GeSi heterostructures*, Phys. Rev. Materials **1**, 044601 (2017).

[197] W. J. Hardy, et al., *Single and double hole quantum dots in strained Ge/SiGe quantum wells*, Nanotechnology **30**, 215202 (2019).

[198] V. A. Shah, et al., *Reverse graded relaxed buffers for high Ge content SiGe virtual substrates*, Appl. Phys. Lett. **93**, 192103 (2008).

[199] G. Capellini, et al., *Strain relaxation in high Ge content SiGe layers deposited on Si*, Journal of Applied Physics **107**, 063504 (2010).

[200] B. Vincent, et al., *Si passivation for Ge pMOSFETs: Impact of Si cap growth conditions*, Solid-State Electronics Papers Selected from the 5th International SiGe Technology and Devices Meeting (ISTDM 2010), **60**, 116 (2011).

[201] G. Capellini, et al., *High temperature x ray diffraction measurements on Ge/Si(001) heterostructures: A study on the residual tensile strain*, Journal of Applied Physics **111**, 073518 (2012).

[202] T. E. Clark, et al., *Diameter Dependent Growth Rate and Interfacial Abruptness in Vapor–Liquid–Solid Si/$Si_{1-x}Ge_x$ Heterostructure Nanowires*, Nano Lett. **8**, 1246 (2008).

[203] J. T. Held, et al., *Obtaining Structural Parameters from STEM–EDX Maps of Core/Shell Nanocrystals for Optoelectronics*, ACS Appl. Nano Mater. **1**, 989 (2018).

[204] X. Mi, et al., *Magnetotransport studies of mobility limiting mechanisms in undoped Si/SiGe heterostructures*, Phys. Rev. B **92**, 035304 (2015).

[205] J. A. Kittl, et al., *Silicides and germanides for nano-CMOS applications*, Materials Science and Engineering: B Front-End Junction and Contact Formation in Future Silicon/Germanium Based Devices, **154-155**, 144 (2008).

[206] E. Alptekin, C. J. Kirkpatrick, V. Misra, and M. C. Ozturk, *Platinum Germanosilicide Contacts Formed on Strained and Relaxed $Si_{1-x}Ge_x$ Layers*, IEEE Transactions on Electron Devices **56**, 1220 (2009).

[207] V. T. Dolgopolov, et al., *Remote-doping scattering and the local field corrections in the 2D electron system in a modulation-doped Si/SiGe quantum well*, Superlattices and Microstructures **33**, 271 (2003).

[208] A. Gold, *Mobility and metal–insulator transition of the two-dimensional electron gas in SiGe/Si/SiGe quantum wells*, Journal of Applied Physics **108**, 063710 (2010).

[209] T. M. Lu, et al., *Upper limit of two-dimensional electron density in enhancement-mode Si/SiGe heterostructure field-effect transistors*, Appl. Phys. Lett. **99**, 153510 (2011).

[210] L. A. Tracy, et al., *Observation of percolation-induced two-dimensional metal-insulator transition in a Si MOSFET*, Phys. Rev. B **79**, 235307 (2009).

[211] J.-S. Kim, A. M. Tyryshkin, and S. A. Lyon, *Annealing shallow Si/SiO_2 interface traps in electron-beam irradiated high-mobility metal-oxide-silicon transistors*, Appl. Phys. Lett. **110**, 123505 (2017).

[212] D. R. McCamey, et al., *Donor activation and damage in Si–SiO_2 from low-dose, low-energy ion implantation studied via electrical transport in MOSFETs*, Semicond. Sci. Technol. **20**, 363 (2005).

[213] P. T. Coleridge, R. Stoner, and R. Fletcher, *Low-field transport coefficients in GaAs/$Ga_{1-x}Al_xAs$ heterostructures*, Phys. Rev. B **39**, 1120 (1989).

[214] D. Laroche, et al., *Scattering mechanisms in shallow undoped Si/SiGe quantum wells*, AIP Advances **5**, 107106 (2015).

[215] C.-T. Huang, J.-Y. Li, K. S. Chou, and J. C. Sturm, *Screening of remote charge scattering sites from the oxide/silicon interface of strained Si two-dimensional electron gases by an intermediate tunable shielding electron layer*, Appl. Phys. Lett. **104**, 243510 (2014).

[216] T. Irisawa, et al., *Hole density dependence of effective mass, mobility and transport time in strained Ge channel modulation-doped heterostructures*, Appl. Phys. Lett. **82**, 1425 (2003).

[217] W. d. Lange, F. A. P. Blom, and J. H. Wolter, *Effective electron mass in GaAs/AlxGa1-xAs heterostructures under hydrostatic pressure*, Semicond. Sci. Technol. **8**, 341 (1993).

[218] P. T. Coleridge, *Magnetic field induced metal–insulator transitions in p-SiGe*, Solid State Communications Advances in Studies of Electrons in Low Dimensional Structures, **127**, 777 (2003).

[219] M. Lodari, et al., *Low percolation density and charge noise with holes in germanium*, Mater. Quantum. Technol. **1**, 011002 (2021).

[220] J. T. Muhonen, et al., *Storing quantum information for 30 seconds in a nanoelectronic device*, Nat. Nanotech. **9**, 986 (2014).

[221] F. Vigneau, et al., *Germanium Quantum-Well Josephson Field-Effect Transistors and Interferometers*, Nano Lett. **19**, 1023 (2019).

[222] D. Sabbagh, et al., *Quantum Transport Properties of Industrial* $^{28}Si/^{28}SiO_2$, Phys. Rev. Applied **12**, 014013 (2019).

[223] B. Paquelet Wuetz, et al., *Multiplexed quantum transport using commercial off-the-shelf CMOS at sub-kelvin temperatures*, npj Quantum Information **6**, 1 (2020).

[224] R. Li, et al., *A crossbar network for silicon quantum dot qubits*, Science Advances **4**, eaar3960 (2018).

[225] S. Das Sarma and F. Stern, *Single-particle relaxation time versus scattering time in an impure electron gas*, Phys. Rev. B **32**, 8442 (1985).

[226] J. P. Harrang, et al., *Quantum and classical mobility determination of the dominant scattering mechanism in the two-dimensional electron gas of an AlGaAs/GaAs heterojunction*, Phys. Rev. B **32**, 8126 (1985).

[227] G. Bauer and H. Kahlert, *Low-Temperature Non-Ohmic Galvanomagnetic Effects in Degenerate n-Type InAs*, Phys. Rev. B **5**, 566 (1972).

[228] S. W. Jung, T. Fujisawa, Y. Hirayama, and Y. H. Jeong, *Background charge fluctuation in a GaAs quantum dot device*, Appl. Phys. Lett. **85**, 768 (2004).

[229] B. M. Freeman, J. S. Schoenfield, and H. Jiang, *Comparison of low frequency charge noise in identically patterned* Si/SiO_2 *and Si/SiGe quantum dots*, Appl. Phys. Lett. **108**, 253108 (2016).

[230] E. J. Connors, et al., *Low-frequency charge noise in Si/SiGe quantum dots*, Phys. Rev. B **100**, 165305 (2019).

[231] F. Jekat, et al., *Exfoliated hexagonal BN as gate dielectric for InSb nanowire quantum dots with improved gate hysteresis and charge noise*, Appl. Phys. Lett. **116**, 253101 (2020).

[232] J. Basset, et al., *Evaluating charge noise acting on semiconductor quantum dots in the circuit quantum electrodynamics architecture*, Appl. Phys. Lett. **105**, 063105 (2014).

[233] F. van Riggelen, et al., *A two-dimensional array of single-hole quantum dots*, Appl. Phys. Lett. **118**, 044002 (2021).

[234] D. N. Basov, R. D. Averitt, and D. Hsieh, *Towards properties on demand in quantum materials*, Nat. Mater. **16**, 1077 (2017).

[235] R. Moriya, et al., *Cubic Rashba Spin-Orbit Interaction of a Two-Dimensional Hole Gas in a Strained-Ge-SiGe Quantum Well*, Phys. Rev. Lett. **113**, 086601 (2014).

[236] C. H. Yang, et al., *Orbital and valley state spectra of a few-electron silicon quantum dot*, Phys. Rev. B **86**, 115319 (2012).

[237] W. Lu, et al., *One-dimensional hole gas in germanium/silicon nanowire heterostructures*, PNAS **102**, 10046 (2005).

[238] G. Katsaros, et al., *Hybrid superconductor–semiconductor devices made from self-assembled SiGe nanocrystals on silicon*, Nat. Nanotech. **5**, 458 (2010).

[239] T. Larsen, et al., *Semiconductor-Nanowire-Based Superconducting Qubit*, Phys. Rev. Lett. **115**, 127001 (2015).

[240] A. Dobbie, et al., *Ultra-high hole mobility exceeding one million in a strained germanium quantum well*, Appl. Phys. Lett. **101**, 172108 (2012).

[241] C. C. Escott, F. A. Zwanenburg, and A. Morello, *Resonant tunnelling features in quantum dots*, Nanotech. **21**, 274018 (2010).

[242] A. V. Nenashev, A. V. Dvurechenskii, and A. F. Zinovieva, *Wave functions and g factor of holes in Ge/Si quantum dots*, Phys. Rev. B **67**, 205301 (2003).

[243] S. Tarucha, et al., *Shell Filling and Spin Effects in a Few Electron Quantum Dot*, Phys. Rev. Lett. **77**, 3613 (1996).

[244] W. H. Lim, C. H. Yang, F. A. Zwanenburg, and A. S. Dzurak, *Spin filling of valley–orbit states in a silicon quantum dot*, Nanotechnology **22**, 335704 (2011).

[245] S. M. Reimann and M. Manninen, *Electronic structure of quantum dots*, Rev. Mod. Phys. **74**, 1283 (2002).

[246] T. Hensgens, et al., *Quantum simulation of a Fermi–Hubbard model using a semiconductor quantum dot array,* Nature **548**, 70 (2017).

[247] S. D. Liles, et al., *Spin and orbital structure of the first six holes in a silicon metal-oxide-semiconductor quantum dot*, Nat. Comm. **9** (2018).

[248] F. Maier, C. Kloeffel, and D. Loss, *Tunable g factor and phonon-mediated hole spin relaxation in Ge/Si nanowire quantum dots,* Phys. Rev. B **87** (2013).

[249] E. Knill, et al., *Randomized benchmarking of quantum gates*, Phys. Rev. A **77**, 012307 (2008).

[250] K. Takeda, et al., *Optimized electrical control of a Si/SiGe spin qubit in the presence of an induced frequency shift*, npj Quantum Information **4**, 54 (2018).

[251] B. Hensen, et al., *A silicon quantum-dot-coupled nuclear spin qubit*, Nature Nanotechnology **15**, 13 (2020).

[252] A. Crippa, et al., *Electrical Spin Driving by g-Matrix Modulation in Spin-Orbit Qubits*, Phys. Rev. Lett. **120**, 137702 (2018).

[253] A. Morello, et al., *Single-shot readout of an electron spin in silicon*, Nature **467**, 687 (2010).

[254] V. S. Pribiag, et al., *Electrical control of single hole spins in nanowire quantum dots,* Nature Nanotechnology **8**, 170 (2013).

[255] K. C. Nowack, F. H. L. Koppens, Y. V. Nazarov, and L. M. K. Vandersypen, *Coherent Control of a Single Electron Spin with Electric Fields*, Science **318**, 1430 (2007).

[256] F. N. M. Froning, et al., *Single, double, and triple quantum dots in Ge/Si nanowires,* Appl. Phys. Lett. **113**, 073102 (2018).

[257] L. He, G. Bester, and A. Zunger, *Electronic Phase Diagrams of Carriers in Self-Assembled Quantum Dots: Violation of Hund's Rule and the Aufbau Principle for Holes,* Phys. Rev. Lett. **95**, 246804 (2005).

[258] R. J. Schoelkopf, et al., *The Radio-Frequency Single-Electron Transistor (RF-SET): A Fast and Ultrasensitive Electrometer*, Science **280**, 1238 (1998).

[259] D. J. Reilly, C. M. Marcus, M. P. Hanson, and A. C. Gossard, *Fast single-charge sensing with a rf quantum point contact,* Appl. Phys. Lett. **91**, 162101 (2007).

[260] C. Barthel, et al., *Fast sensing of double-dot charge arrangement and spin state with a radio-frequency sensor quantum dot*, Phys. Rev. B **81**, 161308 (2010).

[261] S. A. Studenikin, et al., *Enhanced charge detection of spin qubit readout via an intermediate state*, Appl. Phys. Lett. **101**, 233101 (2012).

[262] P. Harvey-Collard, et al., *High-Fidelity Single-Shot Readout for a Spin Qubit via an Enhanced Latching Mechanism*, Phys. Rev. X **8**, 021046 (2018).

[263] G. Zheng, et al., *Rapid gate-based spin read-out in silicon using an on-chip resonator*, Nature Nanotechnology **14**, 742 (2019).

[264] A. Bogan, et al., *Single hole spin relaxation probed by fast single-shot latched charge sensing*, Communications Physics **2**, 1 (2019).

[265] B. D. Gerardot, et al., *Optical pumping of a single hole spin in a quantum dot*, Nature **451**, 441 (2008).

[266] B. M. Terhal, *Quantum error correction for quantum memories*, Rev. Mod. Phys. **87**, 307 (2015).

[267] Y. He, et al., *A two-qubit gate between phosphorus donor electrons in silicon*, Nature **571**, 371 (2019).

[268] M. T. Mądzik, et al., *Conditional quantum operation of two exchange-coupled single-donor spin qubits in a MOS-compatible silicon device*, Nature Communications **12**, 181 (2021).

[269] C. H. Yang, et al., *Charge state hysteresis in semiconductor quantum dots*, Appl. Phys. Lett. **105**, 183505 (2014).

[270] E. Barnes, J. P. Kestner, N. T. T. Nguyen, and S. Das Sarma, *Screening of charged impurities with multielectron singlet-triplet spin qubits in quantum dots*, Phys. Rev. B **84**, 235309 (2011).

[271] J. M. Taylor, et al., *Fault-tolerant architecture for quantum computation using electrically controlled semiconductor spins*, Nature Physics **1**, 177 (2005).

[272] A. E. Seedhouse, et al., *Pauli Blockade in Silicon Quantum Dots with Spin-Orbit Control*, PRX Quantum **2**, 010303 (2021).

[273] K. W. Chan, et al., *Assessment of a Silicon Quantum Dot Spin Qubit Environment via Noise Spectroscopy*, Phys. Rev. Applied **10**, 044017 (2018).

[274] L. DiCarlo, et al., *Demonstration of two-qubit algorithms with a superconducting quantum processor*, Nature **460**, 240 (2009).

[275] C. Song, et al., *10-Qubit Entanglement and Parallel Logic Operations with a Superconducting Circuit*, Phys. Rev. Lett. **119**, 180511 (2017).

[276] G. de Lange, et al., *Realization of Microwave Quantum Circuits Using Hybrid Superconducting-Semiconducting Nanowire Josephson Elements*, Phys. Rev. Lett. **115**, 127002 (2015).

[277] J. D. Sau, R. M. Lutchyn, S. Tewari, and S. Das Sarma, *Generic New Platform for Topological Quantum Computation Using Semiconductor Heterostructures*, Phys. Rev. Lett. **104**, 040502 (2010).

[278] J. Alicea, *Majorana fermions in a tunable semiconductor device*, Phys. Rev. B **81**, 125318 (2010).

[279] S. Hoffman, C. Schrade, J. Klinovaja, and D. Loss, *Universal quantum computation with hybrid spin-Majorana qubits*, Phys. Rev. B **94**, 045316 (2016).

[280] M. Leijnse and K. Flensberg, *Quantum Information Transfer between Topological and Spin Qubit Systems*, Phys. Rev. Lett. **107**, 210502 (2011).

[281] M. Leijnse and K. Flensberg, *Hybrid topological-spin qubit systems for two-qubit-spin gates*, Phys. Rev. B **86**, 104511 (2012).

[282] C. Morrison, et al., *Observation of Rashba zero-field spin splitting in a strained germanium 2D hole gas*, Appl. Phys. Lett. **105**, 182401 (2014).

[283] V. E. Calado, et al., *Ballistic Josephson junctions in edge-contacted graphene*, Nature Nanotechnology **10**, 761 (2015).

[284] Z. Wan, et al., *Induced superconductivity in high-mobility two-dimensional electron gas in gallium arsenide heterostructures*, Nature Communications **6**, 7426 (2015).

[285] W. Yu, et al., *Superconducting proximity effect in inverted InAs/GaSb quantum well structures with Ta electrodes*, Appl. Phys. Lett. **105**, 192107 (2014).

[286] F. Qu, et al., *Strong Superconducting Proximity Effect in Pb-Bi_2Te_3 Hybrid Structures*, Scientific Reports **2**, 339 (2012).

[287] I. O. Kulik and A. N. Omel'yanchuk, *Properties of Superconducting Microbridges in the Pure Limit*, Fiz. Nizk. Temp. **3**, 945 (1977).

[288] R. C. Dynes and T. A. Fulton, *Supercurrent Density Distribution in Josephson Junctions*, Phys. Rev. B **3**, 3015 (1971).

[289] D. Averin and A. Bardas, *ac Josephson Effect in a Single Quantum Channel*, Phys. Rev. Lett. **75**, 1831 (1995).

[290] M. Kjaergaard, et al., *Transparent Semiconductor-Superconductor Interface and Induced Gap in an Epitaxial Heterostructure Josephson Junction*, Phys. Rev. Applied **7**, 034029 (2017).

[291] C. Nguyen, H. Kroemer, and E. L. Hu, *Anomalous Andreev conductance in InAs-AlSb quantum well structures with Nb electrodes*, Phys. Rev. Lett. **69**, 2847 (1992).

[292] C. Nguyen, H. Kroemer, and E. L. Hu, *Contact resistance of superconductor-semiconductor interfaces: The case of Nb-InAs/AlSb quantum-well structures*, Appl. Phys. Lett. **65**, 103 (1994).

[293] C. W. J. Beenakker and H. van Houten, *Josephson current through a superconducting quantum point contact shorter than the coherence length*, Phys. Rev. Lett. **66**, 3056 (1991).

[294] A. Furusaki, H. Takayanagi, and M. Tsukada, *Theory of quantum conduction of supercurrent through a constriction*, Phys. Rev. Lett. **67**, 132 (1991).

[295] H. Takayanagi, T. Akazaki, and J. Nitta, *Observation of Maximum Supercurrent Quantization in a Superconducting Quantum Point Contact*, Phys. Rev. Lett. **75**, 3533 (1995).

[296] T. Bauch, et al., *Correlated quantization of supercurrent and conductance in a superconducting quantum point contact*, Phys. Rev. B **71**, 174502 (2005).

[297] H. Irie, Y. Harada, H. Sugiyama, and T. Akazaki, *Josephson coupling through one-dimensional ballistic channel in semiconductor-superconductor hybrid quantum point contacts*, Phys. Rev. B **89**, 165415 (2014).

[298] A. Furusaki, H. Takayanagi, and M. Tsukada, *Josephson effect of the superconducting quantum point contact*, Phys. Rev. B **45**, 10563 (1992).

[299] M. Tinkham, *Introduction to Superconductivity* (Courier Corporation, 2004).

[300] C. W. J. Beenakker, *Random-matrix theory of quantum transport*, Rev. Mod. Phys. **69**, 731 (1997).

[301] H. Zhang, et al., *Ballistic superconductivity in semiconductor nanowires*, Nat. Comm. **8**, 16025 (2017).

[302] M. Kjaergaard, et al., *Quantized conductance doubling and hard gap in a two-dimensional semiconductor–superconductor heterostructure*, Nat. Comm. **7**, 12841 (2016).

[303] J. J. Hauser, *Penetration depth and related properties of Al films with enhanced superconductivity*, J Low Temp Phys **7**, 335 (1972).

[304] H. J. Suominen, et al., *Anomalous Fraunhofer interference in epitaxial superconductor-semiconductor Josephson junctions*, Phys. Rev. B **95**, 035307 (2017).

[305] N. Klein, et al., *The effective microwave surface impedance of high T_c thin films*, J. Appl. Phys. **67**, 6940 (1990).

[306] A. I. Gubin, et al., *Dependence of magnetic penetration depth on the thickness of superconducting Nb thin films*, Phys. Rev. B **72** (2005).

[307] M. Octavio, M. Tinkham, G. E. Blonder, and T. M. Klapwijk, *Subharmonic energy-gap structure in superconducting constrictions*, Phys. Rev. B **27**, 6739 (1983).

[308] K. Flensberg, J. B. Hansen, and M. Octavio, *Subharmonic energy-gap structure in superconducting weak links*, Phys. Rev. B **38**, 8707 (1988).

[309] A. A. Milne, *Pooh's Little Instruction Book* (Dutton Juvenile, New York, 1995).

[310] M. Kjaergaard, et al., *Superconducting Qubits: Current State of Play*, Annu. Rev. Condens. Matter Phys. **11**, 369 (2020).

[311] Z. Cai, *Resource Estimation for Quantum Variational Simulations of the Hubbard Model*, Phys. Rev. Applied **14**, 014059 (2020).

[312] L. S. Bishop, et al., *Quantum Volume*, Unpublished: https://storageconsortium.de/content/sites/default/files/quantum-volumehp08co1vbo0cc8fr.pdf (2017).

[313] D. P. Franke, J. S. Clarke, L. M. K. Vandersypen, and M. Veldhorst, *Rent's rule and extensibility in quantum computing*, Microprocessors and Microsystems **67**, 1 (2019).

[314] N. C. Jones, et al., *Layered Architecture for Quantum Computing*, Phys. Rev. X **2**, 031007 (2012).

[315] M. F. Gonzalez-Zalba, et al., *Scaling silicon-based quantum computing using CMOS technology: State-of-the-art, Challenges and Perspectives*, arXiv:2011.11753 (2020).

[316] X. Xue, et al., *CMOS-based cryogenic control of silicon quantum circuits*, Nature **593**, 205 (2021).

[317] H. Homulle, et al., *CryoCMOS Hardware Technology a Classical Infrastructure for a Scalable Quantum Computer*, in *Proceedings of the ACM International Conference on Computing Frontiers* (ACM, New York, 2016) pp. 282–287.

[318] L. Geck, et al., *Control electronics for semiconductor spin qubits*, Quantum Sci. Technol. **5**, 015004 (2019).

[319] L. L. Guevel, et al., *19.2 A 110mK 295µW 28nm FDSOI CMOS Quantum Integrated Circuit with a 2.8GHz Excitation and nA Current Sensing of an On-Chip Double Quantum Dot*, in *2020 IEEE International Solid- State Circuits Conference - (ISSCC)* (2020) pp. 306–308, iSSN: 2376-8606.

[320] M. J. Curry, et al., *Single-Shot Readout Performance of Two Heterojunction-Bipolar-Transistor Amplification Circuits at Millikelvin Temperatures*, Scientific Reports **9**, 16976 (2019).

[321] A. Wallraff, et al., *Strong coupling of a single photon to a superconducting qubit using circuit quantum electrodynamics*, Nature **431**, 162 (2004).

[322] J. I. Colless, et al., *Dispersive Readout of a Few-Electron Double Quantum Dot with Fast rf Gate Sensors*, Phys. Rev. Lett. **110**, 046805 (2013).

[323] M. F. Gonzalez-Zalba, S. Barraud, A. J. Ferguson, and A. C. Betz, *Probing the limits of gate-based charge sensing*, Nature Communications **6**, 6084 (2015).

[324] S. D. Liles, et al., *Electrical control of the g-tensor of a single hole in a silicon MOS quantum dot*, arXiv:2012.04985 (2020).

Nico Hendrickx

April 13th 1994, Groningen, The Netherlands

2005–2011	**Secondary School** (cum laude) *Willem Lodewijk Gymnasium, Groningen*
2011–2014	**Bachelor of Science in Applied Physics** (with honours, cum laude) *University of Twente, Enschede*
	Undergraduate research project in the group of prof. dr. ir. H.J.W. Zandvliet *”Rotating a gold nanorod using optically induced torque”*
	Awarded the KNAW Jong Talent Aanmoedigingsprijs
2014–2017	**Master of Science in Applied Physics** (cum laude) *University of Twente, Enschede*
	Research internship in the group of prof. A.S. Dzurak, UNSW, Sydney *”Simulations on spin resonances in silicon qubits”*
	Graduate research project in the group of prof. A. Brinkman *”Transport measurements on S-TI junctions”*
2017–2021	**Ph. D. in experimental physics** *Delft University of Technology, Delft*
	Doctoral research in the group of Dr. M. Veldhorst *Spin qubit arrays in planar germanium*

LIST OF PUBLICATIONS

JOURNAL PAPERS AND PREPRINTS

14. A. Rossi, **N.W. Hendrickx**, A. Sammak, M. Veldhorst, G. Scappucci, M. Kataoka. *Single-hole pump in germanium*, preprint at `https://arxiv.org/abs/2105.14864`.

13. **N.W. Hendrickx**, W.I.L. Lawrie, M. Russ, F. van Riggelen, S.L. de Snoo, R.N. Schouten, A. Sammak, G. Scappucci, M. Veldhorst. *A four-qubit germanium quantum processor*, Nature **591**, 580-585 (2021).

12. M. Lodari*, **N.W. Hendrickx***, W.I.L. Lawrie, T.-K Hsiao, L.M.K. Vandersypen, A. Sammak, M. Veldhorst, G. Scappucci. *Low percolation density and charge noise with holes in germanium*, Materials for quantum technology **1**, 011002 (2021).

11. F. van Riggelen, **N.W. Hendrickx**, W.I.L. Lawrie, A. Sammak, G. Scappucci, M. Veldhorst. *A two-dimensional array of single-hole quantum dots*, Applied Physics Letters **118**, 044002 (2021).

10. W.I.L. Lawrie, **N.W. Hendrickx**, F. van Riggelen, L. Petit, A. Sammak, G. Scappucci, M. Veldhorst. *Spin relaxation benchmarks for hole fillings in germanium*, Nano Letters, **20**, 10, 7237-7242 (2020).

9. **N.W. Hendrickx**, W.I.L. Lawrie, L. Petit, A. Sammak, G. Scappucci, M. Veldhorst *A single-hole spin qubit*, Nature Communications **11**, 3478 (2020).

8. L. Petit, H.G.J. Eenink, M. Russ, W.I.L. Lawrie, **N.W. Hendrickx**, J.S. Clarke, L.M.K. Vandersypen, M. Veldhorst *Universal quantum logic in hot silicon qubits*, Nature **580**, 355-359 (2020).

7. W.I.L. Lawrie, H.G.J. Eenink, **N.W. Hendrickx**, J.M. Boter, L. Petit, S.V. Amitonov, M. Lodari, B. Paquelet Wuetz, C. Volk, S.G.J. Philips, G. Droulers, N. Kalhor, F. van Riggelen, D. Brousse, A. Sammak, L.M.K. Vandersypen, G. Scappucci, M. Veldhorst. *Quantum dot arrays in silicon and germanium*, Applied Physics Letters **116**, 080501 (2020).

6. **N.W. Hendrickx***, D.P. Franke*, A. Sammak, G. Scappucci, M. Veldhorst. *Fast two-qubit logic with holes in germanium*, Nature **577**, 487-491 (2020).

5. A. Sammak, D. Sabbagh, **N.W. Hendrickx**, M. Lodari, B. Paquelet Wuetz, A. Tosato, L. Yeoh, M. Bollani, M. Virgilio, M.A. Schubert, P. Zaumseil, G. Capellini, M. Veldhorst, G. Scappucci. *Shallow and undoped germanium quantum wells: a playground for spin and hybrid quantum technology*, Advanced Functional Materials **29**, 14 (2019).

4. **N.W. Hendrickx**, M.L.V. Tagliaferri, M. Kouwenhoven, R. Li, D.P. Franke, A. Sammak, A. Brinkman, G. Scappucci, M. Veldhorst. *Ballistic supercurrent discretization and micrometer-long Josephson coupling in germanium*, Physical Review B **99**, 075435 (2019).

---

*These authors contributed equally

3. **N.W. Hendrickx**, D.P. Franke, A. Sammak, M. Kouwenhoven, D. Sabbagh, L. Yeoh, R. Li, M.L.V. Tagliaferri, M. Virgilio, G. Capellini, G. Scappucci, M. Veldhorst. *Gate-controlled quantum dots and superconductivity in planar germanium*, Nature Communications **9**, 2835 (2018).

2. M.P. Stehno, **N.W. Hendrickx**, M. Snelder, T. Scholten, Y.K. Huang, M.S. Golden, A. Brinkman. *Conduction spectroscopy of a proximity induced superconducting topological insulator*, Semiconductor Science and Technology **32**, 9 (2017).

1. J.C.C. Hwang, C.H. Yang, M. Veldhorst, **N.W. Hendrickx**, M.A. Fogarty, W. Huang, F.E. Hudson, A. Morello, A.S. Dzurak. *Impact of g-factors and valleys on spin qubits in a silicon double quantum dot*, Physical Review B **96**, 045302 (2017).

POPULAR SCIENCE ARTICLES

3. **N.W. Hendrickx**, M. Veldhorst. *An array of four germanium qubits*, Nature Research Summary, online at: `https://doi.org/10.1038/d41586-021-01116-6`

2. **N.W. Hendrickx**. *Halfgeleiderquantumbits schalen in twee dimensies*, Nederlands Tijdschrift voor Natuurkunde **5**, 10-11 (2021).

1. **N.W. Hendrickx**. *Quantumcomputatie, de rentree van germanium?*, Nederlands Tijdschrift voor Natuurkunde **4**, 22-26 (2020).